Particles in Pores

Stochastic Modeling of Polydisperse Transport

Yuan, Hao; Shapiro, Alexander; Stenby, Erling Halfdan

Publication date:
2012

Document Version
Publisher's PDF, also known as Version of record

Particles in Pores. Stochastic Modeling of Polydisperse Transport

Ph.D. thesis

Hao Yuan

Center for Energy Resources Engineering
Department of Chemical and Biochemical Engineering
Technical University of Denmark
September, 2012

Preface

The present dissertation is written to fulfill the partial requirements of obtaining a Ph.D. degree at Technical University of Denmark. The work has been carried out by the author of this thesis, Hao Yuan, since October 2009 till September 2012 at the Center for Energy Resources Engineering, Department of Chemical and Biochemical Engineering, Technical University of Denmark. Danish Council for Independent Research Technology and Production Sciences (FTP) and DONG Energy E&P are kindly acknowledged for financial support.

The author would like express his deepest gratitude to the supervisors of this project, Associate Prof. Alexander Shapiro and Prof. Erling Stenby. Associate Prof. Alexander Shapiro has played the most academically inspiring and motivated role in the project. Not only did he contribute to discussing, commenting, and writing in the work, but more importantly, he selflessly shared his wisdom and dedicated himself to enlightening the author whenever an obstacle was met. Absolutely without a doubt, the author could not achieve so much in the absence of his help. It has been one of my greatest pleasures, my honor, and my privilege to work with Associate Prof. Alexander Shapiro for the past five years. Prof. Erling Stenby has been most supportive and encouraging throughout the project. He shared an abundance of experiences and perspectives in connecting knowledge and application. Thanks to him, the project has been accomplished from the levels of hypothesis and theories to applications and solutions to engineering problems.

The author would like to thank the advisors from DONG Energy, Jørgen Næumann and Ivanka Orozova-Bekkevold, for their support and advices on the development of the Simulator Software SNY for predicting injectivity decline during waterflooding.

The author would like to express his most sincere gratitude to his colleagues at Technical University of Denmark, especially other coauthors of the publications included here: Prof. Ida Fabricius, Associate Prof. Gürkan Sin, Dr. Sidsel M. Nielsen, Dr. Xuan Zhang and Ms. Esther Rosenbrand. It has been a genuine pleasure working with you all.

The author also would like to thank his colleagues in the Australian School of Petroleum during his academic visit, particularly Prof. Pavel Bedrikovetsky, Dr. Zhenjiang You, and Dr. Alexander Badalyan. Thanks to the hard work and the delightful cooperation of with them, so many fruitful results have been achieved. The author would like to acknowledge the help of K. Aji, C. McLindin, A. Saha and K. Le at the University of Adelaide for the experimental work.

Finally, I would like to thank my beloved family, especially my wife, for their unconditional love and support.

Hao Yuan

Lyngby Kgs., Denmark

September 2012

Summary

Colloid flow, filtration, and migration in porous media are widely observed in important natural and industrial processes, such as pathogen (bacteria) spreading in aquifers, colloid-facilitated migration of heavy metal in soils, mud filtration during drilling wells, injectivity decline during water injection, and deep bed filtration during waste water treatment. The current thesis aims at better understanding the transport and fate of colloids in porous media. A number of methodologies have been applied in this study, such as developing new mathematical models for colloid filtration, comparing the modeling results to experimental observations, uncertainty and sensitivity analysis of the new models, and realizing the pore-scale physics in network models.

This thesis has been compiled in such a way that each chapter arises from a self-contained study targeting a particular problem of colloid filtration: (1) Recent advances in colloids filtration theory; (2) Non-Fickian Transport and heterogeneous attachment of colloids; (3) Uncertainty and sensitivity analysis of models for non-Fickian transport and heterogeneous attachment; (4)Prediction of injectivity decline during waterflooding; (5)Colloid migration and recapture; (6) Induced colloid migration for enhanced oil recovery; (7) Estimating filtration coefficients for straining.

These studies have been spearately published as journal papers, conference papers and book chapters. Nevertheless, they are not independent of one another but logically connected. The connections and main findings can be summarized as follows:

1. The discrepancies between the classical colloid filtration theory and experimental observations have been overviewed in Chapter 1. Many of them are observed under unfavorable attachment conditions, such as hyperexponential and non-monotonic deposition profiles. Such behavior of colloids is attributed to the heterogeneous attachment (Chapters 2 and 3) and the migration of colloids (Chapter 5), respectively.
2. A second reason for the deposition hyperexponentiality is the non-Fickian transport due to the heterogeneity of porous media. It also explains the dispersed and asymmetrical breakthrough curves of tracers in natural porous media (Chapters 2 and 3). Chapter 2 shows that the elliptic equation can be applied to capture the non-

Fickian behaviors of colloids and tracers in porous media. It is closely followed by Chapter 3, the uncertainty and sensitivity analysis of the model predictions and the parameter estimation. Suggestions for experimental design for accurate determination of the model parameters are also provided.

3. Chapters 2 and 3 form a thorough study of the integral model for colloid filtration with non-Fickian transport and heterogeneous attachment. They are followed by the study of applying of such a model in the petroleum industry to predict injectivity decline during waterflooding in Chapter 4. However, the non-Fickian behavior of particles around the injection well is shown not to be significant. The reasons are that the temporal dispersion term is inverse proportional to the particle velocity and that the particle velocity is higher close to the well than that far away from the well.
4. The criterion of an attached colloid particle to be re-entrained by the hydrodynamic drag into the bulk fluid is the torques of detachment exceeding those of attachment. Bearing such a criterion in mind, the erosion of external cake, the migration of surface-associated colloids during one phase flow, and the migration of reservoir fines during two-phase flow are studied in similar fashions (Chapters 4, 5, 6). The erosion of external cakes in the injection wells gives rise to the steady stage of the injectivity and filling rat holes in the well (Chapter 4). The migration of surface-associated colloids gives rise to non-monotonic deposition profiles (Chapter 5). Migration and straining of reservoir fines may enhance oil receovery by increasing the sweep efficiency (Chapter 6).
5. Another important mechanism for particle capture is straining or size exclusion of colloids. Such phenomena are closely tied to the migration of colloids under unfavorable attachment conditions: surface-associated colloids rolling to straining sites (grain-grain contacts, pore throats) in Chapter 5, and the straining of released reservoir fines at pore throats in Chapter 6. However, the straining mechanism is described by nothing more than a straining rate coefficient in these studies. Finally in Chapter 7, a much better understanding of straining is achieved by the study of pore scale physics in a network model. The filtration coefficient for straining is estimated from the particle size and the pore size distributions. A new capture scheme of straining (minimum capture) is proposed to explain the large penentration depths of

colloids in porous media and the power law dependencies of filtration coefficients in the experiments.

Resumé (in Danish)

Kolloid flow, filtrering og migration i porøse medier er almindeligt observeret i både naturlige og industrielle vigtige processer, såsom patogen (bakterier) spredning i grundvandsmagasiner, kolloid-faciliteret migration af tungmetaller i jord, mudder filtrering under bore brønde, injicerbarhed tilbagegang i løbet af vandindsprøjtning, og dyb seng filtrering ved spildevandsbehandling. Denne afhandling sigter mod en bedre forståelse af transport og skæbne af kolloider i porøse medier. Vi bruger mange metoder her, såsom at udvikle nye matematiske modeller for kolloid filtrering, sammenligne modelresultater til eksperimenter, usikkerheds-og følsomhedsanalyse af de nye modeller, og simulere de pore-skala fysik i netværksmodeller.

Denne afhandling er skrevet på en sådan måde, at hvert kapitel er fra en individuel forskning af kolloid filtrering: (1) Nylige fremskridt inden for kolloider filtrering teori, (2) Ikke-Fickian Transport og heterogen fastgørelse af kolloider, (3) Usikkerhed og følsomhedsanalyse af modeller for ikke-Fickian transport og heterogene fastgørelse, (4) Forudsigelse af injicerbarhed tilbagegang i løbet af waterflooding, (5) Colloid migration og recapture (6) Induced kolloid migration for øget olieudvinding, (7) Estimering filtrering koefficienter for størrelse udelukkelse.

Disse undersøgelser er blevet spearately offentliggjort som tidsskriftsartikler, konferencebidrag og bogkapitler. Men de er ikke uafhængige af hinanden, men logisk forbundet. Tilslutninger og hovedkonklusioner kan sammenfattes som følger:

1. Vi overblik forskellene mellem den klassiske kolloid filtrering teori og eksperimenter i kapitel 1. Mange af dem er observeret under ugunstige fastgøring betingelser, såsom hyperexponential og ikke-monoton deposition profiler. De er på grund af den heterogene fastgørelse (Kapitler 2 og 3) og migration af tilfangetagne kolloider (Kapitel 5), henholdsvis.
2. En anden grund til udfældning hyperexponentiality er den ikke-Fickian transport på grund af heterogeniteten af de porøse medier. Det forklarer også de dispergerede og asymmetrisk gennembrud kurver af sporstoffer i naturlige porøse medier (Kapiteler 2 og 3). Kapitel 2 viser, at den elliptiske ligning kan anvendes

til at indfange ikke-Fickian adfærd kolloider og sporstoffer i de porøse medier. Det er tæt fulgt af kapitel 3, usikkerheds-og følsomhedsanalyse af modellen forudsigelser og parameter estimering. Tips af forsøgsplaner til nøjagtig bestemmelse af parametrene er også tilvejebragt.

3. Kapiteler 2 og 3 indeholder en detaljeret analyse af den integrerede model for kolloid filtrering med ikke-Fickian transport og heterogen vedhæftet fil. Det efterfølges af en undersøgelse af anvendelsen af en sådan model i olieindustrien til at forudsige injicerbarhed fald under waterflooding i kapitel 4, men den ikke-Fickian opførsel af partiklerne i injektionsbrønden er ikke signifikant. Dette skyldes, at den tidsmæssige dispersion sigt er omvendt proportional med partiklens hastighed og at partikelhastigheden er højere tæt på det godt end det er langt væk fra brønden.
4. Kriteriet om en vedhæftet kolloid partikel, der skal re-medrevet af den hydrodynamiske kraft er, at momenter af separation overstiger momenter af fastgørelse. Udhulingen af ekstern kage, migreringen af overflade-associerede kolloider i løbet af en-fase flow, og migrationen af reservoiret bøder i løbet af tofasestrømning studeres i lignende mode (Kapiteler 4, 5, 6). Erosionen af eksterne kager i injektionsbrønde giver anledning til den konstante fase af injicerbarhed og påfyldning rotte huller i brønden (Kapitel 4). Migrationen af overflade-associerede kolloider giver anledning til ikke-monotone deposition profiler (Kapitel 5). Migration og størrelse udelukkelse af reservoir bøder kan øge olie receovery ved at øge sweep effektivitet (Kapitel 6).
5. En anden vigtig mekanisme til partikel capture er størrelse udelukkelse af kolloider. Sådanne fænomener er tæt knyttet til migration af kolloider under ugunstige vedhæftede betingelser: overflade-associerede kolloider rullende at belaste steder (korn-korn kontakter, pore halsen) i Kapitel 5, og den belastende af frigivne reservoir bøder på pore struber i Kapitel 6. Imidlertid er mekanismen kun beskrevet af en størrelse eksklusion koefficient. Endelig i Kapitel 7, har vi en meget bedre forståelse af størrelse eksklusion med studiet af pore skala fysik i et netværk model. Filtreringen koefficient for størrelse eksklusion skønnes ud fra den partikelstørrelse og porestørrelse fordelinger. En ny mekanisme

størrelseseksklusion (minimum capture) foreslås. Den forklarer de store penentration dybder af kolloider i porøse medier og power lov afhængigheder af filtrering koefficienter i eksperimenterne.

List of publications

Book chapters:

1. H. Yuan, A.A. Shapiro, Colloid Transport and Retention: Recent Advances in Colloids Filtration Theory, in: P. Ray (Ed.), Colloids: Classification, Properties and Applications, NOVA Science Publisher, New York, 2012. **(Chapter 1)**
2. A.A. Shapiro, H. Yuan, Application of stochastic approaches to modeling suspension flow in porous media, in: A. Skogseid, V. Fasano (Eds.) Statistical Mechanics and Random Walks: Principles, Processes and Applications, NOVA, New York, 2011. **(Partly in Chapter 1)**

Peer reviewed journal publications:

1. H. Yuan, A.A. Shapiro, Modeling non-Fickian transport and hyperexponential deposition for deep bed filtration, Chemical Engineering Journal, 162 (2010) 974-988. **(Chapter 2)**
2. H. Yuan, A.A. Shapiro, A mathematical model for non-monotonic deposition profiles in deep bed filtration systems, Chemical Engineering Journal, 166 (2011) 105-115. **(Chapter 5)**
3. H. Yuan, G. Sin, Uncertainty and sensitivity analysis of filtration models for non-Fickian transport and hyperexponential deposition, Chemical Engineering Journal, 168 (2011) 635-648. **(Chapter 3)**
4. H. Yuan**,** A.A. Shapiro, Induced migration of fines during waterflooding in communicating layer-cake reservoirs, Journal of Petroleum Science and Engineering 78(3-4) (2011) 618-626. **(Chapter 6)**
5. H. Yuan, X. Zhang, A.A. Shapiro, E.H. Stenby, Crossflow and water banks in viscous dominant regimes of waterflooding, Petroleum Science and Technology [in press] (2013).

6. H. Yuan, A. Shapiro, Z. You, A. Badalyan, Estimating filtration coefficients for straining from percolation and random walk theories, Chemical Engineering Journal, 210 (2012) 63-73 **(Chapter 7)**

Oral presentations:

1. Particles and Pores: New transport and capture mechanisms, CERE annual meeting, Copenhagen, Jun. 2011
2. Formation damage: an old enemy or a new EOR technology, SPE monthly meeting in Copenhagen, Oct. 2011
3. Deep bed filtration with application to problems in petroleum industry, BIT's 2nd Well stimulation and EOR conference, May 2011
4. Advanced Waterflooding in Chalk Reservoirs: Crude Oil/Brine Interaction Study, BIT's 2nd Well stimulation and EOR conference, May 2011

Non-peer reviewed publications:

1. E. Rosenbrand, I.L. Fabricius, H. Yuan, Thermally induced permeability reduction due to particle migration in sandstones: the effect of temperature on kaolinite mobilisation and aggregation, in: Thirty-Seventh Workshop on Geothermal Reservoir Engineering, Stanford University, Stanford University, Stanford, California, 2012.
2. H. Yuan, S.M. Nielsen, A.A. Shapiro, P. Bedrikovetsky, A New Comprehensive Approach for Predicting Injectivity Decline during Waterflooding, in: SPE Europec/EAGE Annual Conference, Society of Petroleum Engineers, Copenhagen, Denmark, 2012, SPE 154509. **(Chapter 4)**

Software Development

1. SNY 1.0 Simulator for predicting injectivity decline during waterflooding

2. SNY 2.0 Simulator for predicting injectivity decline during waterflooding, external cake erosion module added comparing to SNY 1.0 **(Chapter 4)**

Publications in preparation

1. H. Yuan, Z. You, A. Shapiro, P. Bedrikovetsky, Improved population balance model for straining-dominant deep bed filtration using network calculations, to be submitted.
2. H. Yuan, Z. You, A. Shapiro, P. Bedrikovetsky, Percolation theory for size-exclusion suspension flow in porous media, to be submitted.
3. H. Yuan, Z. You, A. Shapiro, P. Bedrikovetsky Effects of dispersion on size-exclusion suspension flow in porous media, to be submitted.

Table of Contents

1 Recent advances in colloids filtration theory

There is a fast growing body of research on the transport and fate of colloids in porous media in the past decades. The reason for colloid filtration attracting so much attention and interest is mainly attributed to the following points: (1) the phenomenon is widely observed in both natural and industrial processes; (2) these processes are of great importance due to high risk or high impact; (3) understanding the transport and fate of colloids is paramount in predicting, controlling, or preventing these processes.

This chapter presents an overview of the recent advances in the colloid filtration theory. It reviews the new approaches that overcome the difficulties to incorporate surface charge heterogeneity, straining effects, non-Fickian transport, and migration of deposited particles. The current understanding of the mechanisms, factors, and mathematical models at different scales are reviewed. Remedies for reducing the discrepancies between model predictions and experimental observations are recommended.

1.1 Introduction

Colloids are the particles dispersed in liquids (in most applications, water or water solutions) with the sizes in between dissolved macromolecules and suspended particles that resist rapid sedimentation. The typical size of colloid particles usually ranges from 10 nm to 10 μm [1-3]. Colloids in nature include mineral fragments, microbes, and plant decay debris. The mineral fragments, such as silicate clay, are mainly derived from soil and formation rocks [4-7]. These particles can be released into or from soil, ground water and oil reservoirs via a variety of processes.

There is a considerable and ongoing effort aimed at understanding and predicting the transport, the deposition and the release of colloids in both synthetic (model) and natural porous media [8-13]. The fate and transport of colloids in porous media is of a great concern for the following reasons, among other: (i) The migration of colloids may facilitate the transport of low-solubility contaminants [14-21]; (ii) The spread of pathogenic microbes during waste water reclamation and aquifer recharge poses a risk to

public health [22-31]; (iii) Deposition and migration of colloids cause permeability damage, which subsequently leads to injectivity decline and productivity decline [32-39]; (iv) Injection of the microbes producing surfactants may enhance oil recovery [40-42].

The fundamental filtration theory has been focused on the transport and fate of colloid at different scales: the interface scale, the collector (median grain) scale, and the pore scale. At the interface scale, the interfacial energy of a particle at the solid-water interface (SWI), the air-water interface (AWI), and the colloid-colloid interface can be quantified. Such a technique is used to predict attachment conditions and colloid stability [43-48]. At the collector scale, the flow field of water around a collector or an air bubble can be calculated. The probability of flowing particles being in contact with the collector can be quantified [49-52]. At the pore scale, the fate of colloids is studied in the presence of multiple grains and pores (grain-grain contacts) or solid-water-air triple points [53-55]. The favorable sites of attachment, straining and size exclusion can be identified in different pore geometries.

At the interface scale, the conditions for attachment and the colloid stability are primarily determined by the interaction energies [1, 38, 44]. The interactions can be classified into two main categories: the DLVO, and the non-DLVO interactions. In the classical DLVO theory, the total interaction energy is composed of electrostatic and van der Waals energies [43, 48, 56]. The available expressions for the electrostatic energy are derived from the Poisson-Boltzmann equation for surface-charged bodies of various geometries on the basis of the electrical double layer theory. The classical DLVO theory has been widely accepted as a powerful tool to predict attachment conditions and colloid stability. Nevertheless, it fails to describe biotic and abiotic colloidal behavior in some cases. The discrepancies are attributed to the so-called non-DLVO interactions. Such interactions may include hydrogen bonding, hydrophobic interaction, capillary forces, Lewis acid base interactions, and steric interactions [1, 3, 46, 57].

At the collector scale, the study of deposition rates takes into account the transport of particles from the bulk fluid to the collector surface and the capture via surface attachment. The approaches to simulating the colloid transport can be classified into two types, Lagrangian and Eulerian. The Lagrangian approach focuses on the motion of a

single particle that is governed by Newton's second law. The particle trajectory in a flowing fluid is tracked [58-60]. The Eulerian approach accounts for evolution of the concentration or of the probability density of particles [61-63]. The Lagrangian approach has been extensively applied to describe the capture of non-Brownian particles, the trajectories of which are deterministic and can be solved analytically. Incorporation of Brownian motion into the Lagrangian approach, however, entails tedious and time-consuming step-by-step integration of the stochastic equation. Such an approach is essential for applications like industrial filtration, where the filter efficiency is determined by mesoscale particle behavior in a filter, which structure is presumably known [51, 64-67]. In contrast, the Eulerian approach is more attractive and widely applied for description of filtration in natural porous media and other media of stochastic structures, since it can describe more easily collective particle behavior and takes into account their Brownian motion. The implementation of Eulerian approach requires much less computational effort compared to the Lagrangian approach with Brownian motion, which may require multiscale treatment[68-70] .

In the Eulerian approach, the motion of particles is characterized by the advection flux, the diffusive flux and the external-forced flux, caused by such forces as gravity, the DLVO forces, and the non-DLVO forces [1, 3, 13]. The convective-diffusion equation is usually solved in an ideal representation for the porous medium, such as Happel's sphere-in-cell model [71]. It assumes that identical sphere collectors enveloped in fluid shells are packed densely. The boundary conditions on the collector surface reflect the attachment conditions for the colloids. The most common boundary condition is the perfect-sink model which assumes the disappearance of particles at the collector surface, namely irreversible capture of particles on the surface [63, 72, 73]. Such a boundary condition completely neglects the accumulation and the release of immobilized particles. A more realistic boundary condition is the non-penetration model, which overcomes the above limitations [74-78].

At the pore scale, the convection-diffusion equation is also solved in between packed collectors or in the pores with different shapes. The study of colloid retention, in contrast to that at the collector scale, takes into account both straining and size exclusion at grain-

grain contacts or constrictions. It is suited for examining different colloid capture mechanisms in a variety of pore geometries [79-82]. Such a technique can also be applied to study unsaturated systems, such as the retention at triple contact points (solid-water-air) [53, 83, 84].

The goal of the fundamental filtration theory at the interface, the collector and the pore scales is to arrive at an analytical deposition model which can predict the single collector removal efficiency. It is a parameter reflecting the colloid removal efficiency by a single collector under known physical and chemical conditions [1, 13, 49]. Under favorable attachment conditions, the single collector removal efficiency can be approximated by the single collector contact efficiency since the physical contact can lead to direct chemical capture. Under unfavorable attachment conditions the efficiency must be derived from the product of the single collector contact efficiency and the colloid collision efficiency [1, 45, 85, 86]. The colloid collision efficiency is a parameter reflecting the probability of effective collisions that overcome the energy barrier and lead to attachment.

There have been several theoretical approaches to expressing these efficiencies analytically. The Smoluchowski-Levich approximations [87, 88] and the interaction-force-boundary-layer (IFBL) approximations [89, 90] were used to calculate the single collector removal efficiency under favorable attachment and unfavorable attachment conditions respectively. The Rajagopalan and Tien correlation equation was extensively used for calculating the single collector contact efficiency. Recently, Tufenkji and Elimelech [91] improved this correlation equation by considering the hydrodynamic and van der Waals effects on the deposition of particles by Brownian diffusion. Two types of collision efficiency were proposed to account for the attachment via the primary energy minimum (IFBL) [89, 90] and the attachment via the secondary energy minimum [92-94].

The derived deposition models (single collector removal efficiency) are commonly used to complete the system of equations for the mass balance of colloids at the macro-scale [1, 38, 95-97]. In this approach, the mass balance of suspended colloids is characterized by the advection- dispersion transport and the deposition while the release of retained colloids is neglected. The advection-dispersion equation (ADE) with a single sink term is also referred to as the classical filtration theory approach (CFT) or the perfect sink model

[1, 13]. It can be solved either numerically or, in many cases, analytically [98-100]. The classical CFT, however, is derived under a number of over-simplified assumptions: (i) irreversible deposition, (ii) uniform flow field at the pore scale, (iii) uniform surface charges of colloids and porous media, (iv) straining or size exclusion is not considered. It should be noted that the classical CFT may be based on the classical DLVO theory for the description of interface interactions, but this is not always the case. The Non-DLVO interface interactions may also be incorporated into the classical CFT [1, 3, 13, 46, 47].

There is a growing body of studies suggesting that the classical CFT fails to fully describe a number of practically important processes or phenomena, such as filtration under unfavorable attachment conditions and filtration in stochastically (physically or geochemically) heterogeneous porous media [12, 101-105]. The discrepancies between the model predictions and experimental observations are as follows. Under unfavorable attachment conditions, the classical CFT and the DLVO theory predict the collision efficiencies several orders of magnitude smaller than those observed experimentally. Experimental collision efficiencies and critical deposition are insensitive to particle sizes [1, 86, 106-109]. Hyperexponential or non-monotonic deposition profiles are observed rather than the exponential deposition decay predicted by the classical CFT [101, 102, 110-113]. Long tails are observed in the breakthrough curves [111, 112]. In the porous media with irregular-shaped median grains, hyperexponential deposition is also often observed [79-81, 114, 115]. In heterogeneous porous media, both early arrival and delay of particles are observed in the breakthrough curves [10, 11, 104, 116-118].

Large research efforts were devoted to explaining the above observed discrepancies. Under unfavorable attachment conditions, underestimation of the collision efficiency, insensitivity to particle sizes, and hyperexponential deposition were mainly attributed to the deposition via the secondary energy minimum [92, 93, 101, 103, 119, 120] and heterogeneity of the surface charges [13, 73, 101-103, 110, 113]. Apart from the surface charge heterogeneity, the deposition hyperexponentiality has also been attributed to the effects of straining [79, 121, 122] and non-Fickian transport due to physical heterogeneity of porous media [104, 105, 123]. The non-Fickian transport was also claimed to be responsible for the early arrival and delay of particles [10, 11, 104, 105, 117, 124, 125].

The algebraic-decaying long tails in the breakthrough curves after the end of injection were either attributed to the migration of captured particles [80, 126-133] or to the physical non-equilibrium between the mobile and the immobile regions [134]. Rarely observed non-monotonic deposition profiles were either attributed to the migration of surface-attached particles via weak association or to the detachment of large aggregates [111, 135, 136].

1.2 Traditional theories

This section reviews the traditional theories of colloid filtration, including the DLVO theory for surface interactions, the Eulerian approach for colloid transport and retention at the collector scale, and the macroscopic approach for modeling colloid filtration in porous media. These studies related to the three different scales have been the theoretical foundations of many further developments and consistency examinations for the colloid filtration theory.

1.2.1 DLVO surface interactions

The traditional theory for the colloid surface interactions is the Derjaguin-Landau-Verwey-Overbeek (DLVO) theory. The interaction energy between the two surfaces is calculated as the sum of the electrical double-layer interaction and the van der Waals interaction energies:

$$\Phi_{total} = \Phi_{dl} + \Phi_{vdW}, \tag{1.1}$$

where Φ_{total} Φ_{dl} and Φ_{vdW} are the total, the double-layer, and the van der Waals interaction energies respectively. The expressions for the electrical double-layer interaction energy are available for varying geometries and different assumptions [1, 44]. These expressions were derived on the basis of the Poisson equation for the charge density potential and the Boltzmann equation for the ion concentration dependency on the

potential. The commonly applied expression for Φ_{dl} is based on the sphere-sphere interactions [1]:

$$\Phi_{dl} = 64\pi \frac{a_1 a_2}{a_1 + a_2} \left(\frac{kT}{ze} \right) \tanh\left(\frac{ze\psi_1}{kT} \right) \tanh\left(\frac{ze\psi_2}{kT} \right) \exp(-\kappa h), \tag{1.2}$$

where k is the Boltzmann constant, T is the temperature, a is the colloid radius, z is the valence of the ions, e is the elementary charge, h is the separation distance between two surfaces, and the subscripts '1' and '2' represent the two surfaces. The Debye reciprocal length κ is calculated by:

$$\kappa = \sqrt{\frac{2e^2 N_A I}{\varepsilon \varepsilon_0 kT}} \tag{1.3}$$

where ε is the dielectric constant, ε_0 is the vacuum permittivity, and I is the ionic strength. For the colloid-collector system, the radius of the collector is assumed to be far larger than that of the colloid particle, leading to $a_1 a_2 / (a_1 + a_2) \approx a_1$. The zeta potentials measured by electrophoresis are usually applied as substitutions for the surface potentials.

The classical approach to evaluate the van der Waals interaction between two bodies is derived by Hamaker [137] from the pairwise summation of all the relevant interaction energies. The expressions stemming from this approach can be split into the product of a purely geometric multiplier and of the so-called Hamaker constant. The total Hamaker constant of the different bodies is typically estimated by the geometrical mean value of the individual Hamaker constants [138]:

$$\begin{aligned} A_{12} &= \sqrt{A_{11} A_{22}}; \\ A_{123} &= \left(\sqrt{A_{11}} - \sqrt{A_{33}} \right) \left(\sqrt{A_{22}} - \sqrt{A_{33}} \right) \end{aligned} \tag{1.4}$$

where A_{11} and A_{22} are the Hamaker constants for the two solid bodies, A_{33} is the Hamaker constant for the aqueous solution, A_{12} A_{123} are the resulted mean Hamaker constants for multi-body system. The approximate Hamaker constant for a material can

be expressed in terms of the limiting refractive index and characteristic dispersion frequency [137]. The geometrical mean assumption is only valid if the dispersion frequencies of the particle and the medium are not very different. For sphere-sphere interactions, Φ_{vdW} can be calculated by [56]:

$$\Phi_{vdW} = \frac{A_{123}}{6h} \frac{a_1 a_2}{a_1 + a_2} \left(1 + \frac{14h}{\lambda}\right)^{-1} \tag{1.5}$$

where λ is the characteristic wavelength, usually 100 *nm* [56]. It should be noted that the van der Waals forces may be retarded, since electrodynamic interactions leading to dispersion forces are propagated at the finite speed of electromagnetic radiation. Retardation effects have been revealed experimentally by Israelachvili and his coauthors [139]. The last term on the right hand side of Equation (1.5) results from this retardation effect, which is implicitly included in the full Lifshitz treatment [140]. The van der Waals interaction is attractive in the systems of polystyrene-water-glass and polystyrene-water-quartz, while it is repulsive in the system of polystyrene-water-air [138].

The DLVO theory has been widely applied as a tool to explore the influence of the solution chemistry and the particle size on the attachment conditions. Figure 1.1 presents the comparison of colloid radii and ionic strengths for the polystyrene-quartz-water system. The DLVO calculations exhibit significant energy barrier to attachment via the primary energy minimum. Under such unfavorable conditions the effect of colloid interactions is often expressed in terms of the collision efficiency, which is the ratio between the number of effective collisions leading to the attachment (via the primary energy or the secondary energy minima) and the total number of collisions.

In many cases, the attachment condition and colloid stability can be successfully predicted by such calculations as shown in Figure 1.1. For example, the larger the energy barriers are as in Figure 1.1, the more stable the colloidal system is. Nevertheless, the analytical expressions for interface interaction energies are based on the two strong assumptions: (i) the colloids and the collectors possess uniform and regular shapes; (ii) the surface charges of colloids and collectors are homogeneous.

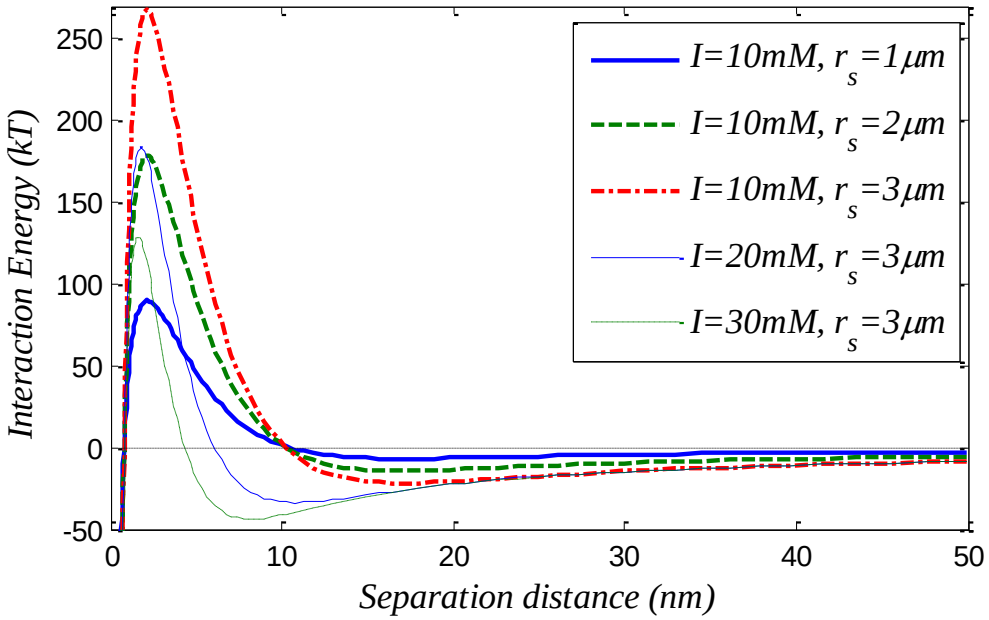

Figure 1.1 Particle size and ionic strength effects on the interaction energy, colloid surface potential is -77mV, collector surface potential is -35mV, polystyrene-quartz-water system

1.2.2 Colloid transport

At the interface scale, the attachment condition is primarily determined by the surface interaction energies between the collectors and the colloids in their close proximity. The deposition rate, however, is dependent on both the collector-colloid surface interactions and the rate with which the particles are transported toward the collector walls. There are two approaches for calculating the deposition rate on a stationary collector surface, the Lagrangian and the Eulerian approaches. As mentioned above, the Lagrangian approach tracks the trajectory of each single colloid governed by Newton's second law, leading to the Langevin-Ito stochastic differential equations for the particles in the flow [141-143], while the Eulerian approach (the Fokker-Planck-Kolmogorov-Feller partial differential equation for the particle distribution) treats the particles as an ensemble [144-146]. Introduction of the Brownian motion into the Lagrangian approach leads to a series of step-by-step integration of the stochastic equation which requires intensive computation. In contrast, the Brownian motion can be easily taken into account by the diffusion term in the convective-diffusion equation within the Eulerian method. Extensive discussions on

the two approaches are available in the literature [50, 63, 147, 148], while only the Eulerian method is discussed in details here.

The convective diffusion equation describing the concentration or the probability density of colloid particles is usually given by [13, 62, 63, 85]:

$$\frac{\partial c}{\partial t} + \nabla \cdot \mathbf{J} = Q \tag{1.6}$$

where c is the particle concentration with regard to pore volume, Q is the source term, and $\mathbf{J}$ is the flux which can be decomposed into the advection flux, the diffusive flux, and the external-forced flux:

$$\mathbf{J} = \mathbf{u}c - \mathbf{D}\nabla c + \frac{\mathbf{D} \cdot \mathbf{F}}{kT} c \tag{1.7}$$

Here $\mathbf{D}$ is the diffusion tensor, $\mathbf{u}$ is the fluid velocity field which can be found by solving the Navier-Stokes equation in the corresponding geometry, and $\mathbf{F}$ is the external force vector determined by the total colloid interaction energy:

$$\mathbf{F} = -\nabla \Phi_{total} \tag{1.8}$$

The non-DLVO forces can also contribute to Equation (1.8), if the non-DLVO interaction energies are added in Equation (1.1).

Equation (1.6) can be solved numerically and provide insight into the deposition rate when proper boundary conditions at the collector surface are given. Due to insufficient knowledge of the physical and chemical conditions at the surfaces, only simplified forms of the boundary conditions have been studied. Two types of the boundary conditions are commonly adopted: the perfect sink model and the non-penetration model.

The most commonly used boundary condition is the perfect sink model. This approach assumes the suspended concentration to be zero or constant convective flux at the surface or close proximity of a collector, corresponding to irreversible capture of colloid at the collector surface [74, 149-151]. Mathematically, the boundary condition can be expressed by:

$$c\big|_{h=\Delta} = 0, \quad or \quad \left.\frac{\partial(uc)}{\partial h}\right|_{h=\Delta} = 0; \tag{1.9}$$

The first boundary condition and the second boundary condition in Equation (1.9) were proved to produce the same results by Song and Elimelech [73]. The second boundary condition is the constant convective flux condition, namely that the radial flux at the collector surface equals to that at the fluid shell (forward difference regime), and that the particles may flow through the collector surface and disappear. The value of Δ was assumed to be either zero or an arbitrary separation distance beyond the surface interaction energy barrier. Equation (1.9) and non-zero values of Δ reflect the physics that after overcoming the energy barrier the particle will effectively captured and that the convective flux will be zero. The particles at this point will be "penetrate" in the collector body and "disappear" due to the external forces.

Based on the perfect sink assumption, many expressions for the deposition rate have been established, such as the Smoluchowski-Levich and the interaction force boundary layer (IFBL) approximations of the single collector removal efficiency. Nevertheless, one major disadvantage of this approach is the neglect of the accumulation of retained particles on the collector surface. On the contrary, the next boundary condition, the non-penetration model, takes into account the deposition concentration at the collector surface [63, 74].

In the non-penetration model, flowing particles are prohibited to penetrate the collector surface or disappear. Mass balance is formulated for two particle populations, the mobile and the immobile species. Mathematically the boundary condition takes the following form:

$$J_{\perp}\big|_{h=0} = 0; \tag{1.10}$$

$J_{\perp}$ is the total flux perpendicular to the collector surface. Equation (1.10) neglects the growth of the deposition thickness on the collector surface. The source term Q_{in} Equation (1.6) may also be used to account the non-DLVO interactions.

1.2.3 Porous medium model

One of the simplest and widely applied porous medium models for colloid filtration is Happel's sphere-in-cell representation [1, 13, 51, 71, 85, 152-154] . In the Happel model, the packed bed is composed of identical spherical grains enveloped by fluid shells, as seen in Figure 1.2. The thickness of a fluid shell b is selected so that the overall porosity of the medium is maintained for each single collector:

$$b = r_c \left(1-\phi\right)^{-\frac{1}{3}} \tag{1.11}$$

where r_c is the radius of the collector (median grain) and ϕ is the overall medium porosity. The convection-diffusion equation can be solved numerically in the Happel porous medium model, with the flow field derived from the Navier-Stokes equation.

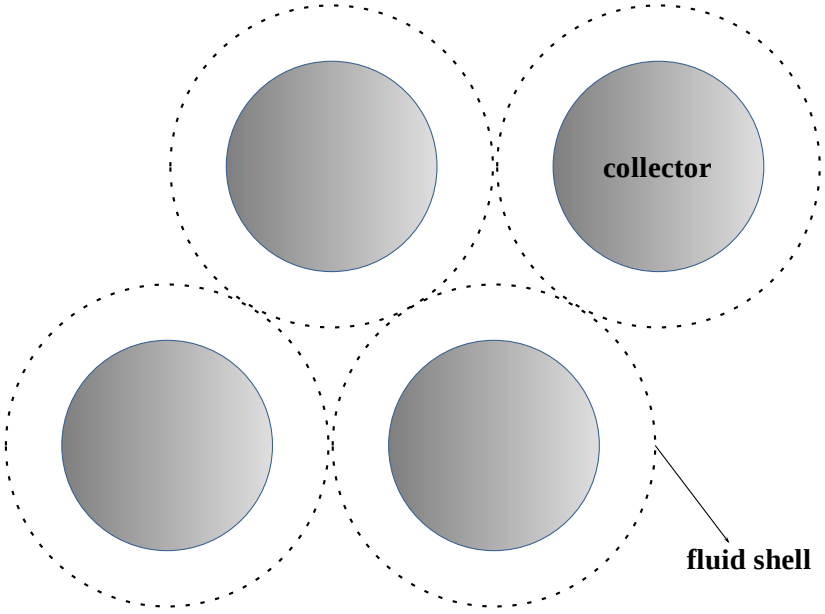

Figure 1.2 Happel's representation of granular porous media

Many theoretical studies were performed with other porous medium models, such as parallel capillaries, capillary networks, and fibers [106, 155-161]. A 2D network of capillaries with the nodes representing pore bodies amd the bonds for pore throats will be discussed in details in Chapter 7 .

These models were suited for the filtration in some specific natural and engineering processes, such as the fines in petroleum reservoirs, the industrial filtration with filter presses, and the membrane filtration. Generally, selection of a model depends on particular tasks of a researcher and his ideas about the structure of the porous medium under study. In this chapter we will refer to the Happel model as a specific example.

1.2.4 Single collector removal efficiency

A useful concept for studying the deposition rates is the single collector removal efficiency, a dimensionless parameter as defined in Equation (1.12). This parameter is convenient to incorporate into the classical CFT of colloid transport and retention, which will be discussed later.

$$\eta = \frac{rate\ of\ \ particle\ capture\ on\ a\ collector\ surface}{particle\ \ flux\ toward\ the\ \ projected\ area\ of\ the\ collector} \tag{1.12}$$

The removal efficiency can be found from the numerical solution of the convective-diffusion equation or the trajectory equation in any given geometry of collectors. The main disadvantage of this approach is the lack of exact analytical solutions. Thus, an approximate expression for the efficiency is desirable.

Ruckenstein and Prieve [89] and Spielman and Friedlander [90] derived an approximate analytical solution for the deposition rate for Brownian particles under the condition of repulsive double-layer interactions. This approach, as the most classical theory for the removal efficiency under unfavorable attachment conditions, is often referred to as the interaction force boundary layer (IFBL) approximation. The interaction force boundary layer represents the transport in the close proximity of a surface, where the surface interactions dominate and the convective transport is negligible. The thickness of the layer is usually deemed to be in the same order of magnitude as the Debye length. The interaction forces are neglected outside this layer, where the convective transport dominates.

As derived in [89, 90], the single collector removal efficiency may be approximated by:

$$\eta = 4.04 A_s^{\frac{1}{3}} \left(\frac{D_\infty}{2 r_c U} \right)^{\frac{2}{3}} \left(\frac{\beta}{1+\beta} \right) S(\beta) \tag{1.13}$$

$$\beta = \frac{\sqrt[3]{2}}{3} \Gamma\left(\frac{1}{3}\right) A_s^{\frac{-1}{3}} \left(\frac{D_\infty}{r_c U} \right)^{\frac{1}{3}} \left(\frac{k_F r_c}{D_\infty} \right) \tag{1.14}$$

where A_s is a porosity-dependent parameter of Happel's model ($A_s \approx 38$ for porosity of 0.4), D_∞ is the bulk diffusion coefficient, U is the fluid approach velocity, and $S(\beta)$ is a slowly varying function of β with tabulated numerical values [90]. k_F is the pseudo-first-order rate constant given by [90, 162]:

$$k_F = D_\infty \left\{ \int_0^\infty \left[f(h, r_s) \exp\left(\frac{\Phi_{total}}{kT} \right) - 1 \right] dh \right\}^{-1} \tag{1.15}$$

where $f(h, r_s)$ is a hydrodynamic function which accounts for the reduced mobility of the colloids in close proximity of collectors. An approximation for this function is suggested by Dahneke [162]:

$$f(h, r_s) = 1 + \frac{r_s}{h} \tag{1.16}$$

It is worth mentioning that Equation (1.13) in the absence of all the parts depending on β is reduced to the Smoluchowski-Levich approximation for the single collector removal efficiency for Brownian particles under favorable attachment conditions. The efficiency reflects how fast the Brownian motion can bring particles to the collector surface. It is regarded as the single collector contact efficiency in the IFBL approximation:

$$\eta_0 = 4.04 A_s^{\frac{1}{3}} \left(\frac{D_\infty}{2 r_c U} \right)^{\frac{2}{3}} \tag{1.17}$$

The parts depending on β in Equation (1.13) are responsible for the interactions between the hydrodynamic forces and the colloidal forces. They are usually referred to as the

collision efficiency: the probability of the fact that a collision results in attachment. Here in IFBL approximation, these terms reflect the effective collisions that overcome the repulsive double-layer force and drag the colloids into the primary energy minimum:

$$\alpha = \left(\frac{\beta}{1+\beta} \right) S(\beta) \tag{1.18}$$

Typical values of the collision efficiency vary from 10^{-3} to 1 [1, 85, 86, 163-165]. A more general form of the single collector removal efficiency can be inferred by substituting Equations (1.17) and (1.18) into Equation (1.13). The single collector removal efficiency becomes the product of the single collector contact efficiency and the collision efficiency:

$$\eta = \eta_0 \alpha \tag{1.19}$$

The IFBL approximation takes into account only the colloid transport by Brownian motion to the collector surface for the single collector contact efficiency (see Equation (1.17)). This assumption makes it impossible to apply the IFBL approximation to the capture of larger particles, where the effects of interception and gravity are not negligible. Limitations and further developments of the single collector contact efficiency will be discussed in the following sections.

1.2.5 Classical CFT approach

The goal of introducing the single collector removal efficiency is to express the deposition rate explicitly, and to further apply this expression in the macroscopic approach for modeling colloid transport and retention. At the macroscopic scale, the transport and retention of colloid particles is usually described by an advection-dispersion equation (ADE) with a first-order kinetic sink term representing the deposition rate of colloid. Such an approach is also referred to as the classical colloid filtration theory (CFT) approach. For a simple 1-D problem, it is written as [1, 95]:

$$\frac{\partial c}{\partial t} + v\frac{\partial c}{\partial x} = D\frac{\partial^2 c}{\partial x^2} - \frac{\rho_b}{\phi}\frac{\partial s}{\partial t} \tag{1.20}$$

where c is the bulk concentration of colloid with regard to pore volume, s is the deposited concentration with regard to unit mass of the porous medium, ρ_b is the bulk density of the dry porous medium, v and D are the particle velocity and dispersion coefficient. The accumulation of deposition is calculated by:

$$\frac{\rho_b}{\phi}\frac{\partial s}{\partial t} = k_d c \tag{1.21}$$

where k_d is usually referred to as the deposition rate constant, related to the filtration coefficient in a deep-bed filtration process: $\lambda = k_d / v$. The deposition rate constant is calculated on the basis of the single collector removal efficiency:

$$k_d = \left[\frac{3}{4}\frac{(1-\phi)}{r_c}v\right]\eta \tag{1.22}$$

It can be seen from the above expression that the deposition rate constant is a parameter depending on the fluid velocity, while the filtration coefficient is not. The multiplier in square parentheses in Equation (1.22) represents the particle flux towards the projected area of a single collector. This multiplier may vary depending on the particular flow model on micro-level. For example, for the sphere-in-cell envelope (Happel) model of the porous space, multiplier $(1-\phi)$ in Equation (1.22) should be replaced by $(1-\phi)^{1/3}$ [1, 13, 166].

The analytical solutions to Equation (1.20) with various boundary conditions have been studied in the literature [98-100]. For the steady state flow problem (although with non-steady deposition), the temporal derivative in Equation (1.20) is zero. The analytical solutions for clean bed filtration in such cases can be expressed in terms of the logarithm of attenuation. Neglecting dispersion, the solutions are given by:

$$\ln\left[\frac{c(x)}{c_0}\right] = -\lambda x \tag{1.23}$$

$$\ln\left(\frac{s(x,t)\rho_b / \phi}{c_0 k_d t}\right) = -\lambda x \tag{1.24}$$

Such solutions are commonly applied for examining the agreement between the experimental collision efficiency and the model predictions. The collision efficiency determined from a column experiment can be calculated by:

$$\alpha = -\frac{4}{3}\frac{r_c}{L(1-\phi)\eta_0}\ln\left(\frac{c_L}{c_0}\right) \tag{1.25}$$

where L is the column length, and c_L is the effluent concentration at $x = L$. It should be noted that an accurate determination of the collision efficiency from experiments is essentially dependent on the accuracy of the single collector constant efficiency. More accurate expressions of the single collector constant efficiency will be discussed later.

1.2.6 Equilibrium and non-equilibrium attachment

Beside the permanent deposition via the primary energy minimum, the Langmuir and Freundlich isotherms were applied to describe the equilibrium "adsorption" of colloids [132, 167-175]. Such theories have been widely applied to describe the equilibrium "adsorption" of multi-components in the flowing fluid, such as solutes, onto solid surfaces [99, 100, 176-179]. The simplest form of isotherm is the linear dependency $s = K_{eq}c$, where K_{eq} is the equilibrium attachment constant. The mass balance equation for the CFT taking into account the equilibrium "adsorption" can be rewritten as:

$$R\frac{\partial c}{\partial t} + v\frac{\partial c}{\partial x} = D\frac{\partial^2 c}{\partial x^2} \tag{1.26}$$

where R is the retardation factor calculated as $R = 1 + \rho_b K_{eq} / \phi$. It can be seen from the above equation that the equilibrium "adsorption" mechanism does not result in actual

retention of colloid particles, but only slowing down the colloid transport. In more complex models, like the Langmuir model for adsorption, the retardation coefficient becomes dependent on the concentration (see more detailed discussion in Section 3.4).

A more general model describes reversible attachment of the particles, with the possibility of detachment. This model is also referred to as the two-site non-equilibrium model [99, 100, 134]:

$$\left(1+f\frac{\rho_b K_{eq}}{\phi}\right)\frac{\partial c}{\partial t}+v\frac{\partial c}{\partial x}=D\frac{\partial^2 c}{\partial x^2}-k\left[(1-f)K_{eq}c-s\right] \tag{1.27}$$

$$\frac{\partial s}{\partial t}=k\left[(1-f)K_{eq}c-s\right] \tag{1.28}$$

where f is the fraction of surface sites for equilibrium attachment, and $(1-f)$ is the fraction of those for non-equilibrium attachment; k is the kinetic constant for the non-equilibrium processes, or the release rate constant. In the absence of equilibrium sorption, the deposition rate constant is reduced into $k_d = kK_{eq}$.

1.3 Limitations and extensions of the CFT

The classical CFT has been widely applied to simulate colloid transport and retention in both the engineered and the natural porous media. The model predictions were tested with both laboratory and field data. The traditional approach seems to be successful only within certain limitations: under favorable attachment conditions, for small particles, whose transport can well be described as the Brownian motion, for physically and chemically homogeneous porous media, for uniform particle populations, and under the absence of the developed collective behavior (like bridging etc.).

Large ongoing efforts aimed at understanding the transport and deposition of colloids in porous media beyond these limitations. The deviations from the classical CFT were attributed to non-DLVO interactions, blocking of collector surfaces, unfavorable attachment conditions, chemical and physical heterogeneity of porous media, population

heterogeneity of colloids, and migration of deposited colloids. In this section, the limitations and advances in the colloid filtration theory are discussed in details.

1.4 Non-DLVO interactions

The DLVO theory has been widely applied to predict colloid-collector interactions and colloidal stability for the last decades. Nevertheless, it failed to match the experimental observations in many cases [46, 180, 181]. The deviations, often referred to as the non-DLVO effects, were attributed to the following reasons: hydrogen bonding and hydrophobic effects, hydration pressure, non-charge transfer Lewis acid base interactions, and steric forces.

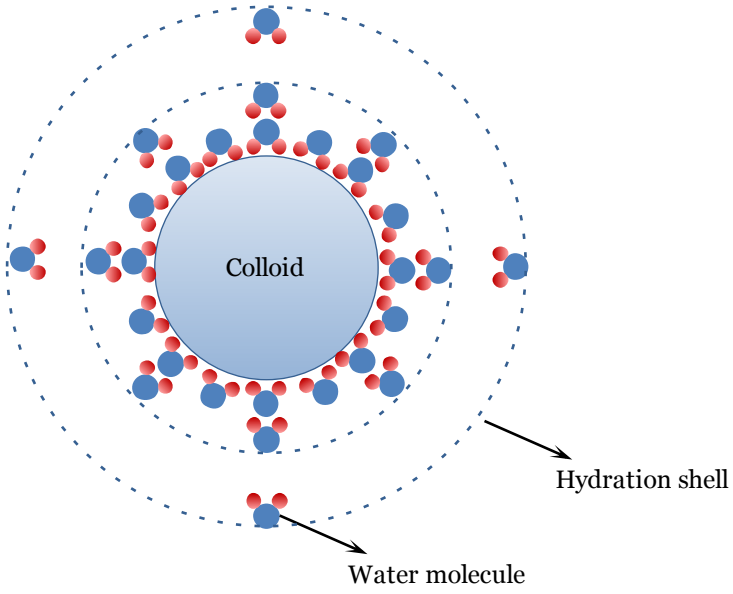

Figure 1.3 Illustration of hydration shells

Most of the colloidal interactions in the nature take place under the presence of water molecules, which exhibit hydrogen bonding between each other. Hydrophobic colloids tend to aggregate in the aqueous phase. The water molecules are ordered around them [182-184]. The ordered water molecules can be regarded as hydration shells radially propagating and decaying from the particle surface. Similar effects can be found on polar surfaces. It has been suggested in the literature that ordering of the water molecules results in “hydration pressure” or “structural forces”.

The interactions of hydration shells contribute to the total interaction energy. It has been suggested by a number of authors [13, 57, 185-187] that non-DLVO interactions can be incorporated as additives to the right hand side of Equation (1.1). Many of these non-DLVO interactions are still incompletely understood. Only few empirical expressions for the non-DLVO interactions are available in the literature. Some of them are based on the assumption about the exponentially decaying hydration pressure [188, 189], while other are based on the short range Lewis acid base interactions [47, 57]. Additivity of the DLVO and non-DLVO interactions, assumed in the literature, may also be questioned. Further study is required to provide more insight to the extensions of DLVO theory.

1.5 Single collector contact efficiency

In the IFBL and Smoluchowski-Levich approximations, calculation of the single collector contact efficiency takes into account only the Brownian motion, while other mechanisms of particle transport to the collector surfaces, such as interception and gravity of large non-Brownian particles, are neglected. Inaccurate calculation of the single collector contact efficiency leads directly to inaccurate determination of the collision efficiency from experiments (see Equation (1.25)). Subsequently, examination of the consistency between the model predictions and the experimental observations is compromised. Hence, a more comprehensive model for the contact efficiency is desirable, to consider as many transport mechanisms as possible.

It has been suggested on empirical grounds [51, 89-91, 107] that the single collector contact efficiency may be calculated by summing individual contributions from the different transport mechanisms. The total efficiency can be expressed as the sum of the diffusion, the interception, and the gravity contributions to colloid transport toward the collector:

$$\eta_0 = \eta_D + \eta_I + \eta_G \tag{1.29}$$

where η_D is the contribution from diffusion, η_I is the contribution from interception, and η_G is the contribution from gravity.

The regression analysis of the rigorous numerical solution to the transport equation (either the stochastic differential or the convective diffusion equations) leads to semi-empirical expressions for the different efficiencies. Each contribution is expressed in terms of the power functions of some dimensionless numbers. The most commonly applied dimensionless numbers are listed in Table 1.1.

Table 1.1 Dimensionless numbers for single collector contact efficiency

Number	Definition	Physical interpretation
N_R	r_s / r_c	Aspect ratio
N_{Pe}	$2Ur_c / D_\infty$	Ratio of convection transport to diffusion transport
N_{vdW}	A_{123} / kT	Ratio of van der Waals interaction energy to thermal energy
N_G	$2(\rho_s - \rho) g r_s^2 / (9\mu U)$	Ratio of Stokes particle settling velocity to fluid approach velocity
N_A	$A_{123} / (12\pi\mu r_s^2 U)$	Combined influence of van der Waals and viscous interactions on particle capture via interception

Apart from the IFBL or Smoluchowski-Levich approximations, there are two approaches for calculating the single collector contact efficiency, the RT correlation (after Rajagopalan and Tien [51]) and the TE correlation (after Tufenkji and Elimelech [91]). A summary of these expressions is useful for selecting the proper expressions for different conditions, as seen in Table 1.2.

The RT correlation was derived in [51] to account for gravity and the combined influence of van der Waals and the viscous interactions on the particle capture via interception. Neither of the RT and the IFBL correlations takes into account the effects of the van der Waals and the viscous interactions on the particle capture.

Unlike the RT correlation, the TE correlation incorporates the effects of the van der Waals and the viscous interactions on the particle capture. The other distinction between the TE correlation and the RT correlation lies in the expression for the gravity contribution. This contribution is independent of the medium porosity in the TE

correlation (absence of A_s), while this parameter is present in the RT correlation. Lastly, in the TE correlation the effect of the van der Waals interactions is incorporated in all the three transport mechanisms, namely the three expressions include either N_{vdW} or N_A. It has been shown by Tufenkji and Elimelech [91] that the TE correlation matches the numerical solution for the particle transport at the collector scale better than the RT correlation.

Table 1.2 Expressions of the contributions from diffusion, interception and gravity

	η_D	η_I	η_G
IFBL approximation**[89, 90]**	$4.04A_s^{\frac{1}{3}}N_{Pe}^{-\frac{2}{3}}$	0	0
RT correlation**[51]**	$4.04A_s^{\frac{1}{3}}N_{Pe}^{-\frac{2}{3}}$	$1.04A_sN_A^{0.125}N_R^{1.875}$	$3.38\times10^{-3}A_sN_G^{1.2}N_R^{-0.4}$
TE correlation**[91]**	$2.4A_s^{\frac{1}{3}}N_{Pe}^{-0.715}N_{}$	$0.55A_sN_A^{0.125}N_R^{1.675}$	$0.22N_G^{1.11}N_R^{-0.24}N_{vdW}^{0.053}$

It is worth mentioning that the above expressions of the single collector contact efficiency are derived from the deposition rate normalized by the flux toward the projected area of a single collector. The expressions for the efficiency with regard to the projected area of the sphere-in-cell envelope (Happel's model) can also be found in the literature [1, 13, 166]. In such cases, a factor of $(1-\phi)^{2/3}$ is introduced into the right hand side of (1.29).

1.6 Collision efficiency

The collision efficiency determined by Equation (1.18) only accounts for the effective collisions that overcome the repulsive double-layer force and drag the colloid particles into the primary energy minimum. It does not take into account the particles captured via the secondary energy minimum, as seen in Figure 1.4. This expression for the efficiency has been widely applied to predict the collision efficiency and to compare with experiments [1, 12, 45, 73, 85]. Despite the widespread use of the expression, a growing

body of evidence suggests that the predicted collision efficiency is several orders of magnitude smaller than the experimentally observed one [85, 86, 106, 107, 190]. Several explanations were proposed to account for the reported derivations, including the heterogeneity of surface charges and the deposition via secondary energy minima [13, 73, 92, 93, 101-103, 110, 113, 119, 120].

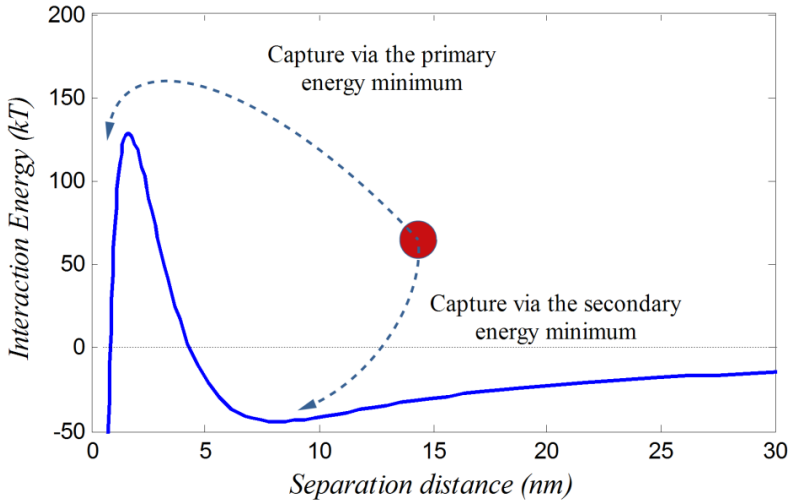

Figure 1.4 Particle capture via the primary and the secondary energy minima

A simple model for calculating the collision efficiency, which takes into account the deposition via the secondary energy minimum, was proposed by Hahn [92-94, 120]. In this model, the value of α in Equation (1.18) is derived from the Maxwell distribution of kinetic energies:

$$\alpha = 1 - \int_{-\Phi_{2\min}}^{\infty} f(\Phi)\, d\Phi$$
$$f(\Phi) = 2\sqrt{\frac{\Phi}{\pi (kT)^3}} \exp\left(-\frac{\Phi}{kT}\right) \tag{1.30}$$

where $\Phi_{2\min}$ is the total interaction energy at the secondary energy minimum, $f(\Phi)$ is the Maxwell distribution of interaction energies. The calculation of the collision efficiency accounts for the particles with insufficient energy to escape from the secondary energy well. The collision efficiency may be also expressed in terms of the particle velocity rather than the interaction energy. In such cases, Φ in Equation (1.30) is substituted by

$0.5m_s v_s^2$ where m_s and v_s are the colloid mass and the colloid velocity in the close proximity of the collector.

The effects of deposition via the secondary energy minimum were demonstrated by the complimentary experiments in a packed bed filter and radial stagnation point flow (RSPF) system [119, 191-193]. In the RSPF system, the microorganisms (interpreted as "colloid particles") captured via the secondary energy minimum are swept away by the radial flow component. The microorganisms captured via the primary energy minimum are left in the filter. There are mounting experimental evidences showing that the calculation of α based on the deposition via the secondary energy minimum improves the accuracy of model predictions [92-94, 101, 103, 120]. The resulted collision efficiency from (1.30) is larger than that from (1.18) since (1.30) takes into account for both the particles captured via the primary minimum and those via the second energy minimum.

1.7 Blocking dynamics

In the classical CFT, the deposition of colloids is described as a kinetic process, reflecting the fact that for the most colloid particles their attachment to the surface is irreversible [1, 12, 13, 186]. As a consequence, the kinetic equation of deposition (1.21) can also be written in terms of the fractional surface coverage θ:

$$\frac{\partial \theta}{\partial t} = \pi r_s^2 k_d c \tag{1.31}$$

The accumulation of particles on the surface has its limits. In most cases, the rate of deposition declines as the retained particles block subsequent attachment. Due to the blocking effects, the kinetic equation of deposition rate is usually modified into:

$$\frac{\partial \theta}{\partial t} = \pi r_s^2 k_d c B(\theta) \tag{1.32}$$

where $B(\theta)$ is the blocking function describing the probability of a particle contacting the unoccupied collector surface. It is a correction factor that accounts for the effects of

blocking. The expressions of the blocking function may be of the two types: the Langmuir and the random sequential adsorption (RSA).

The simplest Langmuir blocking function was produced by analogy with the Langmuir expression for molecular adsorption [194-197]:

$$B(\theta) = 1 - \varphi\theta \tag{1.33}$$

where φ is the normalized collector surface area which is blocked by an attached particle, namely the ratio of the average excluded area to the projected particle area πr_s^2. Parameter φ is also referred to as the parameter of excluded area. It can be inferred from the limit of $B(\theta) = 0$ that φ equals to the reciprocal of the maximum surface coverage $\theta_{\max}$ or the jamming limit.

The Langmuir blocking function is usually applied for description of adsorption of the point-sized molecules, such as solute ions. Such a function may be insufficient to describe deposition of the finite-sized colloidal particles [195, 197]. A more advanced blocking function accounting for the areal dimension and interaction of the attached particles is desirable for colloid filtration processes. Schaaf and Tabot proposed an expression of the blocking function based on the random sequential adsorption mechanism [197]. Their blocking function is based on a viral expansion of the surface exclusion to third order in density and may be applied to "hard" spheres attached to flat surfaces. This expression was generalized onto the double-layer interactions ("soft") between colloids and onto more complex collector geometry [195, 198]:

$$B(\theta) = 1 - 4(\theta_\infty \varphi\theta) + \frac{6\sqrt{3}}{\pi}(\theta_\infty \varphi\theta)^2 + \left(\frac{40}{\sqrt{3}\pi} - \frac{176}{3\pi^2}\right)(\theta_\infty \varphi\theta)^3 \tag{1.34}$$

where θ_∞ is the jamming limit for hard spheres. This extended blocking function applies to only surface coverage below 80% of $\theta_{\max}$. For the coverage above this value separate expression is applied [195, 198]:

$$B(\theta) = \frac{(1-\varphi\theta)^3}{2m^2\varphi^3} \tag{1.35}$$

where m is the jamming limit slope which can be determined from the experimental breakthrough curves [195].

1.8 Surface charge heterogeneity

Most natural and engineered porous media exhibit surface charges when immersed in water or water solutions of the different salts [199]. The origins of the surface charges include the ionic substitution within the crystal lattice of minerals, complexation or ionization of surface functional groups, or specific adsorption of ions onto solid surfaces [1, 200]. The internal surfaces of the porous media are inherently heterogeneous due to physical and chemical imperfections, such as cracks, edges, lattice defects, and chemical impurities [12, 13, 201]. The natural porous media may also possess a composite structure consisting of different minerals [202]. The second type of surface charge heterogeneity stems from colloid surface roughness and colloid size distribution.

1.8.1 Geochemical heterogeneity

The effects of surface charge heterogeneity in porous media have been introduced into the classical CFT via nominal surface potential [1, 12, 73, 203, 204]. The nominal potential is a homogeneous analog of the heterogeneously charged surface. It is equal to the potential of a homogeneous surface which exhibits the same double-layer interactions as the heterogeneous surface considered. The nominal potential is determined by the distribution of the surface potentials at different sites of the surface. There are two approaches to characterize the surface charge distribution: patchwise heterogeneity and random heterogeneity [73].

In the patchwise heterogeneity approach, the surface sites in the porous medium are grouped into macroscopic patches, each of which can be deemed to a homogeneous

surface [73, 203]. It is assumed that the patches are isolated homogeneous surfaces in contact with the bulk solution. Interactions at the patch boundaries are neglected.

In the random heterogeneity approach, the equipotential sites are assumed to be distributed randomly over the entire surface [73, 203]. A random distribution can be applied to the collectors that do not possess obvious large patches, such as glass beads and other amorphous materials. A truncated normal distribution of the surface potentials (without unphysical negative "tail") is most often used in this approach.

The nominal surface potential is calculated as the mean surface potential of the heterogeneous surface. The resulted nominal surface potential can be used for calculating the overall single collector removal efficiency. The single collector removal efficiency for the geochemically heterogeneous medium can be calculated by:

$$\eta = \sum_i \lambda_i \eta_i \text{ , for the patchwise heterogeneity, or} \tag{1.36}$$

$$\eta = \int \eta(\Phi) p(\Phi) d\Phi \text{ , for the random heterogeneity} \tag{1.37}$$

where λ_i is the surface fraction of ith patch for the patchwise heterogeneity, and $p(\Phi)$ is the distribution of surface potentials for the random heterogeneity. The calculation of single collector removal efficiency can be coupled with the blocking dynamics, where a blocking function is assigned to each patch [12, 204]. It is worth mentioning that geochemical heterogeneity does not give rise to non-exponential deposition with monodisperse suspension, since only one filtration coefficient enters the mass balance equation.

It was shown by Elimelech and his coauthors [204] that the most sensitive factor that controls the deposition behavior is the geochemical heterogeneity determined by parameters λ_i in Equation (1.36)and distribution $p(\Phi)$ in Equation (1.37). The deposition behavior is relatively insensitive to the ionic strength and the mineral grain surface potentials [204].

1.8.2 Particle population heterogeneity

As discussed above, particles may be captured via the secondary energy minimum under unfavorable attachment conditions. The resulted collision efficiency is several orders of magnitude larger than that predicted from accounting only for the primary energy minimum and matches the experimental observation better [92-94, 101, 103, 120]. A nominal potential as a homogeneous analogue can be applied to incorporate the geochemical heterogeneity effects. In spite of this improvement, the predicted deposition decays are still exponential. Meanwhile, hyperexponential deposition profiles are observed in in the presence of repulsive double-layer interactions [101, 103, 110, 205, 206]. The exponential deposition is revealed as a straight line in the logarithmic plot, while hyperexponential deposition is depicted by a concave line, as illustrated in Figure 1.5. Exponential decay of deposition is the standard solution to the advection-dispersion equation with a single sink term for the deposition, as seen in Equation (1.24).

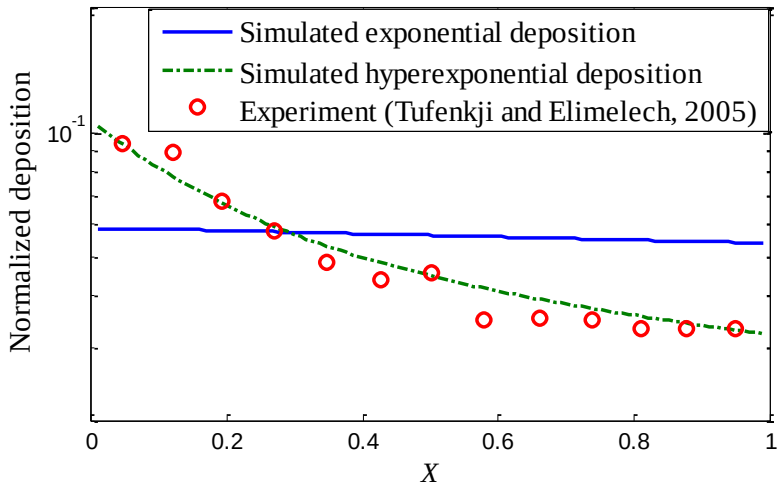

Figure 1.5 Simulated exponential and hyperexponential deposition [104] and experimental deposition [103].

It was demonstrated by a number of authors that hyperexponentiality of the deposition profiles can be explained by the surface charge heterogeneity of particles [101, 103-105, 207, 208]. A more general approach to the deposition rates accounts for the particle capture via heterogeneous energy minima. The particle population should be represented by at least two kinds of particles, one of which is subject to faster deposition (e.g. via the secondary energy minimum) and the other deposits slower (e.g. via the primary energy minimum). A bimodal distribution of the filtration coefficients is typically applied to

describe this type of heterogeneity. Other distributions, such as log-normal in (1.38) and power-law in (1.39), can also produce similar hyperexponential deposition profiles:

$$p(\lambda) = \frac{1}{\lambda\sigma\sqrt{2\pi}} \exp\left[\frac{\left(\ln\lambda - \mu\right)^2}{2\sigma^2}\right] \tag{1.38}$$

$$p(\lambda) = \lambda^{-b} \tag{1.39}$$

Here $p(\lambda)$ is the probability density function (PDF), μ and σ are the mean and the standard deviation for the log-normal distribution. b is the power in the power-law distribution controlling the shape of the PDF curve.

Instead of a single deposition rate for the whole particle population, a separate transport equation for each kind of particles (corresponding to each separate value of the filtration coefficient).

Many authors [101, 103-105, 186, 207, 208] conclude that the distribution of filtration coefficients is sufficient and necessary to produce the hyperexponential deposition decay caused by the surface and the surface charge heterogeneity. Apart from the colloid deposition in geochemically heterogeneous porous media, the particle population heterogeneity approach can be also applied to describe particles with a wide size distribution and particle surface roughness. The particle population approach can express the heterogeneity effects directly while the nominal potential approach can only resemble the heterogeneous population with a homogeneous analogue.

1.9 Physical heterogeneity

1.9.1 Straining

Another explanation for the deposition hyperexponentiality is the straining of the particles due to the physical heterogeneity at the pore scale [79, 81, 109, 115, 118, 121, 209]. Straining is the physical screening of particles by the porous medium, such as

particle retention at the collector-collector contacts/constrictions. The retention of particles is enhanced in the low-velocity or stagnant zones.

Straining is often accompanied by the size exclusion, where the particles of the different sizes retain or deposit with the different rates. These phenomena are often treated as connected and even identical, although, strictly speaking, this is not always the case.

Straining and size exclusion are neglected in many traditional studies of colloid filtration at the collector scale, since they require analysis of the heterogeneous particle population. Pore scale observations, on the other hand, show that straining plays a significant role in the porous media with irregular-shaped pores or under unfavorable attachment conditions [55, 84, 109, 135, 210, 211]. Torque analysis at the pore scale can identify regions favorable for straining. Constrictions and grain-grain contacts, where flow may be slow or stagnant, are observed to be such regions. As a consequence, pore geometry and collector surface roughness determine the degree of straining.

Classical filtration theories treated the straining of particles as a pure physical phenomenon [95, 96, 212, 213]. A number of authors focused on the effects of colloid sizes, pore sizes, and pore geometry on the straining phenomena [95, 109, 118, 126, 212-214]. Geometrical models were developed to describe straining as a physical process [95, 212, 213]. The predicted straining threshold ratio r_s / r_c ranged from 0.05 to 0.154. However, it was found in the experiments that the straining effects could be significant even when the ratio r_s / r_c is as small as 0.002~0.008 [109, 118, 126, 214].

On the macro-level, colloid filtration with straining may be modeled by a dual-permeability model [122] or a physical non-equilibrium model [134], which accounts for the particles flowing in the high-velocity and the low-velocity regions, respectively. In the works [155-157] size exclusion is described as a random process involving interacting distributed populations of particles and pores. The simplest approach to account for straining in colloid filtration is based on the consideration of the accessibility of pore networks. Bradford and his coauthors [121] expressed the straining rate as a function of the penetration depth:

$$\frac{\rho_b}{\phi}\frac{\partial s}{\partial t} = \left(\psi_{att} k_{att} + \psi_{str} k_{str}\right) c \tag{1.40}$$

where ψ_{att} is a dimensionless parameter accounting for attachment ripening, blocking (such as the blocking function $B(\theta)$), and others. k_{att} and k_{str} are attachment and straining rate constants. ψ_{str} is a parameter of straining depending on the depth:

$$\psi_{str} = \left(\frac{2r_c + x}{2r_c}\right)^{-\omega} \tag{1.41}$$

where ω is a fitting parameter that controls the shape of the spatial distribution of deposition. The depth dependency is explained in the following way: Straining of particles causes the blocking of the thin pores close to the inlet. It re-directs the colloid flow to a network of larger pores, resulting in bypassing thin pores at the downstream. As a consequence, the straining effect is strongest at the inlet $\left(x = 0,\ \psi_{str} = 1\right)$, and it decreases with depth. It was suggested in [118, 121, 215] that an integral model involving both straining and attachment is more realistic, especially in the system with intermediate particle and collector sizes.

As discussed above, the geometrical models based on the physical description of straining failed to predict the straining threshold ratio. On the other hand, a number of authors [79, 115, 135, 216] noticed that straining was also influenced by the chemical conditions, along with physical. In [136] we proposed an approach to colloid migration based on both the attachment conditions and hydrodynamics. Under unfavorable attachment conditions, the attached particles via weak association (secondary energy minimum) are subject to hydrodynamic drag from the fluid and migrate to the region that is chemically (attachment via the primary minimum) and physically (straining) favorable for deposition [3, 112, 135, 136]. The approach for incorporating straining effects into the CFT should take into account both the physical and the chemical factors influencing the process, such as the pore and particle size distributions, hydrodynamics, and solution chemistry.

1.9.2 Non-Fickian transport

The third explanation for the deposition hyperexponentiality is distribution of the particle times of flight and residence times, resulting in the non-Fickian character of particle dispersion in porous media [11, 104, 105, 125, 217-222]. This mechanism is to some extent similar to the physical straining, since they both consider longer residence times for the particles in low-velocity regions. However, the non-Fickian transfer mechanism describes also particles that travel faster than the average particle velocity, as seen in Figure 1.6. As a result, the non-Fickian transport gives rise to more dispersed breakthrough curves for pulse injection and hyperexponential deposition profiles [104, 105, 123, 217, 218].

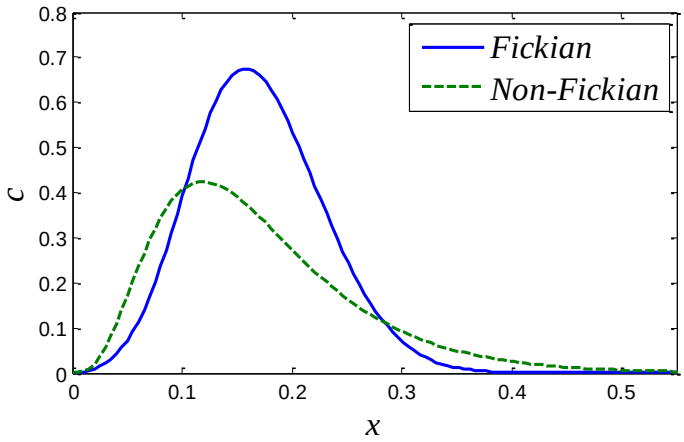

Figure 1.6 Concentration distribution of a pulse injection

Two approaches have been commonly applied for modeling the non-Fickian transport of colloids in porous media: the continuous time random walk (CTRW) approach and the elliptic equation approach as an important reduction of the CTRW [104, 105, 217-219, 223]. The CTRW approach, as many other developments in stochastic processes, has started from the famous works of Einstein, Langevin and Smoluchowski about Brownian motion of the particles [224-227] (see extensive discussion in Ref. [228]). In terms of physical effects, a major difference between the CTRW and the previously considered approaches is consideration of the particle residence time distribution accounting for the small-scale heterogeneity effects on the transport.

The CTRW theory has been extensively applied to describe the non-Fickian transport of tracers in porous media [10, 11, 117, 124, 125, 221]. Colloid transport and particle

deposition were considered in several CTRW works, mainly, based on the elliptic equation approach [104, 105, 123, 217, 218, 220]. The CTRW approach was capable of describing some phenomena that were previously interpreted as the action of the different other physical mechanisms. In particular, the long tails in the breakthrough curves were usually interpreted as a result of reversible deposition [111, 112]. The deposition hyperexponentiality could also be interpreted as a result of straining [79-81, 114, 115]. Effect of non-Fickian transport provides alternative or additional explanation for these experimental observations.

Until now, the physical picture of particle deposition adopted within stochastic approaches was rather incomplete. Such phenomena as migration of deposited particles or distinction between strained and attached particles have not been considered. A more comprehensive stochastic model that can incorporate the migration of deposition, the straining, and the non-Fickian transport effects is desirable.

It has been shown that the CTRW description of tracer and particle flow may be reduced into an elliptic partial differential equation in the limit of infinitely many infinitesimal step lengths and residence times [217]. Unlike the full CTRW approach, such an equation needs only characteristic information from the residence time distribution, the variance and the mean value. As a result, the elliptic equation can be solved numerically and even analytically for some 1-D flow problems [123, 218]. The elliptic equation for transport is given by [217, 218]:

$$\frac{\partial c}{\partial t} + v\frac{\partial c}{\partial x} = D\frac{\partial^2 c}{\partial x^2} + D_t\frac{\partial^2 c}{\partial t^2} - \frac{\rho_b}{\phi}\frac{\partial s}{\partial t} \tag{1.42}$$

where D_t is called the temporal dispersion coefficient, which is defined as the ratio between the variance and the mean of the particle residence time distribution. Furthermore, the elliptic equation was coupled with the distribution of filtration coefficients representing the particle population heterogeneity [104, 105].

Experimental verifications of the stochastic approach were extensively discussed in Refs [10, 11, 104, 105, 124, 125, 220-223], although most of the CTRW applications were to

the tracer flows. A growing body of evidence shows that the CTRW is able to catch the three important effects that were observed in experiments [10, 11, 223] and in the nature [124, 220, 221], but cannot be adequately described by the ADE: 1) Under pulse injection, the maximum of concentration moves slower than the flow rate of the carrying fluid; 2) The concentration distribution around the maximum is asymmetric, and 3) The forward "tail" of the concentration distribution contains much more particles and decreases much slower than predicted by the traditional approach. The authors showed that the elliptic equation approach excels the Fickian approach in matching both the breakthrough curves and deposition profiles for highly heterogeneous porous media. For nearly homogeneous or slightly heterogeneous porous media the elliptic or CTRW formalism is not necessary, but the particle distribution should sometimes be introduced for modelling the deposition curves. This requires the application of the population balance approach [104, 105].

1.10 Straining of particles with distributed sizes

In many natural and industrial processes both the colloid particles and pores are distributed by their sizes. Straining and size exclusion may occur at various rates for different-sized particles. Since the capture criterion for straining depends on the relationship between the particle and pore throat sizes, adequate mathematical models should involve pore and particle size distributions. A number of studies on the population balance approach for straining of colloids in porous media have emerged in the past decade [123, 156, 158, 229].

The population balance approach originates in the works of Boltzmann on the gas kinetic theory and the subsequent work of Smolukhowski, who applied a similar formalism to the problem of particle coagulation [225]. In the approach to deep bed filtration developed in papers [155-158, 229] the particles and the pores are described as the two populations (ensembles) distributed by the particle sizes r_s and pore sizes r_p (it should be remarked that by "sizes" one may understand not only geometrical sizes, but also other physical parameters or even their sets). "Collisions" between particles and pores may result in passing through or entrapping a particle.

Probably, the first population balance model for deep bed filtration was suggested in work [230]. In our discussion, we mainly follow the study [158], where, to the best of our knowledge the formalism was, apparently, first described in its present form. Several modifications and extensions of the formalism were suggested in paper [229].

1.10.1 Particle flow characteristics

The assumption taken in this section is that the particle sizes are much smaller than the pore sizes. These conditions are characteristic of many experimental works [101, 103, 111, 135, 205, 206, 231, 232]. This eliminates the volumetric and velocity corrections to the particle flow, which become important for the particles, whose sizes are comparable to the pore sizes and may result in the fractional-flow filtration theories of the different kinds [157, 158, 229]. An opposite case, where the particle sizes are comparable to the pore sizes, and when the deposition is caused by the size exclusion mechanism, may also be considered in the framework of the described formalism [155-157].

Any model of deep bed filtration involves the two types of characteristics. The a priori characteristics (the constituting dependences and parameters) are assumed to be known in advance and invariable in the course of the filtration. The variable characteristics obey a system of kinetic balance equations to be derived.

Under assumption above, the main a priori characteristic in the proposed model is the particle-pore interaction probability $p\left(r_s, r_p \to r_p^{'}\right)dr_p'$: a probability of the event that a particle of the size r_s is captured in a pore of the size r_p, as a result of which the pore size changes to r_p'. Such a probability takes into account a possibility of incomplete plugging a pore after particle capture. The distribution function $p\left(r_s, r_p \to r_p^{'}\right)$ possesses the following properties:

$$p\left(r_s, r_p \to r_p'\right) = 0: \;\; r_p \le r_p'; \tag{1.43}$$

$$\int_0^\infty p\left(r_s, r_p \to r_p'\right) dr_p' = p\left(r_s, r_p\right)$$

where $p(r_s, r_p)$ is a probability of capturing a particle r_s at a pore r_p, which will also be used in the following.

Another a priori characteristics is the reference (correlation) length of the porous medium l. This is, essentially, an adjustment parameter determining the spatial frequency of particle-pore "collisions". In Ref. [229] a model porous medium have been described as a system of "paths" and "chambers". The particles move along the paths and mix in the chambers. The value of L is defined as a characteristic distance between the two chambers.

Let us define now the variable functions to be determined. The classical filtration theory [95, 233] describes the transport of suspended particles in terms of the averaged concentration per unit pore volume, $c(x,t)$. It does not distinguish between the particles of the different sizes. The population balance approach [123, 156-158, 229] adopts more detailed characteristics, e.g. the particle size distribution $C(r_s,x,t)$ by the values of r_s:

$$c(x,t) = \int C(r_s, x, t) dr_s; \quad f(r_s, x, t) = \frac{C(r_s, x, t)}{c(x,t)} \tag{1.44}$$

where $f(r_s,x,t)$ is the distribution density of the suspended particles. The ensemble of pores is characterized by their distribution by sizes r_p:

$$h(x,t) = \int H\left(r_p, x, t\right) dr_p; \quad f\left(r_p, x, t\right) = \frac{H\left(r_p, x, t\right)}{h(x,t)} \tag{1.45}$$

where $h(x,t)$ is the number of pores per unit cross-section of porous media, $H(r_p,x,t)$ and $f(r_p,x,t)$ are the pore size distribution by r_p and the corresponding distribution density. The two distributions, $C(r_s, x, t)$ and $H(r_p, x, t)$, vary with time due to flow and deposition of the different particles. The balance equations for these ensembles are further derived.

1.10.2 Particle flow kinetics

The mass balance equation for the particles of a given size in one dimension can be written as [156-158]:

$$\frac{\partial\phi(x,t)C(r_s,x,t)}{\partial t}+\frac{\partial Q(r_s,x,t)}{\partial x}=-\frac{\partial\Sigma(r_s,x,t)}{\partial t} \tag{1.46}$$

where $\phi(x,t)$ is the porosity, $Q(r_s,x,t)$ is the flux of particles, and $\Sigma(r_s,x,t)$ is the concentration of deposited particles of r_s. For particles much smaller than pores we do not have to introduce the porosity $\phi(r_s,x,t)$ accessible for particles of r_s, as done, for example, in [158]. The flux of particles may be expressed as the total flow of particles through all the pores at a unit surface [158]:

$$Q(r_s,x,t)=C(r_s,x,t)\int q(r_p,x,t)H(r_p,x,t)dr_p \tag{1.47}$$

Here $q(r_p,x,t)$ is the average flow rate through a pore of the size r_p. In assumption that the particles are much smaller than pores the flux expression may be simplified to:

$$Q(r_s,x,t)=UC(r_s,x,t) \tag{1.48}$$

where U is the average fluid velocity. More sophisticated expressions accounting for incomplete accessibility of the pore space and the velocity corrections for the particles of the different sizes are discussed in [156-158, 229].

1.10.3 Particle capture kinetics

The particle capture rate is usually assumed to be proportional to the frequency of collisions between particles and pores [123, 156-158]. Providing that the capture probability of a particle r_s in the pore r_p is $p(r_s,r_p)$, the kinetic equation for the particle capture can be expressed by [158]:

$$\frac{\partial \Sigma(r_s,x,t)}{\partial t} = C(r_s,x,t)\frac{1}{l}\int_0^\infty p(r_s,r_p)q(r_p,x,t)H(r_p,x,t)dr_p \tag{1.49}$$

Equation (1.49) is based on the assumption that particles coming to the pores are distributed independently of the pore sizes. It is similar to the Boltzmann assumption about "molecular chaos" [234].

$1/l$ in Equation (1.49) is the frequency of particles "forgetting" their past and being distributed independently of the pore sizes in a unit length. A simple example of the assumption is the porous medium of parallel tubes intercalated by mixing chambers, as seen in Figure 1.7. The distance between two neighboring chambers is l, while particles are completely mixed in the chambers.

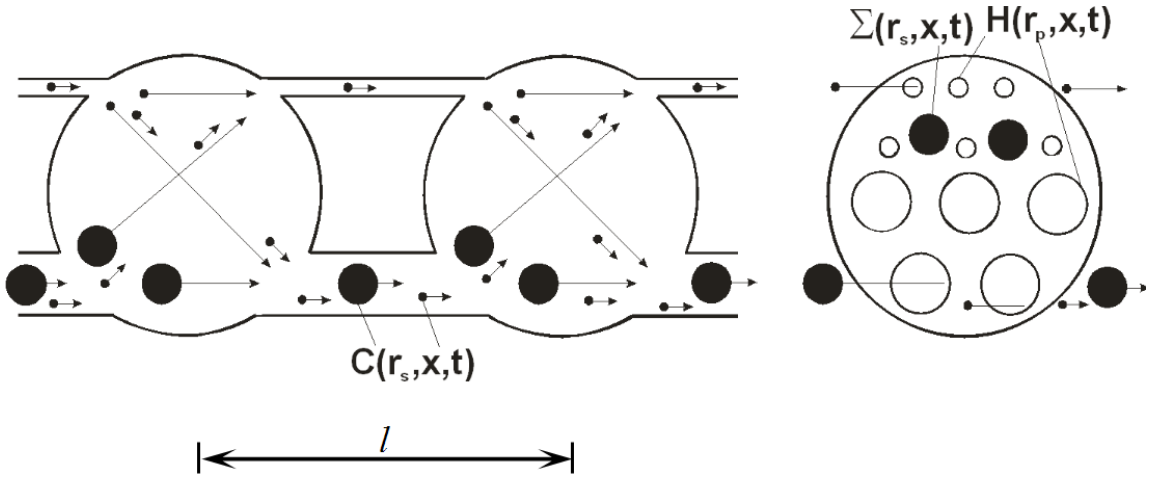

Figure 1.7 Schematic of parallel tubes intercalated by mixing chambers

The equation above requires an expression for the flow rate $q(r_p,x,t)$ in a single pore. In the simplest case of the parallel flows in the different flows in a cross-section, this expression is given by [158]:

$$q(r_p,x,t) = \frac{k_1(r_p)}{K(x,t)}U = \frac{k_1(r_p)U}{\int_0^\infty k_1(r_p)H(r_p,x,t)dr_p} \tag{1.50}$$

Here $K(x,t)$ is the total permeability of the porous medium, which generally may vary due to the particle deposition. The value of $k_1(r_p)$ is a conductivity of a single pore

(capillary) with regard to the flow. For example, for the Hagen-Poiseuille flow in a cylindrical capillary $k_1(r_p) = \pi r_p^4 / 8$. More complicated effective medium-based or percolation-based schemes of permeability may also be suggested [230, 235].

A special role of the characteristic distance L in integral (1.49) should be discussed. The value of L arises from the fact that the deposition (1.49) (and the balance equation (1.46)) is written for the unit of *volume*, while the pore concentration $H(r_p, x, t)$ is the amount of pores per unit *cross-section.* In principle, the value of l should be distributed. However, this is difficult to introduce in the framework of the "pure" population balances. The distribution of l is partly reflected by the distribution of the particle flights introduced in the framework of the CTRW approach.

1.10.4 Pore plugging kinetics

Generally, variation of the number of pores of a given size in a cross-section may be represented as a difference between the increase and decrease terms [158]:

$$\frac{\partial H\left(r_p, x, t\right)}{\partial t} = I\left(r_p, x, t\right) - D\left(r_p, x, t\right) \tag{1.51}$$

The value of $H(r_p, x, t)$ increases if a larger pore captures a particle and acquires size r_p . $H(r_p, x, t)$ decreases if a pore of the size r_p captures a particle and becomes smaller. In the assumption about independence of the particle and the pore characteristics prior to collision, the increase term $I\left(r_p, x, t\right)$ and the decrease term $D\left(r_p, x, t\right)$ can be expressed in the form

$$I\left(r_p, x, t\right) = \int_{r_p}^{\infty} dr_p^{'} \int_0^{\infty} dr_s \left\{ p\left(r_s, r_p^{'} \to r_p\right) q\left(r_p, x, t\right) H\left(r_p, x, t\right) C\left(r_s, x, t\right) \right\} \tag{1.52}$$

$$D\left(r_p, x, t\right) = \int_0^{\infty} dr_s \int_0^{r_p} dr_p^{'} \left\{ p\left(r_s, r_p \to r_p^{'}\right) q\left(r_p, x, t\right) H\left(r_p, x, t\right) C\left(r_s, x, t\right) \right\} \tag{1.53}$$

By integration over $r_p^{'}$ Equation (1.53) can then be reduced to (cf. Equation(1.43)):

$$D\left(r_p,x,t\right)=q\left(r_p,x,t\right)H\left(r_p,x,t\right)\int_0^\infty dr_s\left\{p\left(r_s,r_p\right)C\left(r_s,x,t\right)\right\} \tag{1.54}$$

In these equations the value of $q(r_p,x,t)$ is expressed by Equation (1.50). Thus, the integral terms(1.52), (1.53) are nonlinear with regard to $H(r_p,x,t)$. Presence of the flux is important: it expresses the fact that the number of collisions between particles and pores is proportional to the particle flux.

1.10.5 Coupled particle and pore kinetics

The resulting system of equations is obtained by exclusion of the fine deposition $\partial\Sigma/\partial t$ from the balance equation (1.46) with its substitution from Equation (1.49). It is also demonstrated in [123, 158] by volume balance considerations that the porosity and velocity may simultaneously be taken out of differentiation. The resulting system of equations for suspended particles and for pores assumes the form

$$\begin{aligned}&\phi\frac{\partial C\left(r_s,x,t\right)}{\partial t}+U\frac{\partial C\left(r_s,x,t\right)}{\partial x}=\\&-C\left(r_s,x,t\right)\frac{1}{l}\int_0^\infty p\left(r_s,r_p\right)q\left(r_p,x,t\right)H\left(r_p,x,t\right)dr_p;\end{aligned} \tag{1.55}$$

$$\begin{aligned}&\frac{\partial H\left(r_p,x,t\right)}{\partial t}=\\&\int_{r_p}^\infty dr_p^{'}\int_0^\infty dr_s\left\{p\left(r_s,r_p^{'}\to r_p\right)q\left(r_p,x,t\right)H\left(r_p,x,t\right)C\left(r_s,x,t\right)\right\}\\&-q\left(r_p,x,t\right)H\left(r_p,x,t\right)\int_0^\infty dr_s\left\{p\left(r_s,r_p\right)C\left(r_s,x,t\right)\right\}\end{aligned} \tag{1.56}$$

where $q(r_p,x,t)$ is given by (1.50).

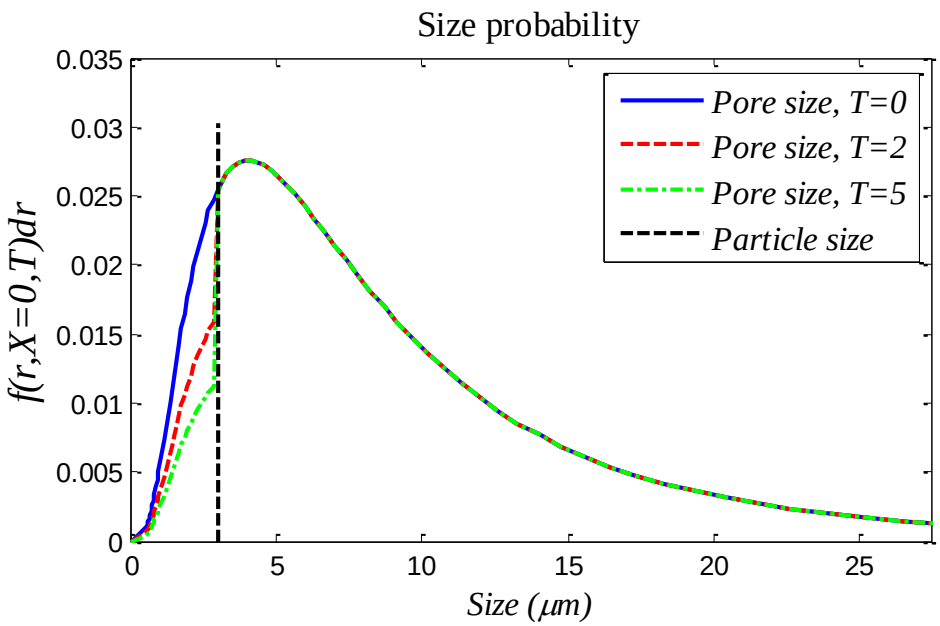

Figure 1.8 Sample calculation: Pore size distribution variation from the population balance approach for straining

Equations (1.55) and (1.56) form a system of nonlinear integral-differential equations for the two functions: $C(r_s, x, t)$ and $H(r_p, x, t)$. Other values in this system are either known a priori or may be computed in terms of C and H. For example, in Equation (1.55) velocity U may be treated either as constant or as a known function of time, due to incompressibility of the carrying liquid [229]. Porosity ϕ may be set constant for dilute suspensions. Otherwise, it may be computed in terms of $H(r_p, x, t)$. Considering porosity to be a free area per unit cross-section, we obtain:

$$\phi(x,t) = \int s(r_p) H(r_p, x, t) dr_p \tag{1.57}$$

where $s(r_p)$ is the cross-section of one capillary (for example, πr_p^2 for cylindrical capillaries). System (1.55) and (1.56) requires one initial condition $H_0(r_p, x)$ for the pore concentration and one initial and one boundary condition for the particle concentration.

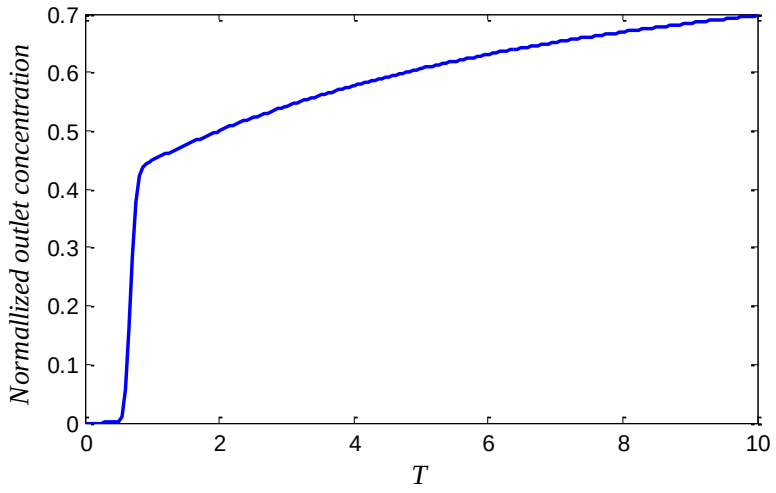

Figure 1.9 Sample calculation: Breakthrough curve from the population balance approach for straining

Sample calculations shown in Figure 1.8 and Figure 1.9 are carried out under the assumption of complete pore plugging, namely that the increasing term in (1.52) contributes completely to zero pore size. It can be seen from Figure 1.8 that the pore plugging kinetics exhibits faster reduction of larger pores than that of the smaller pores. It is explained by the proportionality of the particle capture rate to the fractional flow through pores of different sizes. On the other hand, the total particle capture rate decreases due to the reduction of smaller pores. An increasing outlet concentration is observed with time, which is a typical behavior for straining of colloids in porous media.

1.11 Migration of deposited particles

Release and migration of deposited colloids, such as microorganisms in aquifers and clay fines in oil reservoirs, is of considerable importance in some environmental and engineering applications. For example, detachment of pathogenic microbes can pose great risk to public health [22-31]. Migration of reservoir fines during waterflooding can cause severe permeability damage, which subsequently reduces injectivity and productivity of the injection and production wells, correspondingly [34-38, 236, 237].

1.11.1 Mechanisms of colloid release

Colloid release in environmental systems has been attributed to physical, chemical, or biological processes. Particles may also be produced from the erosion of porous media, such as acid treatment for well stimulation in oil reservoirs [238-241]. Specifically, physical perturbations of the rock in the course of reservoir development include drilling wells, sampling, rapid infiltration, waterflooding, water production, and others [242-244]. Chemical perturbations include increase of pH, decrease of salinity, generation of surfactants, and others [34-37, 40, 236, 245-250]. Generation of surfactants is also regarded as a biological perturbation since surfactants may be produced by microbes [40, 250]. Bacteria forming large aggregates at grain-grain contacts which are re-entrained by flowing fluid is another example of biological perturbation [80].

At the collector scale, a study of colloid release usually focuses on the torques exerted on the attached particles [9, 35, 216, 248, 251, 252]. It has been demonstrated that the balance of the hydrodynamic torque, the lifting torque, the resisting adhesive torque and the torque of the gravity force determines whether the particles attached to the pore walls will be immobilized and re-entrained into the carrying fluid, as seen in Figure 1.10 . The erosion number, a dimensionless parameter indicating the ratio between the torques for the detachment and the attachment of particles, can be expressed in the following way:

$$\varepsilon = \frac{F_l l_n + F_d l_d}{\left(F_e + F_g\right) l_n} \tag{1.58}$$

where $F_l, F_d, F_e,$ and F_g are respectively the lifting force, the hydrodynamic drag, the electrostatic force, and the gravity exerting on the particles attached to the pore walls. l_d and l_n are respectively the levers of drag and normal forces.

A mechanistic model has been proposed by Bedrikovetsky and his co-workers [248, 252] to express the maximum deposition concentration as a function of the particle size, the pore size, the ionic strength, the fluid velocity and a number of other factors. The model assumes that the attached particles will release if the detachment toques are larger than

the adhesive torques ($\varepsilon > 1$). A good agreement has been observed between the model prediction and the experimental injectivity decline [252].

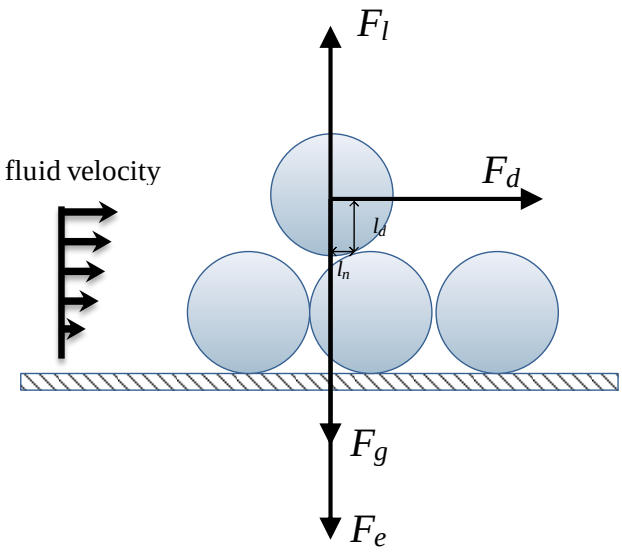

Figure 1.10 Forces exerted on the attached particles

1.11.2 Effects of colloid migration

At the pore scale, the migration of colloids is often coupled with other processes, such as re-entraining back into fluid and straining at throats and constrictions, as seen in Figure 1.11. As a result, the released particles may be re-entrained by the bulk fluid and migrate further to the downstream or subsequently strained at thin pore throats. The release of attached particles may give rise to permeability increase to a small degree, while the subsequent straining usually causes severe permeability damage [34, 37, 236, 247, 253].

It has been shown by Bedrikovetsky and his coauthors [247] and Yuan and Shapiro [236] that the effects of fines migration induced by low salinity waterflooding may be used as a mobility control technique to alter the flow field in layer-cake petroleum reservoirs. Such effects will be discussed in details in Chapter 6. In the cases where deposited colloids are associated with low-solubility contaminants in water and straining is insignificant, the re-entrainment of deposited colloids is a major reason for the long distance migration of the contaminant, such as the migration of plutonium associated particles observed in [16].

It can be inferred from the torque balance analysis (1.58) that the larger particles attached to the collector surface are more subject to release and migration under unfavorable attachment conditions. In such cases, long tails of the breakthrough curves after the end of particle injection are usually observed, while the deposition concentration may be non-monotonously distributed along the column [80, 111, 135, 136]. In the cited works migration of released colloids is described as a third particle population migrating with a different rate and probably re-entrapped. Such a model captures non-monotonous particle deposition profiles. Bradford and his coworkers [80] found that the colloid release is not limited to the attached particles (in their study, bacteria E. coli), but may also stem from large E. coli aggregates at straining sites.

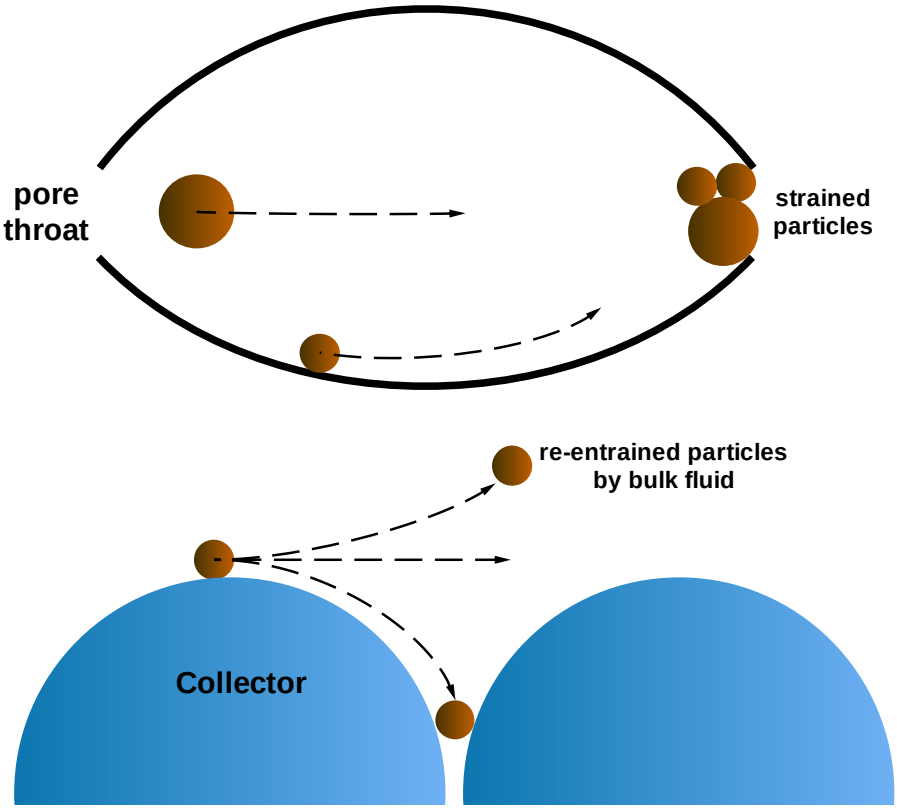

Figure 1.11 Migration of deposition coupled with other processes

1.12 Nomenclature of Chapter 1

c	Number of suspended particles per unit pore volume (m^{-3})
C	Particle size distribution in suspension (m^{-4})
Σ	Particle size distribution in deposition (m^{-4})
s	Number of retained particles per unit volume of porous media (m^{-3})
h	Number of pores per unit cross-section of porous media(m^{-2})
H	*Pore size distribution (m-4)*
t	Time (s)
T	temperature (K)
x	x coordinate in space
Φ	interaction energy (J)
a	radius of a sphere
k	Boltzmann constant
z	valence of ions
e	elementary charge
h	separation distance between two surfaces
ε	dielectric constant
ε_0	vacuum permittivity
I	ionic strength (mM)
A	Hamaker constant
λ	characteristic wavelength(m) or filtration coefficient(m^{-1})
dl	Electrical double layer
vdW	van der Waals
str	straining
att	attachment
N_A	Advogadro number
$\mathbf{J}$	Total flux of particles (advection and diffusion at pore scale)
Q	*Source term at pore scale(number of particles per unit time)*
Q	*Darcy flux of particles (s-1m-2)*
q	*Flow rate (m3/s)*
D	*Diffusion coefficient (m2/s)*
u	*fluid velocity (m/s)*
v	*particle velocity(m/s)*
U	*fluid approach velocity(m/s)*
F	*External force (N)*
h	*separation distance (m)*
b	*thickness of a fluid shell in Happel's sphere-in-cell representation(m) or exponent in power laws*
ϕ	*porosity*
r_c	radius of the collector(m)
r_s	sphere particle radius(m)
r_p	pore radius(m)
η	single collector removal efficiency
α	collision efficiency

k_d	deposition rate constant(s^{-1})
R	retardation factor due to equilibrium adsorption
B	surface blocking function
θ	surface coverage
p	probability
K	permeability of the porous medium
k_1	permeability of a capillary

2 Non-Fickian Transport and heterogeneous attachment of colloids

In this chapter, an integral model is developed to capture the non-Fickian transport and heterogeneous attachment of colloids in porous media. It incorporates both the distribution of the filtration coefficients (as in Refs[207, 208]) and the distributed particle flight time (as in Refs[123, 217, 218]). The factors controlling the deposition profiles and the shape of breakthrough curves are systematically studied. A large set of data obtained in the experiments with homogeneous and heterogeneous porous media is compared with the results from the numerical modeling. Apart from the data on deep bed filtration experiments, data on tracer injection have been used, since tracers may be considered as "suspensions with a zero-filtration coefficient". The goal of the comparison is to find out which mechanisms incorporated in the model are necessary in order to reproduce the experimental results successfully: either temporal dispersion of particle flights or distribution of filtration coefficients, or both of them.

2.1 Introduction

Non-Fickian behavior of the suspensions in porous media may be caused by the physical heterogeneity of porous media [10, 11, 104, 117, 123, 220, 222, 254, 255]. It has been indicated by a number of works [10, 11, 104, 123, 217, 218, 220, 254] that non-Fickian transport of a solute or a suspension may be modeled more accurately by approaches based on the continuous time random walk (CTRW) theory compared to the classical advection dispersion equation (ADE). The first CTRW model for colloidal transport in porous media was studied in Ref.[220].

A macroscopic elliptic equation for non-Fickian transport in porous media in the framework of CTRW [123, 217, 218] was developed by A. Shapiro and P. Bedrikovetsky. The equation can be applied to describe either the transport of macroscopic particles or that of the solute in porous media. The elliptic equation and the distribution of filtration

coefficients can be integrated as an integral model to describe non-Fickian transport of polydisperse suspension in heterogeneous porous media [104, 123].

The commonly reported hyperexponential deposition has been attributed to the heterogeneity of the surface charge and energy minima (see Chapters 2 and 3 and Refs. [101, 110, 207, 208]) or to the enhanced retention at low-velocity zones of pore space (physical straining) [79, 121, 122]. Based on the described mechanisms, the authors developed various models which produce hyperexponential deposition. In Chapters 2 and 3 and [101, 104, 207, 208], distributions of filtration coefficients were applied to reflect the heterogeneity of particle population and particle-pore interactions. In Refs. [122, 134], dual-permeability models were developed to take into account the high-velocity zones and low-velocity zones of pore space.

The conventional methodology, ADE with a single filtration coefficient, merely predicts exponentially decreasing deposition profiles (see Chapter 2 and [103]). Many of the experimental results, on the other hand, show hyperexponential deposition profiles or even non-monotonic deposition profiles under some specific conditions [80, 103, 111].

It is believed that the heterogeneity of the particle population or the heterogeneity of particle-medium-interaction is the main reason for hyperexponential deposition profiles in homogeneous porous media [102, 103]. The heterogeneity of the particle population encompasses the physical heterogeneity (size and shape) and the physiochemical heterogeneity (surface charge and multiple energy minima). For instance, in a deep bed filtration system which the size exclusion mechanism dominates, the larger particles deposits faster and correspond to larger filtration coefficients. The distribution of filtration coefficients is most likely dependent on the particle size distribution [123]. Even flow of a monodisperse suspension (uniform shape and size) in a homogeneous porous medium under unfavorable attachment conditions is observed to result sometimes in a hyperexponential deposition profile, due to the heterogeneity of particle surface charge and second energy minimum[101, 103, 205, 206]. Mathematically, the heterogeneity of the particle population is described by the distribution of the filtration coefficients. The deposition patterns may be interpreted by application of various

distribution types: the log-normal distribution, the power law distribution, the bimodal distribution and others [207, 208].

In order to study how the heterogeneity of the particle population leads to hyperexponential deposition profiles, it is important to separate its influence from the effect of heterogeneity of porous media. Lots of the relevant studies focus on the physically homogeneous porous media, e.g. packed glass beads in the column [108, 132, 256]. Some experiments have been carried out in micro-heterogeneous porous media, e.g. packs of natural quartz sand [115, 205, 206]. Other experiments adopt specially constructed porous media with heterogeneity on a mesoscale [10, 257]. The data from pilot experiments of mainly tracers in natural/highly heterogeneous porous media and porous rocks is also available [116].

2.2 Modeling methodology

2.2.1 Elliptic Equation

It has been suggested in Refs. [123, 217, 218] that transport of a dilute monodisperse suspension in a porous medium may be described by an elliptic equation accounting for particle advection, spatial dispersion, temporal dispersion, mixed dispersion, and deposition. The temporal dispersion represents the effects of the distributed residence time of the particles in various pores. This is a simple way to formalize the Continuous Time Random Walk (CTRW) approach, where dispersion of a time step is usually expressed by means of a distribution kernel [10, 11, 220]. It has been shown [217, 218] that in the limit of infinitely many infinitely small time steps and a finite variance of a single step, the distribution may be represented by the two coefficients D_t, D_{xt} (for temporal and mixed dispersion), and instead of the convolution with the distribution kernel, it is enough to consider the terms with the second time derivative and with the mixed derivative, making the transport equation elliptic.

In this work we study the application of the elliptic formalism to filtration of the diluted suspensions of particles, which are normally applied in the experiments. Since the

suspended concentrations in the reported experiments are fairly low to influence the pore structure, this influence is neglected. The mixed dispersion is also neglected, since it has no qualitative influence on the profiles. In order to reveal the heterogeneity of the particle population the particles are split into portions, i.e. there are multiple equations representing different particle species with various filtration coefficients. Under these conditions, the suspended concentration $c_i(x,t)$ and the deposited concentration $s_i(x,t)$ of the ith component of the suspension at column depth x and time t are modeled by the elliptic equation with a sink term representing the deposition of the particles:

$$\frac{\partial c_i}{\partial t} + v_i \frac{\partial c_i}{\partial x} = D_x \frac{\partial^2 c_i}{\partial x^2} + D_t \frac{\partial^2 c_i}{\partial t^2} - \lambda_i c_i \tag{2.1}$$

After this equation has been solved the deposition of the particles of the ith type may be found by integrating

$$\frac{\partial s_i}{\partial t} = \lambda_i c_i \varphi \tag{2.2}$$

Summation of s_i gives the total deposition at a given time.

In Equation (2.1) v_i is the interstitial particle velocity, D_x is the spatial dispersion coefficient, D_t is the temporal dispersion coefficient, which by definition is the second moment of the particle residence time divided by the first moment of the particle residence time to zero, λ_i is the filtration coefficient of the ith species of the particles, and φ is the bed porosity. The suspended concentration has the dimension of the number of particles per pore volume and the retention concentration of the number of particles per unit volume of the porous medium. For convenience of comparison to the experiments, the following practical quantities are often adopted: N_c is the number of the retained particles per gram of dry porous media, and N_t the total number of injected particles [103, 115, 118].

$$N_c = \sum_{i=1,2,3\ldots}^{N} \frac{s_i}{\rho_b};$$
$$N_t = c_0 t_0 v;$$

where ρ_b is the bulk density of the dry porous media, t_0 is the particle injection duration, and c_0 is the influent concentration. In dimensionless coordinates the elliptic equation for the ith particle species takes the form [123]:

$$\frac{\partial C_i}{\partial T} + u\frac{\partial C_i}{\partial X} = uR_{xi}\frac{\partial^2 C_i}{\partial X^2} + \frac{R_{ti}}{u}\frac{\partial^2 C_i}{\partial T^2} - \Lambda_i C_i \tag{2.3}$$

$$\frac{\partial S_i}{\partial t} = \Lambda_i C_i \varphi \tag{2.4}$$

where the following substitutions are introduced to the system:

$$x = LX; \quad t = (L/v_0)T; \quad c_i = C_i c_0; \quad s_i = S_i c_0;$$
$$v = uv_0; \quad R_{xi} = \frac{D_{xi}}{v_0 L}; \quad R_{ti} = \frac{D_{ti} v_0}{L}; \quad \Lambda_i = \frac{\lambda_i L}{v_0};$$

Here R_{xi} is the dimensionless longitudinal dispersivity and R_{ti} is the dimensionless temporal dispersivity of the ith component. The value of L is the reference length (m), v_0 is the average pore water velocity (m/s), and c_0 is the reference concentration. The inverse Peclet number R_{xi} describes the magnitude of the spatial dispersion compared to the product of the reference velocity and the reference length, while the similar parameter R_{ti} describes the magnitude of the temporal dispersion compared to the reference time.

2.2.2 **Distributed Filtration Coefficients**

The log-normal distribution, the power law distribution and the bimodal distribution are commonly adopted to reflect the particle population heterogeneity [113, 207, 208, 258, 259]. The probability density function (PDF) for the log-normal distributed filtration coefficients is of the following form:

$$p(\Lambda_i) = \frac{1}{\Lambda_i \sigma\sqrt{2\pi}} \exp\left[\frac{\left(\ln\Lambda_i - \mu\right)^2}{2\sigma^2}\right] \tag{2.5}$$

where μ and σ are the mean and the standard deviation of the natural logarithm of the filtration coefficients. The power law distribution takes the form:

$$p(\Lambda_i) = a\left(\Lambda_i\right)^{-b}, \quad \Lambda_i \in \left[\Lambda_{\min}, \Lambda_{\max}\right] \tag{2.6}$$

where *a* and *b* are two positive constants controlling the shape of the distribution. The larger *b* the more asymmetric PDF curve. Constant *a* is selected so that the sum of the probabilities of appearance of the different values of Λ is equal to unity (the value of $\Delta\Lambda=\Lambda_i- \Lambda_{i-1}$ is selected to be constant):

$$a = \frac{1}{\sum_{i=1,2...}^{N} \left(\Lambda_i\right)^{-b}} \tag{2.7}$$

The limitation $[\Lambda_{\min}, \Lambda_{\max}]$ is necessary, since otherwise the integral of the distribution is divergent on $[0,\infty]$. In accordance with previous works, the distribution is selected so that the integral is divergent at infinity, and so that dependence on the upper limit of integration becomes important.

Discrete binary filtration coefficients reflecting heterogeneity of a particle population are proposed in several studies [113, 258, 259].This type of distribution is adopted to model the following case scenarios. Under unfavorable surface conditions, the colloid deposition can be classified into two categories: the unhindered particle deposition into a relatively deep secondary energy well (fast) and the particle deposition overcoming an energy barrier to reach the primary energy minimum [101, 103, 260]. Here a bimodal distribution consisting of two normal subdistributions is adopted and takes the following form:

$$\begin{aligned} p(\Lambda_i) = {} & f_{low} \frac{1}{\sigma_{low}\sqrt{2\pi}} \exp\left[-\frac{1}{2}\left(\frac{\Lambda_i - \Lambda_{low}}{\sigma_{low}}\right)^2\right] \\ & + f_{high} \frac{1}{\sigma_{high}\sqrt{2\pi}} \exp\left[-\frac{1}{2}\left(\frac{\Lambda_i - \Lambda_{high}}{\sigma_{high}}\right)^2\right] \end{aligned} \tag{2.8}$$

where Λ_{low} and Λ_{high} are the mean filtration coefficients of the two normal subdistributions,σ_{low} and σ_{low} are the corresponding standard deviations, and f_{low} and f_{high} are the fractions of the total population associated with each subdistribution.

In the following computations, it is assumed that the interstitial velocities of the particles of various sizes are the same. They may either be approximated by the average pore velocity, or need to be fitted to the experimental results. On the contrary, the filtration coefficients may be different. To approximate the continuous distribution of them, the particle population is simply discretized into 1000 representative species, each of which is assigned a single filtration coefficient. The proportion of each species is calculated in accordance with the continuous expression. However, the sum of the proportions is not unity, due to a local truncation error and a truncation of Λ close to infinity. It is then normalized by dividing the sum by itself. The procedure needs two artificial values: the minimum and the maximum of the filtration coefficients. This is especially related to the power distribution, as discussed above.

2.2.3 Boundary conditions

The adopted boundary conditions here are ad hoc for the system of elliptic equations. There are four boundary conditions in the space-time plane: the initial condition (2.9) the terminal condition (2.10) the inlet condition (2.11) (2.12) and the outlet condition (2.13):

$$C_i(X,0)=0 \tag{2.9}$$

$$C_i(X,\xi T_0)=0 \tag{2.10}$$

$$C_i(0,T)=1, \quad 0<T<T_0 \tag{2.11}$$

$$C_i(0,T)=0, \quad T_0 \le T \le \xi T_0 \tag{2.12}$$

$$\left.\frac{dC_i}{dX}\right|_{X=1}=0 \tag{2.13}$$

This is rather different from the boundary conditions for the parabolic ADE, in that the second derivative in the temporal dispersion term here requires an additional temporal boundary condition. The details are discussed in Ref. [123].

The four boundary conditions are selected to model column experiments in most labs. Before the injection the column is often flooded with pure water to make the bed clean. Thus, condition (2.9) reflects absence of suspended particles in the bed prior to flooding. The influent concentration is set to be constant during the particle injection time T_0 (boundary condition (2.11)). Pure water is injected after the suspension injection, so that all the suspended particles are flushed out of the system (boundary condition (2.12)). The value ξ is selected so that after ξT_0 the suspended concentration is effectively zero, hence, the final condition (2.10). Our computations show that any value of $\xi \geq 5$ provides the same shape of solutions.

2.2.4 Degree of hyperexponentiality

In order to quantitatively describe the degree of hyperexponentiality in the deposition profiles, the following definitions are introduced. Providing that the dimensionless retained particle concentration is a function in terms of dimensionless X, $S(X)$ and the deposition is monotonically decaying with X, $S'(X) \leq 0$, the degree of the hyperexponentiality is:

$$DH = \frac{\max\left[\frac{d(\ln S)}{dX}\right] - \min\left[\frac{d(\ln S)}{dX}\right]}{\max\left[\frac{d(\ln S)}{dX}\right]} \tag{2.14}$$

The values of DH are listed in the tables reflecting the results of the computations.

2.2.5 Implementation

Direct discretization of Equation (2.3) and Equation (2.4) by a finite difference method results in a system of linear algebraic equations for each point on a rectangular grid. A center difference regime is adopted to achieve accuracy of second order, $O(\Delta X^2)$ and $O(\Delta T^2)$. The computation is implemented in MATLAB, utilizing its fast implementation of the matrix operations [261]. To achieve higher accuracy the mesh grid is set to be 1000×1000. In the calculations sparse matrices are adopted for the purpose of memory optimization and fast computation [262]. In order to demonstrate the reliability of the program, a calculation is performed with the same configurations as those in Refs. [207, 218]. Especially, D_t is set to be zero and for the distribution the number of particle species is 1000 to achieve high accuracy. The numerical solution highly agrees with the analytical solution for the unsteady state in Ref. [207], with an average difference of 0.1%. In order to fit the experimental breakthrough curves, the dispersion coefficients and the filtration coefficients are modified manually. Predicted deposition profiles can then be compared to the experimental observations. Especially for the distributed filtration coefficients further adjustments are needed to fit the hyperexponential deposition profiles.

2.3 Results of Numerical Modeling

The goal of this section is to find out which parameters have most influence on the shapes of the deposition profiles and breakthrough curves. First, a number of computations have been performed with the ADE and the different distributions for Λ. Next, the results of the elliptic modeling have been obtained and the effects of the temporal dispersion on the breakthrough curves and deposition profiles have been studied. Finally, the combined influences of both the temporal dispersion and the distribution of Λ have been studied.

2.3.1 ADE with distributed filtration coefficients

Calculations are first performed without the temporal dispersion but only with the distributed filtration coefficients. The log-normal distribution, the power law distribution and the bimodal distribution are the adopted three types of distributions. Results under the condition of both large and small spatial dispersion are compared for the calculations with the log-normal distribution and the power law distribution.

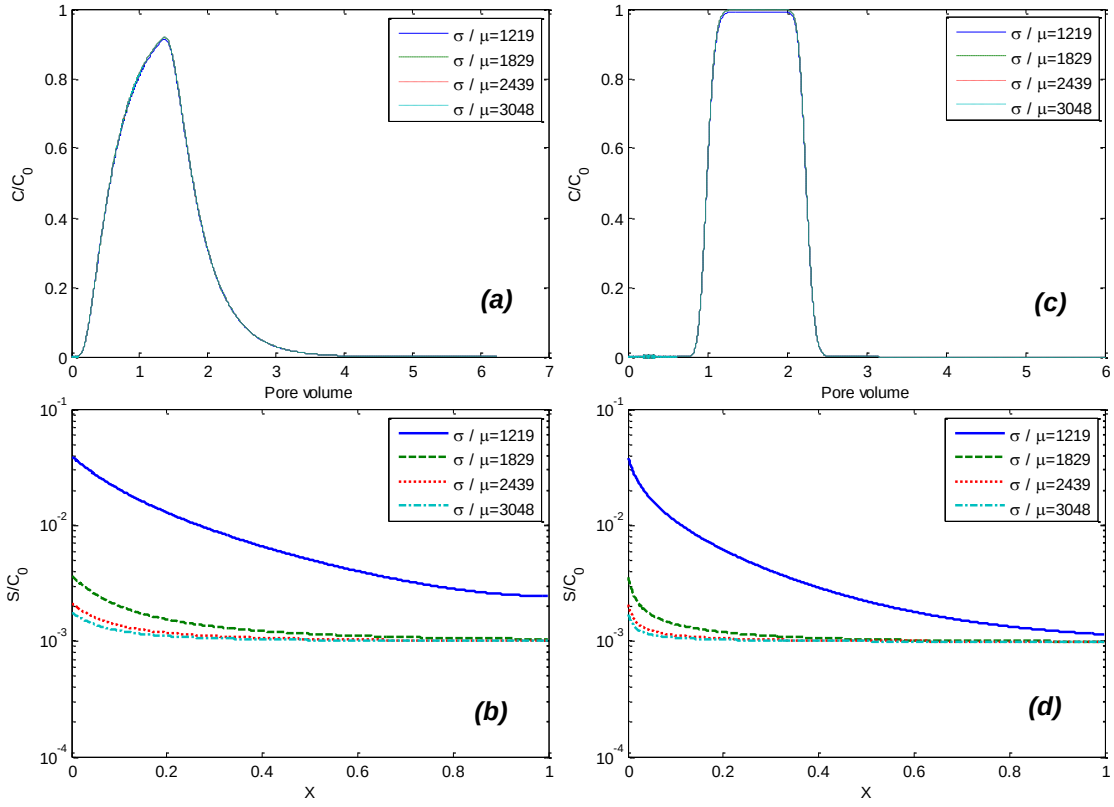

Figure 2.1 Breakthrough curves and deposition profiles with log-normal distribution of filtration coefficients, (a) (b): large spatial dispersion, (c) (d): small spatial dispersion.

For the log-normal distribution the mean value of the filtration coefficients is kept constant, while the standard deviations vary. Other invariable parameters are:μ=1.97, T_0=1.25PV, u=1, R_t=0, R_x=1/30, $\Lambda_{min}=2\times10^{-3}$, Λ_{max}=394. The rest of the parameters adopted in the calculations are shown in Table 2.1. As seen in Figure 2.1, the results show that the log-normal distribution of Λ gives rise to hyperexponential deposition profiles, but only has a minor influence on the breakthrough curves. The degree of hyperexponentiality is limited. Even extremely large standard deviations do not produce extremely hyperexponential profiles.

Table 2.1 Parameters adopted for calculations with the log-normal distribution of filtration coefficients and resulting degrees of hyperexponentiality.

σ/μ	σ	R_x	DH
1219	2.4	$3^{-1}/30^{-1}$	69.03/45.41
2032	4.0	$3^{-1}/30^{-1}$	193.23/724.23
2845	5.6	$3^{-1}/30^{-1}$	362.54/1076.01
3658	7.2	$3^{-1}/30^{-1}$	488.91/1088.23

For the power law distribution, different values of power b (see Equation (2.6)) are chosen to vary the distribution. The maximum and the minimum of the distribution are kept constant. For different calculations: T_0=1.25PV, u=1, R_t=0, R_x=1/30, $\Lambda_{min}=2\times10^{-3}$, Λ_{max}=1968. The rest of the parameters adopted for the calculations are shown in Table 2.2.

Table 2.2 Parameters adopted for calculations with the power law distribution of filtration coefficients and resulting degrees of hyperexponentiality. Results are shown in Figure 2.2.

σ/Λ_{min}	σ (10^3)	R_x	b	DH
26754	574821	$3^{-1}/300^{-1}$	0.80	136320/200920
1871	3682	$3^{-1}/300^{-1}$	1.20	26824/1420
133	263	$3^{-1}/300^{-1}$	1.60	19969/28.35
9	20	$3^{-1}/300^{-1}$	2.00	1.03/1.08

As seen in Figure 2.2, the results are similar to the log-normal distribution: the power law distribution of Λ results in hyperexponential deposition profiles, but only has a minor influence on the breakthrough curves. The distributions with the larger standard deviations yield higher hyperexponentiality. A larger standard deviation reflects a higher heterogeneity of the particle population. This confirms that one of the reasons for hyperexponential deposition profiles may be heterogeneity of the particle population [101, 103]. The degree of hyperexponentiality with the power law distribution of Λ is generally higher than with the log-normal distribution of Λ.

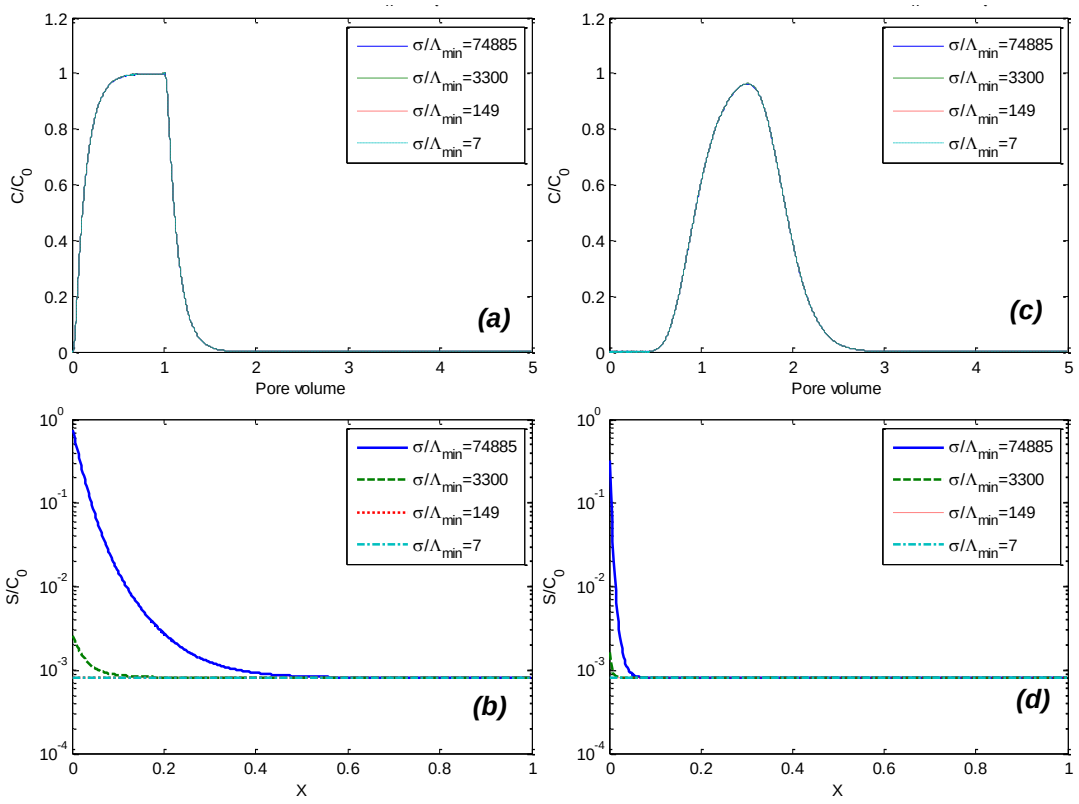

Figure 2.2 Breakthrough curves and deposition profiles with power law distribution of filtration coefficients, (a) (b): large spatial dispersion, (c) (d): small spatial dispersion.

Calculations with the different maxima and minima of the power distribution Λ_{min}, Λ_{max} have also been carried out. Results (not given here) show that the minimum of the distribution does not affect much the degree of hyperexponentiality, but still may slightly change the shape of a deposition profile. Increasing the maximum of the distribution mainly increases the retained concentration close to the inlet; therefore the degree of the hyperexponentiality also increases.

Table 2.3 Parameters adopted for calculations with bimodal distribution of filtration coefficients and resulting degrees of hyperexponentiality. Results are shown in (a) and (b) of Figure 2.3.

$\Lambda_{high}/\Lambda_{low}$	Λ_{high}	Λ_{low}	*DH*
1.00	1.20	1.20	0
67.33	80.80	1.20	35.35
133.67	164.40	1.20	54.71
200.00	240.00	1.20	69.36

For the bimodal distribution, the fractions and the standard deviations of the two groups are set to be equal at first. For different calculations: T_0=1.25*PV*, u=1, R_t=0, R_x=1/30, $\Lambda_{min}=2\times10^{-3}$, Λ_{max}=1968, σ_{high}=1.2, σ_{low}=1.2, f_{high}=0.5.The rest of the parameters are

shown in Table 2.3. First, Λ_{low} is kept constant and various Λ_{high} is selected. The influence of the difference between Λ_{high} and Λ_{low} is seen in Figure 2.3 (a) and (b). The profile may be split roughly into two almost "exponential" parts, with the different inclinations of the decay. With increasing difference between Λ_{high} and Λ_{low}, the deposition profile becomes more hyperexponential.

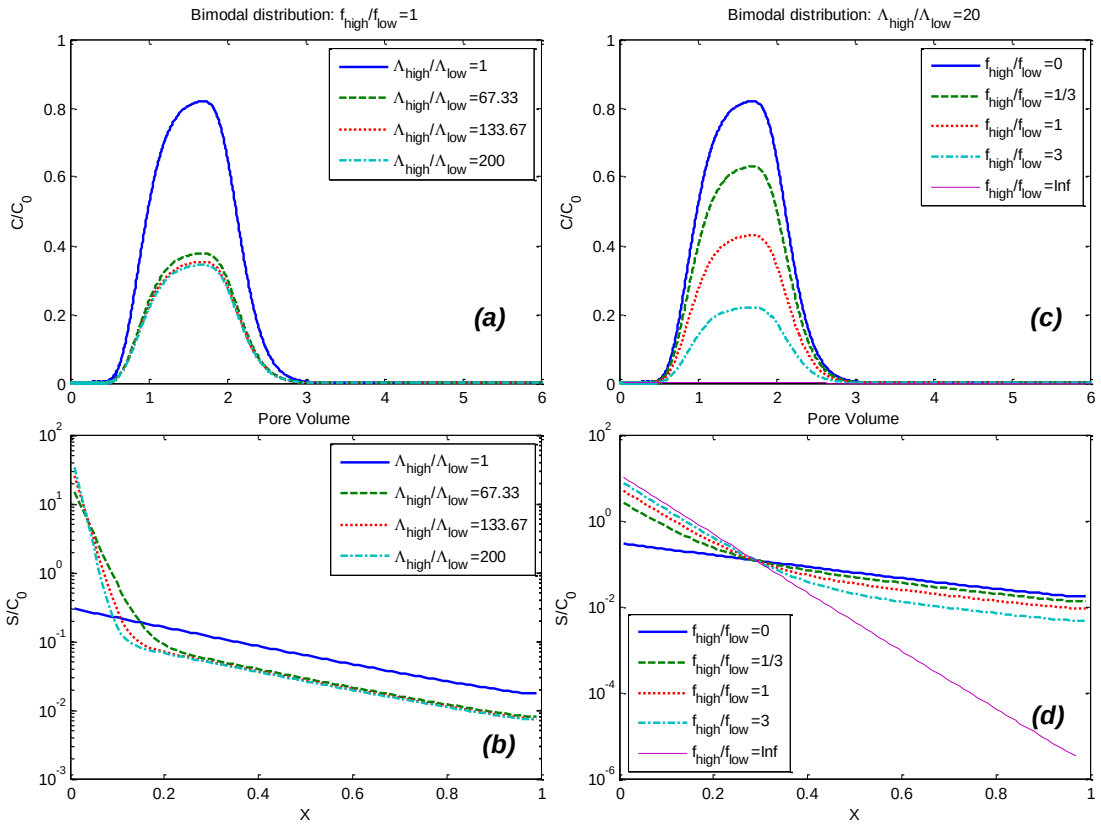

Figure 2.3 Breakthrough curves and deposition profiles with bimodal distribution of filtration coefficients. (a) (b): Keeping the fractions, standard deviations and Λ_{low}, change of Λ_{high}. (c) (d): Keeping Λ_{low}, Λ_{high} and the standard deviations, change of f_{low}, f_{high}.

Then Λ_{high} and Λ_{low} are kept constant, and various fractions of the two species are selected. The selected parameters for the calculations are: Λ_{high}=24, Λ_{low} =1.2, T_0=1.25PV, u=1, R_t=0, R_x=1/30, $\Lambda_{\min}=2\times10^{-3}$, $\Lambda_{\max}$=1968, σ_{high}=1.2, σ_{low}=1.2. and the rest of the parameters are given in Table 2.4. When the fractions of the different particles vary from f_{high}=0, f_{low}=1 to f_{high}=1, f_{low}=0, i.e. from the single component with low Λ to the single component with high Λ, the deposition decay changes from exponentiality to hyperexponentiality, and then to exponentiality again, as seen in Figure 2.3 (d). Thus,

hyperexponentiality is observed in the systems with significant amounts of particles of different sizes, as in Refs.[101, 208].

Table 2.4 Parameters adopted for calculations with bimodal distribution of filtration coefficients and resulting degrees of hyperexponentiality. Results are shown in (c) and (d) of Figure 2.3.

f_{high}/f_{low}	f_{high}	f_{low}	*DH*
0	**0**	**1.00**	**0**
1/3	**0.25**	**0.75**	**13.92**
1	**0.50**	**0.50**	**14.69**
3	**0.75**	**0.25**	**14.94**
Inf	**1.00**	**0**	**0**

As seen in Figure 2.3 (d), the part of the deposition profile close to the inlet is formed by the particles with high Λ. The rest of the profile by the particles with low Λ. The regions of dominance of the two species depend on the ratio f_{high}/ f_{low}. For high values of f_{high}/ f_{low} the particles with high values of Λ remain close to the inlet, while the particles with low Λ travel further, close to the outlet. The resulting deposition profiles look like a combination of the two straight-linear intervals, respectively, corresponding to the high and the low values of Λ.

Unlike the log-normal distribution and the power law distribution, the bimodal distribution of filtration coefficients highly influences the breakthrough curves, as seen in Figure 2.3 (a).

In summary of the above results, the distribution of Λ can give rise to highly hyperexponential deposition profiles if the standard deviations are very large. Similar phenomena have been observed in Refs. [101, 207, 208]. Such a wide distribution of filtration coefficients may be doubted for the systems of similar particles. Therefore, the question arises, whether the temporal dispersion, in combination with somehow narrower distributions of the filtration coefficients (or, even, with a single filtration coefficient), may also result in a hyperexponential deposition profile.

2.3.2 Elliptic equation with a single filtration coefficient

Let us now present the results with $D_t>0$. The calculations are performed for a suspension characterized by a single filtration coefficient. The values used for the calculations are $T_0=5PV$, $u=1$, $\Lambda=0.49$ and the rest of the values are shown in Table 2.5. The effects of the temporal dispersion both on the breakthrough curves and the deposition profiles are illustrated in Figure 2.4.

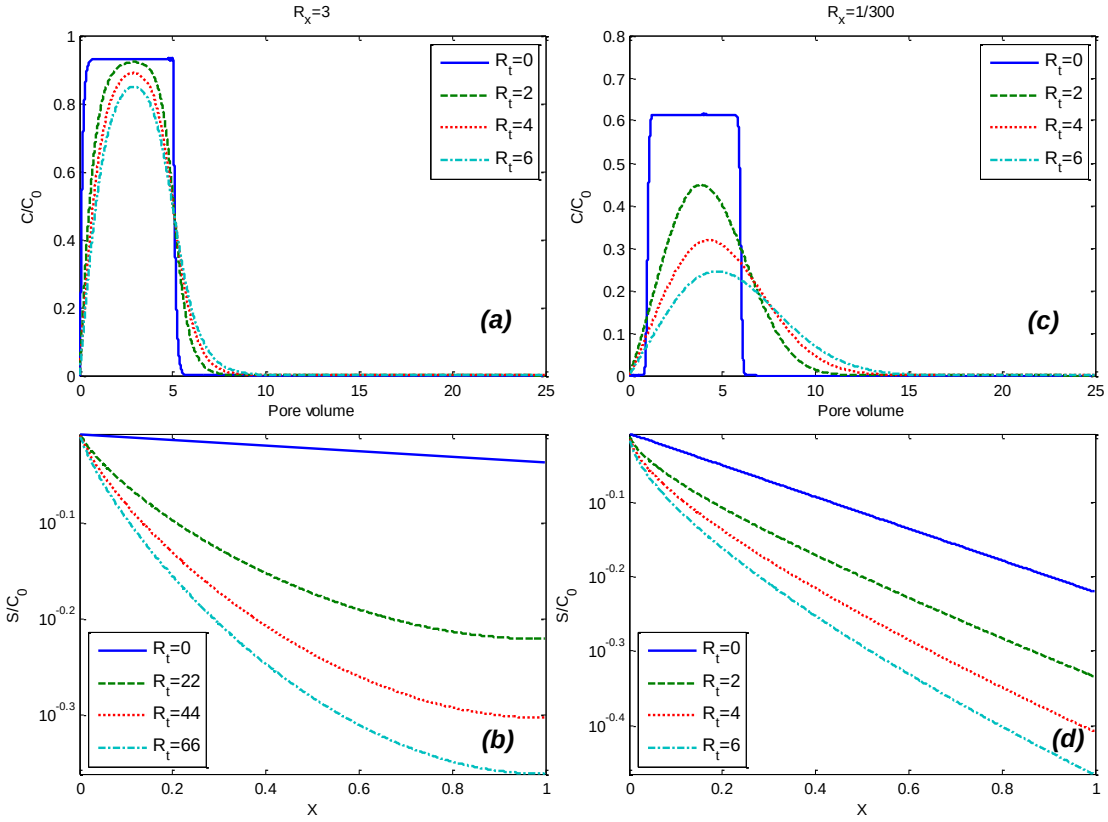

Figure 2.4 Breakthrough curves and deposition profiles with a single filtration coefficient, (a) (b): large spatial dispersion, (c) (d): small spatial dispersion.

As seen from the figure, temporal dispersion not only leads to hyperexponentiality of the deposition but also has a clear influence on the breakthrough curves. The delayed peaks and large ending tails are characteristic of the elliptic dispersivity. Similar effects have been observed in nature and in the experiments with stochastically heterogeneous porous media [10, 11, 123, 217, 218, 263]. The degree of hyperexponentiality caused by temporal dispersion, on the other hand, is relatively limited.

Table 2.5 Parameters adopted for calculations with elliptic equation and a single filtration coefficient and resulting degrees of hyperexponentiality. Results are shown in Figure 2.4.

R_x	R_t	DH
3/300^{-1}	**0**	**0/0**
3/300^{-1}	**22.00**	**155.56/6.17**
3/300^{-1}	**44.00**	**153.27/6.95**
3/300^{-1}	**66.00**	**154.39/6.71**

The temporal dispersion works in combination with the spatial distribution. As seen in Figure 2.4 (a), (c), large spatial dispersion may partly compensate for some influence of the temporal dispersion on the breakthrough curve. This unusual phenomenon is opposite to the effect of the spatial dispersion in absence of the temporal dispersion. On the other hand, it enhances the hyperexponentiality caused by the temporal dispersion in the deposition profiles.

2.3.3 Elliptic equation with distributed filtration coefficients

As seen from the results above, both the temporal dispersion and the distribution of the filtration coefficients give rise to the deposition hyperexponentiality. This section focuses on how the two factors in combination affect the breakthrough curves and the deposition profiles, and whether their effects can be complemented or compensated for by each other.

Table 2.6 Parameters adopted for illustration of the distribution of filtration coefficients, compensated for by temporal dispersion. Results are shown in Figure 2.5.

σ/Λ_{min}	R_t	b
171	**8.9286**	**1.1**
93	**8.9286**	**1.3**
14	**8.9286**	**10**
171	**4.4643**	**1.1**
93	**9.8214**	**1.3**
14	**11.1607**	**10**

As an example, a system with power law distributed filtration coefficients has been studied. In the calculations: T_0=2.17PV, u=1, R_x=1.79, Λ_{min}=0.896, Λ_{max}=1344, and the rest of the parameters are shown in Table 2.6. In the first series of computations, power b in the distribution is increased to reduce the standard deviation, and the minimum and

maximum of the filtration coefficients are kept constant. It causes the deviations both in the breakthrough curves and the deposition profile, as seen in Figure 2.5 (a), (b). Then the temporal dispersion is increased to compensate for loss of the distribution width. The breakthrough curves are recovered, but the deposition profiles still deviate, as seen in Figure 2.5 (c),(d). Thus, the influence of the distribution of Λ on the breakthrough curves can be well compensated for by temporal dispersion, but that on the deposition profiles cannot.

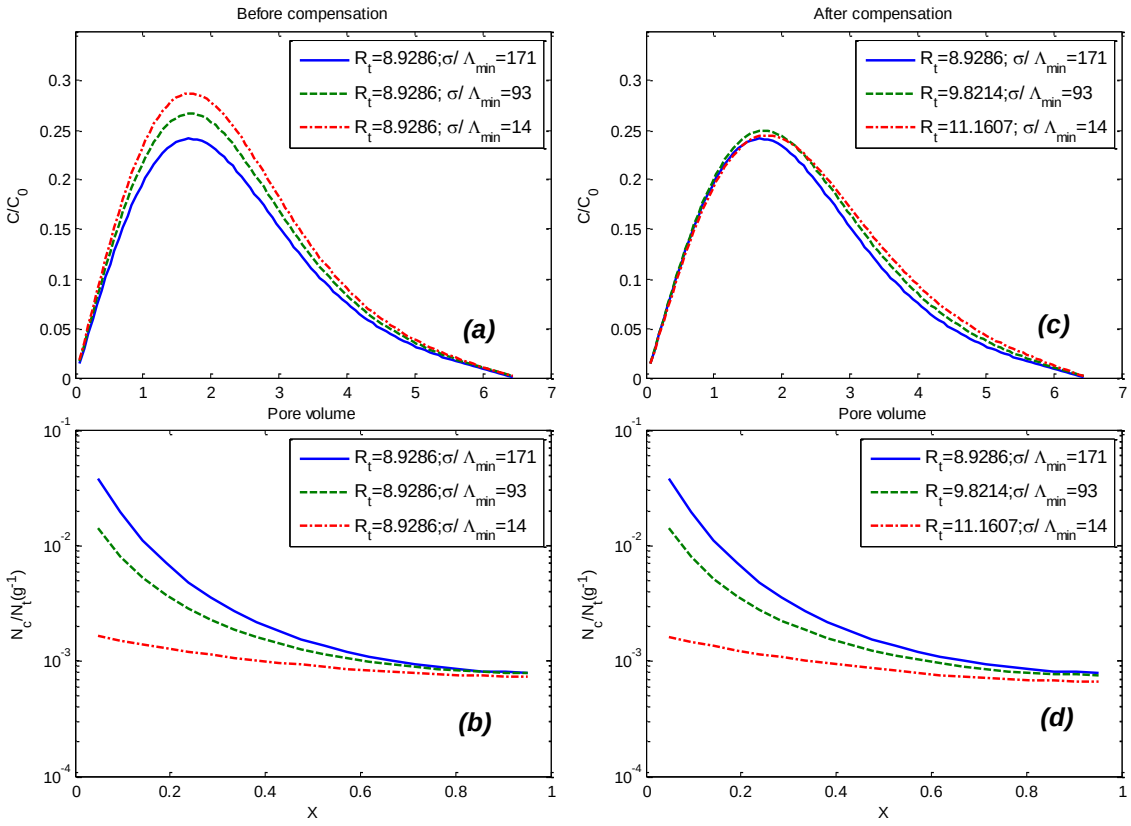

Figure 2.5 Illustration of the distribution of filtration coefficients compensated for by the temporal dispersion. (a) (b): Decrease of the standard deviation of the distribution with constant temporal dispersion. (c) (d): Decrease of the standard deviation of the distribution with increasing temporal dispersion.

A possibility of opposite compensation was also checked. Under the above conditions, the parameters are modified according to Table 2.7. With increased temporal dispersion and invariable distribution of Λ, the deviation in the deposition profile, was minor but the BTC deviated significantly, as seen in Figure 2.6, (a), (b). Then the standard deviation of the distribution is decreased to compensate for the increased temporal dispersion. The

BTC was recovered, but the deposition profiles still deviated (Figure 2.6 (c), (d)). This indicates that the influence of the temporal dispersion can be compensated for by the distribution of the filtration coefficients to some extent, but not entirely.

Table 2.7 Parameters adopted for illustration of temporal dispersion, compensated for by the distribution of filtration coefficients. Results are shown in Figure 2.6.

σ/Λ_{min}	R_t	b
291	**4.4643**	**0.89**
291	**6.6964**	**0.89**
291	**8.9286**	**0.89**
291	**4.4643**	**0.89**
171	**6.6964**	**1.1**
43	**8.9286**	**10**

Selection of more flexible distributions and fitting multiple parameters might, of course, lead to complete compensation for the effect of temporal dispersion. However, these calculations show that, at least, the three distributions considered above provide breakthrough curves and deposition profiles possessing individual features, which may be different from the features of the profiles produced by non-zero temporal dispersion. They are clearly distinguishable, and interaction between them may contribute to better reproduction of the results. Especially breakthrough curves are affected. The cases of clearly dispersed breakthrough curves require introduction of temporal dispersion for fitting, while the cases where the breakthrough curves are not dispersed, but the deposition profiles are hyperexponential, require fitting with the distributed filtration coefficients alone.

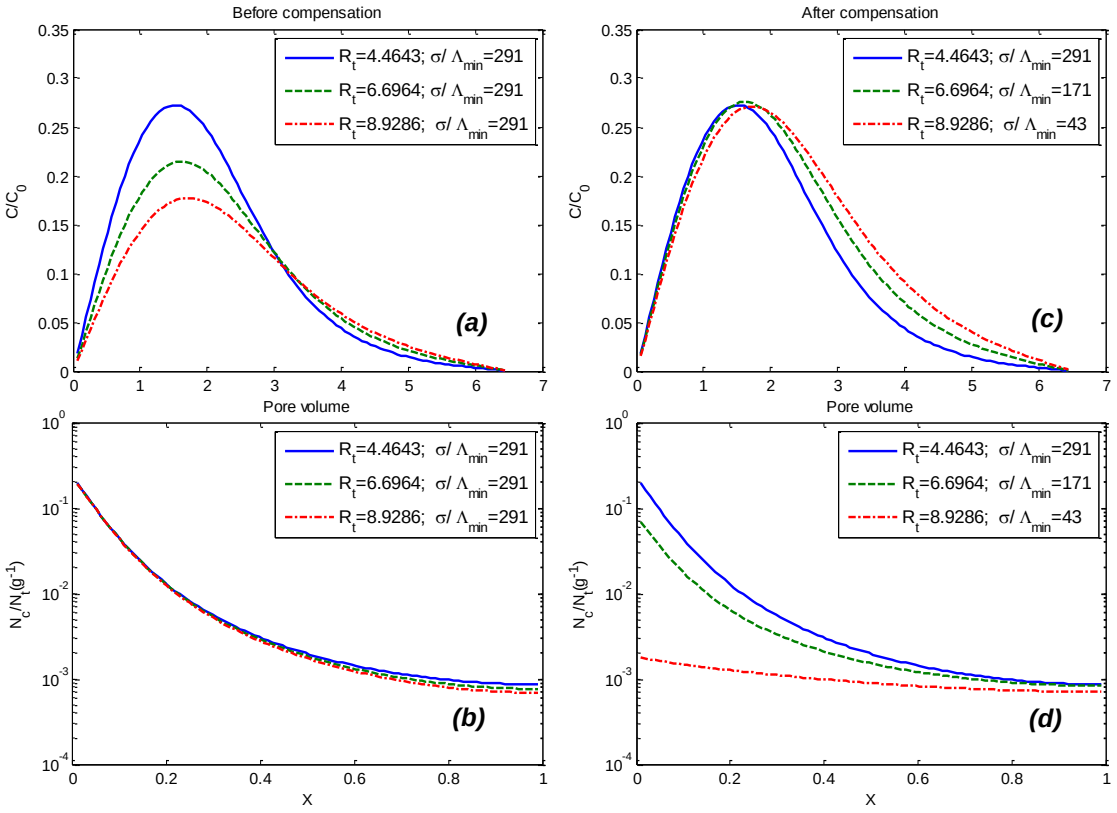

Figure 2.6 Illustration of the temporal dispersion compensated for by the distribution of filtration coefficients. (a) (b): Increase of the temporal dispersion and keeping the standard deviation of the distribution. (c) (d): Increase of the temporal dispersion with decreasing standard deviations of the distribution.

2.4 Verification by experiments

In this section the results of various modeling methodologies are compared to the experiments carried out with the different porous media reported in the literature. The purpose is to find out which modeling methodology is proper under which experimental conditions. The porous media range from the most homogeneous porous media, e.g. packed glass beads, to the most heterogeneous porous media, e.g. natural aquifer material. Since tracers may be considered as suspensions not exhibiting deposition, the experiments with them are also considered.

2.4.1 Colloid in uniformly packed glass beads

In this subsection the results of numerical modeling are compared with the experiments carried out with artificial homogeneous porous media. N. Tufenkji and M. Elimelech [103] conducted column experiments on filtration of uniform polystyrene latex colloid suspension in packed soda-lime glass beads. The particles forming glass beads were of a uniform size and much larger than the colloid particles. A low influent concentration was adopted in order not to influence the pore structure. The solution chemistry was strictly controlled.

Calculations with the integral model are performed so as to reproduce the experimental results. The breakthrough curves predicted by the ADE and the experimental breakthrough curves highly agree with each other. Their shapes are almost not "washed-out" by dispersion. Therefore, it is reasonable to try modeling the experimental results by introducing the distribution of the filtration coefficients. Selection of the Λ distribution types for fitting the experiments follows a practical principle: few parameters to tune the shape of the distribution. Since the log-normal distribution cannot, apparently, provide significant deviations from the exponentiality of the deposition profiles observed in the experiments, it is not used for fitting. The bimodal distribution may seem to be physically reasonable for some cases [103], but there are as many as five parameters to be modified. The power law distribution with only three parameters to be modified is chosen due to its practical convenience in the computations. A similar choice was made in Ref. [207]. Because most of the power law distribution concentrates close to the minimum of the filtration coefficient, it is an important parameter as well as power b in Equation (2.6).

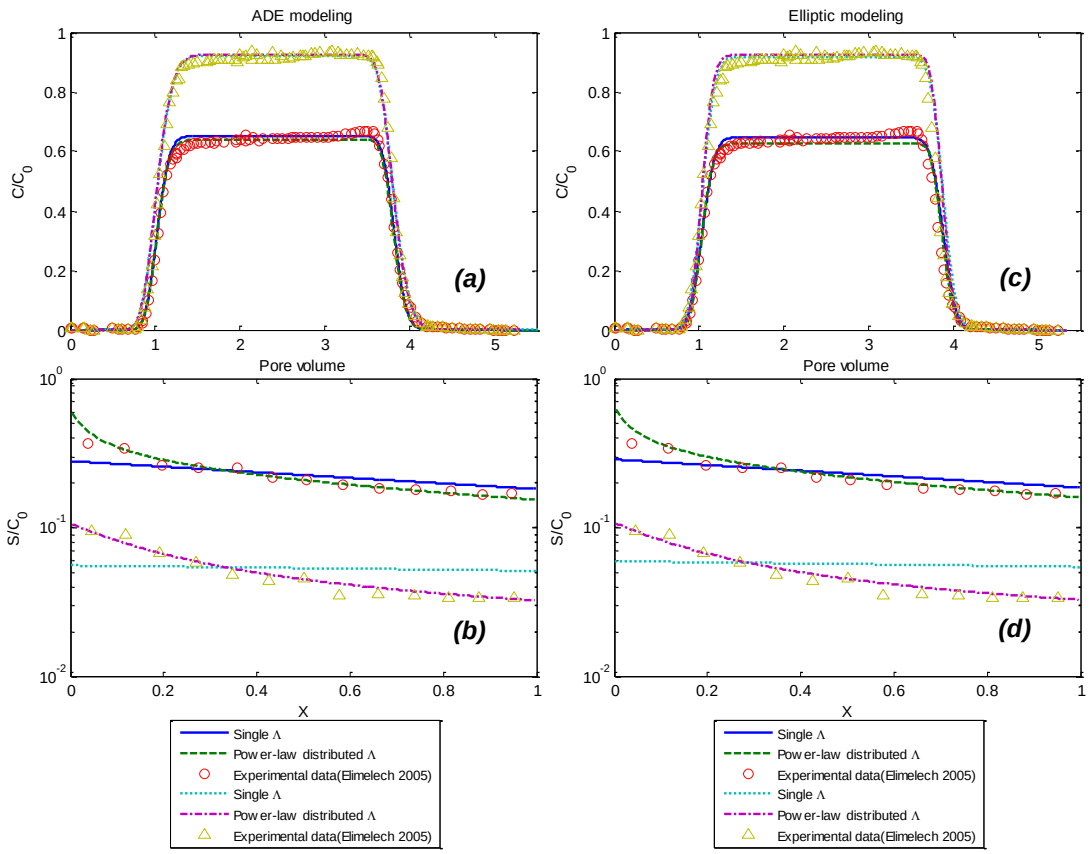

Figure 2.7 Numerical modeling results compared with the experimental data of N. Tufenkji and M. Elimelech [103]. (a) (b): ADE modeling, (c) (d): elliptic modeling. The power law distribution is adopted.

Detailed parameters for the calculations are shown in Table 2.8. As seen in Figure 2.7 (b), (d), after fitting the breakthrough curves, both the ADE with a single Λ and the elliptic equation with a single Λ predict (almost) exponential deposition profiles. The reason is the limitations on the variation of the temporal dispersion coefficient R_t caused by limited dispersion of the breakthrough curves. Meanwhile, the experimental results show that even for these monodisperse colloid suspensions the deposition profiles are hyperexponential. The results of the previous section indicate that the distribution of Λ may not be fully reflected by the shape of the breakthrough curves; therefore the properties of the distribution need to be fitted to the deposition profiles. The results show that the ADE with distributed filtration coefficients is sufficient to fit both the breakthrough curves and the hyperexponential deposition profiles. The fitted temporal dispersion in the elliptic equation is not large enough to yield a clearly hyperexponential deposition profile. Imposing a larger temporal dispersion would result in prohibitive

modification of the breakthrough curve. The fact that the dispersion is not large is probably attributed to a high degree of homogeneity of the porous medium used for the experiment.

Table 2.8 Parameters adopted for calculations in comparison with the experiments of N. Tufenkji and M. Elimelech[103], corresponding to ionic strengths of 200*mM*/100*mM* respectively. Results are shown in Figure 2.7.

Methodology	$R_x(10^{-3})$	$R_t(10^{-3})$	$\Lambda_{min}(10^{-2})$	$\Lambda_{max}(10^{-2})$	b
ADE+single Λ	**4.17/4.17**	**0**	**47.20/8.74**	**47.20/8.74**	**-/-**
ADE+distributed Λ	**4.17/7.93**	**0**	**33.00/2.04**	**9102/955.71**	**1.90/1.50**
Elliptic+single Λ	**1.59/1.59**	**5.15**	**45.50/8.74**	**45.5/8.74**	**-/-**
Elliptic+distributed Λ	**1.59/1.59**	**3.43**	**34.97/2.04**	**9557.10/955.71**	**1.90/1.50**

It should be remarked that the distribution of the filtration coefficients turns out to be rather wide, in spite of the apparent homogeneity of the particle population, as was also observed in Ref. [103]. The reason for the hyperexponentiality in this case is explained by the authors to be the presence of repulsive DLVO interactions. Under the unfavorable surface attachment conditions, the particles overcoming energy barriers to reach the primary energy minimum deposit slower, while others deposit faster. Such heterogeneity of interactions between the particles and the porous medium is the direct cause of the hyperexponential deposition profile. The same authors also managed to apply the ADE with a bimodal distribution of filtration coefficients to fit the experiments under similar conditions in Ref. [101].

2.4.2 Colloid in uniformly packed sand

The next experimental study considers suspension flow in a, apparently, more heterogeneous porous medium. Bradford et al. [115] adopted yellow-green fluorescent latex microspheres as colloid particles and packed Ottawa sand (99.8% quartz) as porous media for the column experiments. The sand particles were randomly shaped but uniformly sized and much larger than the colloid particles. As in the previous experiments, a low influent concentration was adopted in order not to influence the pore structure, and the solution chemistry was strictly controlled.

A number of calculations are carried out, trying to reproduce the results of Bradford et al. with the complete model involving the filtration coefficients distribution and the temporal dispersion. The common parameters in the calculations were u=1, Λ_{max}=1400. The rest of the parameters are given in Table 2.9. As seen in Figure 2.8, for these monodisperse colloid suspensions the experimental deposition profiles are hyperexponential. Although the breakthrough curves are more dispersed than in the previous set of the experiments, the dispersion is still relatively mild.

Table 2.9 Parameters adopted for modeling in comparison with experiments of S. Bradford et al. [115], in sequence: dc/d50= 0.008/0.013/0.020. Results are shown in Figure 2.8 and Figure 2.9.

Methodology	$R_x(10^{-3})$	$R_t(10^{-3})$	$\Lambda_{min}(10^{-2})$	$\Lambda_{max}(10^{-2})$	b
ADE+single Λ	**6.98/4.07/0.78**	**0/0/0**	**0.42/1.70/2.52**	**0/0/0**	**-**
ADE+distributed Λ	**7.75/8.13/7.03**	**0/0/0**	**0.31/1.36/2.24**	**137.54/203.14/268.80**	**1**
Elliptic+single Λ	**4.98/4.07/0.78**	**1.80/4.40/7.10**	**0.42/1.70/2.52**	**0/0/0**	**-**
Elliptic+distributed Λ	**7.75/8.13/7.03**	**0.35/0.44/0.36**	**0.31/1.36/2.24**	**137.54/203.14/268.80**	**1**

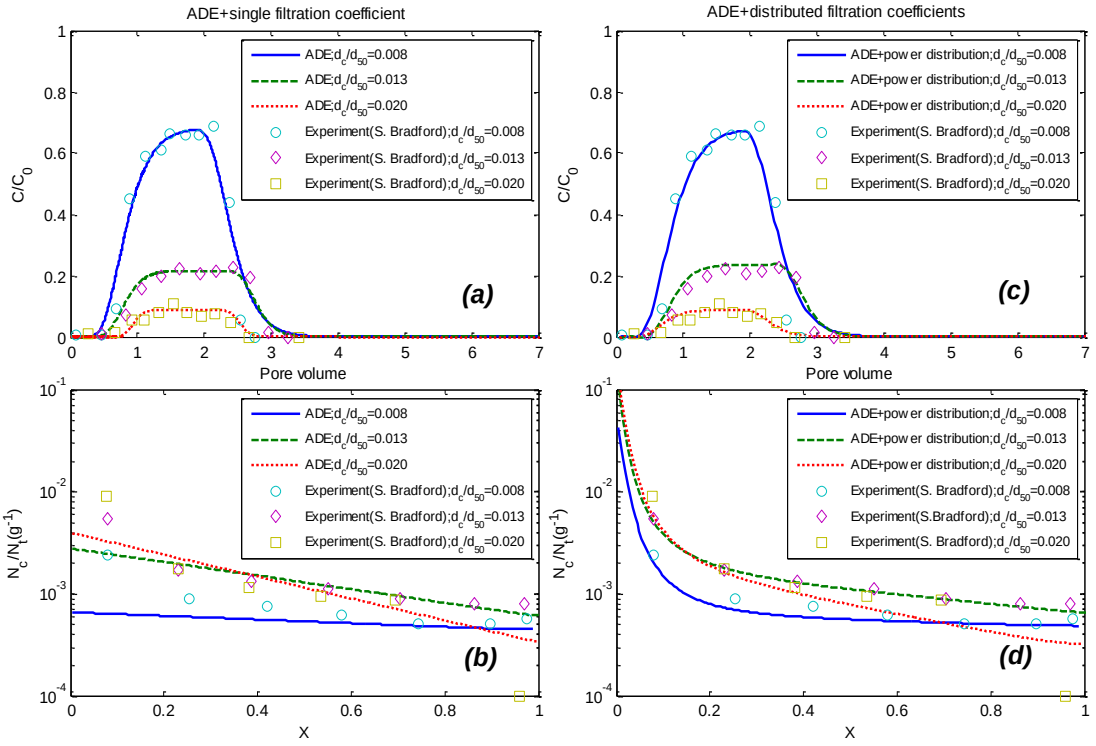

Figure 2.8 ADE modeling results compared with S. Bradford's experimental data [115] with homogeneous porous media. The power law distribution is adopted.

The distribution of Λ gives rise to hyperexponential deposition decay in compliance with the experimental observations. It should be noted, however, that the applied distribution is rather wide, which does not look fully realistic for a monodisperse suspension.

The experiment has also been simulated with a monodisperse suspension (a single value of Λ), but with a non-zero temporal dispersion. As seen in Figure 2.9 (a) and (c), the temporal dispersion fitted to match the observed breakthrough curves is still not large enough to predict clearly hyperexponential deposition profiles. The homogeneity of the porous media used in the experiments is likely to lead to Fickian transport with moderate temporal dispersion coefficients. The experimental results with homogeneous porous media can neither confirm the existence of nor the influence of temporal dispersion. On the contrary, the ADE with distributed filtration coefficients suffices to predict both the breakthrough curves and the deposition profiles. The best-fit parameters for the different ways of modeling are summarized in Table 2.9.

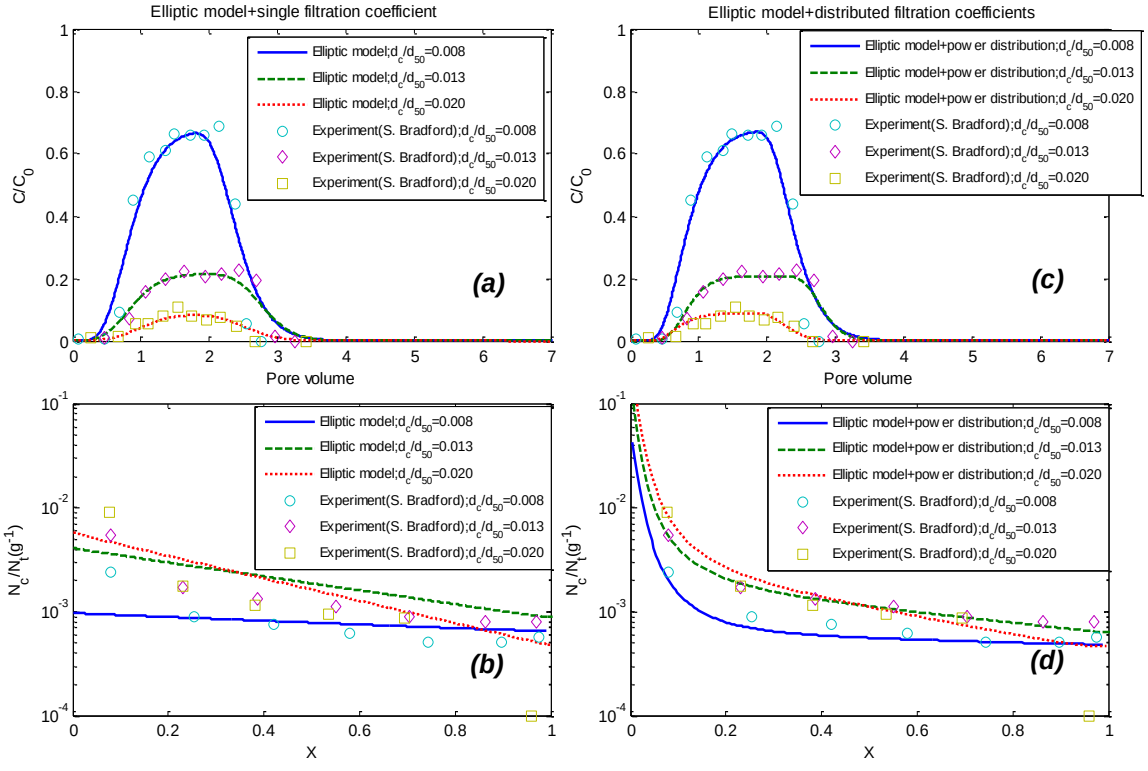

Figure 2.9 Elliptic modeling results compared with S. Bradford's experimental data [115] with homogeneous porous media. The power law distribution is adopted.

The DLVO calculations and the torque analysis by the authors of Ref. [115] show that the experimental conditions are also unfavorable for the surface attachment. The main mechanism of particle deposition is straining by design. Effects of straining are observed to be influenced by the grain sizes, grain shapes, hydrodynamics and solution chemistry. The heterogeneity of these factors is likely to cause the deposition hyperexponentiality. Compared to the experiment by N. Tufenkji and M. Elimelech [103], the authors adopted a more heterogeneous porous medium which gives rise to higher heterogeneity of particle-medium interactions. It may also explain why the degree of the deposition hyperexponentiality in this case is clearly higher. In Ref. [208], one of the same authors proposed a stochastic model for deep bed filtration also applying the distribution of filtration coefficients (log-normal and bimodal).

2.4.3 Colloid in non-uniformly packed sand

Since in relatively homogenous porous media temporal dispersion is not large enough to yield a hyperexponential deposition profile, comparison between the modeling and the experiments with highly heterogeneous porous media is of significance for the present study.

Bradford et al. [118] adopted carboxyl latex microspheres as colloid particles and Ottawa sand (99.8% quartz) as porous media for the column experiments. The heterogeneous system consisted of two types of soil, a soil cylinder lens (2.6cm diameter, 6cm long) embedded in the center of a second soil referred to as the matrix (5cm diameter, 10cm long), as shown in Figure 2.10. Median particle sizes of the lens and the matrix were different. The chosen experiment adopted sand consisting of particles of 710μm as the lens inside and sand of 360μm as the matrix outside. A characteristic size of a colloid particle was 3.2μm.

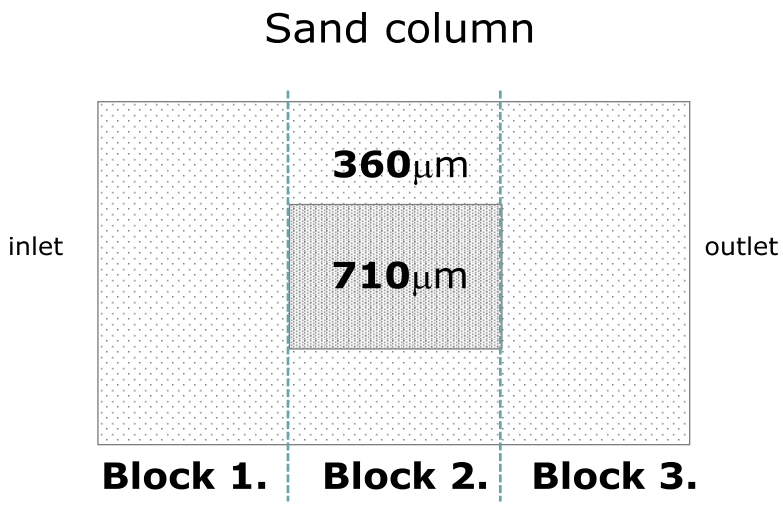

Figure 2.10 Schematic illustration of the experiment conducted by S. Bradford [118] . the sand lens of 710μm is in the center, and the sand matrix of 360μm is outside.

The deposition profile in this experiment is hyperexponential. Whether the hyperexponentiality is caused by temporal dispersion or by the spatial distribution of the filtration coefficients, is to be figured out.

Table 2.10 Parameters adopted for ADE/elliptic modeling in comparison with the experiments of S. Bradford et al. [118]. Results are shown in Figure 2.11 and Figure 2.12.

Upscaling regime		R_x	R_t	Λ
Three blocks	Block 1	0.0033/1.00	0/22.27	1.33/0.85
	Block 2	0.3333/13.33	0/0.05	0.61/0.57
	Block 3	0.0033/13.33	0/22.27	0.61/0.85
Single block		0.10/4.00	0/25.03	1.80/2.94

In this experiment, the heterogeneity of the porous medium is known in advance, and it is essentially two-dimensional. Meanwhile, only a single-dimensional simulator has been prepared in this study. Therefore, two simplified representations of the porous column have been adopted. The first representation approximates the column as three blocks in line, as seen in Figure 2.10. The side blocks are "pure", while the central block is "mixed". The second approach is, simply, to represent the column as a single block. In the latter regime, the effect of the heterogeneity is only encoded in the temporal dispersion term from the elliptic equation. The parameters for the calculations are shown in Table 2.10.

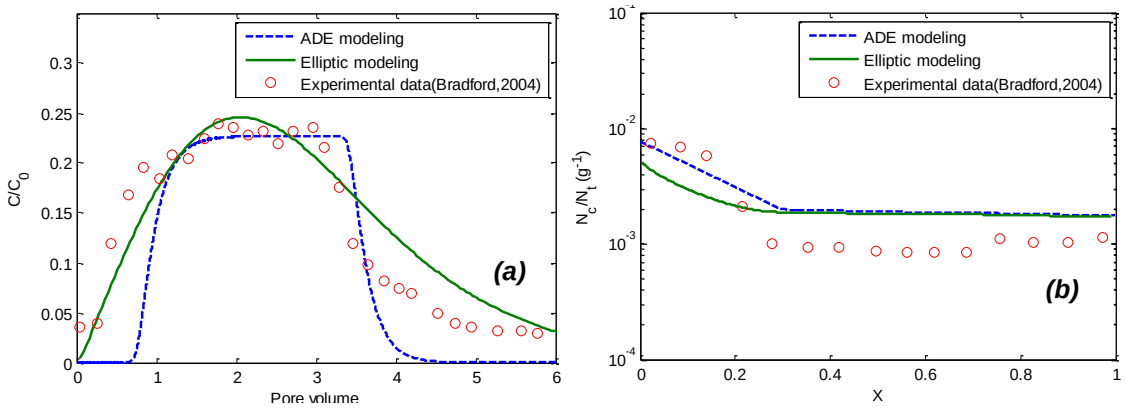

Figure 2.11 Numerical modeling result compared with experimental observations, with the porous media approximated by three blocks in line.

As seen in Figure 2.11, both the ADE modeling and the elliptic modeling with the porous media approximated by three blocks are able to produce hyperexponential deposition profiles. Hyperexponentiality of the deposition is caused by spatial distribution of the filtration coefficients. Unlike the ADE, the elliptic equation can better describe the BTC, "catching" early arrival of the suspension and the large ending tail in the breakthrough curve. The deposition profile predicted by the ADE is composed of the three exponential decays. Transitions between them are abrupt (especially, between the first two cuts). The deposition profile predicted by the elliptic equation also consists of the three parts, the first of which is smoother and is clearly hyperexponential. The transition between the first two phases is much smoother.

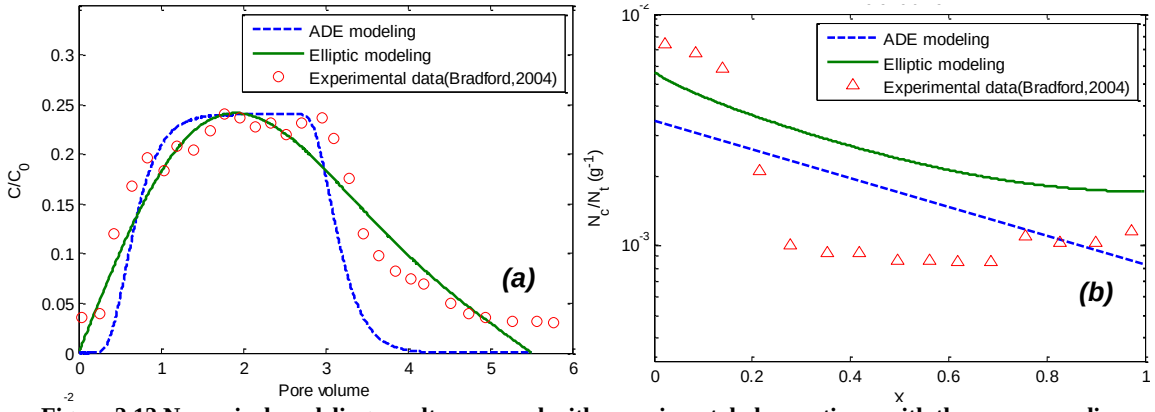

Figure 2.12 Numerical modeling result compared with experimental observations, with the porous media approximated by a single block.

The second approach, where the porous medium is considered as a single block, is represented in Figure 2.12. For this approach, the elliptic model is able to produce a hyperexponential deposition profile, while the ADE is not. Only the elliptic equation can

catch the early arrival and the large ending tail on the breakthrough curve. The degree of hyperexponentiality caused by the temporal dispersion alone is not as high as the degree of hyperexponentiality observed in experiments or that obtained by the model of three blocks described above.

It can be deduced from the results above that, in this case, the deposition hyperexponentiality is caused both by the spatial distribution of the filtration coefficients and by the temporal dispersion. It has not been possible to match the experimental results for this case as precisely as for previous cases, probably due to roughness of the one-dimensional representation.

2.4.4 Tracer injection in natural porous media

In order to confirm the ability of the elliptic equation to model non-Fickian transport in heterogeneous porous media, the modeling results are compared with tracer injection experiments. The physics of tracer injection is similar to that of the monodisperse suspension flow in porous media with a zero filtration coefficient. The experiments described by Boggs et al. have been carried out with natural aquifer material from a field site located at Columbus Air Force base in northeastern Mississippi [116]. They adopted a column with a diameter of 5.2cm and lengths of 100cm. Tracers with tritium and calcium bromide were injected at a flow rate of 4.8cm/day.

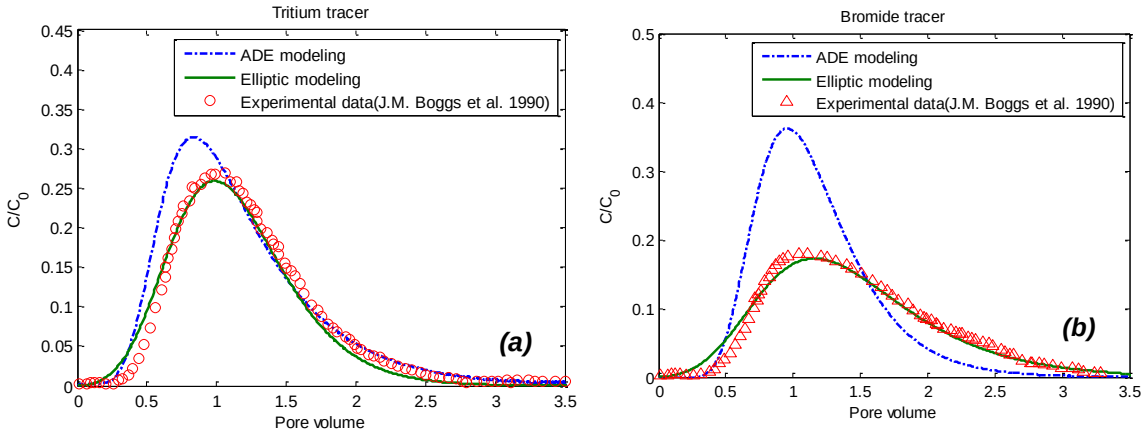

Figure 2.13 Tracer injection in natural porous media. Numerical modeling results compared with the experimental observations by J. M. Boggs et al. [116].

The breakthrough curves from the ADE and elliptic models are compared with the experimental observations, as seen in Figure 2.13. The modeling parameters are summarized in Table 2.11. Compared to the result of the ADE, the experimental breakthrough curve is characterized by the delayed peak and the large ending tail. These are the two distinguishing features of non-Fickian transport in heterogeneous porous media. Unlike the ADE, the elliptic equation succeeds in modeling the highly asymmetric breakthrough curve. Nonetheless, the elliptic equation slightly overestimates the early arrival of the tracer around the breakthrough. In addition, the tracer velocity needs to be different from the average pore water velocity in order to fit the breakthrough curve successfully, as seen in Table 2.11.

Table 2.11 Parameters adopted for ADE/elliptic modeling in comparison with the experiments of J. M. Boggs et al. [116]. Results are shown in Figure 2.13.

Tracer	R_x	R_t	u
Bromide	**0.09/0.10**	**0/0.0518**	**0.90/0.7**
Tritium	**0.18/0.06**	**0/0.0544**	**0.80/1.0**

It is also worth mentioning that, the parameters (velocity and dispersion coefficients) used for fitting the two breakthrough curves in the same porous medium are rather different in this case, while the parameters for fitting the experiments above and below are similar. It indicates that, for not-so-strongly heterogeneous porous media the parameters fitted to one experiment may be used for simulating another experiment, while for highly heterogeneous porous media they may not. It may be due to underestimating the really complicated physics in the natural porous media. Detailed study of this question is beyond the scope of the present work.

2.4.5 Tracer injection in porous media with uniform heterogeneity

Another experiment with heterogeneous media is carried out by Silliman and Simpson [257]. The experiment adopts an artificially heterogeneous porous medium with a coarse sand matrix and a number of small boxes of fine sand inside. The sand boxes are placed uniformly. The degree of heterogeneity is probably lower than in the experiments [116, 118] modeled above.

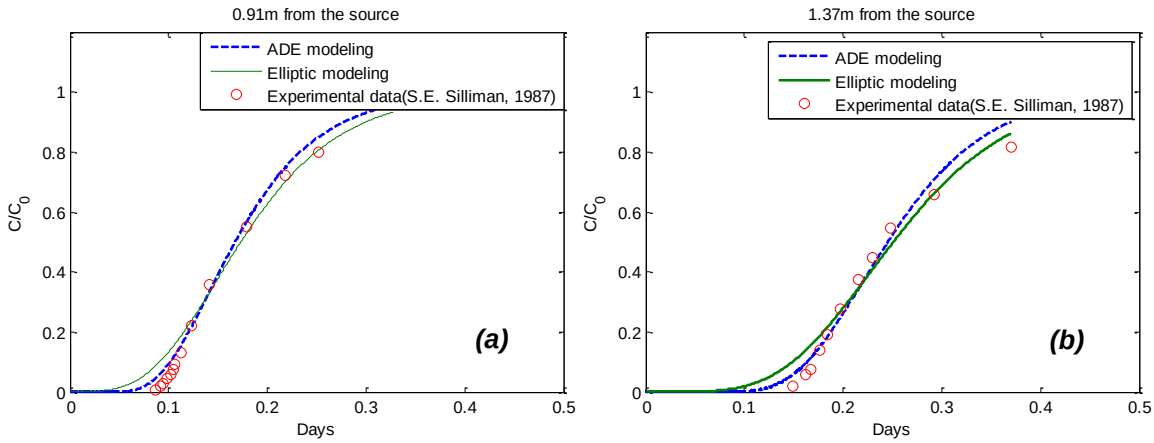

Figure 2.14 Tracer injection in porous media with uniform heterogeneity. Numerical modeling results compared with the experimental observations by Silliman and Simpson [257].

The breakthrough curves from ADE modeling and elliptic modeling are compared with experimental observations, as seen in Figure 2.14. The modeling parameters are presented in Table 2.12. ADE modeling is carried out with the best estimated parameters from Berkowitz et al. [222]. Low temporal dispersion coefficients are adopted in the elliptic equation. Unlike the ADE, the elliptic equation can model the long "tails" of the integral breakthrough curves. However, it overestimates early arrival of the tracer.

Table 2.12 Parameters adopted for ADE/elliptic modeling in comparison with the experiments of Silliman and Simpson [257]. Results are shown in Figure 2.14.

Position from source	R_x	R_t
0.91m	**0.0879/0.0879**	**0/0.029**
1.37m	**0.0547/0.0547**	**0/0.021**

Summarizing the comparisons between the modeling and the experiments, a method for estimating the parameters in the model may be described as follows. Ellipticity of the model may be ruled out in the first place if the effluent concentration profile is clearly stepwise. On the contrary, if this profile is smoothed, one may expect non-zero elliptic dispersion. The distribution of the filtration coefficients may be ruled out if the deposition is exponentially decreasing. For the case with a stepwise breakthrough curve and hyperexponential deposition, the ADE with distributed filtration coefficients is adequate. If ellipticity is nonzero, it may be sufficient to predict moderate hyperexponentiality without introducing distribution of filtration coefficients. The parameters for transport can be fitted to the breakthrough curve alone and the distribution of filtration coefficients

(power law) can be fitted to the deposition profile alone. On the other hand, for the experiment with a widely dispersed breakthrough curve (early arrival, large tail) and hyperexponential deposition, the temporal dispersion coefficient needs to be fitted to the breakthrough curve first, and then the distribution is fitted to the deposition. After separate fitting of the dispersion coefficient and the distribution to match different curves, some “fine tuning” is required, to better match both curves. It is because the deposition hyperexponentiality may be attributed to both the temporal dispersion and the distribution of filtration coefficients.

2.5 Summary of Chapter 2

In this chapter, an integral model of the deep bed filtration process has been developed. It incorporates pore and particle population heterogeneity (surface charges or sizes), as well as the particle residence time distribution in the framework of the continuous time random walk theory. Numerical modeling is carried out to study the factors influencing breakthrough curves and deposition profiles for the deep bed filtration systems.

The experimental data and our computations indicate that hyperexponentiality of the deposition can be caused by the following three mechanisms: particle population heterogeneity in connection with the distribution of the filtration coefficients, midscale heterogeneity in connection with non-Fickian transport, and macroscale heterogeneity in connection with spatial distribution of the filtration coefficients. The degree of "wash-out" of a breakthrough curve indicates whether the elliptic formalism is necessary. In cases where a breakthrough curve is (almost) stepwise (which is commonly observed for artificial uniform porous media), application of the elliptic formalism seems to be inadequate, and hyperexponentiality of the deposition profiles, if observed, should be caused by the explicit or implicit distribution of the parameters of the particles in the suspension. In non-uniform porous media the breakthrough curves may be more dispersed. For such cases the elliptic transport equation, probably, coupled with the particle distribution, seems to be more adequate.

The effects of the temporal dispersion and the distribution of filtration coefficients can be compensated for by each other, but not entirely. It implies that attributing the deposition hyperexponentiality to particle population heterogeneity alone or non-Fickian transport alone may be to overestimate this factor.

2.6 Nomenclature of Chapter 2

c_i	Number of suspended particles per unit pore volume(m^{-3})
C_i	Dimensionless suspended particle concentration
s_i	Number of retained particles per unit volume of porous media
S_i	Dimensionless retained particle concentration
t	Time(s)
T	Dimensionless time(pore volume)
x	x coordinate in space
X	Dimensionless x
N_c	Number of retained particles per gram of porous media
N_t	Number of total injected particles
v	Interstitial velocity of particles
u	Dimensionless interstitial velocity of particles
D_x	Coefficient of spatial dispersion(m^2/s)
D_t	Coefficient of temporal dispersion(s)
R_x	Dimensionless longitudinal dispersivity
R_t	Dimensionless temporal dispersivity
p	Probability density function
a	Coefficient in power law distribution
b	Power in the power law distribution
f_{low}	Fraction of the component with low Λ in the bimodal distribution
f_{high}	Fraction of the component with high Λ in the bimodal distribution
t_0	Particle injection duration(s)
T_0	Particle injection duration (pore volume)
c_0	Influent concentration
μ	Mean value
σ	Standard deviation
λ	Filtration coefficient(s^{-1})
Λ	Dimensionless filtration coefficient
ξ	Total injection time is ξ times the particle injection duration
φ	Porosity of the porous media
ρ_b	Bulk density of the dry porous media

3 Uncertainty and sensitivity analysis of models for non-Fickian transport and heterogeneous attachment

In this chapter, uncertainty and sensitivity analyses are carried out to investigate the predictive accuracy of the filtration models for non-Fickian transport and heterogensou attachment (mainly arising from Chapter 2). Five different modeling approaches, involving the elliptic equation with different types of distributed filtration coefficients and the CTRW equation expressed in Laplace space, are selected to simulate a number of experiments. These experiments involve both porous media and colloid-medium interactions of different degrees of heterogeneity. Experiments with tracers injected to heterogeneous porous media are also studied.

3.1 Introduction

The temporal dispersion term and the distribution of filtration coefficients introduced in chapter 2 are two advances compared to the traditional approach. To the best of our knowledge, their properties can only be estimated by fitting breakthrough curves and deposition profiles to the experimental data [101, 104, 207]. Whether the additional parameters can be uniquely identified or how large is the uncertainty of parameter estimation remains unknown.

Generally, there are various sources of uncertainty of the model outputs, such as the input uncertainty reflecting the lack of knowledge or accuracy of the model inputs, and the structural uncertainty related to the mathematical interpretation of the model [264]. From the uncertainty analysis, a probability distribution of model outputs can be obtained, including the mean value, the variances and the quantiles [265-267].

The uncertainties of the integral elliptic model may come from the following sources. (i) The approximation of particle velocity by the average pore water velocity; It has been observed that the particles of different sizes may travel faster or slower that the carrying fluid in porous media [268]. (ii) Estimation of dispersion coefficients by fitting to

experiments; For highly heterogeneous porous media the observed breakthrough curves are more dispersed and contain more scattered points [104, 118]. (iii) Lack of understanding heterogeneity of particle population. The heterogeneity of particle population may be reflected by distributions of particle properties [104, 207, 208]. The relation between the distribution types and the heterogeneity has not been fully understood, yet.

On the other hand, the sensitivity analysis aims at quantifying the individual contribution from each parameter's uncertainty to the uncertainty of outputs. Correlations between parameters may also be inferred from sensitivity analysis. It is a frequent routine and recommended to perform the uncertainty and sensitivity analysis in tandem [265, 269-272].

3.2 CTRW equation expressed in Laplace space

Beside the elliptic equation (see Section 2.2), it has been shown in a number of Refs [10, 11, 124, 220, 222, 254, 255] that the CTRW transport equation can be formulated in Laplace space, to represent the time derivative in an algebraic expression [11, 124, 220, 222, 254]. In one dimension, the concentration of the solute/particles in Laplace space is $\tilde{c}(x,u)$ and can be calculated by the following equation.

$$u\tilde{c}(x,u)-c_0(x)=-\tilde{M}(u)\left[v_\psi \frac{\partial \tilde{c}(x,u)}{\partial x}-D_\psi \frac{\partial^2 \tilde{c}(x,u)}{\partial x^2}\right] \tag{3.1}$$

$$\tilde{M}(u)=\bar{t}u\frac{\tilde{\psi}(u)}{1-\tilde{\psi}(u)} \tag{3.2}$$

where $\tilde{M}(u)$ is a memory function which accounts for the median heterogeneity (small scale), u is the Laplace variable with the dimension of s^{-1}. Here $c_0(x)$ is the initial concentration of the solute/particles. $\bar{t}$ is a characteristic time. v_ψ and D_ψ are the transport velocity and the dispersion coefficient from CTRW interpretations. $\tilde{\psi}$ is the core of the

CTRW formations and characterizes the motion of solute in porous media. In this work, the truncated power law is adopted for the expression of $\tilde{\psi}$:

$$\tilde{\psi}(u) = \left(1+\tau_2 u t_1\right)^{\beta} \exp\left(t_1 u\right) \frac{\Gamma\left(-\beta, \tau_2^{-1} + t_1 u\right)}{\Gamma\left(-\beta, \tau_2^{-1}\right)}; \quad \beta \in (0,2) \tag{3.3}$$

where Γ is the incomplete gamma function. Substitution of Equation (3.3) back into Equation (3.2) with $\bar{t} = t_1$ give rise to the full expression of the memory function. t_1 is the approximate median transition time and the lower bound of the power law behavior. t_2 is the upper bound of the power law behavior and also has the dimension of time. Larger values of t_2 lead to better representation of the pure power law model. The CTRW formulations can be reduced to the parabolic advection dispersion equation with $\tilde{\psi}(u) = \left(1+\bar{t}u\right)^{-1}$.

3.3 Analysis methods

3.3.1 Linear error propagation

The model parameters are estimated by fitting experimental data with the least squares method. The confidence intervals of parameter estimators and the correlation matrix were determined using the inverse of the Fisher information matrix (FIM) [273]. The uncertainties from experimental measurements are mapped as the errors of parameter estimators. Details of this method can be found in Refs. [273-276].

3.3.2 Monte Carlo procedure

Monte Carlo procedure involves a number of simulations with randomly sampled parameters and the statistical analysis of these results. The parameter space is sampled with the Latin hypercube sampling (LHS) method. LHS as an *n*-dimensional randomized generalization of Latin square sampling is an extension of quota sampling method [277].

It can provide effective coverage of the full parameter space and take into account the correlations between parameters with the correlation matrix [264, 278-280]. The sampling size is selected to be 500. It results in a sampling matrix with a dimension of $500 \times n$, rows of which correspond the LHS samples, and columns of which correspond to the n parameters.

For LHS two pieces of information need to be specified: the valid range of parameters and the correlation of them. Parameter estimators plus/minus their 95% confidence intervals from the linear error propagation analysis are selected as the upper/lower bounds of the valid range. The physical meaning of parameters should also be taken into account, e.g. the dispersion coefficients cannot be negative. The parameters are sampled following Latin hypercube sampling scheme from their corresponding probability distribution functions (in this case assumed uniform distribution) [265, 270, 271]. After sampling, a correlation control is induced using Iman and Conover method [280]. The correlation between the parameters were obtained from the parameter estimation routine, that is the from the covariance matrix of parameter estimators. More details of the method can be found in Refs. [266, 267, 280]. These LHS samples are both outputs from linear error propagation analysis and the inputs for Monte Carlo simulations.

3.3.3 Differential analysis

First order derivatives of model outputs to different parameters are calculated at their estimators. Such derivatives only represent the local sensitivity of model predictions around the parameter estimators. In order to rank the local sensitivity of different parameters, the following definition of sensitivity measure is adopted [281-283].

$$S_{nd,ij} = \frac{\partial y_i}{\partial \theta_j} \frac{\theta_j}{\mu_{yi}}; \qquad \delta_j^{msqr} = \sqrt{\frac{1}{N} \sum_{i=1}^{N} \left(S_{nd,ij} \right)^2}; \tag{3.4}$$

where $S_{nd,ij}$ is the non-dimensional sensitivity of jth parameter at ith data point, y_i is the ith model output, θ_j is the jth parameter estimator, μ_{yi} is the mean of ith model outputs. N

is the number of calculated data points (different T points or X point in this case). δ_j^{msqr} is the local sensitivity measure.

3.3.4 Linear regression of Monte Carlo simulations

After Monte Carlo simulations, linear regression of the results is performed for a quasi-global sensitivity analysis. Outputs of the original models and their representative linear models are usually scaled with respect of the statistics of simulation results, as follows:

$$C_i^s = \frac{C_i - \mu_C}{\sqrt{\mu_{C^2}}}; \qquad S_i^s = \frac{S_i - \mu_S}{\sqrt{\mu_{S^2}}}; \tag{3.5}$$

where i is the Monte Carlo simulation index, superscripts 's' represent the scaled outputs. μ_C and μ_S are respectively the mean values of model outputs C and S while μ_{C^2} and μ_{S^2} are the mean values of C^2 and S^2.

Such an analysis is only proper for the models that can be linearized to a certain degree (R^2>0.7) [265, 271, 272]. The linearity of the elliptic model is checked in the first place. If the model can be highly linearized, the quasi-global sensitivities are reflected by the absolute values of standardized regression coefficients of model parameters.

3.3.5 Implementation

CTRW calculations are implemented with the help of *CTRW tool box v3.1* developed by Brian Berkowitz et al. [10, 11, 124, 222, 255]. A numerical inversion algorithm [284] for the Laplace transform of the solution is used to obtain a time-domain solution. Such an algorithm requires careful tuning of the tolerance for convergence.

For local absolute sensitivity analysis, central, backward and forward difference regimes are applied to approximate the first order derivative of different parameters. The value of perturbation is modified until the three regimes give the same result. This ensures the accuracy of the finite difference approximation for the local sensitivity.

3.4 Selected experiments and modeling approaches

In this section, eight experiments are selected for case study, as listed in Table 1. They are conducted with different types of porous media, from highly heterogeneous porous media to highly homogeneous porous media. Either colloids or tracers are injected to different porous media. Heterogeneous colloid-medium interactions are observed, including physical straining and/or surface attachment (heterogeneous surface charge) of colloids in porous media. Five different modeling approaches for non-Fickian transport in porous media are adopted to simulate these experiments: the CTRW equation expressed in Laplace space, the elliptic equation with a single non-zero filtration coefficient, normal-distributed filtration coefficients, power-law-distributed filtration coefficients, and a zero filtration coefficient. The purpose of such a selection is to ensure the analysis covers a wide range of experiments under different conditions and test the performances of different modeling approaches for non-Fickian transport.

3.4.1 Colloids in heterogeneously packed sand

S. Bradford et al. [118] adopted carboxyl latex microspheres as colloid particles and Ottawa sand (99.8% quartz) as porous media for the column experiments. Details can be found in Section 2.4.3. In this case the known median heterogeneous structure is upscaled into a single block in one dimension. The elliptic equation only with a single filtration coefficient is adopted to fit the experimental data. This experiment will be referred to as Experiment No.1 as in Table 3.1 in the further contexts.

Table 3.1 Summary of selected experiments and modeling approaches.

	Median Heterogeneity	Injected materials	Heterogeneity of colloid-medium interactions	Modeling approaches	Refs.
(1)	Large scale	colloids	Physical straining + surface attachment	Elliptic equation + single non-zero Λ	[118]
(2)	pore scale	colloids	Physical straining + surface attachment	Elliptic equation + truncated normal distribution of Λ	[115]
(3)	pore scale	colloids	Physical straining + surface attachment	Elliptic equation + truncated normal distribution of Λ	[115]
(4)	pore scale	colloids	Physical straining + surface attachment	Elliptic equation + truncated normal distribution of Λ	[115]
(5)	Minimal	colloids	Heterogeneous surface charge and energy minima	Elliptic equation + truncated power law distribution of Λ	[103]
(6)	Minimal	colloids	Heterogeneous surface charge and energy minima	Elliptic equation + truncated power law distribution of Λ	[103]
(7)	Mediate	tracer	none	Elliptic equation+ zero Λ and CTRW expressed in Laplace space	[10]
(8)	Mediate	tracer	none	Elliptic equation+ zero Λ and CTRW expressed in Laplace space	[10]

3.4.2 Colloids in uniformly packed sand

The next experimental study considers suspension flow in a, apparently, less heterogeneous porous medium. S. Bradford et al. [115] adopted yellow-green fluorescent latex microspheres as colloid particles and packed Ottawa sand (99.8% quartz) as porous media for the column experiments. Details can be found in Section 2.4.2. Three sets of experimental data from the literature are selected for study. Here the elliptic equation and the normal distribution of filtration coefficients are applied to describe the heterogeneity of the particle-pore interactions. These experiments will be referred to as Experiments No.2 No.3 and No.4 as in Table 3.1 in the further contexts.

3.4.3 Colloids in uniformly packed glass beads

N. Tufenkji and M. Elimelech [103] conducted column experiments on filtration of uniform polystyrene latex colloid suspension in packed soda-lime glass beads. Details can be found in 2.4.1. Two sets of experimental data are selected for study from the literature. It is assumed that the particle velocity can be approximated by the average pore water velocity due to low median heterogeneity .Here the elliptic equation with power-law-distributed filtration coefficients is adopted to reproduce the results. These experiments will be referred to as Experiments No.5 and No.6 as in Table 3.1 in the further contexts.

3.4.4 Tracer in heterogeneously packed sand

M. Levy and B. Berkowitz [10]conducted tracer injection experiments in heterogeneously packed sands. These sands are well-rounded quartz sands with minimal surface coatings (99.8% pure SiO_2). Two types of median heterogeneity were established in the experiments. One is “uniform heterogeneity” as in Ref. [257], i.e. a number of sand boxes uniformly embedded in the matrix the sand of which is different from the embedded boxes. The other type of medium is randomly packed sand with exponentially correlated structure.

Two sets of the experimental data with different types of media are selected for study. It has been shown in Ref. [10] that the ADE fails to describe the breakthrough curves accurately, while the CTRW approach does. Here both the elliptic equation with a zero filtration coefficient and the CTRW equation expressed in Laplace space are applied to reproduce the experimental results.

3.5 Results of numerical modeling

3.5.1 Non-Fickianity from two CTRW approaches

Preliminary modeling results are first obtained from both CTRW approaches for non-Fickian transport in porous media: the elliptic equation of CTRW and the CTRW equation expressed in Laplace space. A 1-D tracer injection in porous media (without adsorption or desorption) for 5 pore volumes is simulated. After the tracer injection, pure water is injected to flush away the rest of the tracer in porous media. For the CTRW equation expressed in Laplace space, $t_1=10^{-1}$, $t_2=10^5$ and β is modified to obtain multiple breakthrough curves, as seen in Figure 3.1 (a). For the CTRW elliptic equation the temporal dispersion coefficient is modified, as seen in Figure 3.1 (b).

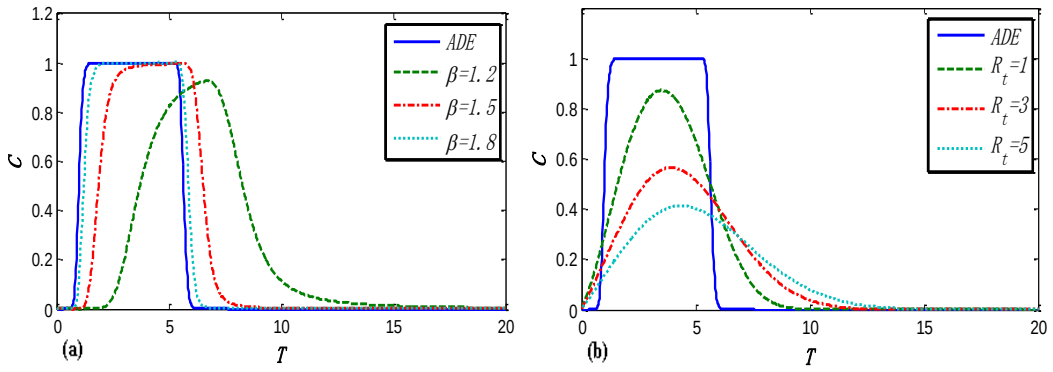

Figure 3.1 Comparison of breakthrough curves: (a). Modeling with the CTRW equation in Laplace space (b). Modeling with the elliptic equation

It can be seen that β and the temporal dispersion coefficient are two key parameters in the two approaches to tune the shape of the breakthrough curves. The smaller β and the larger temporal dispersion coefficients lead to higher non-Fickian deviations from the ADE solution. It agrees with the conclusions in Ref. [124] that the solution is more Fickian

with the value of β approaching 2, and the conclusions in Refs. [104, 218] that the equation is reduced to be parabolic Fickian ADE with the temporal dispersion coefficient approaching zero.

Such a comparison shows that the two models are both able to reveal the early arrivals before breakthrough and the late tails after injection in breakthrough curves. High non-Fickianity in both models leads to compressed and delayed peaks. The CTRW equation expressed in Laplace space presents an algebraic decaying tail after the peak, while the tail from the elliptic equation ends much earlier. The resulting peak is highly compressed when the elliptic equation produces a long delayed tail.

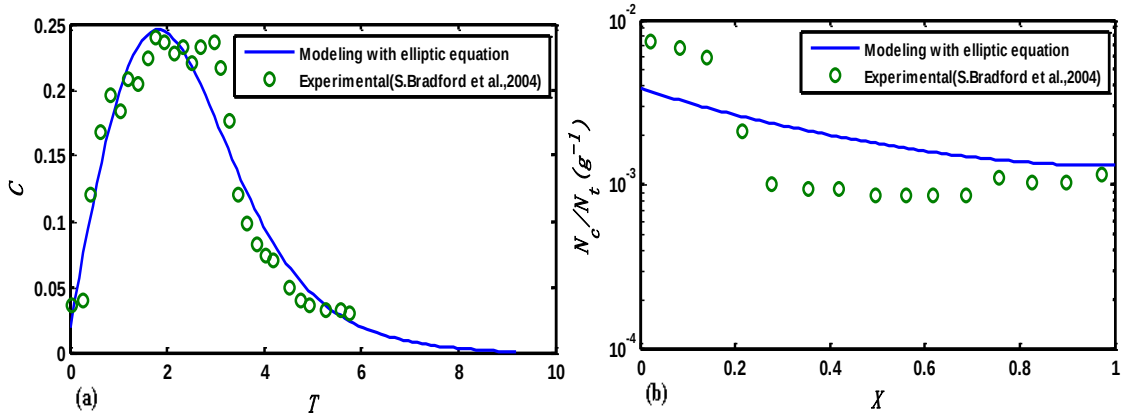

Figure 3.2 Elliptic equation with a single filtration coefficient modeling and Experiment No.1 [118], (a). Breakthrough curves (b). Deposition profiles

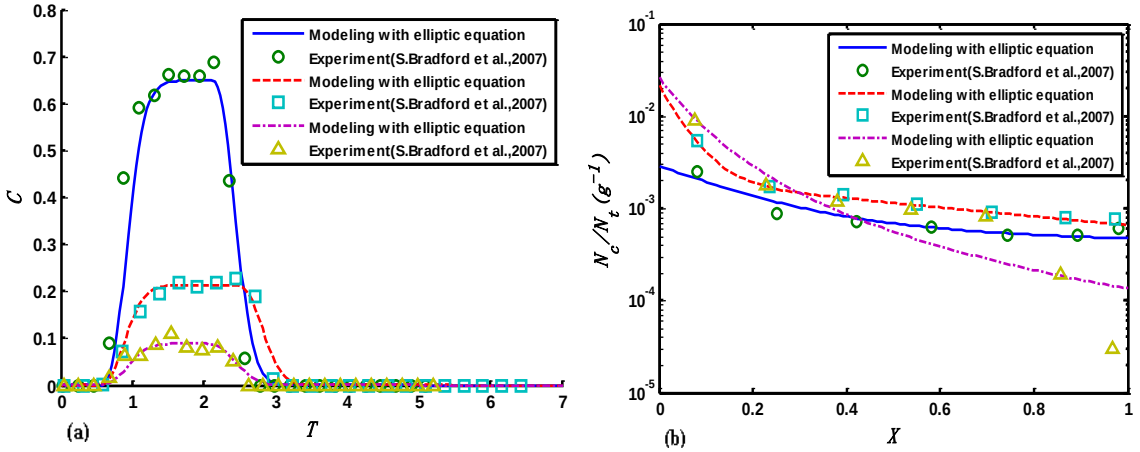

Figure 3.3 Elliptic equation with normal-distributed filtration coefficients modeling and Experiment No.2~ No.4 [115], (a). Breakthrough curves (b). Deposition profiles

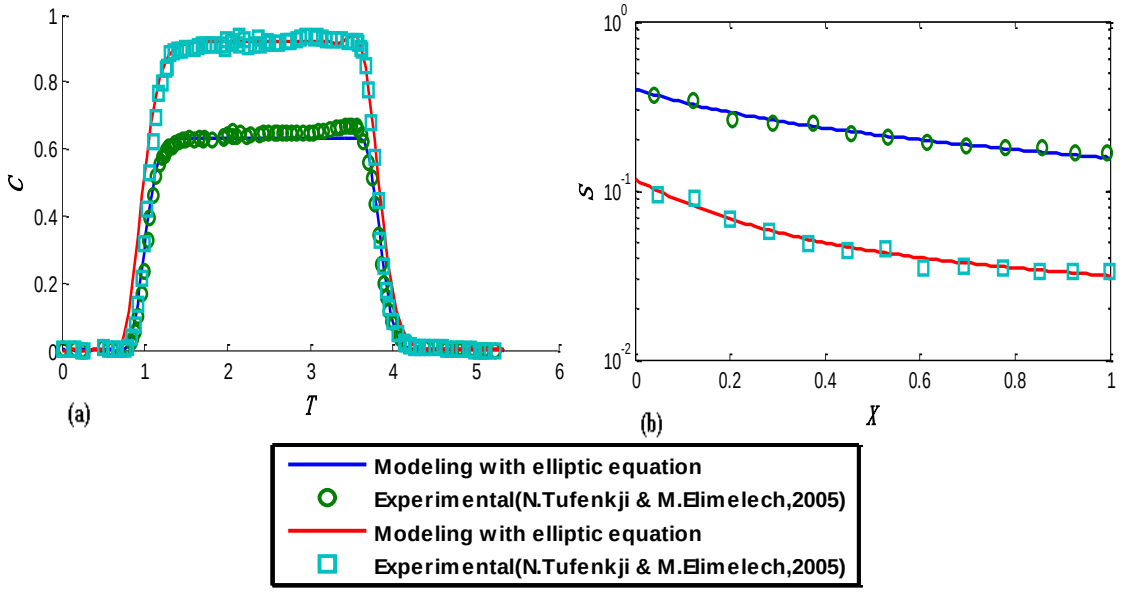

Figure 3.4 Elliptic equation with power-law-distributed filtration coefficients modeling and Experiment No.5and No.6 [103], (a). Breakthrough curves (b). Deposition profiles

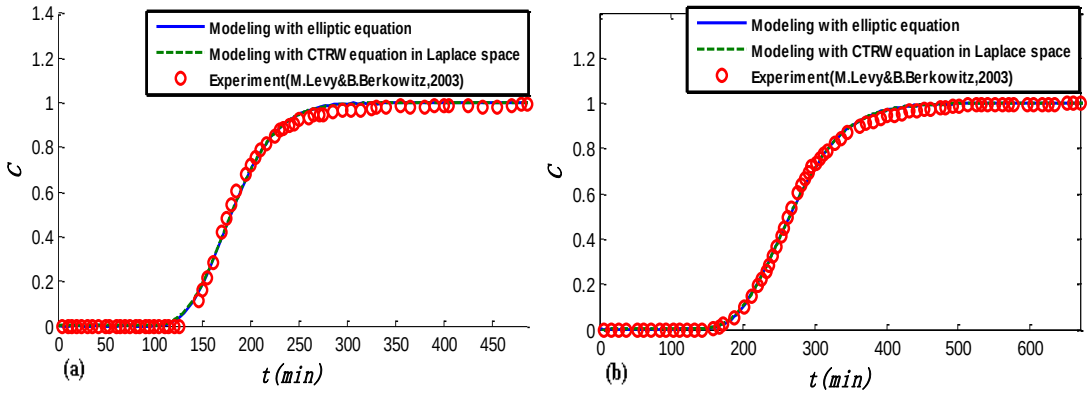

Figure 3.5 (a): Elliptic equation and CTRW equation expressed in Laplace space modeling Experiment No.7. (b): those to Experiment No.8 [10].

3.5.2 Linear Error Propagation Analysis

The model parameters are estimated by fitting the models to the experimental data. Some parameters are not estimated but selected manually. For Experiments No. 2~No. 4 V=1, $\Lambda_{min}=\mu$, and $\Lambda_{max}=10^3\times\mu$. For Experiments No. 5and No. 6 V=1and Λ_{max}=9.56. For modeling Experiments No. 7and No. 8 with the CTRW equation expressed in Laplace space, t_1=0.05, $t_2=10^6$. While estimating the parameters of distribution of filtration coefficients, attempts are made to estimate them by fitting only breakthrough curves and

predicting deposition profiles. The predicted and the experimental deposition profiles not are highly coincident. It is then decided that the parameters are estimated by fitting both the breakthrough curves and deposition profiles. Comparisons between the model outputs and the experimental data are shown in Figure 3.2 to Figure 3.5. It can be seen that the experiments can be well matched by the selected modeling approaches.

Table 3.2 Parameter estimators and 95% confidence intervals (CI) of different models estimated by fitting experiments.

	No.(1)	No.(2)	No.(3)	No.(4)	No.(5)
Estimator	R_x=1.71 ±0.22	$R_x/10^{-2}$=1.12 ±1.29	$R_x/10^{-2}$=0.99 ±0.32	$R_x/10^{-2}$=0. 79 ±1.81	$R_x/10^{-3}$=1.00 ±0.01
±	R_t=10.0 ±1.37	$R_t/10^{-2}$=0.44 ±1.31	$R_t/10^{-2}$=0. 82 ±0. 50	$R_t/10^{-2}$=1.29 ±2.56	$R_t/10^{-3}$=5.69 ±0.05
95%CI	Λ=2.46±0.25	$\sigma/10^{-4}$=0.92 ±6.69	$\sigma/10^{-4}$=4.03 ±1.15	$\sigma/10^{-4}$=0.22 ±0.58	Λ_{min}/10=2.98 ±0.01
	V=1.20 ±0.18	$\mu/10^{-2}$=0.10 ±0.37	$\mu/10^{-2}$=0. 67 ±0.13	$\mu/10^{-2}$=0. 52 ±0. 57	b=2.02 ±0.01

	No.(6)	No.(7)	No.(8)	No.(7)	No.(8)
Estimator	$R_x/10^{-3}$=1.00 ±0.02	$D_\psi/10^{-6}$= 9.12 ±10^{-4} (m^2/s)	$D_\psi/10^{-6}$=1.92 ±0.29(m^2/s)	$R_x/10^{-2}$=1.86 ±0.01	$R_x/10^{-2}$=2.27 ±0.01
±	$R_t/10^{-2}$=9.44 ±0.01	$v_\psi/10^{-4}$= 1.34 ±0.02 (m/s)	$v_\psi/10^{-4}$= 2.33 ±0.03(m/s)	$R_t/10^{-3}$=0.53 ±0.13	$R_t/10^{-3}$=1.00 ±0.03
95%CI	$\Lambda_{min}/10^{-2}$= 3.32 ±0.17	β=1.70 ±0.06	β=1.32 ±0.04	V=0.96 ±0.45E-3	V=0.93 ±0.23E-3
	b=1.29 ±0.02				

The estimated parameters and their 95% confidence intervals (CI) are listed in Table 3.2. Compared to the parameter estimators the CIs from the experiments with porous media of higher physical heterogeneity and more heterogeneous colloid-medium interaction are higher, e.g. Experiments No. 1~No. 4. On the other hand, the CIs from the experiments with more homogeneous porous media or tracer (no colloid-medium interaction) are lower, e.g. Experiments No. 5~No. 8. It is worth mentioning that Experiments No. 5 and No.6 are conducted with heterogeneous colloid-medium interactions but in highly homogenous porous media. The lower uncertainty from these experiments may be attributed to the median homogeneity or that the heterogeneity of surface attachment (surface charge/energy minima) is lower than the heterogeneity of both physical straining and surface attachment in Experiments No. 2 ~ No. 4.

Correlations between parameters are inferred from the resulting correlation matrices (not shown here). Strong correlations between the R_x, R_t and Λ are observed for modeling Experiment No.1, while no correlations are observed for modeling Experiment No. 7 and No. 8. Strong correlations between the parameters of the distributions of Λ are observed for Experiments No. 2~No. 6 (correlations between μ and σ; correlations between Λ_{min} and b). Strong correlations are observed for CTRW modeling Experiments No. 7 and No. 8. Strong correlations between parameters indicate that the parameters may not be uniquely identified. In such cases, parameters estimated by one set of experiment may not be able to predict another experiment.

By comparing the correlation matrices for Experiment No. 1 and Experiments No. 7& No. 8, it can be seen that the parameter correlations in the elliptic equation may depend on the available data sets. The major differences between them are the degrees of physical median-heterogeneity and the degrees of colloid-medium interaction heterogeneity. The median heterogeneity in Experiment No. 1 is macroscopic and higher while the latter is mediate. The heterogeneity of colloid-medium interactions in the first experiment involves both physical straining and surface attachment of colloids in porous media while the latter is none (no colloids but solute injected). It may be speculated that parameter correlations are connected to these heterogeneities. Little can be concluded further until more analyses of more experiments with heterogeneous porous media are performed, which are beyond the scope of current study.

Correlations between the parameters of the distributions of Λ may be explained by the either of the two reasons: Deposition hyperexponentiality may be interpreted by different types of distribution of filtration coefficients mathematically [104, 207, 208]. Nevertheless, the physics behind them has not been thoroughly understood. Deposition hyperexponentiality may also be attributed to other mechanisms, such as the enhanced retention at low-velocity zones of pore space [79, 121, 122]. The other reason may be the non-uniqueness of the discrete form of distribution. Similar distributions may be represented by different types of distribution or distribution properties. The parameters for the distribution of Λ may not be uniquely identified either due to the inconsistency

between the real physics and its mathematical interpretation or due to the non-uniqueness of its mathematical interpretation.

3.5.3 Uncertainty Analysis

The LHS sampling procedures are performed for all the cases. The correlation matrices from linear error propagation analysis are adopted for correlation control in the sampling procedure. The correlations between parameters can be visualized by such sampling results, as shown in Figure 3.6 ~ Figure 3.9.

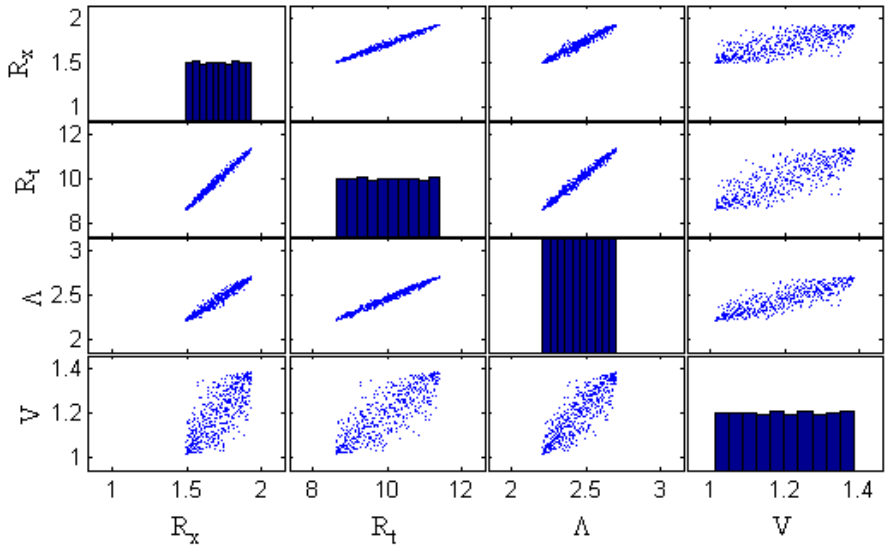

Figure 3.6 LHS sampling of model parameters for Experiment No.1 [118].

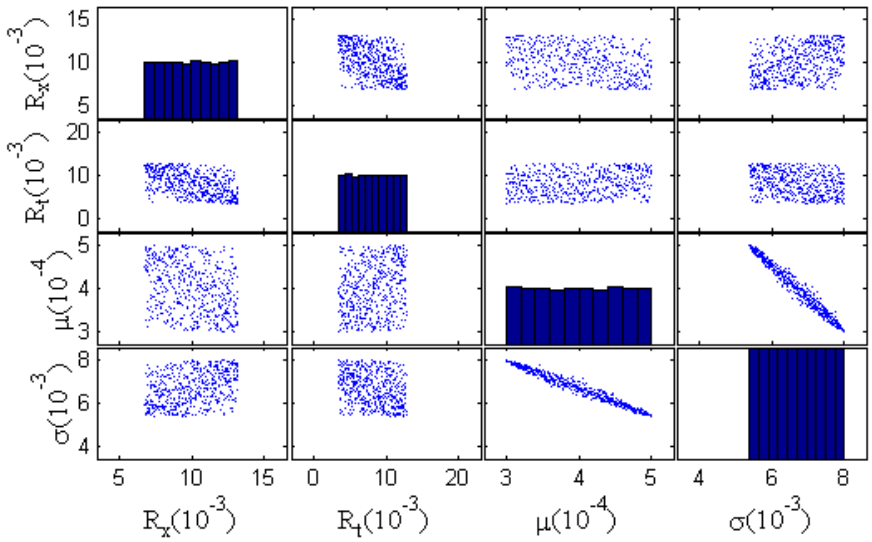

Figure 3.7 LHS sampling of model parameters for Experiment No.3 [115].

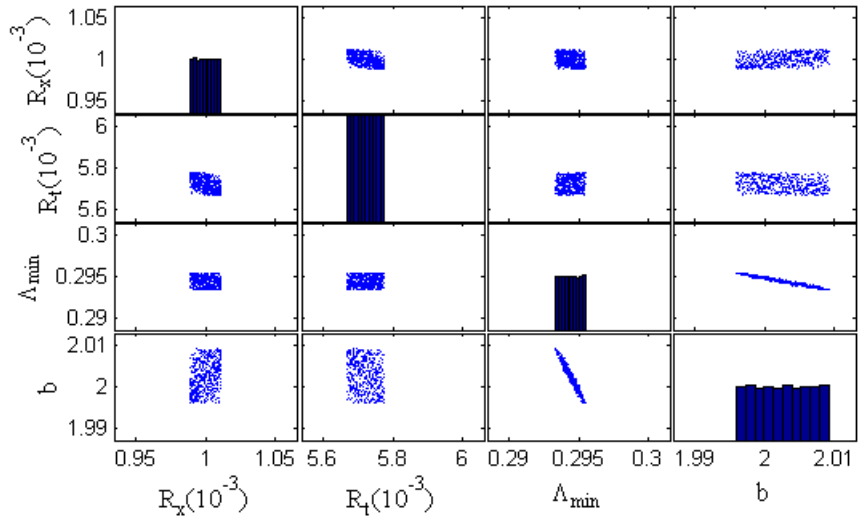

Figure 3.8 LHS sampling of model parameters for Experiment No.5 [103].

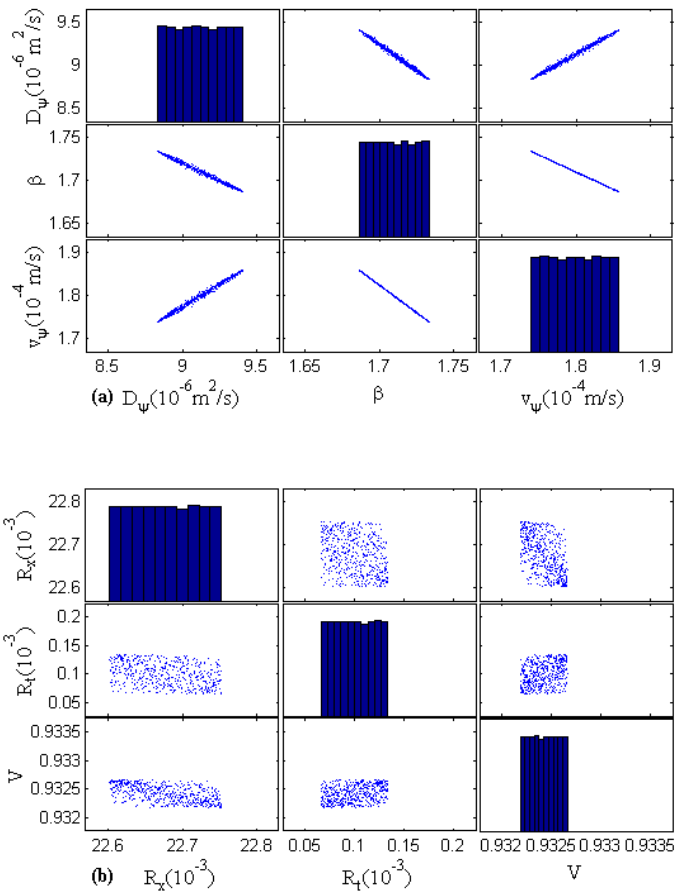

Figure 3.9 (a): LHS sampling of CTRW model parameters (b): LHS sampling of elliptic equation parameters for Experiment No.8 [10].

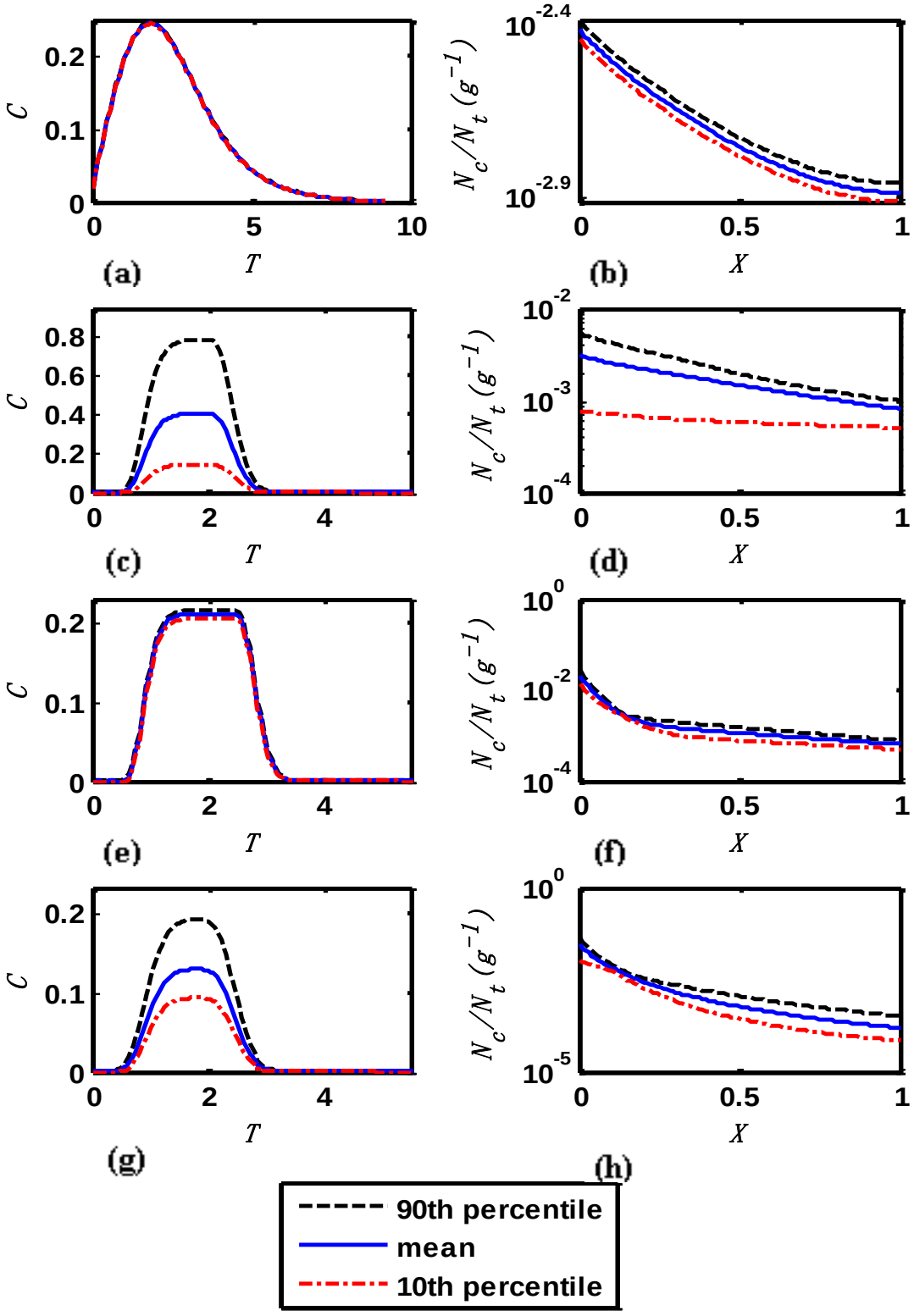

Figure 3.10 Representation of model prediction uncertainty by mean, 10th and 90th percentile values of Monte Carlo simulations. (a) and (b) for Experiment No. 1 [118]; (c) and (d) for Experiment No. 2; (e)and (f) for Experiment No. 3; (g) and (h) for Experiment No. 4 [115].

The results of Monte Carlo simulations are analyzed statistically. The mean, the 10^{th} percentile, and the 90^{th} percentile of Mote Carlo simulations are plotted in Figure 3.10 to reveal the uncertainty of modeling Experiments No. 1~No. 4. For modeling Experiments No. 5~No. 8 the uncertainty is minimal and not shown here. The uncertainty of model outputs are larger in Experiments No. 1~No. 4. It agrees with the observations of confidence intervals where uncertainty is larger in the experiments with porous media of higher physical heterogeneity and more heterogeneous colloid-medium interactions. The uncertainty of elliptic equation predictions with distributed filtration coefficients is larger than that with a single filtration coefficient. The uncertainty of both the elliptic equation and CTRW equation predictions are minimal for tracer transport in heterogeneous porous media.

3.5.4 Sensitivity Analysis

Differential Analysis

Differential analysis is then performed to quantify the local sensitivity of model outputs to different parameters and examine the correlations. The results for modeling Experiments No. 1, No. 5 and No. 8 are selected to be shown in Figure 3.11 ~Figure 3.13 respectively.

For Experiment No. 1, as seen in Figure 3.11, the spatial dispersion coefficient contributes positively to the early arrival of particles, while the temporal dispersion coefficient contributes negatively. The spatial dispersion coefficient does not give rise to the late arrival of particles at all, while the temporal dispersion coefficient contributes positively. For Experiment No. 5, as seen in Figure 3.11, the spatial dispersion coefficient seems to move the entire stepwise breakthrough curve earlier (to the left). The temporal dispersion coefficient, on the other hand, seems to suppress the breakthrough curve and contribute positively to both the early and late arrival of particles. These results highly agrees with previous observations [104]. It is worth mentioning that both the effluent concentration and deposition are insensitive to the temporal dispersion coefficient for Experiment No. 1. It may be explained by the fact that the temporal dispersion

coefficient R_t is much larger in cases where non-Fickian transport is observed in highly heterogeneous porous media [104]. The significance of the temporal dispersion may not be negated in this case.

In logarithm scales, the deposition hyperexponentiality is represented by the linearity of the deposition profile. If the deposition's derivative to the parameter is not linear in logarithm scales but hyperexponential, the parameter contributes to the deposition hyperexponentiality. Figure 3.11 and Figure 3.12 both show that the sensitivity of deposition to the temporal dispersion coefficient is hyper-exponential. It confirms temporal dispersion's positive contribution to the deposition hyperexponentiality reported in Refs. [104, 123].

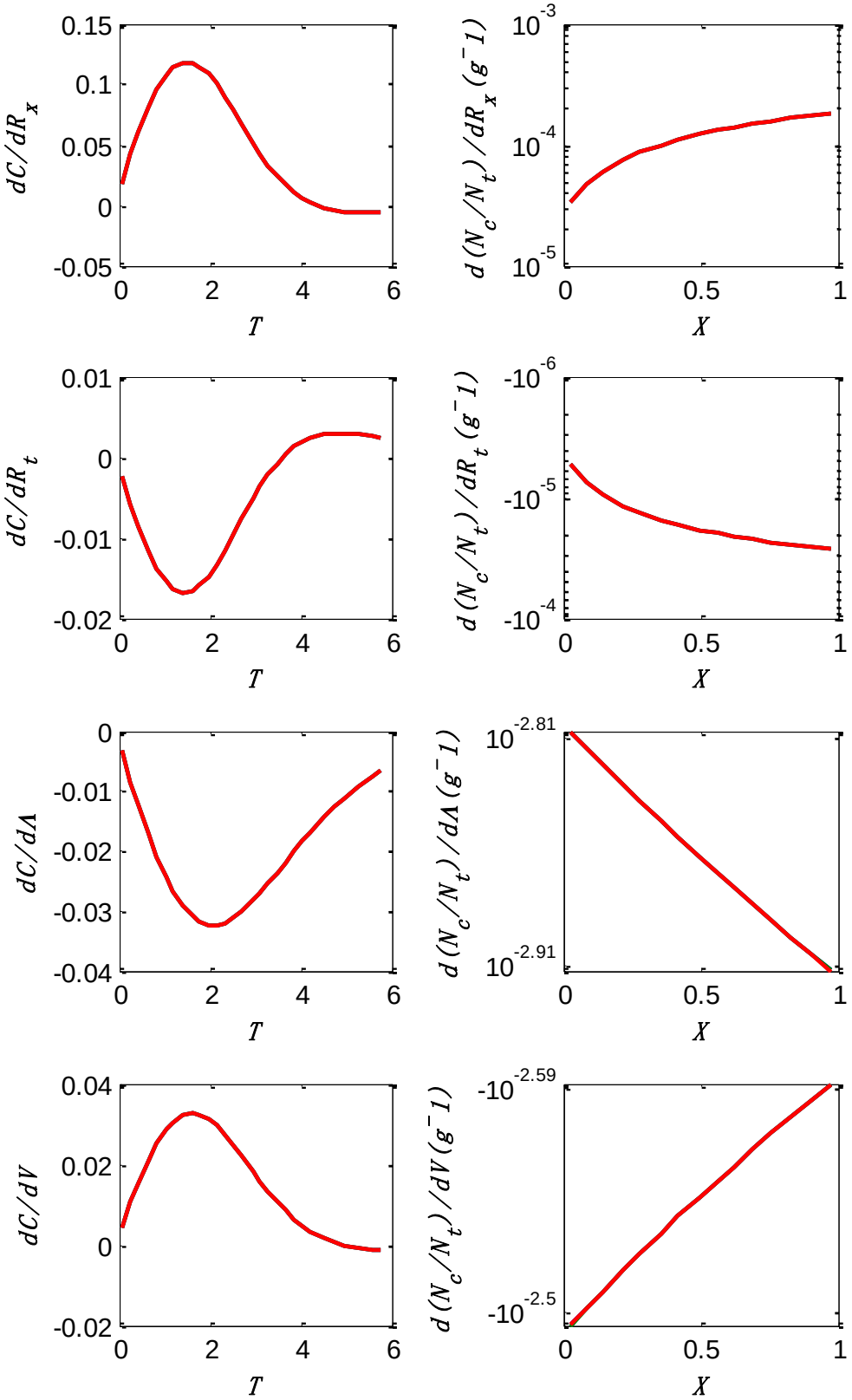

Figure 3.11 Differential analysis for the elliptic equation modeling Experiment No. 1[118].

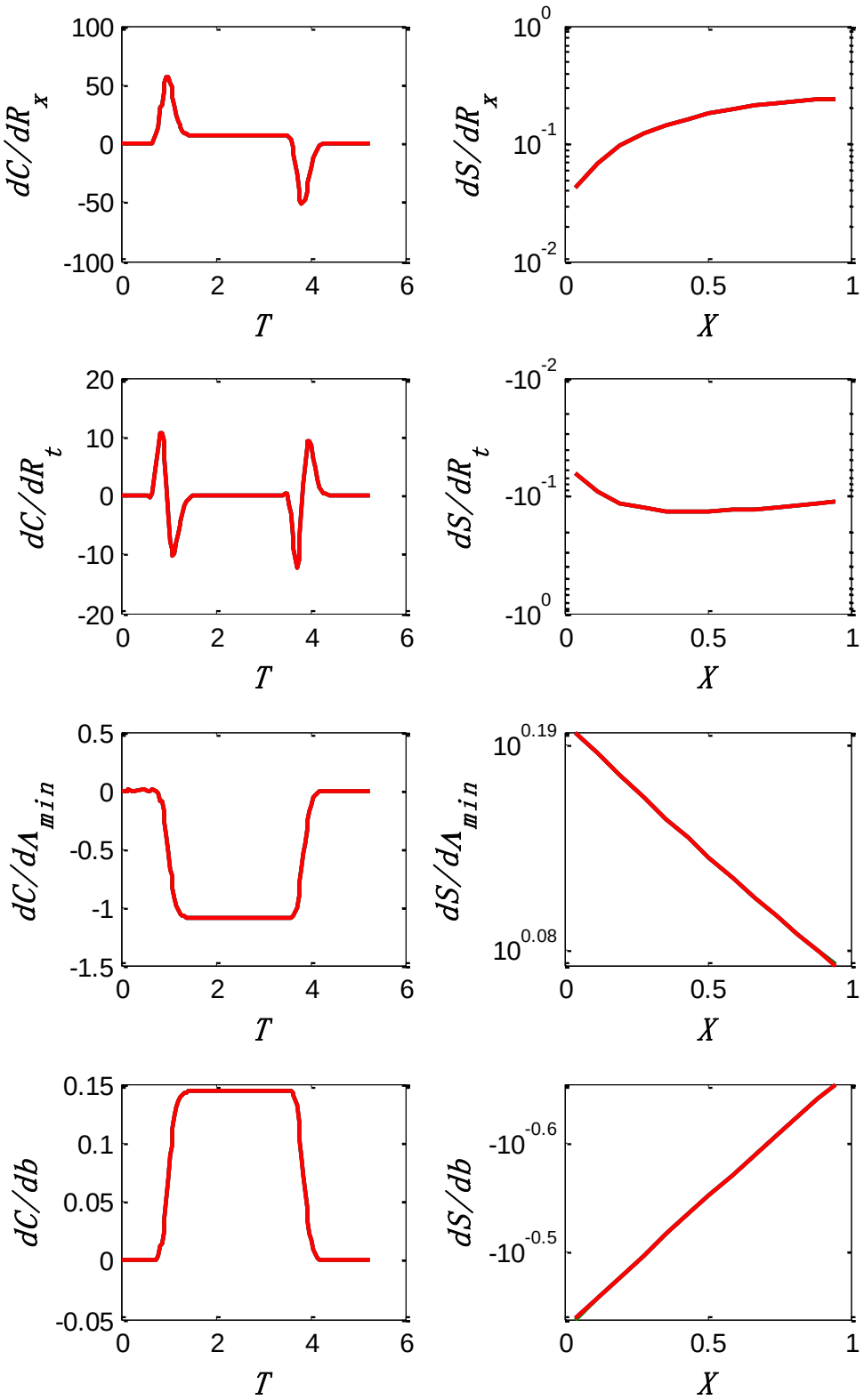

Figure 3.12 Differential analysis for the elliptic equation with power-law-distributed filtration coefficients modeling Experiment No. 5 [103].

Both Figure 3.11 and Figure 3.12 show that the sensitivities of deposition to all parameters are monotonous, and the sensitivities of effluent concentration contain either peaks or stepwise curves. More measurements of effluent concentration around the dramatic variations are preferable to determine parameters more accurately. The measurement of deposition is less important.

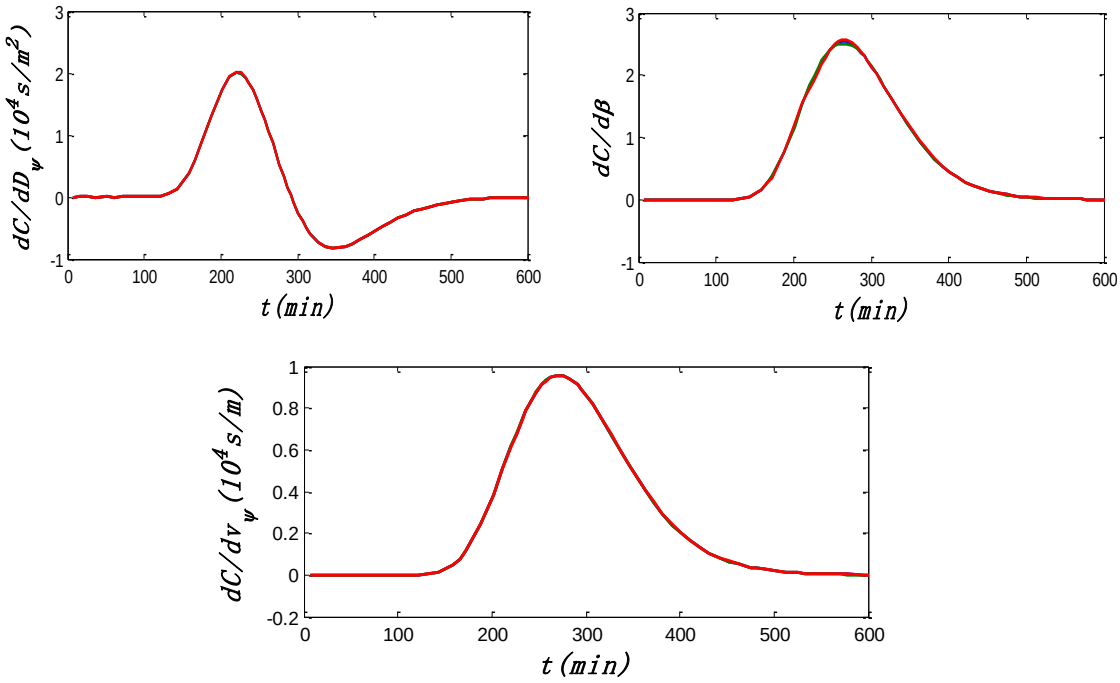

Figure 3.13 Differential analysis for CTRW equation in Laplace space modeling Experiment No. 8 [103].

As seen in Figure 3.13, the sensitivities of the effluent concentration around breakthrough to the velocity and dispersion coefficients from CTRW interpretations are similar to the velocity and the spatial dispersion coefficient in the elliptic equation as in Figure 3.13, while the β behaves oppositely to the temporal dispersion in the elliptic equation. It agrees the observation in Figure 3.1 that the smaller β and the larger temporal dispersion coefficients lead to higher non-Fickian deviations from the ADE solution.

Correlations between parameters can also be inferred from the analysis. Figure 3.11 shows that the spatial and the temporal dispersion coefficients seem to cancel each other's effects. The filtration coefficient and the velocity behave similarly. Figure 3.12 shows similar correlations but different shapes. Figure 3.13 shows the correlation between the velocity and β in a way that they may be compensated by each other.

Local sensitivities of parameters are ranked according to their values of sensitivity measure δ^{msqr} , as seen in Table 3.3. It shows that the effluent concentration profiles in most cases are the most sensitive to the dispersion coefficients except for Experiments No. 2~No. 4. The deposition profiles are more sensitive to the filtration coefficients than the dispersion coefficients. In the case of high median heterogeneity (Experiment No. 1), model outputs are lowly sensitive to temporal dispersion coefficients, while the opposite is observed in other cases (Experiments No. 5 and No. 6).

Table 3.3 Parameter sensitivity ranking based on values of δ^{msqr} in descending order.

Model outputs	No.1	No2~No.4	No.5 & No.6	No.7 & No.8	No.7 & No.8
C	R_x Λ V R_t	μ σ R_x R_t	R_x R_t $\Lambda_{\min}$ b	R_t R_x V	D_ψ β v_ψ
S	V Λ R_x R_t	μ σ R_x R_t	$\Lambda_{\min}$ R_x b R_t	- - -	- - -

3.5.4.1 Standardized regression coefficients

Linear models are established based on the regression of Monte Carlo simulation results. The effluent concentrations around the breakthrough, at the steady stage, and around the end of colloid injection are selected for linear regression. The deposition at X=0.3 is also selected for linear regression.

In most of the cases the resulting coefficients of determination R^2 are around 0.80~0.99 except for Experiments No. 7 and No. 8 modeled by the CTRW equation expressed in Laplace space, where R^2 are around 0.2. The high coefficients of determination indicate that the linear models can be representative for the original models, and that the variances of the linear models can explain 80%~99% of the variances of the original models.

By sorting the absolute values of standardized regression coefficients (SRC), the sensitivity of the model parameters can be ranked, as seen in Table 3.4. In the case of low median heterogeneity (Experiments No. 2 ~ No. 6), the effluent concentrations around the breakthrough and the end of colloid injection are more sensitive to the dispersion coefficients than the filtration coefficients. The steady-state effluent concentration and the deposition are more sensitive to the filtration coefficients.

Table 3.4 Parameter sensitivity ranking based on values of standardized regression coefficients in descending order.

Model outputs	No.1				No2~No.4				No.5 & No.6				No.7 & No.8		
C(around breakthrough)	R_x	R_t	Λ	V	R_x	μ	R_t	σ	R_x	R_t	Λ_{min}	b	R_x	V	R_t
C(steady state)	R_x	R_t	Λ	V	μ	σ	R_x	R_t	Λ_{min}	b	R_t	R_x	-	-	-
C(around end of colloid injection)	R_x	R_t	Λ	V	R_x	μ	R_t	σ	R_x	R_t	Λ_{min}	b	-	-	-
$S(X=0.3)$	V	Λ	R_t	R_x	μ	R_t	R_x	σ	Λ_{min}	b	R_t	R_x	-	-	-

For Experiments No. 1, the effluent concentrations around the breakthrough and the end of colloid injection are also more sensitive to the dispersion coefficients. The deposition is also more sensitive to the filtration coefficient. However, the steady-state effluent concentration is more sensitive to dispersion coefficients. Such a result is different from that of the classical filtration theory, where the steady-state effluent concentration depends on the filtration coefficient alone. It agrees with the previous observations that the steady-state effluent concentration from the elliptic equation depends on both the filtration coefficient and the dispersion coefficients [104].

3.5.5 Suggestions for experimental design

In this section, suggestions of optimizing experimental designs for more accurate parameter estimation are provided largely referring to the sensitivity analysis above. Linear error propagation analysis, local sensitivity results (differential analysis) and global sensitivity results (ranking of SCR) from previous sections are all taken into account.

More experimental measurements of the effluent concentrations around the breakthrough and the end of colloid injection are suggested to determine dispersion coefficients more accurately. In the case of high median heterogeneity, non-Fickian transport may be represented by the early arrival of particles and the large tail after the end of colloid injection. More measurements of the steady-state effluent concentration or the deposition are suggested to determine filtration coefficients more accurately. Similar suggestions

may also be found in the classical filtration theory, where the filtration coefficient is calculated by the minus logarithm of the steady-state effluent concentration [1, 95].

In the cases of heterogeneous colloid-medium interactions where hyperexponential deposition is observed, the distribution of filtration coefficients could not be accurately determined by the effluent concentration profile alone. Measurements of deposition are necessary.

3.6 Summary of Chapter 3

In this chapter, uncertainty and sensitivity analyses are carried out to investigate the predictive accuracy of the filtration models for describing non-Fickian transport and heterogeneous attachment. Five different modeling approaches, involving the elliptic equation with different types of distributed filtration coefficients and the CTRW equation expressed in Laplace space, are selected to simulate eight experiments. These experiments involve both porous media and colloid-medium interactions of different heterogeneity degrees.

Both the elliptic equation and the CTRW equation expressed in Laplace space are able to model the non-Fickian transport in heterogeneous porous media. The described non-Fickian behaviors by both models are similar. The latter model can predict an algebraic decaying tail at the end of particle injection while the elliptic equation presents a more compressed peak and a shorter tail.

The uncertainty of the elliptic equation predictions with distributed filtration coefficients is larger than that with a single filtration coefficient. The uncertainty of both the elliptic equation and CTRW equation predictions are minimal for tracer transport in heterogeneous porous media. Higher uncertainties of parameter estimation and model outputs are observed in the cases with the porous media and the colloid-medium interactions of higher heterogeneity. Lower uncertainties are observed in the cases with homogeneous porous media and lowly heterogeneous colloid-medium interaction.

Dispersion coefficients in the elliptic equation can be uniquely identified in the cases of low median heterogeneity. In the case of high median heterogeneity, model parameters of the elliptic equation are strongly correlated and may not be uniquely identified. The parameters for the distribution of filtration coefficients (normal distribution and power-law distribution) may not be uniquely identified due to the correlation between them. In the cases of heterogeneous colloid-medium interactions where hyper-exponential deposition is observed, the distribution of filtration coefficients may not be accurately determined by the effluent concentration profile alone. Measurements of deposition are necessary.

The effluent concentrations around the breakthrough and around the end of colloid injection are more sensitive to dispersion coefficients than filtration coefficients, while deposition is more sensitive to filtration coefficients. In the case of low median heterogeneity, the steady-state effluent concentration state is more sensitive to filtration coefficients while it is more sensitive to dispersion coefficients in the other case.

More experimental measurements of the effluent concentrations around the breakthrough and the end of colloid injection are suggested to determine dispersion coefficients more accurately. In the case of low median heterogeneity, more measurements of the steady-state effluent concentration or deposition are suggested to determine filtration coefficients more accurately.

3.7 Nomenclature of Chapter 3

c_i	Number of suspended particles per unit pore volume(m^{-3})
C_i	Dimensionless suspended particle concentration
s_i	Number of retained particles per unit volume of porous media(m^{-3})
S_i	Dimensionless retained particle concentration
t	Time(s)
T	Dimensionless time(pore volume)
x	x coordinate in space
X	Dimensionless x
N_c	Number of retained particles per gram of porous media
N_t	Number of total injected particles
v	Interstitial velocity of particles(m/s)
V	Dimensionless interstitial velocity of particles
v_ψ	Velocity of CTRW interpretations
D_ψ	Dispersion coefficient of CTRW interpretations(m^2/s)
D_x	Coefficient of spatial dispersion(m2/s)
D_t	Coefficient of temporal dispersion(s)
R_x	Dimensionless longitudinal dispersivity
R_t	Dimensionless temporal dispersivity
M	Memory function in CTRW theory
$\tilde{\psi}$	Core expression in the memory function of CTRW
β	Parameter of the truncated power law model for CTRW
$\bar{t}$	Characteristic time of porous media(s)
t_1	Lower limit of the truncated power law model for CTRW(s)
t_2	Upper limit of the truncated power law model for CTRW(s)
u	Laplace variable
p	Probability density function
t_0	Particle injection duration(s)
T_0	Particle injection duration(pore volume)
c_0	Influent concentration
μ	Mean value
σ	Standard deviation
λ	Filtration coefficient(s^{-1})
Λ	Dimensionless filtration coefficient
Λ_{min}	Lower limit of the distribution of filtration coefficients
Λ_{max}	Upper limit of the distribution of filtration coefficients
ξ	Total injection time is ξ times the particle injection duration
n	Number of parameters for estimation
φ	Porosity of the porous media
ρ_b	Bulk density of the dry porous media
δ_{msqr}	Sensitivity measure
C_s	Scaled concentration with respect to Monte Carlo simulations
S_s	Scaled deposition with respect to Monte Carlo simulations
$S_{nd,ij}$	Non-dimensional sensitivity of *j*th parameter at *i*th data point
θ	Any parameter

y	Any model output
N	Number of experimental data/calculation points
SRC	Standardized regression coefficients

4 Prediction of injectivity decline during waterflooding

In this chapter, a new comprehensive approach for predicting injectivity decline during waterflooding is proposed to incorporate the deep bed filtration, the fluid displacement, the external cake formation, and the cake erosion processes. The model takes into account the median heterogeneity by including dispersions and the particle population heterogeneity by applying distributed filtration coefficients. The methods arise from Chapters 2 and 3. A piece of software (SNY 2.0) based on optimized numerical implementations is developed from the model.

4.1 Introduction

Injectivity decline due to the formation damage around injectors is a widely observed disaster in offshore and onshore waterflood projects, such as produced water re-injection (PWRI) [285, 286]. Prediction and simulation of the processes are of great importance for the water management and the well stimulation strategies [287-290]. There is a considerable and ongoing effort aimed at understanding the complicated mechanisms causing the formation damage and the measures to minimize it.

One of the main reasons for the formation damage around injectors is the deep bed filtration of suspended solid particles in the injected water [39, 289, 291]. The solid content of the water and the particle sizes may be controlled and reduced to a certain level before injection. It is practically impossible to process the water for injection to such a high hygienity degree that it is free of colloidal-sized particles, such as bacteria or clay fines [292, 293].The accumulation of the deposited particles reduces the pore sizes, blocks thin pore throats, and leads to permeability damage.

Another reason for the injectivity decline is the formation of external filter cakes in the well bores [294, 295]. After the porosity of the rock being reduced to a certain level (percolation threshold), the accessibility of the inflow particles drops drastically to zero. The average pore size of the external cake is far smaller than that of the reservoir rocks. The permeability of the external cake is far lower. After the transition from deep bed

filtration to the external cake formation the injectivity is usually reduced much faster [294-296].

Some of the injection wells exhibit temporary steady states of injectivity after the transition to external cake formation [291, 297]. This effect is attributed to the erosion of the cake by the cross-flow fluid [295]. At the equilibrium state, the forces maintaining the external cake are balanced by the erosion forces. As a result, the external cake thickness may be limited to a value smaller than the well bore radius. During the period of external cake erosion, the inflow particles neither deposit on the cake surface nor penetrate through it. The particles are carried to the rat holes and fill the volume. After the rat holes are filled, the particles will accumulate in the well column and gradually close the well.

In the model for the deep bed filtration we have applied the non-Fickian transport model, involving abnormal dispersion of the particles. The conventional method for modeling deep bed filtration, the advection-dispersion equation (ADE) with a single filtration coefficient, merely predicts step-wise breakthrough curves and exponentially decreasing deposition profiles in the linear injection schemes [1, 95, 298]. Many of the core flooding experiments with tracers or suspensions, on the other hand, show widely dispersed breakthrough curves, hyperexponential or even non-monotonic deposition profiles [80, 103, 111, 116, 135, 185, 207, 231, 299]. The anomaly transport of the tracers or suspensions is usually referred to as the non-Fickian transport.

The median heterogeneity (small scale) is believed to be the main reason for the non-Fickian transport of tracers in porous media [10, 11]. On the other hand, the non-exponential deposition profiles are mainly attributed to the heterogeneities of both the particle population and the porous medium (see Chapters 2 and 3) [104, 105, 123, 218]. Especially the particle population heterogeneity may lead to strongly hyperexponential or even non-monotonic deposition profiles under unfavorable attachment conditions (see Chapter 5 for details). The particle population heterogeneity encompasses the physical heterogeneity (size and shape) and the physiochemical heterogeneity (surface charge and multiple energy minima) [80, 101, 103, 136]. For homogeneous particle population, the model for deep bed filtration in micro heterogeneous media is equivalent to the classical ADE [229].

The particle population heterogeneity may be significant while applying some enhanced oil recovery (EOR) methods, such as low salinity water injection, fines-assisted waterflooding, and microbial enhanced oil recovery (MEOR) [36, 250, 300-303]. Low salinity of water is unfavorable for particle attachment [236, 304]. It may be required to maintain the bacterial growth for EOR. Under such unfavorable attachment conditions, the particles may be captured via both the primary and the secondary energy minimum [101, 103, 305]. The deposition profiles under such conditions are highly hyperexponential and cannot be captured by the ADE with a single filtration coefficient.

One of the novel approaches for modeling the non-Fickian transport in porous media is the elliptic equation approach in the framework of continuous time random walk (CTRW) theories. It has been demonstrated in Chapters 2 and 3 that the elliptic equation for deep bed filtration excels the ADE in matching both the breakthrough curves and the deposition profiles [104, 105].

Distributed filtration coefficients, such as log-normal distribution or power-law distribution, can be applied to reflect the particle population heterogeneity [104, 207, 208]. It has been demonstrated that the application of such a distribution with the ADE is sufficient to capture the hyperexponential deposition in homogeneous porous media, such as uniformly packed glass beads and sands in the previous chapters.

An integral model was proposed to account for both the non-Fickian transport caused by the median heterogeneity and the particle population heterogeneity. The model applied the elliptic equation for the particle transport and the distribution of filtration coefficients for particle deposition. It was shown that the integral model could match both the dispersed breakthrough curves due to the non-Fickian transport and the hyperexponential deposition caused by the particle population heterogeneity. The model was only developed for linear injection scheme, such as core flooding experiments.

A comprehensive approach for the prediction of injectivity decline during PWRI was proposed by Paiva et al. [291, 297]. The model took into account the deep bed filtration, the external cake formation, the cake erosion, and the rat hole filling by erosion products. Analytical formulae for the radial injection scheme were adopted to enable fast

calculation. The adopted model for deep bed filtration neglects the median heterogeneity around the injectors (no dispersions) and the heterogeneity of the particle population (single filtration coefficient).

4.2 Multiphysics and model integration

The comprehensive approach describes four physical processes in four modules: 1) deep bed filtration; 2) fluid displacement; 3) external cake formation; 4) external cake erosion. Among the four processes only the fluid displacement occurs during the entire process. At the transition time for external cake formation, the deep filtration process is terminated, while the external cake formation commences. The external cake erosion limits the growth of the cake thickness.

The mass transport in the system involves a number of phases: the suspended solid phase, the water phase as the carrying fluid, the displaced oil phase, the external cake phase in the well bore, and the internal cake phase in the damaged zone. The relatively small penetration depth of the suspended particles (several meters from the injector) makes it possible to approximate the deep bed filtration as a single phase flow problem. It also allows us to approximate the fluid displacement as a particle-free process.

For the momentum analysis, the external cake, the damaged zone, and the particle-free reservoir bulk are regarded as a sequence of conductors forming a pie shape with the well bore at the center. The impedances along them are calculated separately. The total impedance change is the sum of the individual impedance changes.

4.2.1 Deep bed filtration

It has been suggested in Chapters 1 and 2 that the transport of a dilute monodisperse suspension in a porous medium may be described by an elliptic equation accounting for particle advection, spatial dispersion, temporal dispersion, mixed dispersion, and deposition. The temporal dispersion represents the effects of the distributed residence time of the particles in various pores. This is a simple way to formalize the Continuous

Time Random Walk (CTRW) approach, where dispersion of a time step is usually expressed by means of a distribution kernel[104, 105, 217, 218]. It has been shown that in the limit of infinitely many and infinitely small time steps and a finite variance of a single step, the distribution may be represented by the two coefficients D_t, D_{xt} (for temporal and mixed dispersion), and instead of the convolution with the distribution kernel, it is enough to consider the terms with the second time derivative and with the mixed derivative, making the transport equation elliptic.

In order to simulate the flow pattern in a vertical injection well, we apply the elliptic equation in the polar (radial) coordinates. The mixed dispersion is neglected, since it has no qualitative influence on the profiles. In order to reveal the heterogeneity of the particle population the particles are split into portions, i.e. there are multiple equations representing different particle species with various filtration coefficients. Under these conditions, the suspended concentration $c_i(r,t)$ (suspended volume per unit pore fluid) and the deposited concentration $s_i(r,t)$ (deposited volume per unit volume of porous media) of the ith component of the suspension at distance r from the injector and time t are described by the elliptic equation with a sink term representing the deposition of the particles:

$$\frac{\partial c_i(r,t)}{\partial t} + v_i(r)\frac{\partial c_i(r,t)}{\partial r} = \frac{1}{r}\frac{\partial c_i}{\partial r}\left(D_{xi}(r) r \frac{\partial c_i(r,t)}{\partial r} \right) + D_{ti}(r)\frac{\partial^2 c_i(r,t)}{\partial t^2} - \lambda_{vi}(r) c_i(r,t) \tag{4.1}$$

$$\frac{1}{\phi_a}\frac{\partial s_i(r,t)}{\partial t} = \lambda_i v_i(r) c_i(r,t) \tag{4.2}$$

where $v_i(r)$, $D_{xi}(r)$, $D_{ti}(r)$, and λ_i are respectively the particle velocity (m/s), the spatial (normal or Fickian) dispersion coefficient (m^2/s), the temporal dispersion coefficient (s), and the filtration coefficient (m^{-1}) at the distance r from the injection well. Here subscript 'i' is for the ith particle species. And ϕ_a is the accessible porosity.

The dependency of the dispersion coefficients on r is due to the assumptions that the spatial dispersion coefficient and the filtration coefficient are proportional to the local velocity $v_i(r)$, and that the temporal dispersion coefficient is inverse proportional to the

local velocity. Here particle velocity is approximated by the average pore water velocity. The log-normal distribution, the power law distribution and the normal distribution of λ are adopted to reflect the particle population heterogeneity. Any of the continuous distributions of the filtration coefficients is approximated by a discrete distribution with upper and lower bounds. The bounds are necessary to maintain the convergence of the distributions at [0, ∞].

The interactions between the residual oil and the particles are neglected, i.e. for the deep bed filtration the pore volume saturated by the residual oil is dead volume. The porosity accessible to the particles ϕ_a is calculated by:

$$\phi_a = \phi\left(1 - s_{or}\right) \tag{4.3}$$

The following assumptions are made: the particle velocity is equal to the pore water velocity; the spatial dispersion and the filtration rate are both proportional to the particle velocity; the temporal dispersion is inversely proportional to the particle velocity; the mixed dispersion is negligible.

$$v_i = \frac{U_i}{\phi_a};\ D_{xi} = R_{xi}\frac{U_i}{\phi_a};\ D_{xti} = 0;\ D_{ti} = R_{ti}\left(\frac{U_i}{\phi_a}\right)^{-1}; \tag{4.4}$$

Substitution of these equations to (4.1) and (4.2) leads to:

$$\begin{aligned} &\phi_a\frac{\partial c_i}{\partial t} + U_i\frac{\partial c_i}{\partial r} = U_i\frac{1}{r}\frac{\partial}{\partial r}\left(R_{xi}r\frac{\partial c_i}{\partial r}\right) + \phi_a^2\frac{R_{ti}}{U_i}\frac{\partial^2 c_i}{\partial t^2} - \frac{\partial s_i(r,t)}{\partial t} \\ &\frac{\partial s_i}{\partial t} = \lambda_i U_i c \end{aligned} \tag{4.5}$$

Here U_i is the radial Darcy's velocity and given by:

$$U_i = \frac{Q(t)}{2\pi rH} = \frac{q(t)}{2\pi r} \tag{4.6}$$

where $q(t)$is the permeate flow per unit length of well bore in the dimension of m^2/s. Now let us introduce the following dimensionless variables:

$$R=\frac{r}{r_e};\quad T=\frac{t}{t_p};\quad C_i=\frac{c_i}{c_0};\quad S_i=\frac{s_i}{\phi_{a0}c_0};\quad t_p=\frac{\phi_{a0}r_e}{2U_0\left(r_e\right)};$$
$$\phi_a=\Phi\phi_{a0};\quad U_i(r,t)=u_iU_0(r);\quad R_{xi}=r_{xi}r_e;\quad R_{ti}=r_{ti}r_e;\quad \lambda_i=\Lambda_i/r_e; \tag{4.7}$$

Substitution of the variables into the equations leads to:

$$\Phi\frac{\partial C_i}{\partial T}+\left(\frac{u_i}{2R}\right)\frac{\partial C_i}{\partial R}=r_{xi}\left(\frac{u_i}{2R}\right)\frac{\partial^2 C_i}{\partial R^2}+\frac{\Phi^2 r_{ti}}{\left(\frac{u_i}{2R}\right)}\frac{\partial^2 C_i}{\partial T^2}-\Lambda_i\left(\frac{u_i}{2R}\right)C_i$$
$$\frac{\partial S_i}{\partial T}=\Lambda_i\left(\frac{u_i}{2R}\right)C_i \tag{4.8}$$

The porosity change can be estimated by:

$$\frac{\partial\Phi}{\partial T}=-\sum\frac{\partial S_i}{\partial T}c_{0i} \tag{4.9}$$

Neglecting the velocity difference among particle species, for constant flow rate injection u_i=1, while for constant pressure drop injection it can be calculated by 1/J, where J is the dimensionless impedance.

Following previous studies [290, 306, 307], it is assumed that the inverse to normalized permeability k/k_0 is a linear function of retained particle concentration.

$$\frac{k_0}{k\left(r,t\right)}=1+\beta\sum_i s_i\left(r,t\right) \tag{4.10}$$

where k_0 is the initial permeability, $k(r,t)$ is the permeability of the reservoir rock, and β is the formation damage coefficient. The impedance change due to deep bed filtration $\Delta J_d(t)$ can be calculated by:

$$\Delta J_d(t)=\int_{r_w}^{r_e}\left(\frac{\beta\sum_i s_i\left(r,t\right)}{r}\right)dr\Bigg/\ln\left(\frac{r_e}{r_w}\right) \tag{4.11}$$

where r_e and r_w are the effective reservoir radius and the well bore radius. More detailed derivations for the impedance calculation are shown in Appendices. In this work, the filtration coefficient is assumed to be a constant depending only on the particle type, while the formation damage coefficient is assumed to be a constant for all particles types. More sophisticated forms of the coefficients may also be incorporated, such as distributed formation damage coefficients with the particle types, and their dependencies on the retained particle concentrations [308].

4.2.2 External cake formation

The impedance change due to the external cake formation is calculated based on the following assumptions. The instantaneous transition from deep bed filtration stage to the external cake build-up takes place after the porosity of the reservoir rock in contact with the injector is reduced to a certain value. The ratio of the porosity reduction to the initial porosity is referred to as the critical porosity ratio for external cake formation. The heterogeneity (layer structure) and the compressibility of the filter cake are neglected. The consideration of these factors requires a more sophisticated model for the external cake [287]. It is beyond the scope of the current work.

It is usually observed that after the deposited solids exceed a critical amount, the external filter cake starts to form inside the well bore. The transition time for external cake formation is calculated as below:

$$\alpha\phi_{a0} = \sum s_i\left(r_w, t_{tr}\right) \tag{4.12}$$

where α is the critical ratio of deposition to porosity over which the external cake formation starts. t_{tr} is the dimensional transition time. Since at the injector the suspension concentration is assumed to be constant c_0, the deposition can be substituted by:

$$\alpha\phi_{a0} = c_0 \int_{\lambda_{\min}}^{\lambda_{\max}} p(\lambda)\lambda \left[\int_0^{t_{tr}} U\left(r_w\right)dt\right] d\lambda \tag{4.13}$$

Rearranging of the equation leads to:

$$T_{tr} = \frac{2r_w\alpha}{c_0 r_e^2 \int p(\lambda)\lambda d\lambda} \tag{4.14}$$

The impedance change caused by external cake in the axis-symmetrical injection case can be calculated by [291, 297]:

$$\begin{cases} \Delta J_c(T) = 0 & (T < T_{tr}) \\ \Delta J_c(T) = m_c (T - T_{tr}) & (T \geq T_{tr}) \end{cases} \tag{4.15}$$

where k_c and ϕ_c are the permeability and the porosity of the external cake, the factor m_c is given by:

$$m_c = \frac{k_0 k_{rwor} c_0 \phi_{a0}}{2k_c (1-\phi_c)\left(\frac{r_w^2}{r_e^2}\right)\left[-\ln\left(\frac{r_w^2}{r_e^2}\right)\right]} \tag{4.16}$$

4.2.3 External cake erosion

The erosion of the external cake can be described by the torque balance or the force balance on the particles at the surface of the external cake. The force balance criterion has the same form as the torque balance criterion but only differences on coefficient meanings. The particles at the surface of the external cake are subject to the hydrodynamic drag from the cross-flow, the gravity/buoyancy, the lifting force, the hydrodynamic drag from the permeate flow, and the electrostatic forces [295, 309]The forces on the particles in a vertical injection well are depicted in Figure 4.1, while in the case of horizontal wells the gravity is perpendicular to the cross-flow instead.

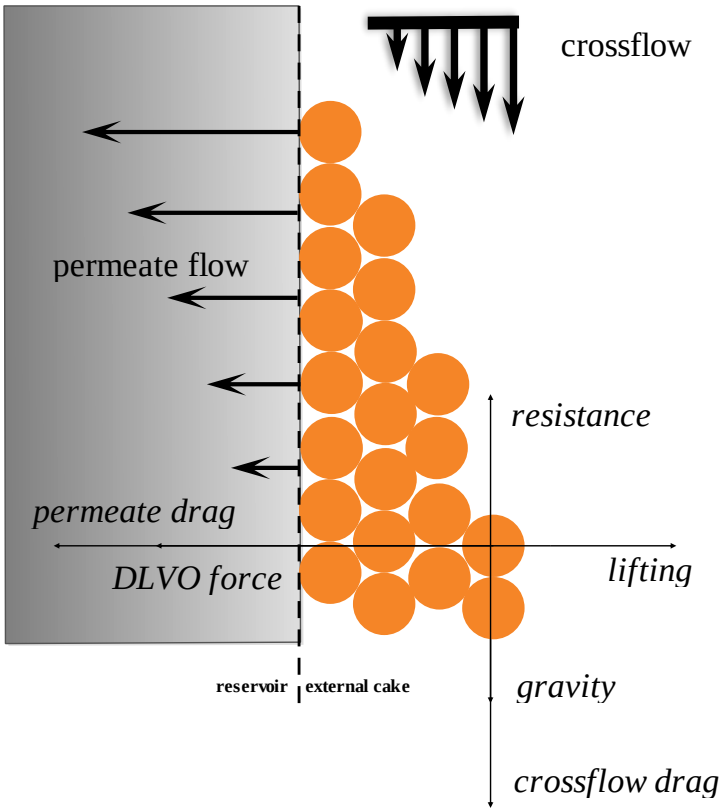

Figure 4.1 Illustration of forces on the particles at the surface of external cake in a vertical well

The cross-flow drag exerting on the particles at the surface of the external cake can be expressed as below[295, 310]:

$$F_{cf} = \frac{\omega \mu_w r_s^2 Q}{\left(r_w - h_c\right)^3} \tag{4.17}$$

where ω is a proportionality factor in the range [10, 60], μ_w is the water viscosity; r_s is the particle radius Q is the flow rate of the cross-flow, and h_c is the thickness of the external cake. The permeate drag force is given by [295]:

$$F_p = 6\pi \mu_w r_s A_H \frac{q}{2\left(r_w - h_c\right)} \tag{4.18}$$

where A_H is the hydrodynamic correction factor, which is applicable when the concentration of the suspension above the cake is high; i.e. above 250ppm [311, 312]. It can be estimated by [313]:

$$A_H = 0.36\left(k_c / r_s^2\right)^{2/5} \tag{4.19}$$

The total cross flow Q can be calculated from the leak-off flow q:

$$\frac{dQ}{dz} = -q \tag{4.20}$$

where z is the distance from the wellbore top. The gravity difference of the particles and the carrying fluid is calculated as:

$$F_g = \frac{4\pi r_s^3}{3}\Delta\rho g \tag{4.21}$$

The net normal force of the particles at the surface of the external cake is expressed as:

$$F_N = F_p - F_e - F_L \tag{4.22}$$

The resistance of the particles from the surface is calculated by:

$$F_f = fF_N \tag{4.23}$$

where f is the resistance coefficient in the force balance.

Monte-Carlo simulations under common conditions of water injection have shown that the forces ranges are: DLVO activation barrier between primary and secondary energy minima $F_e \approx 10^{-9} N$, permeate force $F_p \approx 10^{-11} N$ cross-flow force $F_{cf} \approx 10^{-13} N$; gravity force $F_g \approx 10^{-14} N$; and lift force $F_L \approx 10^{-19} N$ [296]. Since the activation energy required for the particles to move from the secondary minimum to the primary minimum is by far larger than any opposing force, it can be concluded that all particles reside in the vicinity of the secondary minimum. If the particles are assumed to lie in the secondary energy minimum then the net electrostatic force reduces to zero. Furthermore, the lift force is negligible and will be neglected in the forthcoming analysis:

$$\frac{\omega\mu_w a^2 Q}{\left(r_w - h_c\right)^3} + \frac{4\pi r_s^3}{3}\Delta\rho g = \frac{f\,6\pi\mu_w r_s A_H}{2\left(r_w - h_c\right)} q_p \tag{4.24}$$

At constant pressure drop, according to Darcy's law, the permeate flow (leak-off) can be calculated by:

$$q = \frac{2\pi k_0 \Delta p}{\mu \ln\left(r_e / r_w\right)} \frac{1}{J} = \frac{q_0}{J} \tag{4.25}$$

where k_0 is the initial permeability of the reservoir, J is the dimensionless impedance. The system of equations (4.24) (4.25) can be solved for the cross flow and the thickness of the external cake, which are both depend on the distance from the top of the bottom hole. For the constant pressure drop case, the equation of force balance can be written as:

$$\frac{\omega\mu_w r_s^2 Q(z)}{\left(r_w - h_c(z)\right)^3} + \frac{4\pi r_s^3}{3}\Delta\rho g = \frac{f\,6\pi\mu_w r_s A_H}{2\left(r_w - h_c(z)\right)} \frac{q_0}{\Delta J_c(z) + J_{tr}} \tag{4.26}$$

In the case of horizontal wells, the gravity term on the left hand side can be neglected. The maximum impedance change caused external cake is calculated by:

$$\Delta J_{c,\max}(z) = \frac{k}{k_c} \ln\left(\frac{r_w}{r_w - h_c(z)}\right) \ln\left(\frac{r_e}{r_w}\right)^{-1} \tag{4.27}$$

After solving the system of equations, the average maximum impedance change caused by the external cake can be calculated by:

$$\overline{\Delta J_{c,\max}} = \frac{\int \Delta J_{c,\max}(z)\,dz}{\int dz} \tag{4.28}$$

The distribution of the maximum external cake thickness can be obtained by solving the equation of flow in the cannonade with the equation of the force balance.

4.2.4 Fluid displacement

The impedance change due to fluid displacement is described by the classical Buckley-Leverett equation. It is assumed that the injection well is placed at the center of a homogeneous pie-shaped reservoir. The application of such a simple model is only indicative for fluid displacement effects, while a more sophisticated reservoir model can be incorporated, such as a stratified reservoir [314, 315]. This is outside the scope of the present work. During the particle-free water injection into a reservoir saturated by oil that is less mobile than water, the total local mobility ratio increases, roughly, M times (end-point mobility ratio of water to oil) due to displacement of less mobile fluid by more mobile one[316]:

$$M = \frac{k_{rwor}\mu_o}{\mu_w k_{rowi}}, \tag{4.29}$$

where k_{rwor} and k_{rowi} are the relative permeabilities of water and oil at the residual oil saturations s_{or} and the irreducible water saturation s_{wi} respectively . The asymptotical value of the impedance J_{BL} due to the fluid displacement can be calculated by:

$$J_{BL} \to \frac{1}{M} \tag{4.30}$$

In the radial injection schemes the impedance at the close proximity of the injector contributes most significantly to the total impedance. The fluid displacement close to the injector is completed during a short period. As a result, the impedance J_{BL} drops dramatically at the initial stage of waterflooding, and approaches the limit $1/M$ asymptotically, as seen in Figure 4.3.

4.3 Model integration and GUI

The well injectivity varies during water injection due to above mentioned processes: formation damage by deep bed filtration, mobility change due to fluid displacement, external cake build-up in the cannonade, and external cake erosion. The assumption of the external cake, the damaged zone, and the intact zone as conductors in series

connections allow the summation of the individual impedance changes as the total impedance change:

$$J(T) = J_{BL}(T) + \frac{1}{M}\Delta J_d(T) + \frac{1}{M}\Delta J_c(T) \tag{4.31}$$

The four modules are integrated and implemented in FORTRAN. With the finite difference method, the elliptic equations are converted into a series of algebraic equation and solved with the linear equation solvers for sparse matrices. The Adams method (predictor-corrector) is used to solve the flow equation in the wellbore with the force balance equation for the external cake erosion. A Windows graphical user interface (GUI) is developed with the Microsoft Visual Basic .Net, as seen in Figure 4.2.

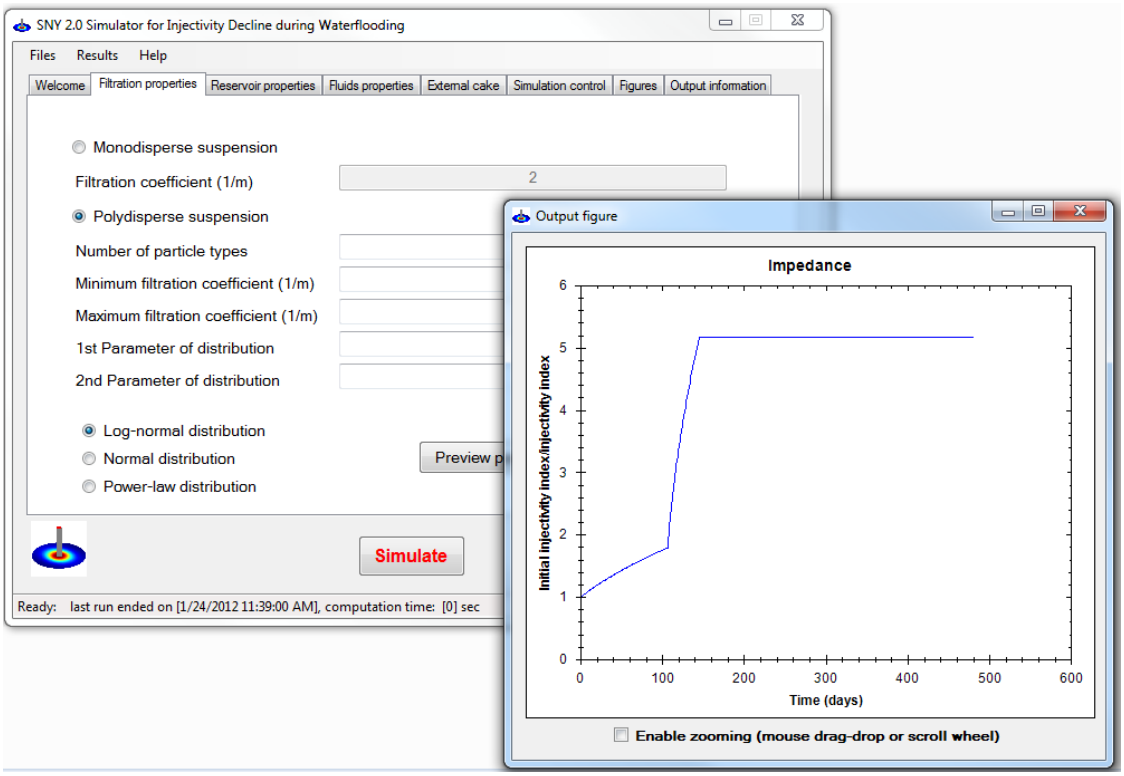

Figure 4.2 Graphical user interface of SNY simulator for injectivity decline during waterflooding

4.4 Impedance change interpretation

Sample calculations are first carried out to reveal the impedance change due to different mechanisms during waterflooding. The parameters used for the simulation are listed in Table 4.1. As seen in Figure 4.3, the impedance decreases monotonously during the

damage-free waterflooding. It is attributed to the displacement of the less mobile fluid (oil) with the more mobile fluid (water). The major impedance change happens at the very beginning of the water injection. The impedance approaches the limit $1/M$ asymptotically.

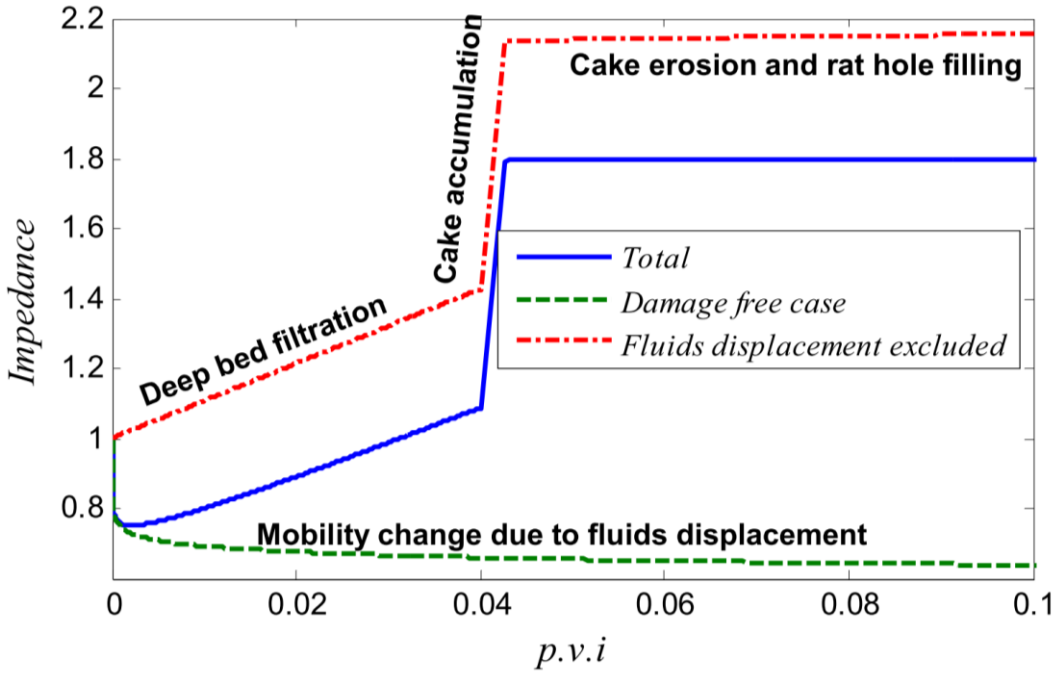

Figure 4.3 Total impedance, impedance during damage free waterflooding, and impedance in a single phase flow case

The impedance change in the single phase injection case can be divided into three phases. The initial phase of linear increase of impedance is attributed to the deep bed filtration. The later and faster increase of the impedance is due to the build-up of the external cake. The steady stage of the impedance is due to the equilibrium between the external cake erosion and the external cake build-up.

The total impedance, as a result, decreases dramatically at the start of waterflooding due to fluid displacement. The rest of it resembles the shape of the impedance curve in the single phase injection case. After the initial stage of waterflooding, the fluid displacement has little effect on the entire impedance change curve and the calculation of formation damage or skin factors. It indicates that the comprehensive approach can provide reliable skin information regardless of what waterflooding model is applied.

Table 4.1 List of parameter values used for the sample calculations

Meanings	Values
Wellbore radius (m)	0.1
Effective reservoir radius (m)	500
Reservoir thickness/length of wellbore (m)	30
Critical porosity ratio for external cake	0.1
Filtration coefficient (m^{-1})	2
Spatial dispersion length (m)	30
temporal dispersion length (m)	30
Mean of lognormal distribution ($\ln(m^{-1})$)	1.1
Standard deviation of lognormal distribution $_{v}(\ln(m^{-1}))$	1.1
Injection concentration	10^{-6}
Formation damage coefficient	300
Initial permeability (D)	4
Initial porosity	0.2
External cake permeability (mD)	0.5
External cake porosity	0.6
Relative permeability of water at residual oil saturation	0.2
Relative permeability of oil at irreducible water saturation	0.7
Irreducible water saturation	0.2
Residual oil saturation	0.25
Water viscosity (cP)	1.23
Oil viscosity (cP)	7.2
Hydrodynamic factor	60
Particle radius (μm)	2
Particle density (kg/m^3)	2600
Water density(kg/m^3)	1030
Friction coefficient	0.5
Initial pressure drop(bar)	20

4.5 Effects of median heterogeneity

Sample calculations are carried out to investigate the effects of the normal dispersion and the temporal dispersion (non-Fickian transport) due to median heterogeneity on the deep bed filtration process. The elliptic equation with a single filtration coefficient is applied to model the deep bed filtration around the injector. As seen in Figure 4.4, the increase of normal dispersion lengths leads to deeper penetration of the deposited particles and slower increase of the impedance. It can be explained by the competition between the

dispersion and the particle capture processes. The larger the normal dispersion is, the faster particles travel. In other words, the particles with stronger dispersion can travel further before they are captured by the pores. The impedance change, on the other hand, is relatively insensitive to the normal dispersion. It may be attributed to the relatively fast particle capture that shadows the effects of normal dispersion under such conditions.

Modeling results with different values of temporal dispersion lengths (not shown here) indicate that the increase of the temporal dispersion coefficient leads to little deviation of the deposition profile and the impedance. It can be attributed to the assumption that the temporal dispersion coefficient is inversely proportional to the local particle velocity. In the radial injection scheme, the particle velocity is much higher at the close proximity of the injector than far away from it. On the other hand, the deposition rate is proportional to the particle velocity. The average penetration depth of particles is usually within one meter around the injector.

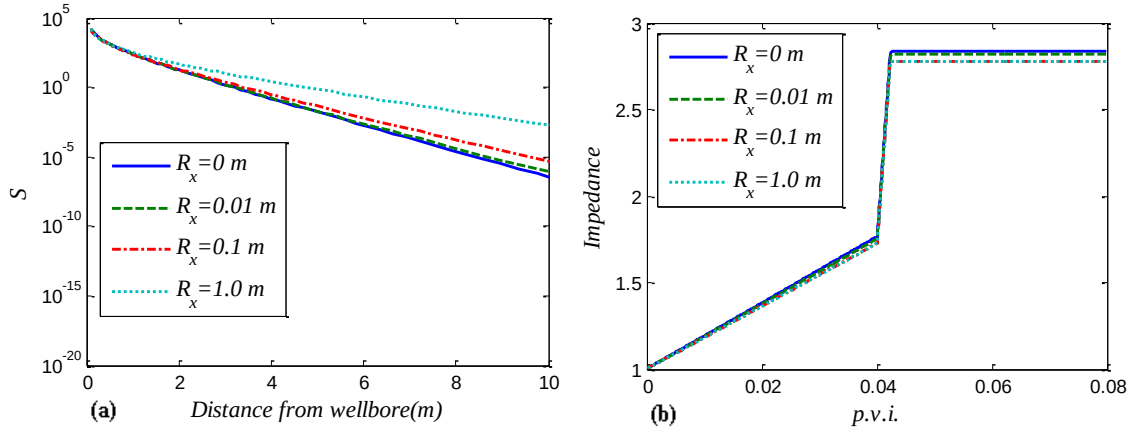

Figure 4.4 Effects of spatial dispersion on deep bed filtration, R_x is the normal dispersion length

4.6 Effects of particle population heterogeneity

Calculations are then carried out to investigate the effects of the particle population heterogeneity on the impedance change in a vertical well. The lognormal distribution of filtration coefficients is adopted to reflect the particle population heterogeneity. The effects of fluid displacement are neglected. The mean values of the logarithm of the filtration coefficients are kept constant. The rest of parameters used for the simulation are

listed in Table 4.1. As seen in Figure 4.5, the increase of the standard deviation has little influence on the impedance increase rate during the deep bed filtration phase. On the other hand, it decreases significantly the transition time for the external cake formation. This indicates that the distribution of filtration coefficients may be better determined from the data on the transition times for external cake than from the core flooding experiments alone. Neglecting the particle population heterogeneity may lead to underestimation of the formation damage and predict late transition to external cake formation.

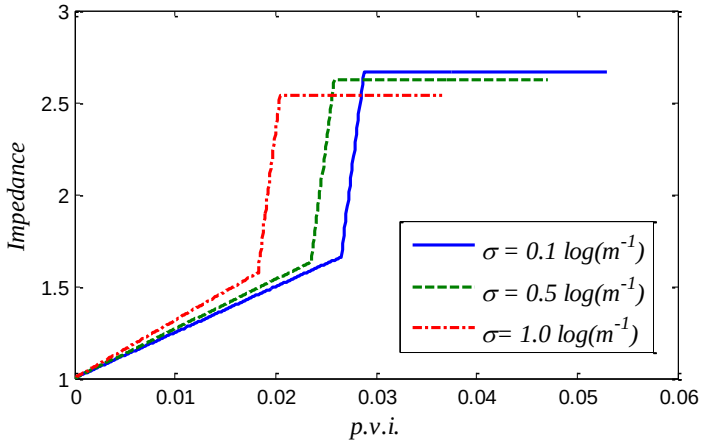

Figure 4.5 Effects of particle population heterogeneity; σ is the standard deviation of the logarithm of filtration coefficients

4.7 External cake distribution

Sample calculations are performed to investigate the external cake thickness in a vertical well at the equilibrium state. The effects of fluid displacement are neglected. The parameters used for the simulation are listed in Table 4.1. It can be seen in Figure 4.6 that the thickness of the external cake increases in the cross-flow direction. This can be attributed to the following reasons: a.) downward drag from cross-flow and the gravity; b.) decreasing cross-flow along the depth leading to decreasing drag and lifting forces. Comparative calculations show that larger particles are more affected by the hydrodynamic drag and gravity. As a result, the distribution of the external cake is more concentrated in the downstream. The external cake in the upstream may be entirely eroded. It can be seen that the impedance at the steady state and the starting time are highly influenced by the cake properties and therefore by the water quality.

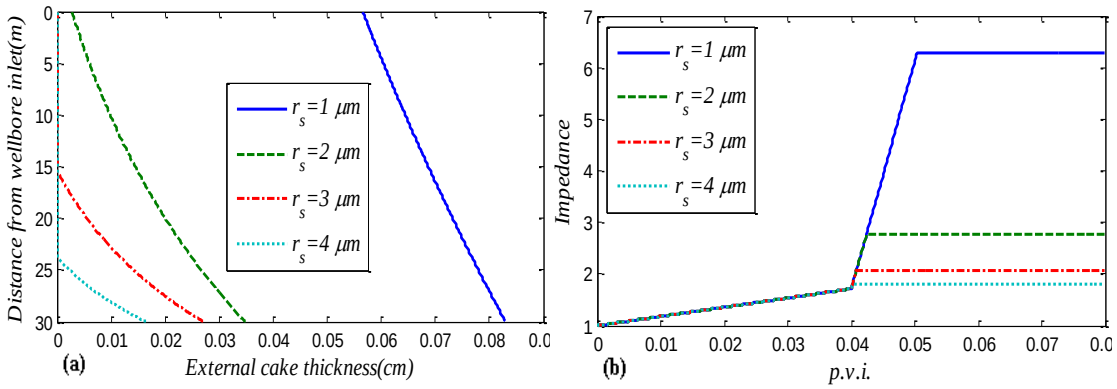

Figure 4.6 Effects of the particle size on the external cake thickness distribution and impedance in a vertical well

The calculation for a horizontal well with the same parameters is performed to investigate the effects of well orientation. The torque balance on the cake particles in a horizontal well is slightly different from that in a vertical well, as seen in Figure 4.7. Gravity is not in line with the cross-flow drag but perpendicular to it. It may contribute positively to or negatively to cake erosion, depending on the location of the cake (top or bottom of the cylinder). Nevertheless, gravity is negligible compared to the permeate drag. As a result, the thickness of the cake is independent of it location.

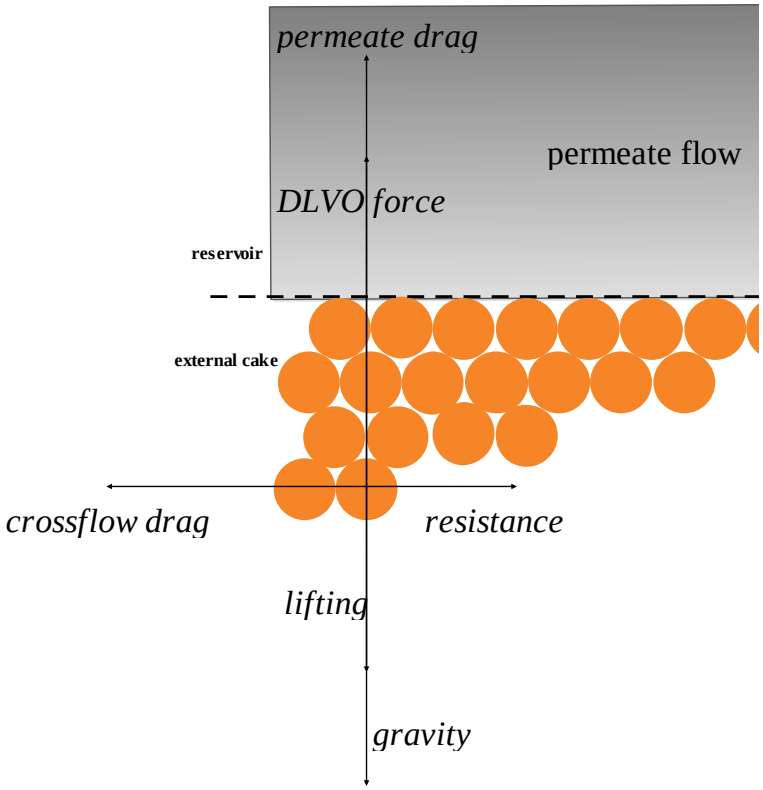

Figure 4.7 Illustration of forces on the particles at the surface of external cake in a horizontal well

As seen in Figure 4.8, the external cake thickness is larger in the horizontal well than that in the vertical well. It is because gravity contributes positively to the erosion of the external cake in the vertical well while it perpendicular to the cross-flow in the horizontal well. As a result, the impedance at the steady state is higher in the horizontal well.

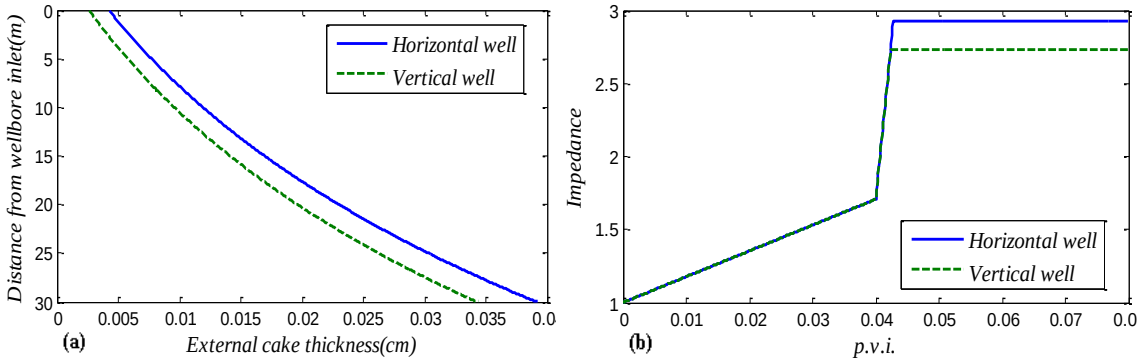

Figure 4.8 Comparison of the external cakes and impedances in horizontal and vertical injection wells

4.8 Verification with the field data

The integral model is then applied to simulate the injectivity decline during waterflooding of the two horizontal injectors (deep-water offshore field X in Campos Basin, Brazil) reported in [291, 297] . The parameters used for the simulation are taken from the literature. It can be seen in Figure 4.9 and Figure 4.10 that the modeling results can match the filed data on the injectivity decline. The comprehensive approach can capture the initial injectivity decline due to the deep bed filtration, the faster decline due to the external cake formation, and the equilibrium stage due to the external cake erosion and the rat hole filling. Most of the model parameters are taken from experimental measurements, while others can be from the empirical correlations, such as the correlation between the critical ratio for external cake formation and the formation damage coefficient [317], and the estimation of hydrodynamic corrector from cake properties[313]. Few parameters that are not easily available can be estimated by fitting the field data, such as the friction coefficient depending on the lever ratio and the erosion factor for the non-ideality of the erosion process.

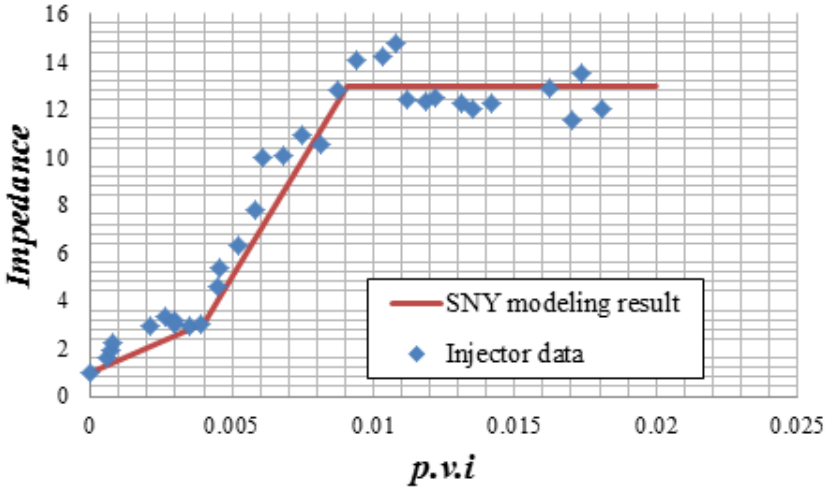

Figure 4.9 Comparison between modeling results and injector data

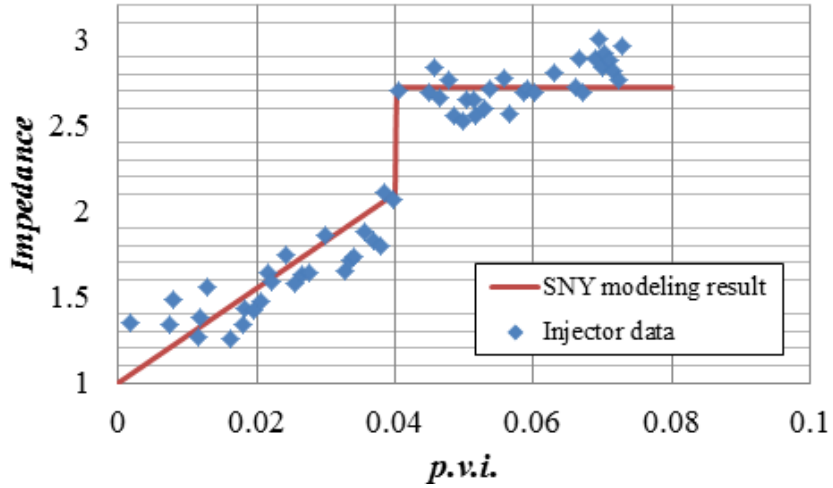

Figure 4.10 Comparison between modeling results and injector data

4.9 Summary of Chapter 4

In this chapter, a new comprehensive approach for predicting injectivity decline during water flooding is proposed. The deep bed filtration is described by novel stochastic random walk equations studied in Chapters 2 and 3. The injectivity decline model takes into account the reservoir heterogeneity and the distribution of solid particles by sizes. It accounts also for the later formation of the external filter cake and its erosion.

The model is able to capture the behaviors of the injectors in the field: the initial slow injectivity decline due to the deep bed filtration of suspended particles, the later faster decline due to the build-up of the external cake, and the steady state due to the cake erosion. Stronger normal dispersion or median heterogeneity close to the injector leads to farther penetration of the particles and slower impedance increase. Neglecting the particle population heterogeneity may lead to underestimation of the formation damage and predict late transition to external cake formation. The impedance at the steady state and the starting time are highly influenced by the cake properties. The impedance and the external cake thickness at the steady state are likely to be higher in horizontal wells than those in vertical wells.

4.10 Nomenclature of Chapter4

A_H	hydrodynamic corrector for dense suspensions
c	suspended concentration
c_0	injected concentration
D_x	spatial dispersion coefficient (m^2/s)
D_t	temporal dispersion coefficient (s)
D_{xt}	mixed dispersion coefficient (m/s)
f	friction coefficient
F	forces on the particles (N)
g	gravity acceleration (m/s^2)
h_c	external cake thickness
J	dimensionless impedance
k	reservoir permeability (m^2)
k_c	external cake permeability (m^2)
k_{rwor}	relative permeability of water at residual oil saturation
k_{rowi}	relative permeability of oil at irreducible water saturation
m	impedance increase slope
M	end-point mobility ratio of water to oil
Δp	pressure drop (Pa)
p	probability distribution
q	permeate flow (m^2/s)
Q	injection rate, cross-flow rate (m^3/s)
r	distance from injector (m)
r_w	wellbore radius (m)
r_e	effective reservoir radius (m)
r_s	particle radius (m)
r_x	spatial dispersivity
r_t	temporal dispersivity
R	dimensionless distance from injector
R_x	spatial dispersion length (m)
R_t	temporal dispersion length (m)
s_{wi}	irreducible water saturation
s_{or}	residual oil saturation
s	deposition concentration
S	deposition concentration
t	time (s)
T	time (p.v.i.)
u	dimensionless velocity
U	Darcy's velocity (m/s)
v	particle velocity (m/s)
z	distance from well bore inlet (m)
α	critical porosity ratio for external cake
λ	filtration coefficient (m^{-1})
Λ	dimensionless filtration coefficient
ϕ	reservoir porosity

ϕ_a accessible reservoir porosity
ϕ_c external cake porosity
μ_w water viscosity ($Pa{\cdot}s$)
μ_o oil viscosity ($Pa{\cdot}s$)
ω hydrodynamic factor
ρ density (kg/m^3)
μ mean of lognormal distribution ($\ln(m^{-1})$)
σ standard deviation of lognormal distribution ($\ln(m^{-1})$)
β formation damage coefficient
Φ dimensionless porosity with regard to initial porosity

Subscripts

a accessible
BL Buckley Leverett
c external cake
d deep bed filtration
e effective or electrostatic
cf cross-flow
F friction
G gravity
L lifting
i *i*th particle type
min minimum
max maximum
N normal
o oil
p permeate
s spheres or particles
tr transition to external cake
w water or well
0 initial or boundary condition

5 Colloid migration and recapture

The purpose of this chapter is to establish a model for deep bed filtration considering the migration of the surface associated phase under unfavorable attachment conditions [135]. The effects of the different migration properties (migration velocity, deposition rates, etc.) are studied. The modeling results are also compared to the experiments where non-monotonic deposition profiles are observed. To investigate the mathematical condition for deposition non-monotonicity, the proposed model is compared to the BSW (S. Bradford, J. Simunek, and S. Walker) model [80] for the migration of large aggregates

5.1 Introduction

The conventional methodology, ADE with a single filtration coefficient, only predicts exponentially decreasing deposition profiles [95]. Many of the experimental results, on the other hand, show hyperexponential deposition profiles or even non-monotonic deposition profiles under some specific conditions [101, 118, 119, 206, 207]. Most of these experiments are carried out in the presence of an energy barrier, for example similarly charged colloid particles and median particles. The deposition of colloids is theoretically hindered by the repulsion between the colloid and porous media. The mechanisms of the deposition in such cases are likely to encompass enhanced retention at low-velocity zones of pore space, staining at grain-grain contacts, surface charge heterogeneity, deposition in the second energy minimum, and surface roughness [55, 80, 101, 103, 111, 112, 122, 135, 248]. Both pore structure and velocity are observed to have impacts on the deposition profiles [80, 115].

Colloids carried by the flowing fluid may be captured at single-contacts of porous media via the second energy minimum or the primary energy minimum [45, 101, 103, 119]. Deposition of colloids may also occur at grain-grain contacts (pore constrictions, stagnant zones) via straining [79, 80, 114, 115, 118, 121]. The balance between the hydrodynamic torque from the flowing fluid and the resisting adhesive torque determines whether the

colloids adjacent/attached to the pore walls will be immobilized or re-entrained into the carrying fluid [9, 112, 209, 216, 232, 248, 318].

Under unfavorable attachment conditions where the DLVO calculations can preclude most of single-contact deposition via the primary energy minimum, the captured particles via the second energy minimum are subject to the hydrodynamic drag and down-gradient translation [112, 119, 135, 191, 248, 319, 320]. Close to the grain-grain contacts some of the surface-associated particles may be immobilized in the stagnant zones. Others are entrained by the flowing fluid and may either rejoin the bulk phase or jump to the next grain[79, 80, 114, 115, 135, 209, 321].

The commonly reported hyperexponential deposition has been attributed to the heterogeneity of the surface charge and energy minima ([101, 110, 207, 208]) or to the enhanced retention at low-velocity zones of pore space [79, 121, 122]. Based on the described mechanisms, the hyperexponentiality of deposition is captured and discussed in Chapters 2 and 3.

On the other hand, the observed non-monotonic deposition has been attributed to the lagged release of aggregates at straining sites [80], or to the migration of surface associated colloids via the second energy minimum [135]. In the same respective works the authors developed conceptual models based on the mechanisms. Both models considered a third phase flowing in porous media. In Ref. [80], S. Bradford, J. Simunek, and S. Walker described the released aggregates transporting and depositing at different rates from the monodisperse colloids. This model will further be referred to as the BSW model. In Ref. [135] the authors proposed that migration of the surface associated phase should accompany the bulk flow.

The model parameters in Ref. [80] were estimated by fitting the model to experiments. This model was shown to be able to simulate non-monotonic deposition profiles. On the contrary, the model in Ref. [135] was proposed only on the conceptual level. Transport and interactions of the migratory surface phase and the bulk aqueous phase were not assigned with detailed physical and mathematical descriptions. Whether the model

considering the surface flow can be used to simulate deep bed filtration processes remained unknown.

5.2 New Model Establishment

5.2.1 Basic Assumptions

Under unfavorable attachment conditions, the DLVO calculations may preclude most of single-contact deposition via the primary energy minimum. The torque balance calculations may indicate that the captured particles via the second energy minimum are subject to the hydrodynamic drag and down-gradient translation [112, 119, 135, 191, 248, 319, 320]. Under such specific conditions, we may follow Xiqing Li et al. [135] to assume that the particles captured by porous media can be classified into two phases, the migratory surface associated phase (weak association via second energy minima at single-contacts) and the immobilized phase (retention via straining at grain-grain contacts), as seen in Figure 5.1.

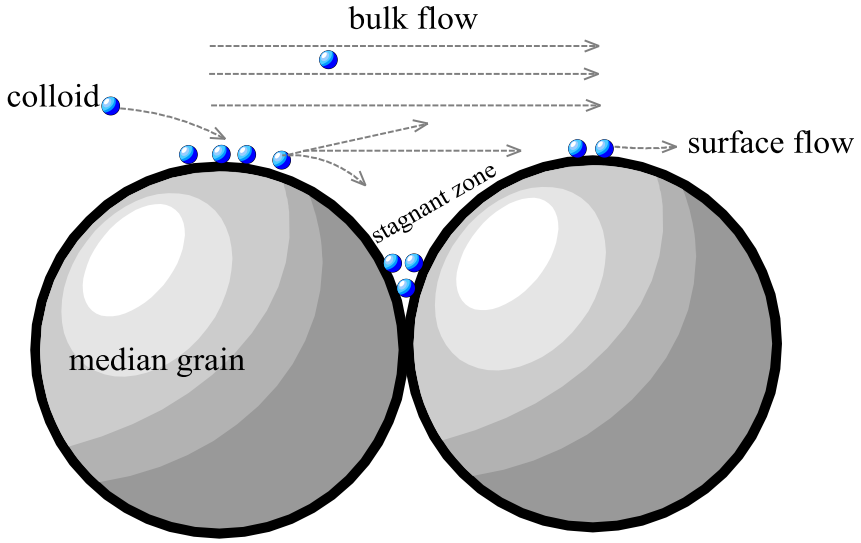

Figure 5.1 Illustration of the surface associated phase and the bulk aqueous phase at pore scale

It is assumed that the transport of the monodisperse particles in the bulk aqueous phase can be characterized by an advection-dispersion equation with a single sink term and a source term. The sink term represents the transport of particles from the bulk phase to the

migratory SA phase and to the immobilized phase while the source term represents the mass transfer from the SA phase and the immobilized phase to the bulk phase.

It is assumed that the migration of the SA phase can be described by the common advection-diffusion formalism. The column inlet is usually connected to an open source of colloids without porous media, hence the zero SA phase is set as the inlet boundary condition. The SA phase may migrate from one grain to another in the following sense: Some of the colloids close to grain-grain contacts are entrained by the flowing fluid and may either rejoin the bulk phase or jump to the next grain. Others may be immobilized in the stagnant zone around grain-grain contacts.

A convective diffusion mechanism of the SA phase may be assumed. A dispersion length is usually interpreted as a characteristic scale of heterogeneity of the porous medium. The dispersion lengths in the bulk phase and the SA phase may, generally speaking, be different, since the surface may be more tortuous than the pore space. However, the orders of magnitude of these parameters in the not-so-highly heterogeneous porous media may be the same. For simplicity of the model and minimization of the number of adjustment parameters, we assume the two dispersion lengths to be equal. This assumption will be validated by comparison with experimental data.

The case of a dilute suspension is considered. The volume of the SA phase and that of the retained particles are assumed to be minimal compared to the bulk aqueous phase, so that their existence does not affect the pore structure significantly. The porosity is assumed to be constant during the entire filtration process. The particle concentration in the SA phase, on the other hand, may be comparable to that in the bulk aqueous phase.

One-dimensional flow is considered, since it is common to most of the experiments and for many applications. The theory is readily generalized onto multiple dimensions.

5.2.2 System of Equations

The system of equations following from the above assumptions has the form of:

$$\frac{\partial c}{\partial t} + v\frac{\partial c}{\partial x} = D\frac{\partial^2 c}{\partial x^2} + \left(\lambda_r s + \lambda_{mr} s_m\right) - \left(\lambda_s + \lambda_d\right)c \tag{5.1}$$

$$\frac{\partial s_m}{\partial t} + v_m \frac{\partial s_m}{\partial x} = D_m \frac{\partial^2 s_m}{\partial x^2} + \lambda_s c - \left(\lambda_m + \lambda_{mr}\right)s_m \tag{5.2}$$

$$\frac{\partial s}{\partial t} = \lambda_m s_m + \lambda_d c - \lambda_r s \tag{5.3}$$

Here c is the number of particles in the bulk aqueous phase per unit pore volume, v is the velocity of the particles in the bulk aqueous phase, and D is the dispersion coefficient in the bulk aqueous phase. Subscript 'm' represents the 'migratory surface associated phase' and s_m is the number of particles in the SA phase per unit pore volume. Correspondingly, v_m is the advection velocity of the particles in the SA phase and D_m is the diffusion coefficient in the SA phase. Finally, s is the concentration of the immobilized particles. $\lambda_s c$ in Equations (5.1) and (5.2)represents the particle transport from the bulk aqueous phase to the SA phase, $\lambda_d c$ in Equation (5.1) is the transport directly from the bulk aqueous phase to the immobilized deposition, and $\lambda_m c$ in Equation (5.2) represents the conversion from SA phase into the immobilized deposition. $\lambda_r s$ represents the release of immobilized particles while $\lambda_{mr} s_m$ represents the release of SA phase back to the bulk phase. In order to connect the motion of the particles in the SA phase to that in the bulk aqueous phase, the following relation is adopted:

$$v_m = f_m v \tag{5.4}$$

where f_m is the ratio of the particle velocity in the SA phase to that in the bulk aqueous phase. The estimation of the fraction will be discussed in detail later. Convective dispersion/diffusion both in the bulk aqueous phase and the surface associated phase is also assumed:

$$D = \alpha v; \quad D_m = f_m D; \tag{5.5}$$

where α is the longitudinal dispersivity/diffusivity possessing the dimension of length, the same both in the bulk aqueous phase and in the SA phase.

Unlike most common formulations, system (5.1) to (5.3) does not involve porosity of the medium, and the deposition and release rates are not proportional to the particle velocity. This is a possible formulation for the case of constant porosity (dilute suspension), if we assume that v and v_m are constant and interstitial, but not superficial, flow velocities and give corresponding re-definitions of the filtration coefficients λ_s, λ_d, λ_m, λ_r, λ_{mr}. These re-definitions should be taken into account when actual values of the coefficients are computed.

Similar to [104, 123], the system of equations (5.1) ~ (5.3) can be reformulated in terms of dimensionless variables:

$$\frac{\partial C}{\partial T} + u\frac{\partial C}{\partial X} = uR\frac{\partial^2 C}{\partial X^2} + \left(\Lambda_r S + \Lambda_{mr} S_m\right) - \left(\Lambda_s + \Lambda_d\right)C \tag{5.6}$$

$$\frac{\partial S_m}{\partial T} + u_m\frac{\partial S_m}{\partial X} = u_m R_m\frac{\partial^2 S_m}{\partial X^2} + \Lambda_s C - \left(\Lambda_m + \Lambda_{mr}\right)S_m \tag{5.7}$$

$$\frac{\partial S}{\partial T} = \Lambda_m S_m + \Lambda_d C - \Lambda_r S \tag{5.8}$$

Here:

$$x = LX;\quad t = (L/v_0)T;\quad c = Cc_0;\quad s_m = S_m c_0;\quad v_m = u_m v_0;\quad R_m = \frac{D_m}{v_0 L};\quad \Lambda_m = \frac{\lambda_m L}{v_0}$$

$$s = Sc_0;\quad v = uv_0;\quad R = \frac{D}{v_0 L};\quad \Lambda_s = \frac{\lambda_s L}{v_0};\quad \Lambda_d = \frac{\lambda_d L}{v_0};\quad \Lambda_{mr} = \frac{\lambda_{mr} L}{v_0};\quad \Lambda_r = \frac{\lambda_r L}{v_0};$$

where R is the dimensionless longitudinal dispersivity in the bulk aqueous phase and R_m is the dimensionless longitudinal diffusivity in the SA phase. The value of L is the reference length (m), v_0 is the reference velocity (m/s), and c_0 is the reference concentration. The inverse Peclet number R describes the magnitude of the spatial dispersion compared to the product of the reference velocity and the reference length,

while R_m is a similar value for the surface phase. Provided that v_0 is the particle velocity in the bulk phase (v=v_0) and that the longitudinal dispersivities/diffusivities in the bulk phase and in the SA phase are equal, the dimensionless parameters can be expressed as:

$$u = 1; \quad u_m = f_m; \quad R_m = R; \tag{5.9}$$

Equations (5.6) ~ (5.8) represent mass balances of the particles in the bulk, surface, and immobile phase, correspondingly. With given velocities and dispersion/diffusion coefficients, the three equations form a closed system for the entire mass balance among the bulk aqueous phase, the SA phase and the immobilized deposition phase.

A simpler formulation has also been tested: a system where deposition from the bulk to the immobile phase is prohibited, Λ_d=0. Sample calculations (not shown here) indicated that with such a formulation the deposition at the inlet is zero because the SA phase concentration is assumed to be zero at the inlet. Indeed, all the particles deposited at the inlet belong to the SA phase and immediately start moving forward along the sample. This is in contradiction with the observed deposition profiles [80, 111, 135] with non-zero deposition near the entrance. Therefore, deposition from the bulk directly to the immobile phase should be introduced to avoid discrepancy with the observed experimental data.

Summing Equations (5.6) ~ (5.8) together leads to the mass conservation law:

$$\frac{\partial\left(C + S + S_m\right)}{\partial T} + u\frac{\partial\left(C - R\dfrac{\partial C}{\partial X} + f_m S_m - f_m R_m \dfrac{\partial S_m}{\partial X}\right)}{\partial X} = 0 \tag{5.10}$$

Equation (5.10) indicates that the boundary conditions at the inlet X=0 should take into account both the advection flux and the dispersion/diffusion flux of the particles.

5.2.3 Boundary Conditions

Clean bed filtration is assumed as the initial condition for the convenience of comparing modeling results with the column experiments in most labs. The initial conditions can be formulated as:

$$C(X,T=0)=0; \quad S_m(X,T=0)=0; \quad S(X,T=0)=0; \tag{5.11}$$

Since Equations (5.6) and (5.7) are both parabolic, it is commonly accepted to apply Neumann boundary conditions at the outlet and two Robin boundary conditions at the inlet for the mobile phases [98]:

$$C - R\frac{\partial C}{\partial X} = \begin{cases} 1 & (X=0, T<T_0) \\ 0 & (X=0, T\geq T_0) \end{cases} \tag{5.12}$$

$$\left.\frac{\partial C}{\partial X}\right|_{X=L} = 0 \tag{5.13}$$

$$S_m - R_m\frac{\partial S_m}{\partial X} = 0 \qquad (X=0,T) \tag{5.14}$$

$$\left.\frac{\partial S_m}{\partial X}\right|_{X=L} = 0 \tag{5.15}$$

Boundary condition (5.12) represents the common injection procedure: before $T_{0,}$ inject particles, and after $T_{0,}$ inject pure water. The ad hoc boundary condition (5.14) is based on the assumption that inlet of the porous medium is usually connected with a source domain without porous media. Thus, no surface associated phase is formed directly at the inlet. Formation of the surface phase does not begin until at the inlet, and any such phase moves further by the surface flux. Of course, in case of an immobile surface phase alone, Equation (5.14) is violated. Neumann boundary conditions (5.13) and (5.15) represent the no-flux setting at the outlet of an experimental column.

Addition of Equations (5.12) to (5.14) lead to the total boundary conditions for both mobile phases indicated by Equation (5.16).

$$C - R\frac{\partial C}{\partial X} + S_m - R_m\frac{\partial S_m}{\partial X} = \begin{cases} 1 & (X = 0, T < T_0) \\ 0 & (X = 0, T \geq T_0) \end{cases} \tag{5.16}$$

$$\frac{\partial C}{\partial X} + \left.\frac{\partial S_m}{\partial X}\right|_{X=L} = 0 \tag{5.17}$$

5.2.4 Implementation

It is assumed that the velocities, dispersivity and diffusivity, as well as the coefficients of particle transport to different phases are all constant and known. The closed system of Equations (5.6) to (5.8), with boundary conditions (5.11) to (5.15), can easily be solved by a finite difference technique and the method of lines. The calculation is implemented in MATLAB with the intrinsic function 'ode45' for solving ordinary differential equations. The numerical solution with Λ_s=0 (no SA phase) is also compared with the analytical solution in Ref. [98]. The error of the numerical solution can be reduced to 0.01% with a properly selected mesh. An approximate analytical solution for the model can also be found in Ref. [98]. A good agreement between the analytical solution and numerical solution is observed (not shown here). This validates the selected numerical method.

In order to reveal the modeling results in the same way as those from the laboratory experiments, the total effluent concentration and the total deposition need to be calculated. The bulk aqueous phase and the SA phase move at two different velocities in parallel. Since the experimentally monitored effluent concentration counts both the number of particles in the bulk aqueous phase and that in the SA phase per unit time, the total effluent concentration can be calculated by:

$$C_{effluent}(T) = \frac{uC(1,T) + u_m S_m(1,T)}{u} = C(1,T) + f_m S_m(1,T) \tag{5.18}$$

At the end of a column experiment (T=$T_{\max}$), the flow in the core is zero and the SA phase remains immobile. The final deposition is then the sum of remaining SA phase and the immobilized phase:

$$S_{final}(X) = S(X, T_{\max}) + S_m(X, T_{\max}) \tag{5.19}$$

The model parameters may be estimated by fitting the modeling results to the experimental data. The MATLAB intrinsic function 'lsqnonlin' for non-linear least square problems is applied for curve fitting. Confidence intervals (CI) and correlation matrices of the model parameters are calculated. Details of the procedure can found in Refs. [274, 275].

5.2.5 Estimation of migration velocity

The section presents a rough estimation method for the magnitude of f_m. Since packed beds of granular media are commonly adopted in filtration experiments, they are also selected for the study here. The type of media can be represented by various geometrical models [67, 153, 322-324]. The constricted tube model [9, 324] is applied in this work. The grains of the porous medium and the colloid particles are assumed to be spherical. It may also be assumed that the velocity of a particle adjacent to the pore wall via the second energy minimum may be approximated by the fluid velocity at its center. In Ref. [9] the diameter of the pore in a different position *z* can be expressed as:

$$d_z = 2\left\{\frac{d_{\max}}{2} + \left[4\left(\frac{d_c}{2} - \frac{d_{\max}}{2}\right)\left(0.5 - \frac{z}{h}\right)^2\right]\right\} \tag{5.20}$$

where $d_{\max}$ is the maximum diameter of the pore, d_c is the constriction diameter, h is the pore length. In Ref. [324] d_c and the effective pore diameter $d_{effecdtive}$ are calculated by:

$$d_c = \frac{d_{media}}{2.5658} \tag{5.21}$$

$$d_{effective} = \frac{d_c}{0.47} \tag{5.22}$$

where d_{media} is the diameter of the bed median particle, and in Ref. [322] $d_{\max}$ is calculated by:

$$d_{\max} = 2.141 d_c \tag{5.23}$$

In Ref. [9] the fluid velocity is then calculated by:

$$v_{colloid} = 2\frac{Q/N_{pore}}{(\pi/4)d_z^2}\left[1-\frac{d_z - d_{colloid}}{d_z}\right] \tag{5.24}$$

where $d_{colloid}$ is the diameter of the colloid particle, Q is the volumetric flow rate, d_z is the pore diameter in the position z, and N_{pore} is the number of pores in a cross-section of the column, which can be expressed as:

$$N_{pore} = \frac{A\varphi}{(\pi/4)d_{effective}^2} \tag{5.25}$$

where A is the cross-section area of the column, φ is the porosity of the column. The fraction f_m can be approximated by the velocity across the center of the associated particle divided by the average pore velocity:

$$f_m = \frac{v_{colloid}}{Q/A\phi} = \frac{2d_{effective}^2 d_{colloid}}{d_z^3} \tag{5.26}$$

With given media particle size and the suspended or colloid particle size, the fraction fm is a function of z/h. Sample calculations are performed for the experimental setting in [111], plots of fm to z/h are shown in Figure 5.2 (a). It is seen that the fraction approaches its maximum at the inlet and the outlet of the pore. The average of the fraction f_m can be calculated by:

$$f_m \approx \overline{f_m} = \frac{\int_0^1 f_m d\left(\frac{z}{h}\right)}{\int_0^1 d\left(\frac{z}{h}\right)} = \frac{d_{colloid}}{d_{media}}\int_0^1 \frac{1.3748}{8\left[0.4172 - 0.8892\left(0.5-\frac{z}{h}\right)^2\right]^3} d\left(\frac{z}{h}\right) \tag{5.27}$$

$$f_m = 5.7396 \frac{d_{colloid}}{d_{media}} \tag{5.28}$$

The plot of average f_m versus typical suspended/colloid particle sizes and typical median particle sizes is shown in Figure 5.2 (b). It is seen that the typical value of f_m varies approximately from 1×10^{-2} to 5×10^{-2}.

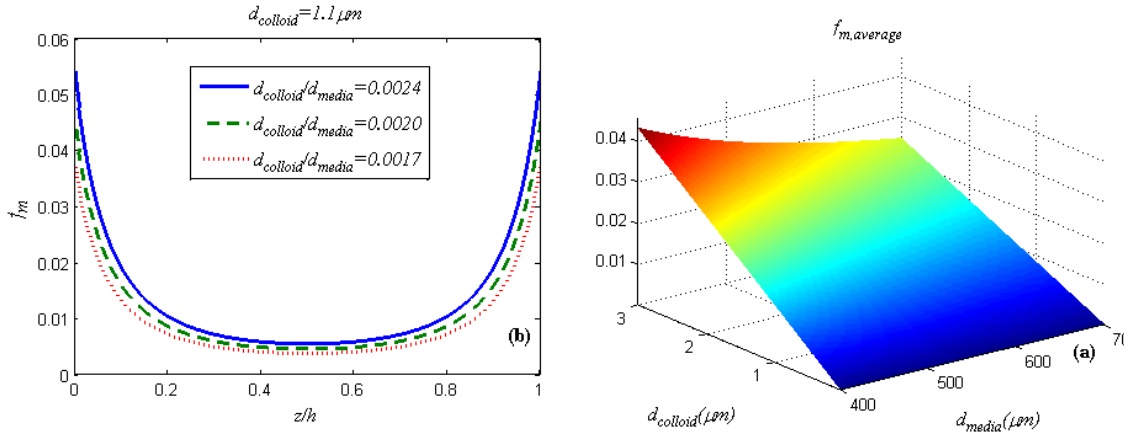

Figure 5.2 (a). f_m at different pore positions (b). Average f_m for different diameters of colloids and those of median particles.

5.3 Results of Modeling

This section aims at studying the basic properties of the proposed model and the effects resulting from changing the properties of the SA phase migration, such as the advection velocity, the diffusivity and the deposition rate of the SA phase.

5.3.1 Numerical Solutions

Numerical solutions are first obtained with all the parameters assumed to be constant and known. Particles are injected in the first five pore volumes, and then water alone is injected to wash away the remaining mobile particles until fifteen pore volumes are injected. For the calculations we use: R=6.67×10^{-3}; u=1.0; Λ_s=0.03; Λ_d=0.012; f_m=0.01; Λ_m=0.15; Λ_{mr}=0.15×10^{-3}; Λ_r=0. The calculated profiles are shown in Figures 2 to 4.

As seen in Figure 5.3 (a), the particle concentration in the SA phase at the outlet is comparable to that in the bulk aqueous phase. However, the major contribution to the

monitored effluent concentration is from the bulk aqueous phase alone. It is explained by the far slower motion of the SA phase than that of the bulk aqueous phase. Figure 5.3 (b) reveals the non-monotonic spatial distribution of the immobilized particles and that of the final deposition. The difference between them indicates that the immobilization of the SA phase due to ceased flooding contributes to the final deposition. It proves that the mechanism of migratory surface phase alone can give rise to a non-monotonic deposition profile.

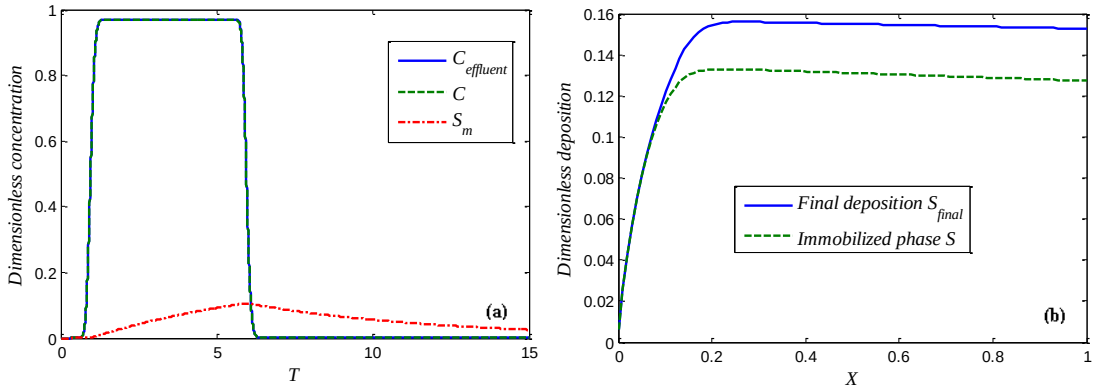

Figure 5.3 (a). Concentrations at the outlet (d). Final deposition and immobilized phase at the end of flooding.

Figure 5.4 (a) and (b) show the displacement fronts of the bulk phase and the SA phase respectively at different time moments before breakthrough. It can be seen that the front of the SA phase lags behind that of the bulk phase. The distribution of the SA phase is strongly non-monotonic and possesses a peak moving towards the outlet. Figure 5.5 shows the evolution of immobilized particles with the SA phase and the resulting total deposition. Before the end of injection (T<5) the SA phase accumulates and is non-monotonic along X, while the peak of the SA phase is flushed to the outlet during water flooding (T>5). The resulting immobilized phase is distributed non-monotonically over the entire process, and its peak moves towards the outlet. It can be inferred from the results that the final deposition is still non-monotonic in the case of no immobilized phase, because the SA phase itself is non-monotonically distributed along X.

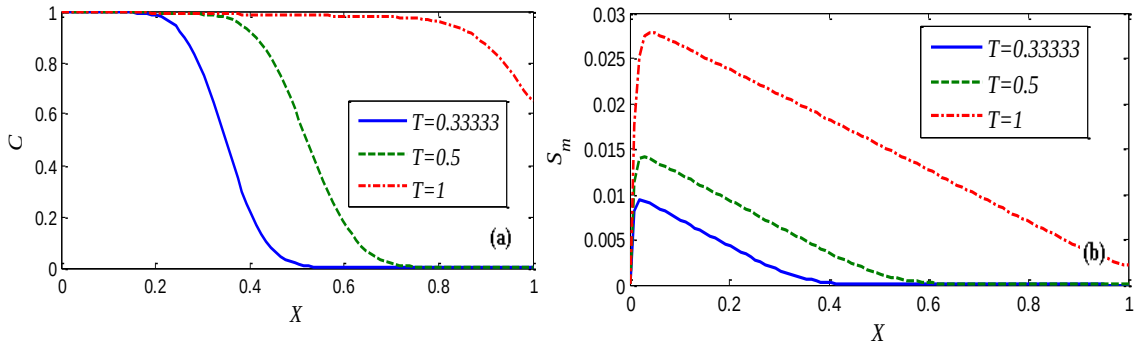

Figure 5.4 Displacement profiles: (a) .Bulk aqueous phase (b). Surface associated phase

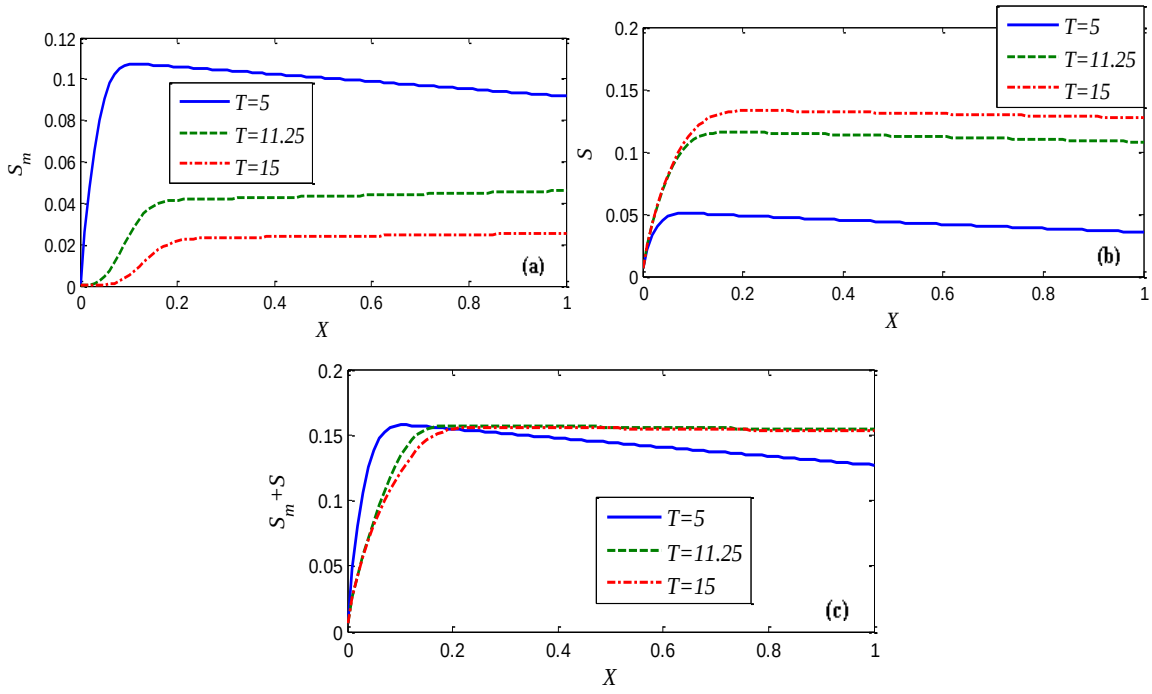

Figure 5.5 (a). Surface associated phase (b). Immobilized phase (c). Total deposition.

5.3.2 Migration of Surface Associated Phase

Calculations are then carried out with different values of f_m. The rest of the parameters are set to the same as in Section 5.3.1. As seen in Figure 5.6 (b), the larger f_m leads to maximum final deposition closer to the inlet. The faster the SA phase migrates the closer the maximum of deposition is to the outlet. On the other hand, since the effluent SA phase contributes little to the total effluent concentration, the breakthrough curve is not much influenced by this factor.

The modeling results may also enlighten some aspects in the experimental design for observing non-monotonic deposition. Since larger values of f_m help non-monotonicity of deposition, larger colloids and smaller median particles are preferable for such experiments. Other aspects, such as the optimal solution chemistry and particle materials, are beyond the scope this work.

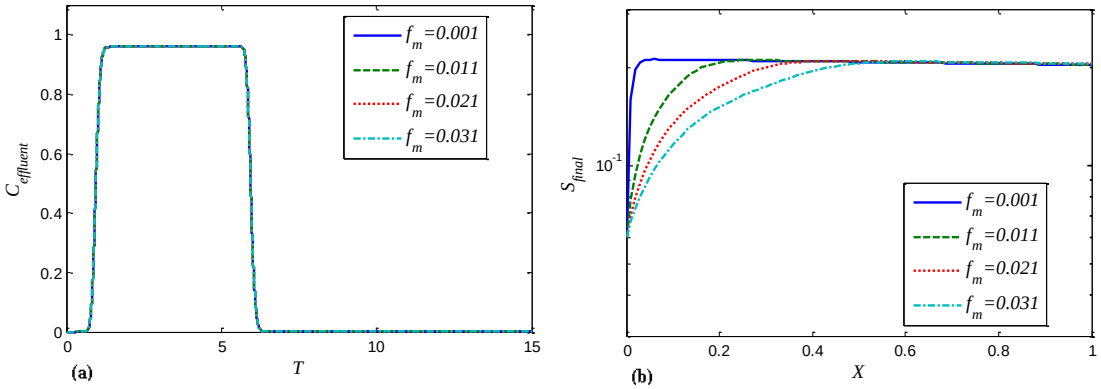

Figure 5.6 Comparison of different values of f_m.

5.3.3 Dispersivity

Calculations are carried out with varying dispersivity R. The chosen value for f_m is 0.01, and the rest of the parameters are the same as in Section 5.3.1. It is shown in Figure 5.7 (b) that larger values of R also lead to the peak of final deposition closer to the outlet. This behavior, however, is also connected with transport of the bulk aqueous phase, as seen in Figure 5.7 (a). As expected, larger values of dispersivity result in a larger wash-out of the breakthrough curve.

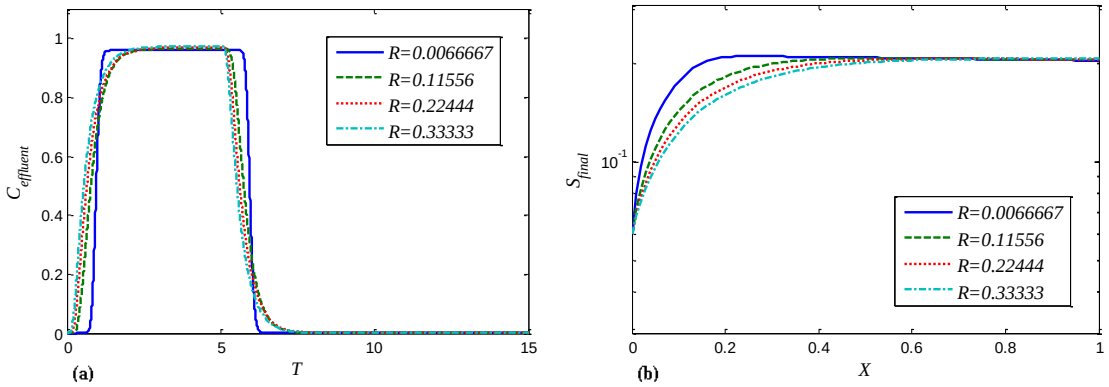

Figure 5.7 Comparison of different values of R.

5.3.4 Production of migratory phase

Calculations are carried out with various SA phase generation rate coefficients Λ_s. The rest of the parameters are the same as in Section 5.3.1. Since at the end of flooding the remaining SA phase in the system also stops flowing, it contributes to the final deposition. The expected effect is confirmed in Figure 5.8 (b). It also shows that the large value of Λ_s leads to maximum deposition slightly closer to the outlet. This can be explained by the fact that the faster SA phase generation gives rise to more SA phase available for migration per unit time. Compared to the classical filtration theory, Λ_s is a part of the total filtration coefficient. Hence, the larger value to Λ_s leads to the lower effluent concentration at the steady stage, as seen in Figure 5.8 (a).

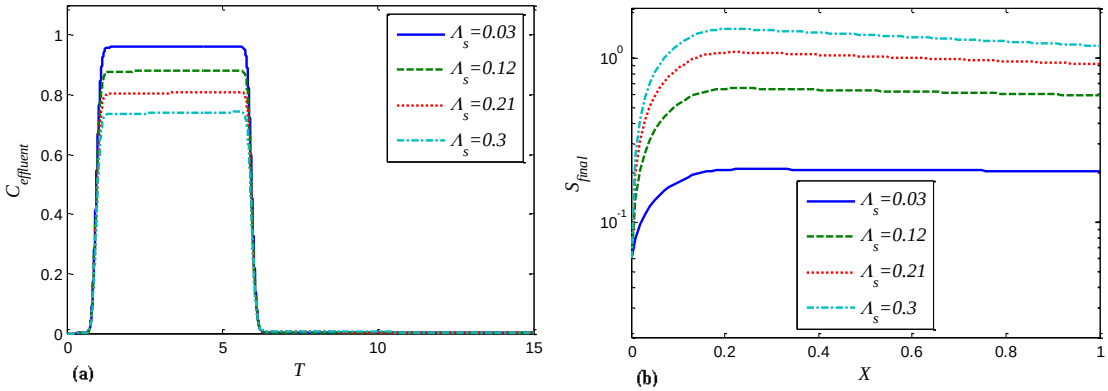

Figure 5.8 Comparison of different values of Λ_s.

5.3.5 Immobilization of SA Phase

Calculations are carried out with various SA phase immobilization rate coefficients Λ_m. The rest of the parameters are the same as in Section 5.3.1. Figure 5.9 (b) shows that the faster deposition of SA phase leads to maximum deposition closer to the inlet. The result corresponds to that in Figure 5.8 (b). In a similar sense, the faster deposition of the SA phase gives rise to less SA phase available for migration in a unit time. In other words, a particle in the SA phase may not have enough time to migrate farther before it is deposited. Again the factor has little influence on the breakthrough curve, as seen in Figure 5.9 (a).

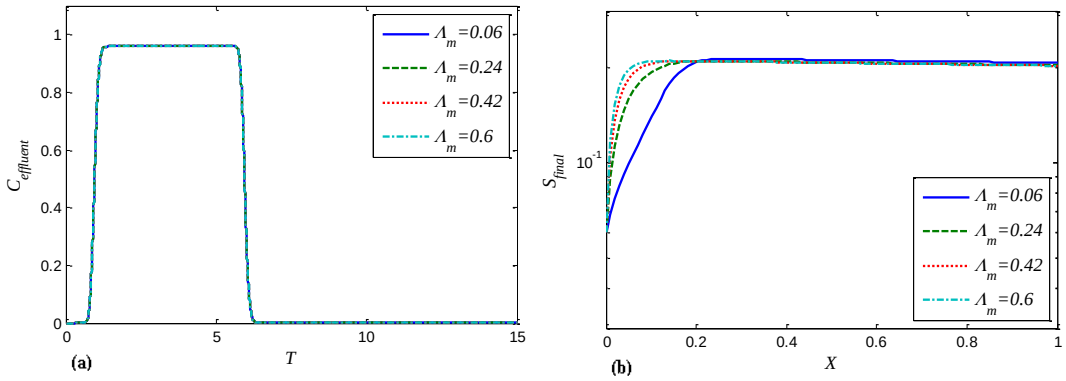

Figure 5.9 Comparison of different values of Λ_m.

5.4 Comparisons with Experiments

In this section, the modeling results are compared to the experimental observations. Model parameters are estimated either by fitting the model to experimental data or by a proposed estimation method. The purpose is to find a fast method for estimating the parameters of the model, and to match the modeling and the experimental results, by applying the knowledge obtained from the numerical modeling above.

Xiqing Li et al. adopted the fluorescent carboxylate-modified polystyrene latex microspheres (diameter 1.1 μm) as colloid particles and packed quartz sand (diameter 417~600 μm) as porous media for the column experiments [111]. Non-monotonic deposition profiles were observed in the experiments.

Table 5.1 Parameter estimators and their confidence intervals (CI) from the proposed model fitting to experiments in Ref.[111]

Experiments		Λ_d	Λ_r	f_m	Λ_s	Λ_m	Λ_{mr}
	Estimator	**6.17×10^{-3}**	**3.74×10^{-4}**	**0.009993**	**1.13×10^{-1}**	**1.32×10^{-1}**	**2.49×10^{-2}**
IS=3*mM*	CI	**2.28×10^{-5}**	**1.77×10^{-6}**	**2.33×10^{-5}**	**1.01×10^{-4}**	**4.58×10^{-4}**	**6.24×10^{-5}**
	Estimator	**3.51×10^{-2}**	**2.71×10^{-4}**	**0.009999**	**4.05×10^{-1}**	**1.35×10^{-1}**	**2.71×10^{-3}**
IS=6*mM*	CI	**1.88×10^{-4}**	**1.62×10^{-6}**	**1.16×10^{-4}**	**2.91×10^{-4}**	**2.18×10^{-3}**	**2.61×10^{-3}**

First, the parameters are estimated by fitting the model to the breakthrough curves and the deposition profiles from Ref. [111]. The parameter estimators and their confidence intervals are listed in Table 5.1. Small dispersion length is assumed: R=10^{-4}. The resulting correlation matrix (not shown here) indicates that there is no strong correlation

among the model parameters. The modeling results and experimental data are compared in Figure 5.10.

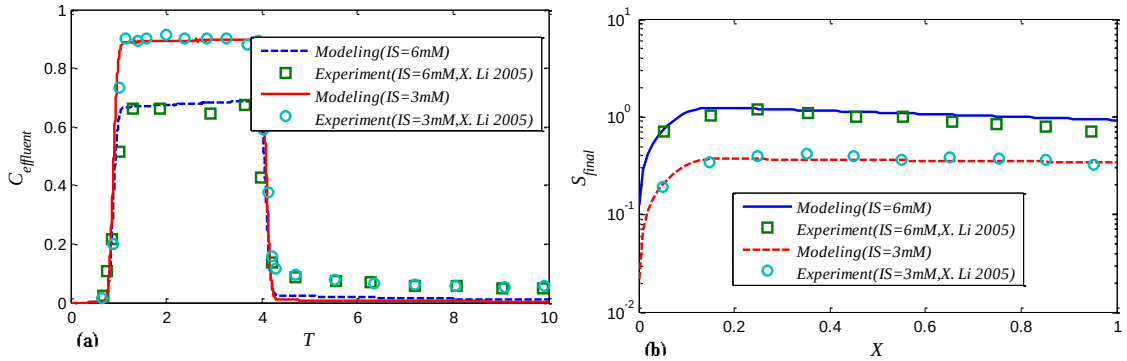

Figure 5.10 Results of the proposed model with the parameters estimated by fitting the model to the experiments in Ref. [111].

Parameters may also be estimated by the following analysis. f_m be estimated by Equation (5.28),with the available information about the colloids and the porous medium. The next parameter to be estimated is the longitudinal dispersivity/ diffusivity. The parameter is relatively low in a homogeneous porous medium, and can be easily fitted to the breakthrough curve.

The estimations of Λ_d and Λ_s are relatively nontrivial. In the case of minimal particle release it is assumed that $\Lambda_r \approx 0$ and $\Lambda_{mr} \approx 0$. The average effluent concentration at the steady state is approximately dependent on $\Lambda_d + \Lambda_s$ alone, since other parameters have little influence on it (see Figure 5.6 (a), Figure 5.7(a) and Figure 5.9 (a)). The sum of the two coefficients can approximately be estimated by the logarithm of the average effluent concentration at the steady stage:

$$\Lambda_d + \Lambda_s = -\ln(C_s) \tag{5.29}$$

where C_s is the average effluent concentration at the steady stage from the experiment. Since the direct deposition from the bulk aqueous phase alone forms the deposited concentration at the inlet, the value of Λ_d can be estimated by fitting the deposition at the inlet. At last, Λ_s is obtained from the estimated value of Λ_d.

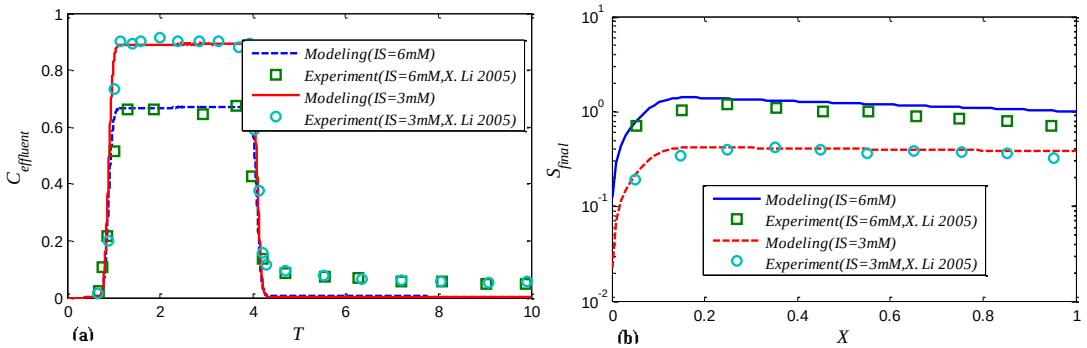

Figure 5.11 Results of the proposed model with the parameters estimated by the proposed method and the experimental results in Ref. [111].

The particle velocity is approximated by the average pore water velocity (superficial velocity divided by porosity). The only remaining parameter for estimation is the SA phase deposition rate coefficient Λ_m. It is tuned at last to match the observed position of the deposition maximum.

Table 5.2 Parameters of the proposed model estimated by the proposed method

Experiments	f_m	Λ_s	Λ_d	Λ_m	Λ_r	Λ_{mr}
IS=3*mM*	**0.01**	**0.108**	**0.0027**	**0.135**	**0**	**0**
IS=6*mM*	**0.01**	**0.405**	**0.0351**	**0.135**	**0**	**0**

All the parameters for the calculations are estimated by the above method and shown in Table 5.2. It can be seen that the estimators by fitting the experiments and those by the analysis are close to each other. The modeling results based on the parameters estimated by the above analysis and the experimental data are compared and shown in Figure 5.11. In the case of *IS*=6*mM* the slight overestimation of the deposition can be attributed to neglecting the release of the SA phase and immobilized phase. Both the modeled non-monotonic deposition profile and the breakthrough curve agree with the experimental data. It confirms the ability of the proposed model to simulate a non-monotonic deposition profile in practice and the feasibility of the method for parameter estimation in the case of minimal particle release.

5.5 Comparison with BSW model

In this section, the proposed model is compared to BSW model from Ref. [80] which can also produce non-monotonic deposition. The purpose is to understand the underlying mechanisms and essence of deposition non-monotonicity by investigating the similarities and differences between the two models.

In Ref. [80], the authors (S. Bradford, J. Simunek, and S. Walker) take into account the release of bacteria aggregates at straining sites. The released aggregates and suspended monodisperse particles are both dispersed in the pore space. The released aggregates are transported and recaptured at different rates from the monodisperse particles. The model in Ref. [80] can be described by the following equations:

$$\frac{\partial C}{\partial T} + u\frac{\partial C}{\partial X} = uR\frac{\partial^2 C}{\partial X^2} - \Lambda_d C \tag{5.30}$$

$$\frac{\partial C_a}{\partial T} + f_a u\frac{\partial C_a}{\partial X} = f_a uR\frac{\partial^2 C_a}{\partial X^2} - \Lambda_{ad} C_a + F_r S + \Lambda_{ar} S_a \tag{5.31}$$

$$\frac{\partial S_a}{\partial T} = \Lambda_{ad} C_a - \Lambda_{ar} S_a \tag{5.32}$$

$$\frac{\partial S}{\partial T} = \Lambda_d C - F_r S \tag{5.33}$$

$$F_r = \begin{cases} \Lambda_r & S \geq S_c \\ 0 & S < S_c \end{cases} \tag{5.34}$$

where the subscripts '*a*' represent the aggregates, S_c is the critical deposition concentration above which the aggregates start to be released. $\Lambda_d C$ represents the deposition of the suspended monodisperse population at straining sites, $\Lambda_{ad} C_a$ is the deposition rate of the released aggregates and $\Lambda_{ar} S_a$ represents the re-release of the deposited aggregates. f_a reflects the different transport behaviour of the aggregates compared to the injected monodisperse particles. Similar boundary conditions as (5.14)

and (5.15) are applied for Equations (5.31) and (5.32) since there is no aggregate assumed to form before the inlet.

Sample calculations (not shown here) indicate that the transport of aggregates is qualitatively similar to that of the SA phase in our model. The aggregates are generated inside the column domain and are transported to the outlet. Unlike the SA phase, the aggregates may contribute much to the breakthrough curve because the velocity of aggregates is comparable to that of the injected monodisperse colloids. The resulting total breakthrough curve may contain two peaks for the monodisperse colloids and the aggregates respectively. Due to the far slower motion of SA phase, it only has little contribution to the total breakthrough curve.

It can be seen that the two models both consider a third mobile population: surface associated phase via second energy minima and released aggregates, correspondingly. Both additional populations may be transported and immobilized at different rates from the injected population. Neither of them is injected from the inlet. The source of the SA phase is the injected population in the bulk phase, and the source of the aggregates is the accumulated deposition. Mathematically, the two models both involve additional equations for the transport and deposition of the third mobile population. The model structures of them are mathematically similar.

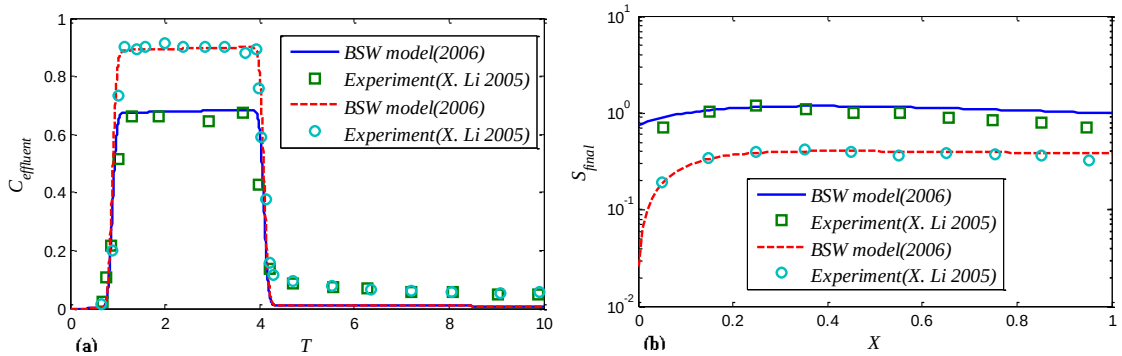

Figure 5.12 Results of BSW model [80] with the parameters estimated by fitting the model to the experiments in Ref. [111]

The model in Ref [80] is also applied to reproduce the experimental results in Ref. [111], as seen in Figure 5.12. The modeling results highly agree with the experimental data. The estimated parameters and their confidence intervals are listed in Table 5.3. A small

dispersion length is also assumed: R=10^{-4}. The resulting correlation matrix (not shown here) indicates that there is no strong correlation among the model parameters.

Table 5.3 Parameter estimators and their confidence intervals (CI) from the model in Ref. [80] fitting to experiments in Ref.[111]

Experiments		Λ_d	Λ_r	Λ_{ad}	S_c	Λ_{ar}	f_a
	Estimator	$\mathbf{1.19\times10^{-1}}$	$\mathbf{3.06\times10^{-1}}$	$\mathbf{1.34\times10^{1}}$	$\mathbf{1.00\times10^{-2}}$	$\mathbf{4.00\times10^{-2}}$	$\mathbf{9.90\times10^{-1}}$
IS=3*mM*	CI	$\mathbf{8.63\times10^{-5}}$	$\mathbf{1.30\times10^{-2}}$	$\mathbf{5.81\times10^{-1}}$	$\mathbf{2.59\times10^{-3}}$	$\mathbf{1.19\times10^{-2}}$	$\mathbf{6.59\times10^{-2}}$
	Estimator	$\mathbf{3.99\times10^{-1}}$	$\mathbf{6.95\times10^{-2}}$	**5.35**	$\mathbf{1.00\times10^{-2}}$	$\mathbf{1.11\times10^{-10}}$	$\mathbf{9.90\times10^{-1}}$
IS=6*mM*	CI	$\mathbf{1.69\times10^{-4}}$	$\mathbf{1.64\times10^{-4}}$	$\mathbf{1.09\times10^{-1}}$	$\mathbf{5.84\times10^{-4}}$	$\mathbf{3.57\times10^{-12}}$	$\mathbf{1.96\times10^{-2}}$

It should be commented that no observation of aggregates has been reported in Ref. [111]. The physics described by the model in Ref. [80] seems to be different from that in these experiments. Nevertheless, the model is still able to reproduce the experimental results. This infers that an additional equation describing a mobile population behaving differently from the injected population seems to be a sufficient condition for producing non-monotonic deposition. The additional equation may reflect different physics in different experimental settings. Selection of a physically correct model requires analysis of the particle behavior on the microscopic scale. Such analysis is not always available and possible. In the last case, in order to match the non-monotonic deposition, the simplest possible model involving the second mobile phase should probably be selected.

5.6 Summary of Chapter 5

In this chapter, a mathematical model for suspension/colloid flow in porous media and non-monotonic deposition is proposed. It accounts for the migration of particles associated with the pore walls via the second energy minimum (surface associated phase). The surface associated phase migration is characterized by advection and diffusion/dispersion.

The proposed model for the suspension/colloid flow in porous media, considering the migration of the surface associated phase, is able to produce non-monotonic deposition profiles. A set of methods for estimating the modeling parameters is provided. The estimation can be easily performed with available experimental information. The results of numerical modeling highly agree with the experimental observations. It confirms the ability of the proposed model to catch a non-monotonic deposition profile in practice and the feasibility of the method for parameter estimation in the case of minimal particle release.

The resulting non-monotonic deposition profiles in Ref. [111] are likely to be caused by the migration of the surface associated phase. An additional equation describing a mobile population behaving differently from the injected population seems to be a sufficient condition for producing non-monotonic deposition profiles.

5.7 Nomenclature of Chapter 5

c	Number of suspended particles per unit pore volume (m^{-3})
C	Dimensionless suspended particle concentration
s	Number of retained particles per unit pore volume (m^{-3})
S	Dimensionless retained particle concentration
s_m	Number of particles in the surface associated phase per unit pore volume (m^{-3})
S_m	Dimensionless particle concentration in the surface associated phase
t	Time(s)
T	Dimensionless time (pore volume)
t_0	Particle injection duration (s)
T_0	Dimensionless particle injection duration (pore volume)
x	x coordinate in space
X	Dimensionless x
v	Advection velocity of particles in the bulk aqueous phase
v_m	Advection velocity of particles in the surface associated phase
u	Dimensionless advection velocity of particles in the bulk aqueous phase
u_m	Dimensionless advection velocity of particles in the surface associated phase
D	Coefficient of dispersion(m^2/s) in the bulk aqueous phase
D_m	Coefficient of diffusion(m^2/s) in the surface associated phase
R	Dimensionless longitudinal dispersivity in the bulk aqueous phase
R_m	Dimensionless longitudinal diffusivity in the surface associated phase
c_0	Influent concentration
f_m	Ratio of v_m to v
d_{max}	Maximum diameter of a pore
d_{media}	Diameter of the median particle
$d_{colloid}$	Diameter of the colloid particle
d_c	Constriction diameter
d_z	Pore diameter in position z
h	Pore length
$v_{colloid}$	Fluid velocity at the center of the particle associated with the pore wall
$d_{effective}$	Effective diameter of pores
N_{pore}	Number of pores in a cross-section of the column
λ_s	Coefficient of particle transport from the bulk aqueous phase to the surface associated phase (s^{-1})
Λ_s	Dimensionless form of λ_s
λ_d	Coefficient of particle transport from the bulk (flowing) phase to the immobilized phase (s^{-1})
Λ_d	Dimensionless form of λ_d
λ_m	Coefficient of particle transport from the surface associated phase to the deposition phase(s^{-1})
Λ_m	Dimensionless form of λ_m
λ_{mr}	Coefficient of particle transport from the surface associated phase to the bulk phase(s^{-1})
Λ_{mr}	Dimensionless form of λ_{mr}
λ_r	Coefficient of particle transport from the immobilized phase to the bulk phase(s^{-1})

Λ_r	Dimensionless form of λ_r
λ_{ar}	Coefficient of particle transport from the deposited aggregates to the flowing aggregates(s^{-1})
Λ_{ar}	Dimensionless form of λ_{ar}
λ_{ad}	Coefficient of particle transport from the flowing aggregates to deposition(s^{-1})
Λ_{ad}	Dimensionless form of λ_{ad}
φ	Porosity of the column/porous medium
C_s	Average dimensionless effluent concentration at the steady stage

6 Induced colloid migration for enhanced oil recovery

The study in this chapter proceeds from the previous works on induced migration of reservoir fines and investigates these effects during low salinity waterflooding in a communicating layer-cake reservoir. First, the maximum retention as a function of both the salinity and the velocity of the injected water is introduced [247, 248]. The concepts behind the use of induced fines migration for mobility control are explained. Then the upscaling model for waterflooding in a communicating layer cake reservoir [314, 325] is adapted to incorporate the effects of fines migration. Finally, sample calculations are carried out to investigate such effects on the water saturation profiles, the pressure drop, the water cut at the production well, and the recovery.

6.1 Introduction

Migration colloid particles in oil reservoirs (usually referred to as reservoir fines in the contexts of petroleum engineering) and subsequent permeability decline has been widely observed in core flooding experiments under various conditions [7, 37, 253, 326, 327]. There is a considerable and ongoing effort aimed at understanding the release, the relocation, and the recapture of reservoir fines. It is usually suggested that such phenomena should be avoided due to its detrimental effects on the permeability and pressure drop. Nevertheless, it can also be considered as a mobility control method for improving waterflooding performance. An induced reduction in the effective mobility of water by the migration of reservoir fines in water swept zones may increase the sweep efficiency of water. This process is similar to the mechanisms of other EOR mobility control techniques, such as polymer flooding.

It has been observed in a number of works that the composition of the injected brine influences significantly the release and relocation of the reservoir fines [35, 36, 249]. The release of fines is affected by salinity, pH, temperature, and velocity of the pore water. The effects of water composition on wettability, relative permeability, capillary pressure, and residual oil saturation were investigated, along with the migration of reservoir fines

[36, 249, 328, 329]. The migration of reservoir fines appears to be a separate phenomenon but occurs simultaneously with other effects.

Injection of low salinity water into a saturated core of high salinity has been observed to give rise to significant reduction of permeability owing to the migration and the recapture of clay fines [7, 35, 37, 253, 330, 331]. There exists a critical salt concentration (CSC) below which the clay particles start to release. The release and relocation of the reservoir fines are almost instantaneous. Since water of low salinity is usually readily available, or easy to produce, reducing the salinity of the injected water is likely to be the most practical method to implement mobility control compared to other alternatives controlling the migration of reservoir fines, such as the *pH*, or the temperature of water.

Several models for the release of deposited particles in porous media were proposed on the basis of detachment kinetics[80, 121, 122, 136, 332, 333], while the maximum retention model assumed instantaneous release of particles which are available to detach under the given condition [247, 248]. These kinetics-based models exhibited a delayed response to an abrupt velocity increase or salinity decrease, which disagreed with the almost instantaneous response in the experiments [37, 327, 334]. The maximum retention model, on the other hand, exhibited response without delay [237, 248] and was chosen for the current study.

In the work of Zeinijahromi et al. [247]the maximum retention function was incorporated into the Dietz model for waterflooding in a non-communicating layer-cake reservoir. Initially deposited fines were assumed to be released instantaneously due to the injection of low-salinity water. The released fines might be recaptured via straining at pore throats and cause the reduction of permeability in the water swept zones. Introduction of these effects allowed for the re-definition of the pseudo fraction flow function and led to lower relative mobility of water. The breakthrough time of water was increased while the water cut at the production well was decreased.

6.2 *Induced fines migration by alteration of injected water chemistry*

The balance of the hydrodynamic torque, the lifting torque, the resisting adhesive torque and the torque of gravity determines whether the reservoir fines attaching to the pore walls will be immobilized and re-entrained into the carrying fluid [9, 35, 216, 248, 251]. The erosion number, a dimensionless parameter indicating the ratio between the torques for the detachment and the attachment of particles, can be expressed in the following way:

$$\varepsilon = \frac{F_l l_n + F_d l_d}{\left(F_e + F_g\right) l_n} \tag{6.1}$$

where $F_l, F_d, F_e,$ and F_g are respectively the lifting force, the hydrodynamic drag, the electrostatic force, and the gravity exerting on the particles attached to the pore walls. l_d and l_n are respectively the levers of drag and normal forces. The forces and their moments on the particles attached to the internal cake surface are illustrated in Figure 6.1.

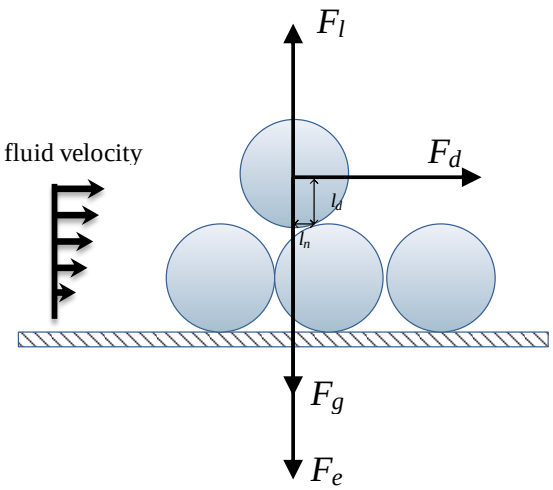

Figure 6.1 Forces and torque balance for the particle attached to the internal cake surface

Particles are released instantly and re-entrained into the carrying fluids if the torque for detachment is larger than that for attachment, i.e. the value of the erosion number is greater than one. It is shown by Bedrikovetsky et al. [248] that the maximum retention is a function of the erosion number:

$$\sigma = \sigma_{cr}\left(\varepsilon\right) \tag{6.2}$$

where σ is the concentration of retained particles (m^3/ m^3). The physical meaning of the maximum retention function can be interpreted as follows. Given a certain setting of injected water chemistry and velocity there exists a maximum retained amount of the particles, above which the excess deposited particles are released. Below the maximum retention the torques from the lifting and the hydrodynamic drag are insufficient to overcome the torques from the electrostatic force and the gravity. The rise of pore water velocity increases the lifting force and the hydrodynamic drag, while the decrease of water salinity reduces the adhesive torque. Consequently, water velocity, salinity, *pH*, temperature and other properties of water chemistry may all be influential on the value of the maximum retention.

It may be assumed that the re-entrained particles are recaptured instantly at the neighboring pore throats via physical straining. The recaptured particles are assumed not to be released due to the change of water chemistry or velocity, since the deposition mechanisms are different from the surface attachment. The total amount of the released particles equals to the sum of the particles captured at pore throats and the effluent ones. In the case of media with thin pore throats, we may assume that all the released particles are instantly re-captured via straining:

$$\sigma_{ini} = \sigma_{cr}\left(\varepsilon\right) + \sigma_{str} \tag{6.3}$$

where the subscripts ‘ini’ represents the amount of deposited particles at the initial condition, and ‘str’ represents straining.

Following Refs. [290, 306, 307], it is assumed that the inverse to normalized permeability k/k_0 is a linear function of retained particle concentration. It is also assumed that the detachment of a particle attaching to the pore walls causes a negligible increase in permeability, while plugging of pore throats via straining causes a significant permeability reduction:

$$\frac{k_0}{k} = 1 + \beta\sigma_{str} \tag{6.4}$$

where k is the permeability, β is the formation damage coefficient. Since the migration of reservoir fines may only occur in the water swept zones, the effects of permeability damage should only be taken into account for water flow. It is therefore reasonable to assume the reduction of the relative permeability of water can be described by a similar expression as Equation (6.4).

The above considerations are sufficient for the inclusion of the induced fines migration and subsequent permeability reduction into a reservoir simulation model. Pore plugging of the released reservoir fines works as a fluid diversion mechanism. The reduction of the permeability in the water swept zones may retard the propagation of water fingers and increase the sweep efficiency. Similar mobility control techniques, such as polymer injection, may be applied to reduce the mobility ratio and decrease the fraction flow of water.

6.3 Upscaling waterflooding in communicating layer-cake reservoirs

The upscaling method proposed in [314, 325] was applied to investigate influence of fines migration on the performance of waterflooding in communicating layer cake reservoirs. The main assumption underlying the upscaling theory is that the gradient of the pressure drop in vertical direction may be set zero due to high anisotropy aspect ratios. As a result, the mass communication between neighboring layers in the vertical direction is instantaneous.

In this work, it is assumed that water is injected into a two dimensional rectangle reservoir from one side to the other at a constant flow rate. The top and bottom of the reservoir is insulated with impermeable boundaries. It is assumed that a stratified reservoir has a span L in the horizontal x direction and a thickness of H in the vertical z direction. The reservoir consists of N communicating horizontal layers. Water is injected

horizontally to displace oil in place. Provided that the water saturation is $s(x,z,t)$, the mass balance equation for water can be written as [316]:

$$\varphi\frac{\partial s}{\partial t}+\frac{\partial f(s)U_x}{\partial x}+\frac{\partial f(s)U_z}{\partial z}=0 \tag{6.5}$$

where φ is the porosity, f is the fractional flow function of water, U_x is the Darcy's velocity in x direction and the U_z is the Darcy's velocity in z direction. The impacts of gravity and capillary forces are neglected. The velocities can be expressed in terms of the pressure gradient according to Darcy's law:

$$U_x=-\lambda_x\frac{\partial p}{\partial x}\ ,\ U_z=-\lambda_z\frac{\partial p}{\partial z} \tag{6.6}$$

where the mobilities λ_x, λ_z and the fractional flow function are:

$$\lambda_x=k_x\left(\frac{k_{rw}}{\mu_w}+\frac{k_{ro}}{\mu_o}\right),\ \lambda_z=k_z\left(\frac{k_{rw}}{\mu_w}+\frac{k_{ro}}{\mu_o}\right),\ f(s)=\frac{k_{rw}/\mu_w}{k_{rw}/\mu_w+k_{ro}/\mu_o} \tag{6.7}$$

where k_{rw} is the relative permeability of water, k_{ro} is the relative permeability of oil, μ_w is the water's viscosity, and μ_o is the oil's viscosity. Here Corey's correlations for relative permeabilities are adopted [335]:

$$k_{rw}=k_{rwor}\left(\frac{s-s_{wi}}{1-s_{or}-s_{wi}}\right)^{\alpha_w},\quad k_{ro}=k_{rowi}\left(\frac{1-s-s_{or}}{1-s_{or}-s_{wi}}\right)^{\alpha_o} \tag{6.8}$$

where s_{or} and s_{wi} are the residual oil saturation and irreducible water saturation, k_{rwor} and k_{rowi} are the relative permeabilities of water and oil at s_{or} and s_{wi}, α_w and α_o are the so-called Corey's exponents for water and oil respectively.

The permeability, porosity, the mobility of each layer may be rescaled as follows:

$$\langle\varphi\rangle=\frac{1}{H}\int_0^H\varphi dz,\quad \Phi=\frac{\varphi}{\langle\varphi\rangle};\quad \langle k_x\rangle=\frac{1}{H}\int_0^H k_x dz,\quad K=\frac{k_x}{\langle k_x\rangle};$$
$$\langle\lambda_x\rangle=\frac{1}{H}\int_0^H\lambda_x dz,\quad \Lambda_x=\frac{\lambda_x}{\lambda_0},\quad \langle\lambda_x\rangle=\frac{\langle\lambda_x\rangle}{\lambda_0},\quad \lambda_0=\frac{\langle k_x\rangle k_{rowi}}{\mu_o};\tag{6.9}$$

The only assumption in the model is that the pressure gradient in vertical direction may be negligible compared to the horizontal pressure drop. Asymptotic analysis resulting in this assumption is carried out in Refs.[314, 325]. Such an assumption gives rise to $\frac{\partial}{\partial z}\left(\frac{\partial p}{\partial x}\right)=0$, which in sequence leads to:

$$\langle U_x\rangle=-\frac{1}{H}\int_0^H\lambda_x\frac{\partial p}{\partial x}dz=-\frac{\partial p}{\partial x}\langle\lambda_x\rangle\tag{6.10}$$

Substitution of the average mobility in the x direction from Equation (6.9) into Equation (6.10) leads to:

$$U_x=\frac{\lambda_x}{\langle\lambda_x\rangle}\langle U_x\rangle\tag{6.11}$$

Due to the assumption of incompressibility of fluids, the mass conservation law for the overall fluid velocity has the form of

$$\frac{\partial U_x}{\partial x}+\frac{\partial U_z}{\partial z}=0\tag{6.12}$$

Substitution of Equation (6.11) into Equation (6.12) leads to the following expression for U_z:

$$U_z=-\int_0^z\frac{\partial U_x}{\partial x}dz=-\langle U_x\rangle\frac{\partial}{\partial x}\left(\frac{\int_0^z\lambda_x dz}{\langle\lambda_x\rangle}\right)\tag{6.13}$$

Finally, substitution of Equations (6.11) and (6.13) back into Equation (6.5) leads to:

$$\varphi\frac{\partial s}{\partial t}+\langle U_x\rangle\frac{\partial}{\partial x}\left(\frac{f\lambda_x}{\langle\lambda_x\rangle}\right)-\langle U_x\rangle\frac{\partial}{\partial z}\left[f\frac{\partial}{\partial x}\left(\frac{\int_0^z\lambda_x dz}{\langle\lambda_x\rangle}\right)\right]=0 \tag{6.14}$$

Equation (6.14) may also take the following dimensionless form:

$$\Phi\frac{\partial s}{\partial T}+\frac{\partial}{\partial X}\left(\frac{f\Lambda_x}{\langle\Lambda_x\rangle}\right)-\frac{\partial}{\partial Z}\left[f\frac{\partial}{\partial X}\left(\frac{\int_0^Z\Lambda_x dZ}{\langle\Lambda_x\rangle}\right)\right]=0 \tag{6.15}$$

where the dimensionless variables are adopted from (6.14):

$$\Phi=\frac{\varphi}{\langle\varphi\rangle},\quad X=\frac{x}{L},\quad Z=\frac{z}{H},\quad T=\frac{t}{\langle\varphi\rangle L/\langle U_x\rangle} \tag{6.16}$$

Equation (6.15) is a two-dimensional partial integro-differential equation involving multiple integral operators. Solving such an equation usually requires intensive computational efforts. The 2-D equation can be converted into a series of equations, each of which represents the mass balance in a layer. The system of equations takes the following form (the details are given in Ref. [314, 315]):

$$\Phi_i\frac{\partial s_i}{\partial T}-\frac{\partial}{\partial X}\left(f_i\frac{B_i-B_{i-1}}{\Delta Z_i B_N}\right)+\frac{1}{\Delta Z_i}\left[G_{i-1}\frac{\partial}{\partial X}\left(\frac{B_{i-1}}{B_N}\right)-G_i\frac{\partial}{\partial X}\left(\frac{B_i}{B_N}\right)\right]=0 \tag{6.17}$$

where indices i and j represent the ith layer. B_i and G_i are expressed as:

$$\begin{aligned}&G_i=f_i\left[\frac{\partial}{\partial X}\left(\frac{B_i}{B_N}\right)<0\right]+f_{i+1}\left[\frac{\partial}{\partial X}\left(\frac{B_i}{B_N}\right)>0\right],\quad i\in[1,N-1]\\&G_N=0,\quad B_i=\sum_j^i\Delta Z_j\Lambda_j\end{aligned} \tag{6.18}$$

Here the result of logic operators $[\circ]$ is one if expression $\circ$ is true, and zero if it is false. The injection boundary condition is 1-s_{or} corresponding to the maximum water saturation while the initial condition is s_{wi}. For model calculations below we assume that the residual saturations are the same for all the layers.

6.4 Maximum attached concentration

In this section, the expression of the maximum retention (attachment) for a cylinder capillary is introduced. The underlying torque balance analysis follows Ref. [248]. Similar approach was utilized for estimation of external filter cake thickness in the fractured and open-hole wells [295, 336]. The porous space is assumed to be a bunch of parallel rectangular pores with the Hele-Shaw flow occurring between the walls [337]. Porosity and permeability can be expressed via the pore opening (width) W and pore concentration n [338]:

$$\varphi = nW^2; \quad k_0 = \frac{nW^4}{8\pi} \tag{6.19}$$

It allows for the calculation of pore opening and concentration for known porosity and permeability:

$$W = \sqrt{\frac{8\pi k_0}{\varphi}}; \quad n = \frac{\varphi^2}{8\pi k_0} \tag{6.20}$$

Following Ref. [248], the balance between the torques of the hydrodynamic drag, the lifting force, gravity/buoyancy and the electrostatic force can be expressed as:

$$F_e + \frac{4}{3}\pi r_s^3 \Delta\rho g - \chi r_s^3 \sqrt{\frac{\rho_w \mu_w U^3}{\varphi^3 \left(W - 2h_c\right)^3}} = \frac{l_d}{l_n} \frac{\omega \pi \mu_w r_s^2 U}{\varphi\left(W - 2h_c\right)} \tag{6.21}$$

where F_e is maximum value of electrostatic DLVO force , r_s is the particle radius, $\Delta\rho$ is the density difference between the solid particle and water, χ is the correction coefficient for the lifting force, h_c is the height of internal cake, ω is the correction coefficient for hydrodynamic drag. The lever ratio for the drag force to the normal force $l_d / l_n = \sqrt{3}$.

Introducing a new dimensionless variable:

$$y = \frac{\mu_w r_s^2 U}{\varphi H \left(1 - 2h_c / W\right) F_e} \tag{6.22}$$

leads to the following form of the previous equation:

$$1+\frac{4\pi r_s^3}{3F_e}\Delta\rho g-\frac{\chi\sqrt{\rho_w F_e}}{\mu_w}y^{\frac{3}{2}}=\sqrt{3}\omega\pi y \tag{6.23}$$

For the rectangular shape of pores, the critical retention concentration is calculated via the properties of the internal cake:

$$\sigma_{cr}=\left[W^2-\left(W-h_c\right)^2\right]\left(1-\varphi_c\right)n \tag{6.24}$$

Substitution of the W^2 in Equation (6.19) into (6.24) leads to:

$$\sigma_{cr}=\left[1-\left(1-\frac{h_c}{W}\right)^2\right]\left(1-\varphi_c\right)\varphi \tag{6.25}$$

Let us express the equilibrium cake thickness via y from Equation (6.22):

$$\frac{h_c}{W}=\frac{1}{2}-\frac{\mu_w r_s^2 U}{2y\varphi W F_e} \tag{6.26}$$

Substitution of Equation (6.26) into Equation (6.25) leads to the final expression of the critical retention concentration:

$$\sigma_{cr}=\left[1-\left(\frac{\mu_w r_s^2 U}{\varphi W F_e y}\right)^2\right]\left(1-\varphi_c\right)\varphi \tag{6.27}$$

The root y of cubic equation (6.23) is independent of velocity U. Thus, Equation (6.23) provides with quadratic polynomial form of the critical retention function $\sigma_{cr}(U)$.

By assuming that the reservoir fines are only released in the water swept zones, and that the porous medium is water wetted, the hydrodynamic dragging force on the fines are only from the water phase. Equation (6.27) can be rewritten as:

$$\sigma_{cr} = \left[1 - \left(\frac{\mu_w r_s^2 U f(s)}{\varphi W F_e y}\right)^2\right](1-\varphi_c)\varphi \tag{6.28}$$

6.5 Adaptation of waterflood model to fines migration

In this section, the maximum retention model for fines migration is incorporated in the upscaling model for waterflooding in communicating layer-cake reservoirs. Both reduction of the permeability due to pore plugging and the subsequent diversion of fluids flow across different layers are taken into account.

Migration of fines causing the reduction of the permeability in the vertical direction is neglected, since perfect communication between the reservoir layers is assumed in this work. The maximum retention model [248] is developed in the framework of single water phase flow. The application of such a model for the waterflooding in an oil reservoir requires more considerations for the spatial distribution of the two immiscible phases. In a water-wet porous medium, due to the capillary pressure and the median wettability, water is inclined to flow along the pore walls, around median grain constrictions and in the smaller pores [339-342]. Under such assumptions the flow of water causing the hydrodynamic drag can be expressed via the fraction of the total flow rate:

$$v_w = \frac{f(s)U}{\varphi s} \tag{6.29}$$

where v_w is the pore velocity of the water phase, U is the total Darcy's velocity, $f(s)$ is the fraction flow of water, φ is the porosity, and s is the water saturation. More detailed considerations for the particle and pore size distributions are possible, while it is beyond the scope of the current work (see Chapters 2 and 3 and Refs. [104, 105, 136, 156, 158] for the distributed flow modeling). Equation (6.29) serves as a simplified assumption. It is also assumed that the presence of small amount of residual oil does not change the process of particle release significantly and can be neglected. This assumption probably needs further refinement in the future work (see experimental evidence from [331]). With

this modification, the expression of the erosion number in Equation (6.1) may be rewritten as (detailed derivations can be found in Section 6.4):

$$\varepsilon = \frac{\mu_w r_s^2 f(s) U}{s\sqrt{k\varphi} F_n} \tag{6.30}$$

where μ_w is the viscosity of water, r_s is the particle radius, and F_n is the normal force exerting on the particles (lifting force, gravity, and electrostatic force). With the consideration of Equation (6.4), the total mobility in the *i*th layer and the fraction flow of water can be written as:

$$\lambda_{xi} = \left(\frac{\lambda_{rwi}}{1+\beta\sigma_{str}} + \lambda_{roi} \right), \quad f_i = \frac{\lambda_{rwi}/(1+\beta\sigma_{str})}{\lambda_{rwi}/(1+\beta\sigma_{str}) + \lambda_{roi}}; \tag{6.31}$$

where λ_x is the horizontal mobility, λ_{rw} and λ_{ro} are the relative mobility of water and oil, index '*i*' represents the *i*th horizontal reservoir layer.

The adapted waterflooding model assumes that the salt (NaCl) behaves as a neutral additive in the reservoir, namely the influence of salt concentration on water viscosity and the adsorption/desorption of salt on pore surface are ignored. It is assumed that the salt in the connate water before the displacement front is immobile and that the dispersion/diffusion of salt is negligible. Such assumptions can ensure that the low-salinity front travels at the same velocity as the water front [316, 343]. The ratio between the tracer and water front velocities usually ranges from 1:1.1 to 1:1.4 in practice which justifies the above assumptions [247, 302]. The model also assumes that the change in the composition of the injected water due to mixing with the connate water is negligible. As a result, the alteration of salinity and consequent permeability decline occurs instantly after the water front passes a given point of the reservoir, leading to Equation (6.31). The above assumptions also allow us to reduce the equation for the mass balance of salt.

Due to the assumption of instant straining of all released particles, the concentration of strained particles is equal to the initial deposition minus the maximum retention. The

maximum retention is dependent on the local velocity of water, which leads to the dependence of strained retention on water velocity:

$$\sigma_{str} = \sigma_{ini} - \sigma_{cr}\left(\frac{\mu_w r_s^2 f(s) U_i}{s\sqrt{k_x \varphi} F_n}\right) \tag{6.32}$$

With the help of Equation (6.11) and Equation (6.13), the norm of the total velocity can be expressed as:

$$U = \sqrt{U_x^2 + U_z^2} = \langle U_x \rangle \sqrt{\left(\frac{\Lambda_x}{\langle \Lambda_x \rangle}\right)^2 + \left[\frac{\partial}{\partial X}\left(\frac{\int_0^Z \Lambda_x dZ}{\langle \Lambda_x \rangle}\right)\right]^2} \tag{6.33}$$

The velocity of water in the *i*th layer can be further transformed by taking into account of Equation (6.17):

$$U_i = \langle U_x \rangle \sqrt{\left(\frac{B_i - B_{i-1}}{\Delta Z_i B_N}\right)^2 + \left[\frac{\partial}{\partial X}\left(\frac{B_i}{B_N}\right)\right]^2} \tag{6.34}$$

Similar to the models for fines migration in non-communicating layer-cake reservoirs [247], the model in this work is also indicative only. The model focuses on the effects of fines migration in the communicating layer-cake reservoirs specifically. Injection of low salinity water is only one example to induce the migration of reservoir fines, while other alternatives may also result in fines migration, such as *pH*. The model does not take into account other effects of the injection of low salinity water, such as the alteration of capillary pressure, residual oil saturation, and pore size distribution [123, 158, 326, 327].The proposed model, under the assumption of constant residual oil saturation, may underestimate the benefit of low salinity water injection in a communicating layer cake reservoir.

One key assumption of this model is that the hydrodynamic drag from the fluid is assumed to be only from the water phase. As a result, the maximum retention function is dependent on the water saturation. Such an assumption is reasonable for completely water-wetted rocks where water flows along pore surface and around constrictions. For

partially wetted or oil-wetted rocks where the wetted pore surface also depends on water saturation, the current model can be extended to account for the available fines for release depending on water saturation. Such effects are currently beyond the scope of this study.

6.6 Results and discussions

In this section, sample calculations are carried out to investigate the effects of fines migration on the water saturation profiles, the pressure drop, the water cut at the production well, and the recovery for a given flow rate.

It is assumed that a reservoir consisting of 30 horizontal layers is flooded with water of low salinity into one side, and oil is produced on the other side. The top and the bottom of the reservoir are insulated with impermeable boundaries. The horizontal permeabilities of different layers are assumed to follow a discrete log-normal distribution. The mean value and the standard deviation of the logarithm of dimensionless permeability are 1.0 and 0.1 respectively. The minimum of the dimensionless permeability is set to be 0.5, and the maximum is selected in such a way that the mean dimensionless permeability $\langle K \rangle = 1.0$. The following properties of fluids are adopted: s_{wi}=0.1, s_{or}=0.3, μ_w=1cP, μ_o=2cP, α_w=2, α_o=2, k_{rwor}=0.8, k_{rowi}=0.4. For the calculations of the maximum retention, the properties of sandstones are taken from the laboratory tests of low salinity waterflooding [34]: the average porosity φ=0.1, the average permeability $\langle k_x \rangle = 100m\text{D}$. The initial deposition $\sigma_{ini} = 0.01$(volume fraction). The radius of the deposited particles $r_s = 1\mu\text{m}$, the density of the particle material $\rho_p = 2\times10^3 \text{kg/m}^3$, the maximum electrostatic force $F_e = 4\times10^{-11}\text{N}$, the lifting coefficient $\chi = 89.5$, the coefficient for hydrodynamic drag $\omega = 60$, the internal cake porosity $\varphi_c = 0.5$. Details of the calculation for the maximum retention can be found in Section 6.4.

6.6.1 Effects of formation damage

Calculations are carried out with different values of the formation damage coefficient β. Previous study on low-salinity waterflooding [34, 247] are taken into account to select the values of β. Water saturation profiles at dimensionless time T=0.1 (measured in porous volumes injected) are revealed at the top, the horizontal center, and the bottom of the reservoir in Figure 6.2.

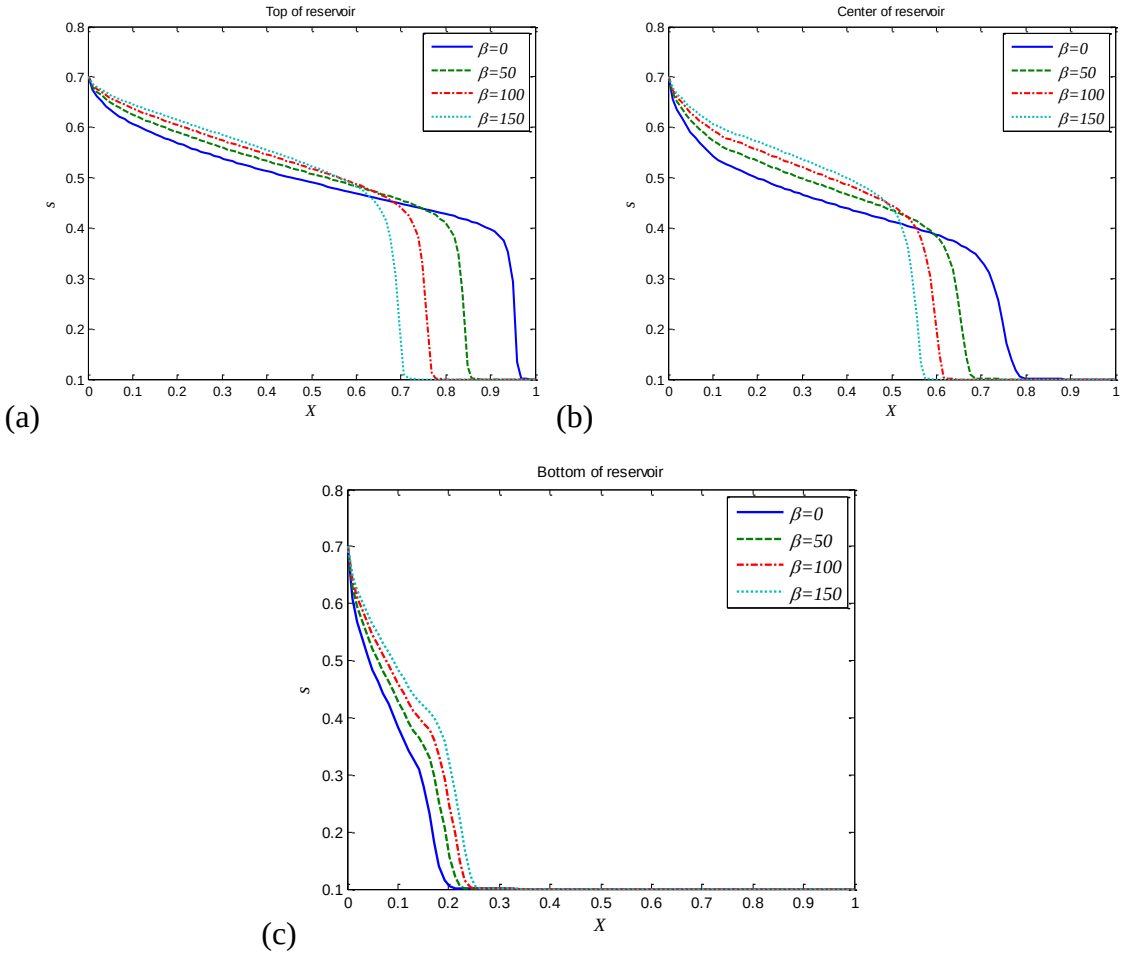

Figure 6.2 Water saturation profiles at the top of the reservoir (a), in the center of the reservoir (b), and at the bottom of the reservoir (c).

With larger values of the formation damage coefficient, the displacement fronts in the more permeable layers are more retarded, as seen in Figure 6.2 (a) and (b). The displacement front in the least permeable layer is accelerated, as seen in Figure 6.2 (c). The averaged water saturation profiles (ξ=X/T) are revealed in Figure 6.3. It can be seen larger formation damage gives rise to more even displacement profiles. The water

saturation profiles at T=0.1 in the X-Z plane are revealed in particular for β=0 and β=150 in Figure 6.4. The displacement fronts are clearly retarded in the more permeable layers (close to top), and accelerated in the less permeable layers (close to bottom).

Such phenomena are resulted from the fluid diversion mechanism in connection with the migration of reservoir fines. In water swept zones the reservoir fines in place are released due to the change of water chemistry. The released fines are instantly captured at the neighboring pore throats and reduce the relative permeability of water subsequently. As a result, water flow is diverted from more permeable layers to the less permeable layers.

Water cut at the producer and the recovery factor are then calculated and plotted in Figure 6.5. It can be seen that the breakthrough of water is delayed with larger values of the formation damage coefficient. After the first breakthrough of water in the most permeable layers, the breakthrough in the less permeable layers occurs and corresponds to the transition points ("corner points" in Figure 6.5 (a)). The breakthrough in the less permeable layers is earlier with larger values of β. As a result, the current recovery is increased due to less water flow at the production site.

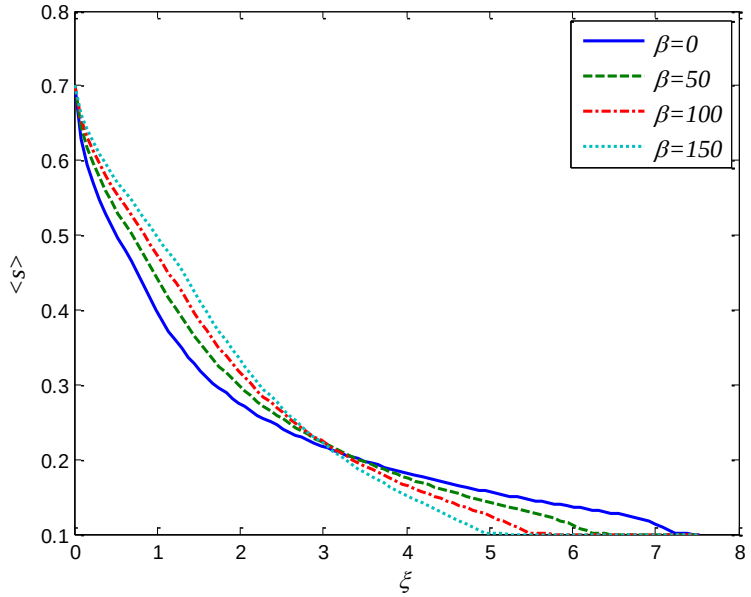

Figure 6.3 Averaged water saturation profiles (ξ=X/T) resulted from different values of M

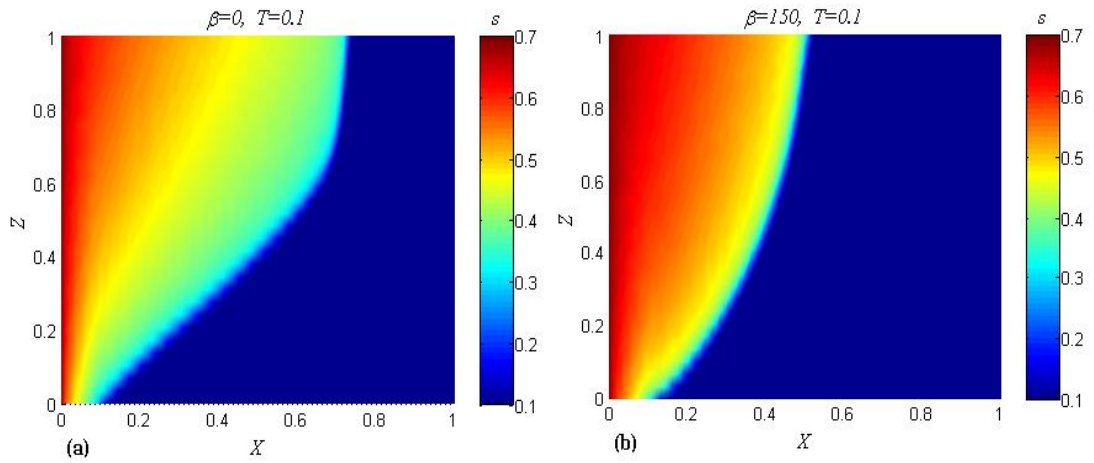

Figure 6.4 Water saturation profiles in the *X*-*Z* plane: (a). *β*=0; (b). *β*=150;

The pressure drop between the injector and the producer, corresponding to a constant overall flow rate, is calculated and revealed in Figure 6.6. It can be seen that the pressure drop decreases more slowly with more formation damage caused by the migration of reservoir fines. After β exceeds a certain value (approximately β =120), the pressure drop becomes a non-monotonous function of time. It indicates that more energy is required due to the formation damage to maintain a constant flow rate.

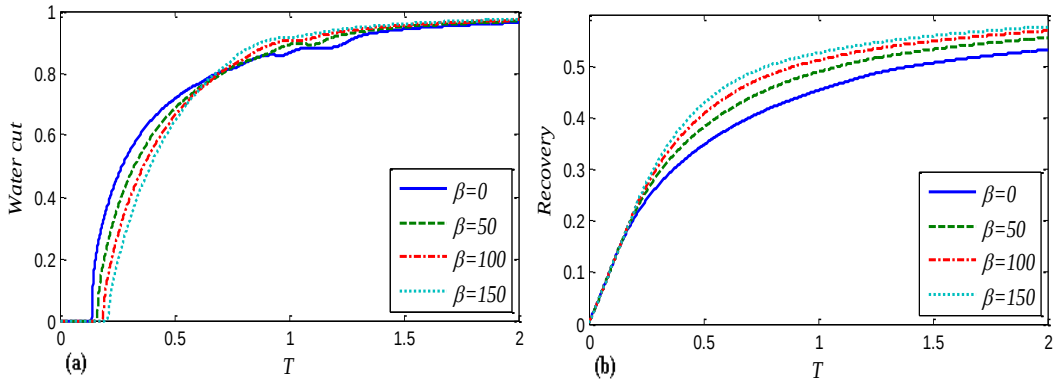

Figure 6.5 Compare formation damage coefficients: (a). Water cut at the production site; (b). Recovery factor

The water saturation profiles indicate that the induced migration of reservoir fines is in favor of increasing water sweep efficiency. The resulting water cut and the recovery show that such phenomena may improve the waterflooding performance for oil production. Nevertheless, more energy is required to increase the pressure drop and maintain a constant flow rate.

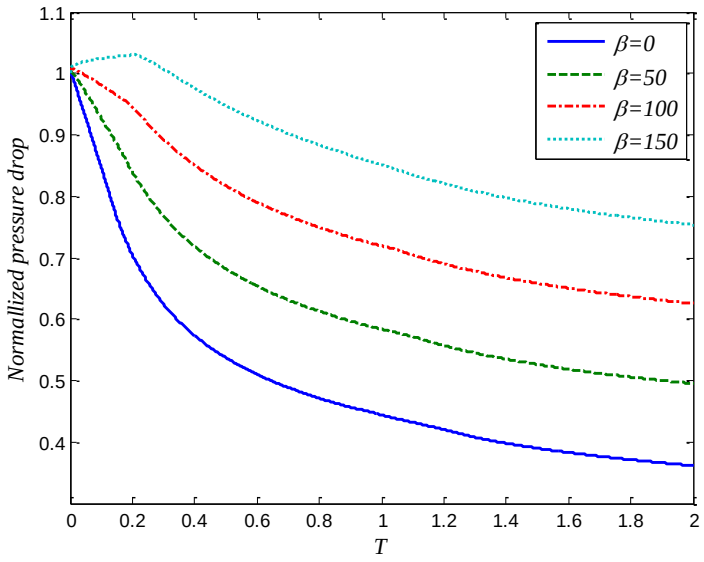

Figure 6.6 Pressure drop between the injector and the producer

6.6.2 Effects of mobility ratios and crossflow

Calculations are carried out with different values of the end-point mobility ratio $M=\left(k_{rwor}\mu_o\right)/\left(k_{rowi}\mu_w\right)$. For the calculations of normal waterflooding $\beta=0$, for the calculations of low salinity waterflooding $\beta=50$. The viscosity ratio of water and oil is modified to obtain the different values of the mobility ratio M.

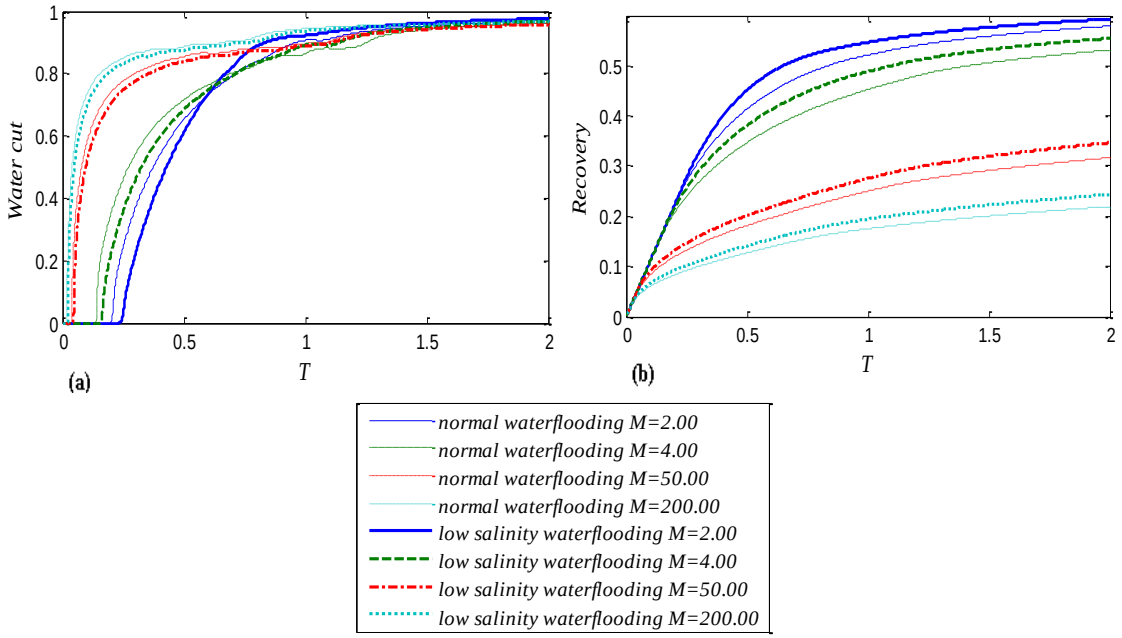

Figure 6.7 Compare mobility ratios: (a). Water cut at the production site; (b). Recovery factor

Figure 6.7 shows that low salinity waterflooding delays the breakthrough of water and increases the oil recovery for all the values of *M*. Larger mobility ratios, on the other hand, result in earlier breakthrough and lower oil recovery. The increased oil recovery due to migration of reservoir fines is larger with larger values of *M*, as seen in Figure 6.8 (a). In the range of high mobility ratios, the increased oil recovery is much less sensitive to the mobility ratio, as seen in Figure 6.8 (b). It seems that the positive contribution from the mobility ratio to the increased oil recovery due to fines migration is limited. Such phenomena may be explained by the enhanced effects of corssflow due to larger water-oil mobility ratios.

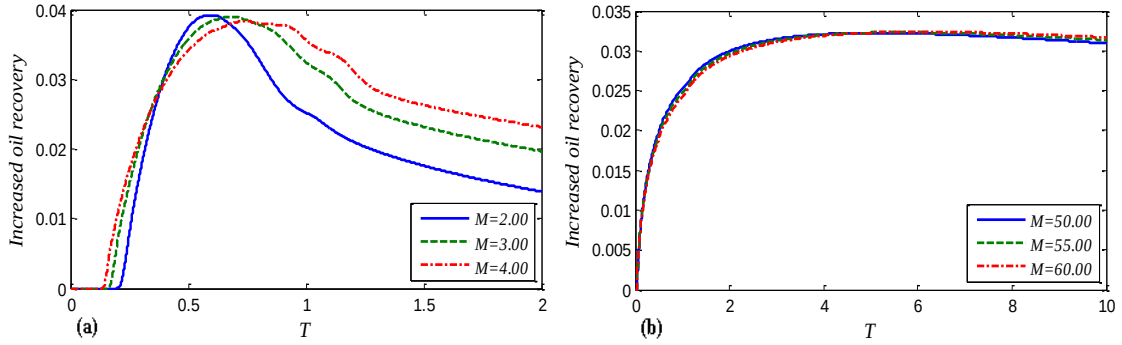

Figure 6.8 Increased recovery due to migration of fines (low salinity waterflooding) with different mobility ratios

A theoretical study of cross-flow in communicating layer cake reservoirs has been carried out in Ref.[315]. Since no fines migration is considered in this theoretical study, details are not presented in this thesis. The essential explanation of the effect of the mobility ratio *M* on the crossflow are drawn from the study [315]: Equation (6.13) indicates that the driving force of crossflow is the difference of the horizontal gradients of accumulated mobility in different layers. The horizontal mobility gradient can be rewritten as a function of the mobility derivative with regard to water saturation, as seen below.

$$\frac{\partial \Lambda_x}{\partial X} = \frac{d\Lambda_x}{ds}\frac{\partial s}{\partial X}$$
$$\frac{d\Lambda_x}{ds} = K\left[\alpha_o \frac{(1-s-s_{or})^{\alpha_o-1}}{(1-s_{or}-s_{wi})^{\alpha_o}} + \frac{M}{1+\beta\sigma_{str}}\alpha_w \frac{(s-s_{wi})^{\alpha_w-1}}{(1-s_{or}-s_{wi})^{\alpha_w}}\right]; \quad (6.35)$$

The values of $d\Lambda_X/ds$ are larger with larger values of *M*. $\partial\Lambda_X/\partial X$ is more sensitive to $\partial s/\partial X$ with larger *M*. As a result, the crossflow between layers is enhanced with larger

values of the mobility ratio. It may facilitate the fluid diversion between layers caused by fines migration.

6.7 Summary of Chapter 6

In this chapter, the effect of fines migration induced by injection of low salinity water has been incorporated into the upscaling model for waterflooding in a communicating layer cake reservoir. The torque balance on the deposited reservoir fines via attachment, the straining of released fines, the consequent permeability damage, and the cross-flow between layers have been taken into account.

Particle release and re-deposition give rise to the reduction of the permeability in water swept zones, which subsequently leads to the diversion of water flow from the more permeable layers to the less permeable ones. As a result, the water cut at the producer is decreased, and the oil recovery is increased. However, more energy for the pressure drop is required to maintain a constant flow rate. Modeling results have shown that higher formation damage coefficients (more permeability damage) give rise to later breakthrough of water, lower water cut, higher oil recovery, and higher pressure drop to maintain a constant flow rate.

In a communicating layer cake reservoir, higher end-point mobility ratio M (water to oil) leads to more crossflow and lowers the water sweep efficiency. However, the effect of fluids diversion caused by fines migration is stronger in this case. The increased oil recovery due to fines migration increases with the mobility ratio in the range of low mobility ratios (2~4), while it is insensitive to the mobility ratio in the range of high mobility ratios (>50). The positive contribution from the mobility ratio to the increased oil recovery due to fines migration seems to be limited. Thus, the enhanced oil recovery method, low salinity water flooding causing the migration of fines, is more efficient with larger mobility ratio in communicating layer-cake reservoirs.

6.8 Nomenclature of Chapter 6

F	Forces exerting on fines attached to pore surface
H	Height of reservoir
L	Length of reservoir
k	Absolute permeability
M	End-point mobility ratio of water to oil
N	Number of layers
s	Water saturation
t	Time
T	Dimensionless time/ pore volume injected
U	Darcy's velocity
x	Coordinate in the horizontal direction
X	Dimensionless x
z	Coordinate in the vertical direction
Z	Dimensionless z
f	Fractional flow of water
r	radius
W	pore opening width
h	height
n	pore concentration
l	lever
g	gravity acceleration
φ	Porosity
Φ	Dimensionless porosity
α	Corey's exponent
β	Formation damage coefficient
χ	Correction coefficient for the lifting force
ω	Correction coefficient for hydrodynamic drag
σ	Retention/concentration of deposited particles
ε	Erosion number
ξ	X/T

Subscripts

i	ith layer of reservoir
o	Oil
or	Residual oil
w	Water
wi	Irreducible Water
r	relative
x	Direction along a reservoir
z	Direction orthogonal to a reservoir
0	Reference variables
s	particles/fines
p	pores

c	internal cake
d	hydrodynamic drag
n	normal
l	lifting
e	electrostatic
g	gravity
cr	critical
str	straining
ini	initial

7 Estimating filtration coefficients for straining

7.1 Introduction

The fundamental filtration theory has been focused on the transport of colloids at different scales: the interface scale, the collector (median grain) scale, and the pore scale. A number of mathematical models for the attachment rate of colloidal particles have been reviewed and discussed in Chapters 1 and 2. On the other hand, the rate of size exclusion and straining of particles was mainly studied at pore scale in the traditional size exclusion theory [81, 82, 114, 121, 344]. The particles could be captured wherever they meet the smaller pores. The random walk of particles was assumed to follow flow-biased probabilities. Such a theory was realized in the network model with random walking particles and used to match the permeability damage data over hundreds of pore volume injected [345]. Nevertheless, little attention was paid to the capture rate during short term injections (negligible formation damage).

$$\frac{\partial \sigma}{\partial t} = \lambda U_a c \tag{7.1}$$

The filtration coefficient is usually defined as the proportionality coefficient between the particle capture rate and the particle flux [95], as in Equation (1). Here σ is the number of retained particles in unit volume of porous media, U_a is the Darcy's velocity through accessible pores, and $\underline{c}$ is the number of suspended particles per unit pore volume. For size exclusion and straining the filtration coefficient may vary with time and space due to the change of pore size distributions. The coefficient can be treated as a constant under the assumptions of dilute suspension and short time injection.

Given the pore size and the particle size distributions, the average exclusion rate was estimated from population balance approaches [156, 158, 229] . It has been proven in [229] that the population balance approach for monodisperse suspension flows in porous media with distributed pore sizes is mathematically equivalent to the classical deep bed filtration model. This treatment of the size exclusion experiments was successfully applied to fit the challenge testing data from dilute suspension flows in randomly packed glass beads with little permeability damage. The population balance approach involved

the characteristic distance l, treated as an adjustable parameter of the model. This distance was interpreted as a distance between "mixing chambers" connected by a system of parallel capillaries [346]. This visualization was shown to be equivalent to the population balance model.

An assumption about constancy of l and its independence of the particle size may be valid for narrow particle size distributions far above the percolation threshold. However, in many natural and industrial processes the particle size distributions may be rather wide [1, 114, 347]. Also, for accurate reconstruction of the pore size distribution on the basis of the particle injection experiments it is required to inject particles of the largely different sizes [348]. For particle sizes close to and below the percolation threshold, the model may overestimate the penetration depths of particles. A puzzling observation of these experiments was that the effective value of l fitted to the experimental data was much larger than the characteristic pore sizes [346]. This indicated the presence of a specific correlation length in a porous medium, which much exceeded the pore sizes. A new stochastic approach to size exclusion filtration, explaining all the observations above, is desirable. In this Chapter, we apply percolation theory and the network modeling in order to analyze the penetration depths of the particles.

Percolation theory is a branch of probability theory for predicting the properties of random media [349, 350]. It is closely tied to the network modeling of transport in porous media and often used to predict medium properties [235, 316, 350-354]. A network model describes a detailed geometry structure of porous media and the physics of pore-scale events. The percolation theory and network models are usually complimentary. The network models yield insight into the effects of pore scale physics while the percolation theory sheds light on effects of randomness on macroscopic properties [351].

Network models have been applied to describe suspension flow in porous media with size exclusion [160, 345]. The random walk theory was used to determine the paths of particles in the network. The authors mainly focused on the permeability damage of the medium and the percolation behavior of the conductivity.

In the study of this chapter, laboratory challenge tests are carried out under unfavorable attachment conditions, so that size exclusion or straining is the only particle capture mechanism. The experimental results show that far above the percolation threshold the filtration coefficients are not proportional to the average flux through the pores smaller than the particles but power functions of them. The experimental penetration depths of particles can be over thousands of pores even if the particle size is larger the average pore size. This cannot be explained by the traditional size exclusion theory or the model of parallel tubes with mixing chambers. A special capture mechanism has been proposed, which makes it possible to explain the experimentally observed power law dependencies of filtration coefficients and large penetration depths of particles. Such a capture mechanism is realized in a 2D pore network model with periodical boundaries and the random walk of particles on the percolation lattice. Geometries of infinite and finite clusters formed by pores of the sizes exceeding the particle size are analyzed with regard to the possibility for particle capture. Two power laws are proposed to describe the filtration coefficients from the network model and one of them is used to match experimental challenge data.

7.2 Challenge testing experiments

In this section, the unfavorable attachment experimental conditions and the subsequent absence of particle retention due to attachment are established by tests in a simplified one-grain-layer engineered porous media. Then the laboratory tests for the flow of colloidal suspensions through glass-bead-packed porous media with size exclusion are carried out. The characteristic particle sizes are smaller than the pore sizes, so that the experiments are carried out away from the percolation threshold.

7.3 Unfavorable attachment conditions

Unfavorable attachment experimental conditions are crucial to ensure straining or size exclusion thin pores to be the only particle capture mechanism. Such experimental

conditions are determined both theoretically and experimentally in a preliminary study [1, 298, 346]. The theoretical study serves as a guideline for the subsequent experimental confirmation of the unfavorable attachment conditions. In the preliminary experimental study, a micro model unit that provides the visual observation of colloidal suspension flow through porous media is designed and constructed. It allows determination and confirmation of such solution compositions that the DLVO forces between the colloids and the medium are repulsive.

7.3.1 DLVO study on unfavorable attachment conditions

In the theoretical study, the interaction energy between the two surfaces is calculated as the sum of the electrical double-layer interaction and the van der Waals interaction energies [1, 298]:

$$\Phi_{total} = \Phi_{dl} + \Phi_{vdW}, \tag{7.2}$$

where Φ_{total} Φ_{dl} and Φ_{vdW} are the total, the double-layer, and the van der Waals interaction energies respectively. The expressions for the electrical double-layer interaction energy are available for varying geometries and different assumptions [1, 44]. The widely adopted expression for Φ_{dl} is based on the sphere-sphere interactions [1]:

$$\Phi_{dl} = 64\pi r_s \left(\frac{k_B T}{ze}\right) \tanh\left(\frac{ze\psi_1}{kT}\right) \tanh\left(\frac{ze\psi_2}{kT}\right) \exp\left(-\frac{h}{L_D}\right), \tag{7.3}$$

where k_B is the Boltzmann constant, T is the temperature, z is the valence of the ions, e is the elementary charge, h is the separation distance between two surfaces, ψ is the surface potential, and the subscripts '1' and '2' represent the surfaces of colloid and median grains, respectively. The Debye length L_D is calculated by:

$$L_D = \sqrt{\frac{\varepsilon\varepsilon_0 k_B T}{2e^2 N_A I}} \tag{7.4}$$

where ε is the dielectric constant, ε_0 is the vacuum permittivity, and I is the ionic strength.

The classical approach to evaluate the van der Waals interaction between two bodies is derived by Hamaker [137] from the pairwise summation of all the relevant interaction energies. The expressions stemming from this approach can be split into the product of a purely geometric multiplier and of the so-called Hamaker constant. The total Hamaker constant of the different bodies is typically estimated by the geometrical mean value of the individual Hamaker constants [138]. For colloid-water-glass interactions, Φ_{vdW} can be calculated by [56]:

$$\Phi_{vdW} = \frac{A_{123}}{6h} r_s \left(1 + \frac{14h}{\lambda_w}\right)^{-1} \tag{7.5}$$

where λ_w is the characteristic wavelength, usually 100 nm [56].

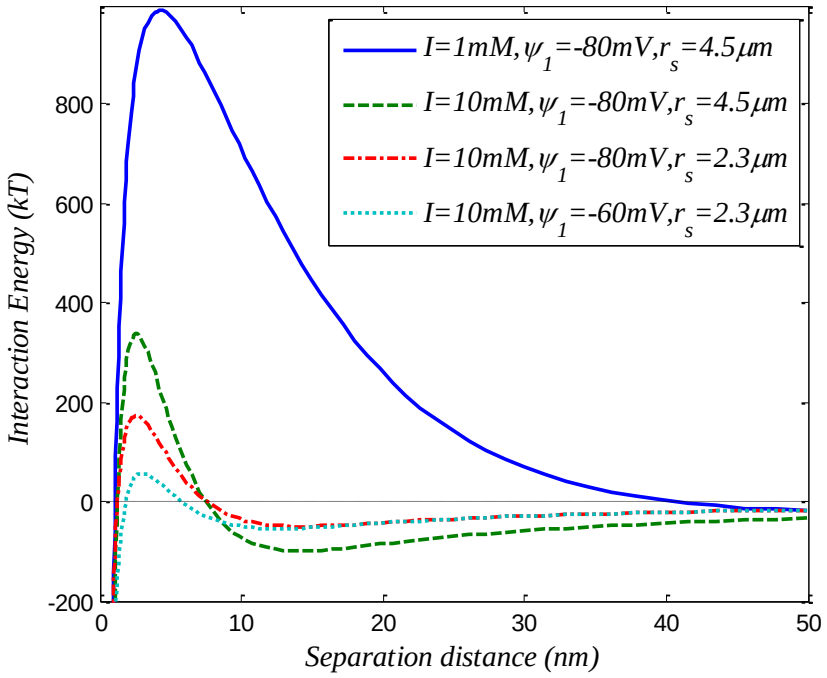

Figure 7.1 Sample calculations of DLVO interactions for colloid-glass-bead

Sample calculations are carried out with different ionic strengths, particle sizes, and zeta potentials. In the following experimental study, packed glass beads are adopted as the porous medium and fluorescent carboxyl latex microspheres are used in preparing the colloidal suspensions. Typical values of the Hamaker constants and surface potentials for such a system are adopted in the sample calculation: $A_{123} = 10^{-20} J$, $\psi_2 = -50mV$,

$\varepsilon = 78.4, T = 298K$. It can be seen in Figure 7.1 that lower salinity (ionic strengths), larger particle sizes, and a more negatively charged surface lead to more repulsion between colloids and collectors. From these conclusions, lower salinity and higher *pH* are suggested to achieve a more unfavorable attachment condition. Attachment via secondary energy minimum should be also avoided, even though the attached particles may migrate to the straining-favored sites due to hydrodynamic drag [112, 135, 136].

7.3.2 Experimental study on unfavorable attachment conditions

In the preliminary experimental study, a colloidal suspension of spherical, fluorescent carboxyl latex microspheres is forced to flow through an engineered porous medium. The yellow-green ($r_s = 4.5\mu m$) fluorescent latex microspheres (Polysciences Inc., Warrington, PA) are selected as the colloidal particles held in suspensions. The surfaces of these colloids are grafted with carboxyl functionalized groups by the manufacturer. It creates a negatively charged hydrophilic colloidal surface possessing a net negative charge in an alkaline solution. The net charge of the surface prevents agglomeration of colloids and reduces electrostatic attraction to the median grains. The colloid concentration is kept constant at 20 ppm in all the preliminary tests, while the injection volume is 3mL.

A single layer of sieved and cleaned spherical glass beads (Ballotini Bead, Potters Industries Pty. Ltd., Australia) is adopted as a 2D porous medium (thickness 600 μm). The main component of the porous medium, silica (SiO2), has a net negative surface charge in alkaline solutions (SiO_4^{4-}). The glass beads possess the following compositions: 72.0% SiO_2, 15.0% Na_2O, 7.0% CaO, 4.2% MgO, 0.4% Fe_2O_3 and 0.3% Al_2O_3.These glass beads (radius: $300\mu m$) are packed homogeneously with an estimated porosity of 39.6%.

In order to examine the attachment and straining of colloids in the medium, the micro model housings are designed to support the observation under an optical microscope. The housings are milled out of polyvinyl chloride (PVC) plastic and are designed in such a way that two glass slides are held in place to contain the medium in a single layer. The

deionised ultrapure MilliQ water (resistivity of 18.2 MOhm×cm at 25 °C) after degassing in vacuum at pressure ≈ 10^{-2} Pa is used for the preparation of a colloidal suspension. The salinity, and the *pH* of the suspensions are adjusted with the addition of NaCl(aq), HCl(aq) and NaOH(aq), respectively. The retained concentration is calculated by counting the number of glowing particles per unit area with the optical microscope. The attachment and straining of particles are distinguished by visual observation. Lower salinities and higher *pH* values are observed to create more repulsive conditions.

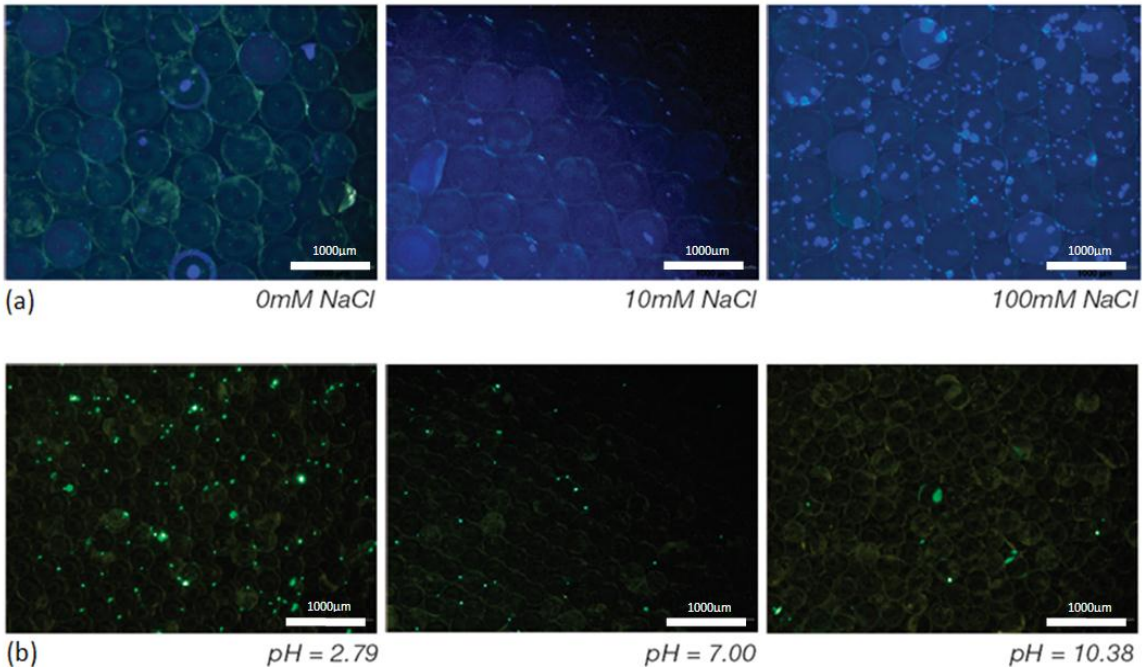

Figure 7.2 Images of particles strained in porous media [346]: (a) different salinities and (b) different *pH* levels

The surface impurities will also carry a negative charge at *pH*=10.4, since it is near or above the isoelectric point of any metal oxides found on the glass bead surface. At such a high *pH*, both the carboxyl latex and the glass bead surfaces are completely deprotonated. Such unfavorable attachment conditions can be confirmed in Figure 7.2. In order to minimize the colloid attachment in further tests, the solutions with high *pH* and zero salinity are employed so that the physical straining would dominate. Long time of washing is carried out to avoid attached particles via secondary energy minima.

Under such unfavorable attachment conditions (high *pH* and low salinity), according to Figure 7.1 and Figure 7.2, there is net repulsion between the colloid and collector

surfaces. Similar repulsive conditions have been visually confirmed under microscopes in [346].

7.4 Challenge testing procedures

Under the unfavorable attachment conditions determined by the preliminary study, a 3D column of porous medium is set up for challenge tests (diameter: 47*mm*, length: 50*mm*). Before the inlet of the column an additional homogenized section is installed to ensure a uniform boundary condition and a plug flow. A 30 μm sized stainless steel mesh and distribution plates are utilized to support the medium within the column.

Table 7.1 Particle sizes used for challenge tests

Type	1	2	3	4	5	6	7
$<r_s>$, μm	0.89	1.03	1.57	2.18	2.84	3.17	4.54

Mono-disperse suspensions of yellow-green fluorescent polystyrene latex microspheres of different sizes are applied in the following experiments, as seen in Table 7.1. The glass beads are sieved twice to constrain the grain sizes within the pore sizes of two sieves. The medium is numbered by its two grain size thresholds as: lower threshold/ upper threshold. For example, Medium 40/63 has a lower grain size threshold of 40 μm and an upper threshold of 63 μm. Sonic baths are applied to achieve dense packing. The grain size distribution is measured by a Malvern Mastersizer.

A complete washing procedure is then performed to remove residual organic impurities with acetone, hexane, and hydrochloric acid. Suspension solutions are prepared with 0.1 M sodium hydroxide and degassed ultrapure MilliQ water to achieve a *pH* of 10.4. The column is placed vertically and connected to a syringe piston pump (New Era-1000) to force a steady state bottom-up flow at the velocity of 10^{-5} m/s. Before colloid injection, 5 pore volumes of solution are injected to ensure a clean initial condition.

Low colloidal concentrations (8 ppm) and low colloid injection time (5-10 p.v.i.) are employed to ensure negligible variation of pore size distributions. It can be validated by

comparing the maximum retained concentration to the pore concentration [346]. The effluence is sent through the PAMAS S4031 GO portable particle counter to determine the effluent particle concentration. The effluent concentration is monitored until it reaches the steady state. Multiple times of measurements are carried out to examine the experimental uncertainties.

7.5 Experimental results and discussions

7.5.1 Treatment of experimental data

The normalized effluent concentrations at the steady state C_e from above tests are listed in Table 7.2. The decrease of effluent concentrations with the increase of particle sizes is observed. The filtration coefficient can be calculated by $\lambda = -\ln(C_e)/L_0$, where L_0 is the column length. The average penetration depth of particles is calculated as $L = 1/\lambda$.

It is worth mentioning that the effluent concentration from large particles is close to zero. Due to the noise from the solution some measurements may even be below zero. The value listed in the table is an average value of a number of measurements over a long period. Short columns may be applied to achieve a higher effluence, while it may also introduce uncertainties from low randomness.

Table 7.2 Normalized effluent concentrations from challenge tests, '-' for not tested

$<r_s>$ (μm)	Medium 30/125	Medium 63/90	Medium 40/63
0.89	-	-	0.9930
1.03	-	0.9910	0.9880
1.57	0.9680	-	0.9690
2.18	0.7990	0.9060	0.7190
2.84	0.5810	0.5200	0.6823
3.17	0.1221	0.1970	0.0700
4.54	0.0003	0.0030	0.00007

The breakthrough time of particles of different sizes is listed in Table 7.3. It can be seen that the breakthrough time decreases with particle sizes in all tests. It can be explained by the by-passing of larger particles in accessible larger pores. The average velocity in the accessible pores is larger for larger particles.

Table 7.3 Breakthrough time (pore volume injected) of particles in challenge tests, '-' for not tested

$<r_s>$ (μm)	Medium 30/125	Medium 63/90	Medium 40/63
0.89	-	-	0.75
1.03	-	0.61	0.62
1.57	0.70	-	0.52
2.18	0.62	0.54	0.48
2.84	0.46	0.54	0.45
3.17	0.53	0.41	0.41
4.54	0.11	0.11	0.25

A Monte Carlo procedure with Latin-Hypercube Sampling (LHS) method is applied to determine the pore size distribution from the measured grain size distribution. Compact packing of grains (three interconnected grains form one pore throat) is assumed in the procedure. The cross-sections of pore throats are assumed to be triangular to determine the pore size from grain sizes more accurately [355, 356]. Details of the procedure can be found in Ref [346]. Such a procedure is able to take into account the uncertainties of experimental packing with a large population of grains. The mean values and standard deviations of the pore size are estimated by fitting the continuous lognormal PSD to the discrete PSD resulted from the Monte-Carlo simulations. They can be found in Table 7.4. High degree of matching is observed. Such a method for evaluating PSD has been validated with literature data in Ref [346].

Table 7.4 Pore size distributions evaluated from grain size distributions with Monte-Carlo simulations

PSD properties	Medium 30/125	Medium 63/90	Medium 40/63
Mean (μm)	5.30	5.78	4.27
Standard deviation (μm)	0.81	0.88	0.67
Mean/ Standard deviation	6.54	6.57	6.37

7.5.2 Fundamental statistical parameters

In the filtration processes with size exclusion as the particle capture mechanism, only the larger pores can let through the injected particles. The first key parameter to be introduced here is the fraction of larger pores f_l, the size of which is larger than the injected particles. In terms of the pore size distribution $f(r_p)$:

$$f_l(r_s) = \int_{r_s}^{\infty} f(r_p)\, dr_p \tag{7.6}$$

The passing probability for the particles is dependent on the conductivities of the pores. If the Poiseuille law for flow resistance in a single capillary is assumed, the average probability of particle random walk through larger pores as the probability of conducting particle flow is:

$$f_l^*(r_s) = \frac{\int_{r_s}^{\infty} r_p^4 f(r_p)\, dr_p}{\int_0^{\infty} r_p^4 f(r_p)\, dr_p} \tag{7.7}$$

The distribution of pores of different sizes is usually assumed to be random. The particle conductivity is effectively zero below the percolation threshold [350, 357]. For the bond percolation, the values of these parameters at the percolation threshold can be calculated as [316, 350]:

$$f_c = \frac{D}{N_c(D-1)} \qquad f_c = \int_{r_{sc}}^{\infty} f(r_p)\, dr_p \tag{7.8}$$

$$f_c^*(r_s) = \frac{\int_{r_{sc}}^{\infty} r_p^4 f(r_p)\, dr_p}{\int_0^{\infty} r_p^4 f(r_p)\, dr_p} \tag{7.9}$$

where f_c is the percolation threshold in the conventional percolation theory, f_c^* is the flow biased percolation threshold, r_{sc} is the particle radius at the threshold, D is the lattice dimension, and N_c is the coordination number of the lattice. For 2D lattice pore network, the percolation threshold f_c is 0.5.

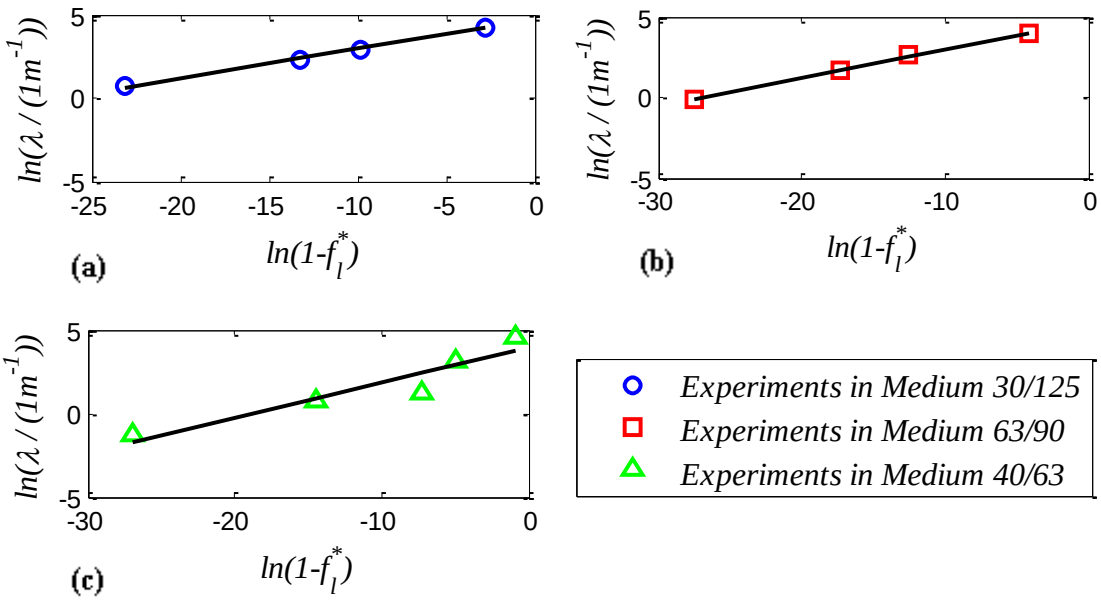

Figure 7.3 Experimental filtration coefficients and correlation lengths from laboratory challenge testing data; (a): Medium 30/125; (b): Medium 63/90; (c): Medium 40/63;

7.5.3 Contradiction with traditional theories

The filtration coefficients and the fraction of flux through smaller pores $(1-f_l^*)$ from experiments are plotted in logarithm scales, as seen in Figure 7.3. Each point in the plot corresponds to the filtration coefficient with the given porous medium and a particle size. The data of particle sizes, pore size distributions, and filtration coefficients can be found in Table 7.1, Table 7.2, and Table 7.4. Clear straight lines in the figures imply power law relations between the filtration coefficients and the average capture probability. The estimated slopes and intercepts are listed in Table 7.5. Hence, an empirical relation between the filtration coefficient and the fraction of flux through the pores smaller than the particles can be drawn:

$$\lambda \propto \left(1-f_l^*\right)^{\beta} \tag{7.10}$$

Table 7.5 Exponents (slopes) estimated from the experimental filtration coefficients in logarithm scales

	Medium 30/125	Medium 63/90	Medium 40/63
β (experiments)	0.18	0.18	0.21
intercepts	4.69	4.73	3.95

None of the estimated slopes is equal to one $(\beta \neq 1)$. This indicates that the filtration coefficients are not proportional to the fraction of flux through the pores exceeding the particle size, but power-law functions of it. Such an observation contradicts the traditional size exclusion theory which will be explained in the next section. It also contradicts the size exclusion model of parallel tubes with mixing chambers[156, 158]. In both models, the filtration coefficient becomes proportional to the fraction of flux through the pores smaller than the particles far above the percolation threshold.

The average fractions of flux through the pores smaller than the particles are calculated with the given pore size distributions for the three sets of experiments, as seen in Figure 7.4. It can be seen that these fractions for the largest particles in the experiments are very close to one. On the other hand the experimental penetration depths of the largest particles can still be over thousands of pores, as seen in Figure 7.5. Under the assumption that the particles can probably be captured wherever they meet the smaller pores, the probability of such large particles traveling over such a large number of pores is minimal. These observations contradict the traditional size exclusion theories [344, 345, 358], which are developed under an assumption that a particle may be captured at each step with a certain probability, and the step size is comparable to the characteristic pore size.

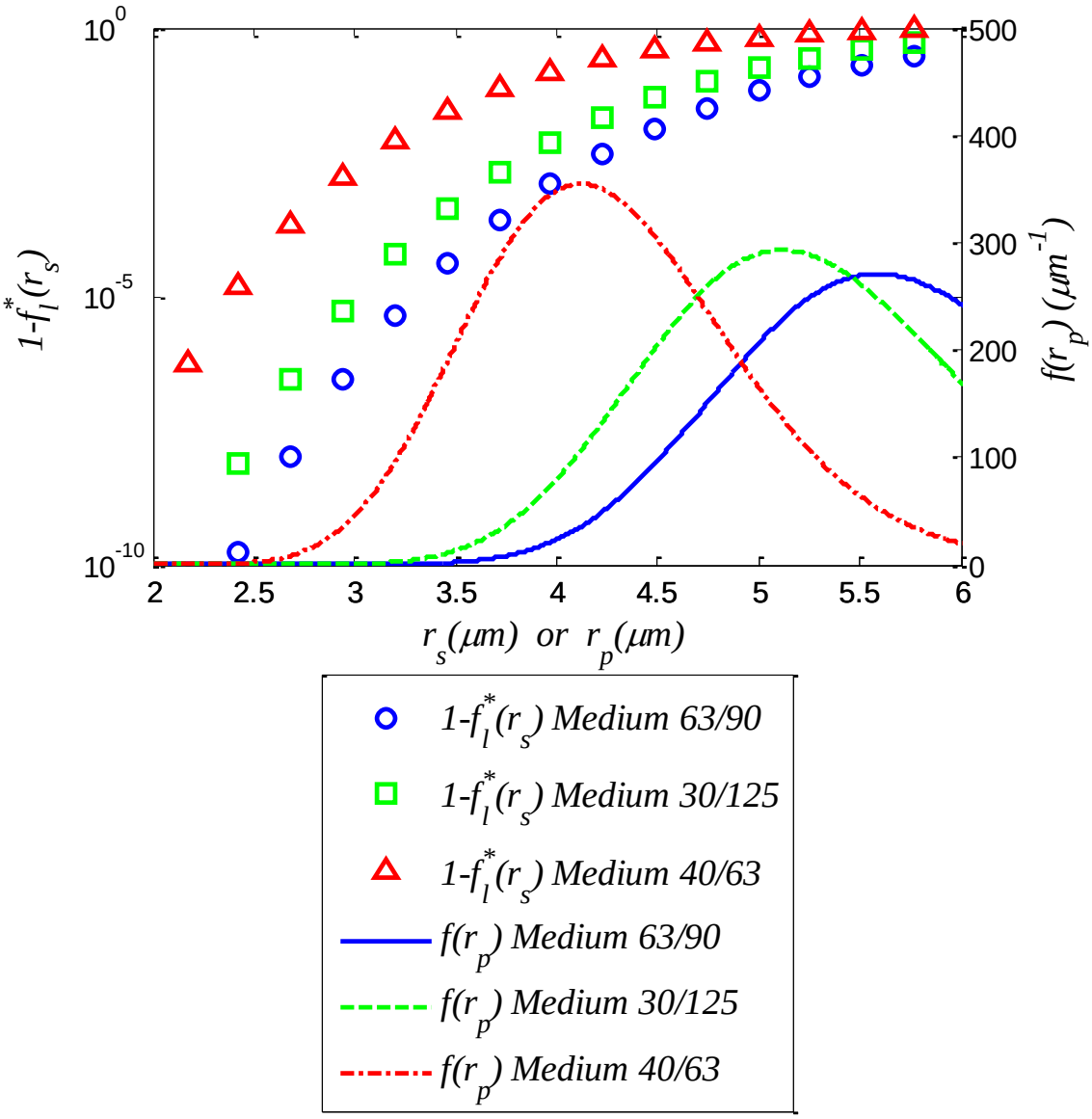

Figure 7.4 Fraction of flux through the pores smaller than the particles and pore size distributions in the experiments

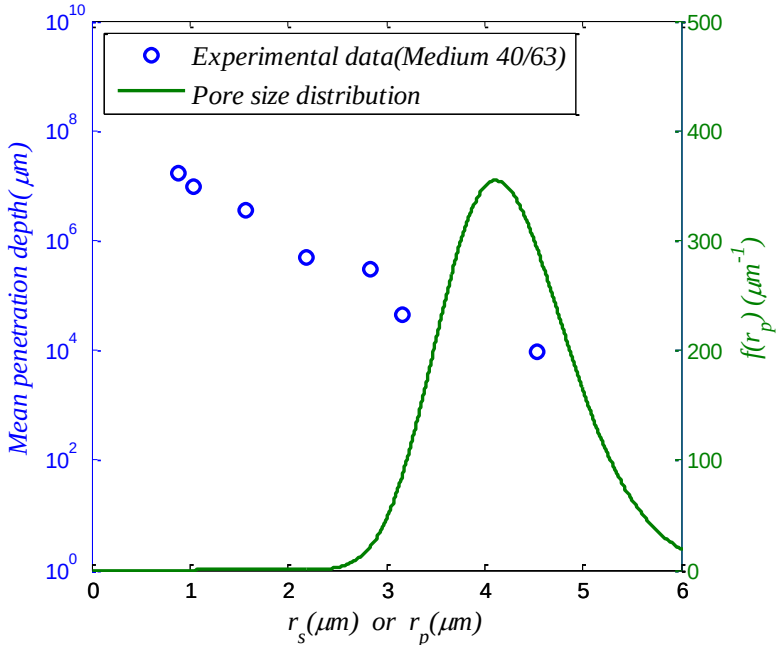

Figure 7.5 Average penetration depths and pore size distributions in the experiment with Medium 40/63

This contradiction is studied below, in the framework of the network modeling with the different particle capture strategies.

7.6 Random walk and network modeling

In this section, a 2D network model for a random porous medium is described. The random paths of injected particles in the network are determined by the random walks. The trial particles are injected into the network to determine the effluence probability and the filtration coefficient. A special capture mechanism is proposed to predict the minimum particle capture probability. It aims at explaining the power law dependency of filtration coefficients on the particle sizes, and the large penetration depths of particles.

7.6.1 Pore network model

A two-dimensional network model with interconnected capillaries is adopted to represent a random porous medium. Periodic boundary conditions are applied to avoid surface effects. The minimum distance between the inlet and the outlet of the medium is L_0. The

radii of capillaries follow a lognormal distribution while the lengths of capillaries are constant. The capillaries are randomly placed in the plane and form a square lattice system with the coordination number z=4. The number of nodes in the 2D network varies from 100×100 to 500×500.

The conductivity of each capillary is determined by its radius. Ignoring the effects of capillary intersections, the flow in each capillary is calculated from the Poiseuille law:

$$k_1 = \frac{\pi r_p^4}{8} \tag{7.11}$$

$$q_1 = \frac{k_1}{\mu}\frac{\Delta p_1}{l} \tag{7.12}$$

where k_1 is the permeability of a capillary, r_p is its radius, q_1 is the flow in the capillary, Δp_1 is the applied pressure difference, and l is the length of the capillary. According to mass conservation, the flows through the four capillaries attached to a vertex follow the Kirchhoff rule:

$$\mathbf{q}_1 + \mathbf{q}_2 + \mathbf{q}_3 + \mathbf{q}_4 = \mathbf{0} \tag{7.13}$$

Constant pressures are applied at the inlet and the outlet vertices of the network. The pressures at the inner vertices can be found by solving system of equations (13) for each vertex and applying the boundary conditions for pressure. With the solution for pressures, the detailed flow field in the network is determined by Equation (12).

7.6.2 Random walks

A number of trial spherical particles of the same radius r_s are sent into the pore network and randomly walk until being captured or arriving at the outlet. In our simulations the particles walk independently and the collective behavior like bridging is not considered. This assumption is valid for dilute suspensions, at short injection times and interactions between particles and walls excluding the attachment. Such conditions are adopted in the experiment described above. At each site a particle "selects" one of the bonds (capillaries) to be passed next. A particle may either pass through a bond or be captured in it. The

passing time is not counted, only the capture probability. Two capture schemes are adopted in the simulations, referred to as the maximum and the minimum capture scheme.

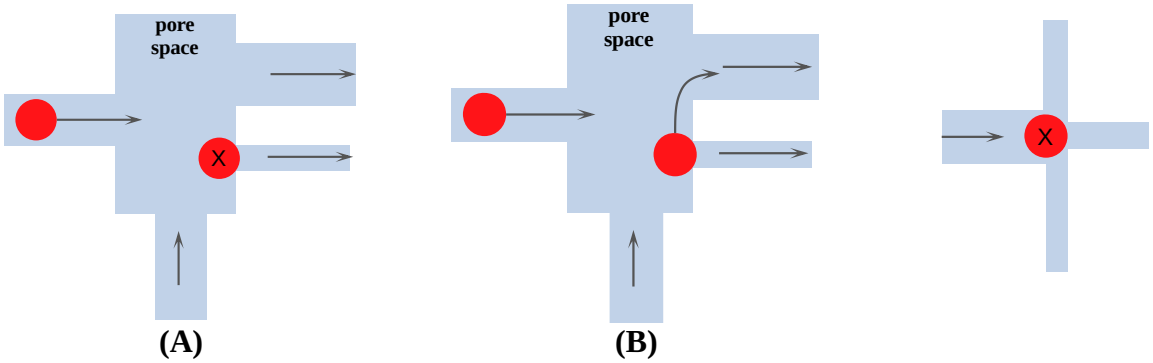

Figure 7.6 (A) Maximum capture scheme (B) Minimum capture scheme (captured particles are marked with 'X')

7.6.2.1 Maximum capture scheme

In the maximum capture scheme, a particle walks randomly on the lattice and can be captured whenever it walks through a smaller pore. It is the same assumption as in the traditional size exclusion theory [345]. The walking direction of the particles is flow-biased. The particle cannot jump against the flow direction, as seen in Figure 7.6 (A). When a particle arrives at node *i*, the rules of the random walk along the neighboring capillaries are as follows:

1) A neighboring capillary is not viable, if the flow in it is toward node *i*.
2) The probability of choosing a jump direction from viable capillaries is distributed in accordance to the flows in them.
3) If the particle selects a capillary with a smaller radius, it is captured.

7.6.2.2 Minimum capture scheme

In the minimum capture scheme, a particle cannot be captured as long as there is a capillary with a larger radius and exiting flow, as seen in Figure 7.6. When a particle arrives at node *i*, the rules of selecting the next step are as follows:

1) A neighboring capillary is not viable, if the flow in it is toward node *i*.
2) A neighboring capillary is not viable, if its size is smaller than the particle.
3) The probability of choosing a jump direction from viable capillaries is distributed in accordance to the flows in them.
4) If a particle does not have a viable capillary to jump through, it is captured at node *i*.

In both capture schemes, the probability of a particle leaving a node via the viable capillary *j* is calculated as:

$$p_j = q_j / \sum q_{k,viable} \tag{7.14}$$

Particles are injected to the network one by one, while the dynamic effects of pore plugging are neglected for different injected particles. In other words, if a particle plugs a capillary the flow field remains the same and the pore is viable for the next particle test. Such a setting aims at obtaining the statistically reliable results from the identical independent particle random walk. The dynamic effects of pore plugging are beyond the scope of this study.

7.7 Numerical modeling implementation

The system of algebraic equations (11) to (13) was solved numerically. Since most elements of the coefficient matrix are zero, a linear solver for sparse systems was applied for fast solution of the system in MATLAB. Mass conservation was checked by calculating the gradient of the total flux along the injection direction. In other words, flow through each cross-section along the injection direction must be constant.

Since the pore plugging and subsequent permeability damage are neglected, the random walks of particles were treated as identical independent events. Only one particle randomly walks on the lattice each time. Such configurations aim at the statistical estimation of the capture probability of size exclusion for dilute suspensions. Two particles may plug the same node in two separate random walks. Also independent walks of the different particles make it possible to apply the parallel computation for the

simulation. For our computations 12 CPUs were applied in parallel. In order to increase the accuracy of the statistical analysis, the number of injected particles was 10^5. Hence the accuracy for the computation of the normalized effluence concentration may be down to 10^{-4}.

7.8 Network filtration coefficients

In the numerical experiments, the pore size distributions are the same as in the challenge test above (Medium 40/63). The size of the network is 500×500 nodes. The positions of the captured particles are recorded. Statistical analysis is carried out to reveal the deposition profiles of different particle sizes, as seen in Figure 7.7 (A). Exponential deposition profiles are observed. A filtration coefficient is therefore suitable to characterize the particle capture rate and the average penetration depth.

The relation between the filtration coefficient λ and the normalized effluent concentration C_e at steady state can be found from the analytical solution of the advection dispersion equation for filtration [98, 298]: $\lambda = -\ln(C_e)/L_0$.

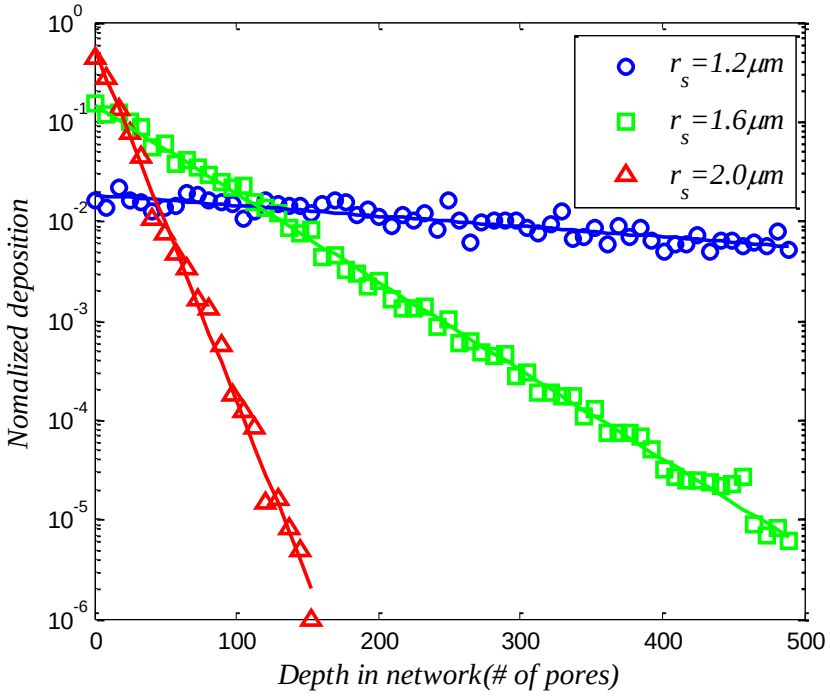

(A)

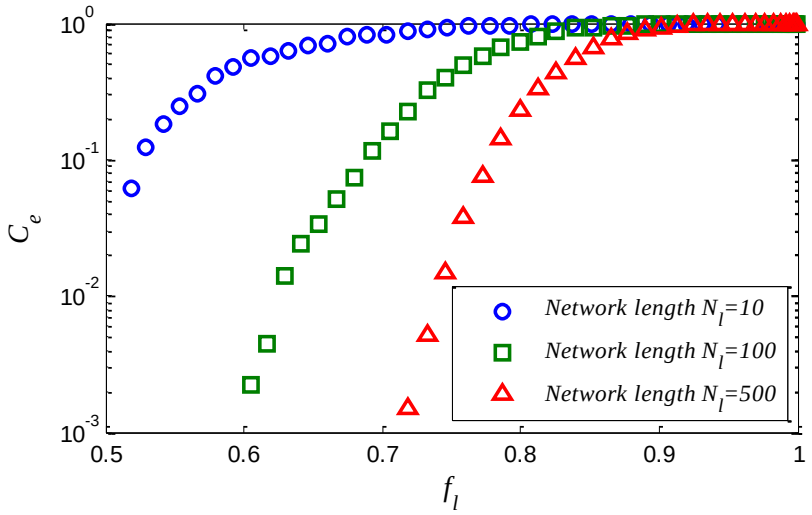

(B)

Figure 7.7 (A) Effluence probability in networks of various sizes (B) Deposition profiles of different particle sizes

A more related property to the pore network is the average capture probability per pore λ_l:

$$\lambda_l = \lambda l = -\frac{\ln(C_e)}{N_l} \tag{7.15}$$

where $N_l = L_0 / l$ is the minimum number of pores connecting the inlet and the outlet. We refer to λ_l as the network filtration coefficient. In the case of undetectable effluent concentrations (extremely large particles), the deposition profiles can be an alternative for estimating the filtration coefficients. In the classical filtration theory the average penetration depth of particles is found as $L = \lambda^{-1}$. Similar to (7.15), a scale-independent property, the average number of pores penetrated by the particles, is

$$L_l = \frac{L}{l} = \frac{1}{\lambda_l} \tag{7.16}$$

We may refer to L_l as the average network penetration depth.

7.9 Modeling results and discussion

7.9.1 Preliminary study

With the same pore size distribution, particles of different sizes (different f_l values) are adopted in the maximum and minimum capture schemes. The effluent probability in the networks of different sizes can be plotted against the fraction of larger pores. For example, Figure 7.7 (B) exhibits the effluent concentrations with f_l corresponding to the minimum capture scheme.

Below the percolation threshold (equal to 0.5 for the square lattice) the larger pores form only finite clusters. The probability of the penetration depth to be larger than the medium length is effectively zero.

$$\begin{cases} (\lambda_l)^{-1} = 0, & f_l < f_c \\ (\lambda_l)^{-1} > 0, & f_l > f_c \end{cases} \tag{7.17}$$

Since the effluent concentration is an exponential function of the product of the filtration coefficient and the medium length (Equation (15)), in order to have a detectable effluence (both experimentally and numerically) this product needs to be small enough. Close to the percolation threshold, the filtration coefficient is extremely large. Hence, the medium length or network size needs to be small to produce detectable effluence. As seen in Figure 7.7 (B), the effluent concentrations in larger network systems may rapidly approach zero even above the percolation threshold.

7.9.2 Penetration depths and power law dependencies

The resulting penetration depths (in numbers of pores) from the two capture schemes are calculated with the pore size distribution of Medium 40/63, as seen in Figure 7.8 (A). It can be seen that the minimum capture scheme predicts the penetration depths that are several orders of magnitude larger than those computed for the maximum capture scheme.

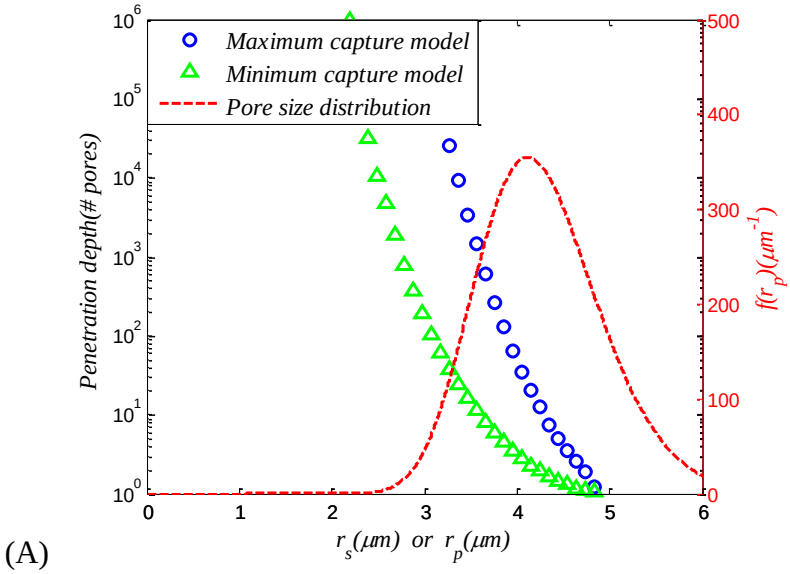

(A)

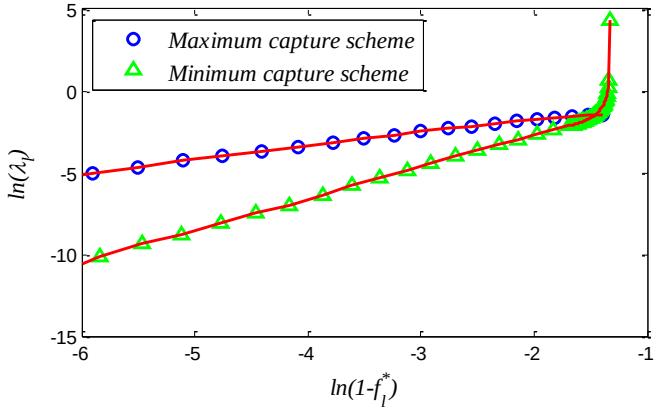

(B)

Figure 7.8 (A) Penetration depths from two capture schemes (B) Filtration coefficients in logarithm scales from two capture schemes

The predicted penetration depths from the network model are not comparable with the experimental results. The difference between the exponents from the network model and from the experiments can be mainly attributed to the difference in the number of dimensions. It has been widely observed that the exponents characterizing the cluster properties in the percolation theory are far different in 2D and 3D structures [235, 350]. The other reason for the difference may be due to the different coordination numbers in experiments and the network. As a consequence of the low number of dimensions and the low coordination number, the network model underestimates the connectivity of large pores and penetration depths compared to the 3D experiments (see the experimental data in Figure 7.5 and network results in Figure 7.8 (A)). Nevertheless, the large difference between the predictions for the two capture schemes indicates that the large penetration

depths in the experiments may be explained by the minimum capture scheme, or, at least, by a combination of the two schemes.

The filtration coefficients for the two capture schemes are plotted against the fraction of flux through the pores smaller than the particles $(1-f_l^*)$ on the logarithmic scale, as seen in Figure 7.8 (B). The straight lines indicate that far above the percolation threshold ($\ln(1-f_l^*)\to-\infty$), the filtration coefficients are power law functions of the fraction of flux through smaller pores. It should be noted that the range for $\ln(1-f_l^*)$ from -6 to -2 covers most of the pore radii above the percolation threshold, since $f_l^* \sim r_p^4$. The corresponding probability f_l varies from 0.65 to 0.97.

Table 7.6 Exponents (slopes) estimated from the network filtration coefficients in logarithm scales

	Medium 30/125	Medium 63/90	Medium 40/63
β (maximum capture scheme)	0.9907	0.9898	0.9945
β (minimum capture scheme)	1.9986	1.9735	1.9808

The exponents of the power laws, listed in Table 7.6, are estimated from the slopes of the dependences. All the exponents for the maximum capture scheme are very close to unity. This indicates that in the maximum capture scheme the filtration coefficient is proportional to the fraction of flux through smaller pores. On the other hand, the minimum capture scheme results in exponents other than one. For this scheme the filtration coefficient is a nontrivial function of f_l^*.

In the traditional size exclusion theory (based on the maximum capture scheme) the filtration coefficients are proportional to the flux through the pores smaller than the particles. The proportionality of filtration coefficients to the flux is also an intrinsic assumption in the model of parallel tubes with mixing chambers regardless of the percolation behavior. While the first approach cannot predict deep penetration of the particles, as shown above, the second approach uses a characteristic correlation length *l* (distance between the chambers) as an adjustable parameter. Hence, neither the traditional size exclusion theory nor the model of parallel tubes with mixing chambers

can explain the experimentally observed power law dependencies of the filtration coefficients. Out of the approaches considered in this study, only the minimum capture scheme may be applied to predict such type of dependences. The reasons for that are analyzed below.

7.9.3 Percolation analysis

In the bond percolation theory, capillaries with the radii larger than those of the injected particles are deemed as active bonds. The connected active bonds form clusters. If the injected particles are larger than all the capillaries, all the bonds are inactive. With the decrease of particle size, more and more bonds become active and form finite clusters. In accordance with the percolation theory, only after the fraction of active bonds exceeds the percolation threshold form the infinite clusters, namely the viable pathways for particles to pass through the entire medium. The infinite clusters comprise of the long "backbones" connecting the inlet and the outlet and short "whiskers" with dangling ends surrounded by the inactive bonds [235, 350].

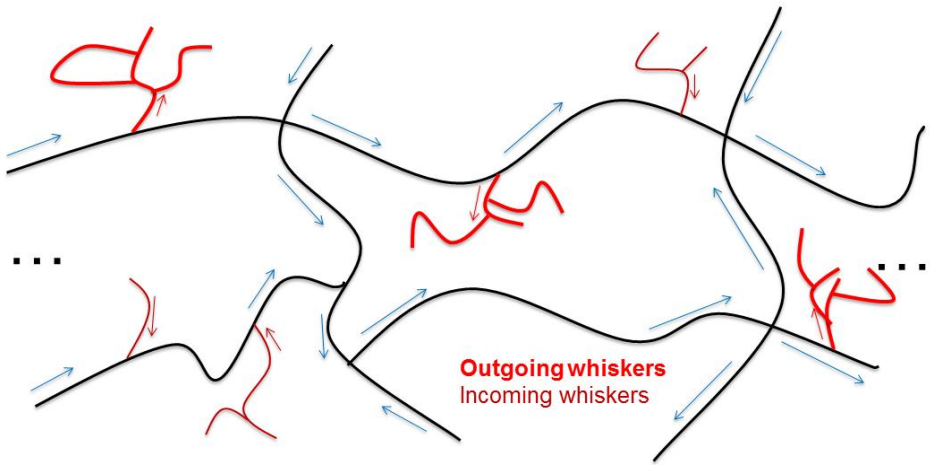

Figure 7.9 Illustrations of the dangling ends and the distance between the whiskers with exiting flow in the infinite cluster. Arrows indicate flux directions, red represents whiskers, and black represents backbones of the infinite cluster.

In the minimum capture scheme, only the particles flowing through the backbones of infinite clusters can pass through the medium, while those through the whiskers are to be captured at the dangling ends. Unlike the common percolation theory, we count the flows

with the directions. Thus, a particle cannot be captured in all the whiskers, but only in those where the flow exits from the infinite cluster, as seen in Figure 7.9.

The particle flow can be assumed to be proportional to the fraction of fluid flow only through backbones (particles flowing through whiskers are to be captured eventually). This fraction may be estimated by [358, 359]:

$$B = 2 f_l^* - f_{\text{inf}}^* - 2\sqrt{f_l^* \left(f_l^* - f_{\text{inf}}^* \right)} \tag{7.18}$$

where f_{inf}^* is the fraction of flow through infinite clusters, and B is the fraction of flow through the backbones of the infinite clusters. Close to the percolation threshold the flux through finite clusters and whiskers can be expressed as [358, 359]:

$$1 - B \propto \left(f_l^* - f_c^* \right)^{\kappa}, \quad f_l^* \to f_c^* \tag{7.19}$$

where κ is some exponent . With the increasing fraction of active bonds, whiskers tend to be absorbed by the backbones (dangling ends reach neighboring backbones). The backbones form interconnected large bundles. Close to the percolation threshold, the distance between two neighboring whiskers may vary by a power law similar to the power law in (7.19):

$$l_w \propto \left(f_l^* - f_c^* \right)^{\theta}, \quad f_l^* \to f_c^* \tag{7.20}$$

Far above the percolation threshold, the whiskers are marginal and the backbones dominate the main body of the pore network: $f_{\text{inf}}^* \to f_l^*$. Equation (7.18) can be reduced into:

$$1 - B \approx 1 - f_l^*, \quad f_l^* >> f_c^* \tag{7.21}$$

The density of whiskers decreases with decreasing particle sizes. The distance between two neighboring whiskers may also be assumed to vary by a power law similar to the power law in (7.21):

$$l_w \propto \left(1 - f_l^*\right)^{\gamma}, \quad f_l^* >> f_c^* \tag{7.22}$$

where γ is some exponent. These exponents may be determined by the shape of the pore size distribution, the pore structure, and the coordination number. The filtration coefficients defined as the capture probability per unit length of porous medium can be calculated as:

$$\lambda \propto \frac{1-B}{l_w} \tag{7.23}$$

Substitution of equations (7.19), (7.20), (7.21), and (7.22) into (7.23) results in:

$$\begin{aligned} \lambda &\propto \left(f_l^* - f_c^*\right)^{\alpha}, \quad f_l^* \to f_c^* \\ \lambda &\propto \left(1 - f_l^*\right)^{\beta}, \quad f_l^* >> f_c^* \end{aligned} \tag{7.24}$$

where α and β are some exponents determined by the shape of the pore size distribution, the pore structure, the coordination number, and the number of dimensions. It is outside the scope of the present work to analyze such dependences. It can be seen, however, that the power law for the filtration coefficients far above the percolation threshold is the same as in Equation (10) describing the experimental observations.

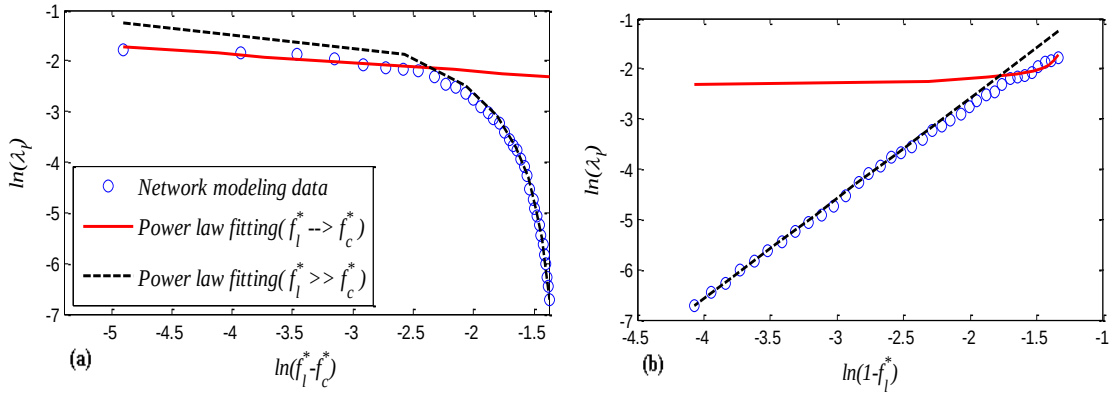

Figure 7.10 Power law dependencies of the filtration coefficients on the fraction of flux through smaller pores (Pore size distribution: Medium 30/125)

In order to validate these power law dependencies, the filtration coefficients from the network model with minimum capture scheme (Medium 30/125) are plotted against

$(f_l^* - f_c^*)$ and $(1 - f_l^*)$ separately in logarithmic scales, as seen in Figure 7.10 (a) and (b). Exponents α and β are estimated as the slopes from the two straight line in the logarithm plots. It can be seen that the filtration coefficients can be well matched by the two power laws. The exponents in the scaling laws are usually smaller in 3D than those in 2D [350, 360]. The exponents estimated by the 3D experiments are also smaller than those by the 2D network model.

In the network model, the power law far above the percolation threshold underestimates the filtration coefficient close to the threshold, while the other power law overestimates the filtration coefficient far above the threshold. Such a behavior is not yet confirmed by the laboratory challenge tests due to lack of experimental results close to the percolation threshold. The effluent concentration close to the threshold is extremely low and undetectable under our laboratory conditions. Challenge tests with shorter column lengths may overcome this difficulty and produce detectable effluence. Measurements of the deposition profiles may be an alternative for estimating the filtration coefficients close to the percolation threshold.

7.10 Summary of Chapter 7

Laboratory challenge tests are carried out under unfavorable attachment conditions, so that size exclusion or straining is the only particle capture mechanism. The experimental results show that far above the percolation threshold the filtration coefficients are not proportional to the average flux through the pores smaller than the particles, are but power-law functions of them. The experimental penetration depths of particles can be over thousands of pores even if the particle sizes are larger the average pore size.

In the traditional size exclusion theory (maximum capture scheme) the filtration coefficients are proportional to the flux through the pores smaller than the particles away from the percolation threshold. The particles can be captured wherever they meet smaller pores and such high experimental penetration depths cannot be predicted. The proportionality of filtration coefficients to the flux is also an intrinsic assumption in the model of parallel tubes with mixing chambers. Hence, neither the traditional size exclusion theory nor the model of parallel tubes with mixing chambers can explain the experimental power law dependencies of the filtration coefficients.

A special capture mechanism (the minimum capture scheme) has been proposed. This mechanism makes it possible to explain the experimentally observed power-law dependencies of filtration coefficients and large penetration depths of particles. Such capture mechanism is realized in a 2D pore network model with periodical boundaries and the random walk of particles on the percolation lattice. Geometries of infinite and finite clusters formed by pores of the sizes exceeding the particle size are analyzed with regard to the possibility for particle capture. Two power laws are proposed to describe the filtration coefficients. They can well match the filtration coefficients from the network model while one of them can match the experimental data far above the percolation threshold. The application of such models may lead to more accurate inverse determination of the pore size distributions from the challenge tests.

7.11 Nomenclature of Chapter 7

A_{123}	Hamaker constant (J)
B	Fraction of particle flow through the backbones of the infinite clusters
C_e	Normalized effluent concentration
D	Number of dimensions of pore network
e	Elementary charge (C)
f	Pore size distribution density
h	Separation distance between two surfaces (m)
I	Ionic strength (M)
k	Permeability (m^2)
k_B	Boltzmann constant (J/K)
l	Length of a capillary (m)
l_w	Average distance between two neighboring whiskers leading to dangling ends
L	Average penetration depth of particles (m)
L_l	Average network penetration depth of particles (number of pores)
L_0	Medium or network length (m)
L_D	Debye length (m)
N_c	Coordination number
N_l	Minimum number of capillaries connecting the inlet and the outlet
N_A	Avogadro constant
Δp	Pressure drop (Pa)
p	Probability of flow through a capillary
q	Flow rate in a single capillary (m^3/s)
r_p	Capillary radius (m)
r_s	Spherical particle radius (m)
f_l	Probability of a pore being larger than the injected particle
f_l^*	Average probability of particle flow through larger pores
f_c	Conventional percolation threshold
f_c^*	Flow-biased percolation threshold
f_{inf}^*	Fraction of particle flow through infinite clusters
T	temperature (K)
U_a	Darcy's velocity through accessible pores (m/s)
x	Coordinate along the injection direction (m)
z	Valence of ions

α Exponent of power-law
β Exponent of power-law
ε Dielectric constant
ε_0 Vacuum permittivity $\left(F/m\right)$
γ Exponent of power-law
θ Exponent of power-law
κ Exponent of power-law
σ Number of deposited particles per unit volume of porous media (m^{-3})
λ Filtration coefficient, capture probability per unit length (m^{-1})
λ_l Network filtration coefficient, capture probability per pore
λ_w Characteristic wave length (m)
μ Viscosity $(Pa \cdot s)$
Φ Interaction energy (J)
ψ Zeta potential or surface potential (V)

8 Conclusions

Chapter 1 of this thesis presents an overview of the recent advances in the colloid filtration theory and the discrepancies between the classical colloid filtration theory and experimental observations. Many of the discrepancies are observed under unfavorable attachment conditions, such as hyperexponential and non-monotonic deposition profiles. Such behavior of colloids is attributed to the heterogeneous attachment (Chapters 2 and 3) and the migration of captured colloids, respectively (Chapter 5). Chapter 1 also reviews the new approaches that overcome the difficulties to incorporate surface charge heterogeneity, particle and pore size distributions, straining effects, non-Fickian transport, and migration of deposited particles. The current understanding of the mechanisms, factors, and mathematical models at different scales are reviewed. Remedies for reducing the discrepancies between model predictions and experimental observations are recommended.

In Chapter 2 an integral model for non-Fickian transport and heterogeneous attachment is developed. It shows that the deposition hyperexponentiality can be attributed to the following three mechanisms: particle population heterogeneity in connection with the distribution of the filtration coefficients, midscale heterogeneity in connection with non-Fickian transport (the elliptic formalism), and macroscale heterogeneity in connection with spatial distribution of the filtration coefficients. The degree of "wash-out" of a breakthrough curve indicates whether the elliptic formalism is necessary. In the case of stepwise breakthrough curves the advection-dispersion equation seems to be adequate. In non-uniform porous media the breakthrough curves may be more dispersed. For such cases, the elliptic equation seems to be more adequate. The development of such an integral model in Chapter 2 is closely followed by the uncertainty and sensitivity analysis of the model predictions and the parameter estimation in Chapter 3.

Chapter 3 shows that both the elliptic equation and the CTRW equation expressed in Laplace space are able to model the non-Fickian transport in heterogeneous porous media. The latter model can predict an algebraic decaying tail at the end of particle injection while the elliptic equation presents a more compressed peak and a shorter tail. The

uncertainty of the elliptic equation predictions with distributed filtration coefficients is larger than that with a single filtration coefficient. The uncertainty of both CTRW models is minimal for tracer transport in heterogeneous porous media. Higher uncertainties are observed in the cases with more heterogeneous the colloid-medium interactions. Dispersion coefficients in the elliptic equation can be uniquely identified in the cases of low median heterogeneity. The parameters for the distribution of filtration coefficients are correlated. In the cases where hyper-exponential deposition is observed, the distribution may not be accurately determined by the effluent concentration profile alone. Measurements of deposition are necessary. More measurements of the effluent concentrations around the breakthrough and the end of colloid injection are suggested to determine dispersion coefficients more accurately. In the case of low median heterogeneity, more measurements of the steady-state effluent concentration and deposition are suggested to better determine filtration coefficients.

Chapters 2 and 3 form a thorough study of the integral model for colloid filtration with non-Fickian transport and heterogeneous attachment. They are followed by the study of applying of such a model to simulate the deep bed filtration around injection wells during waterflooding in Chapter 4.

In Chapter 4, a comprehensive model is developed to predict injectivity decline during waterflooding. It applies the elliptic equation for deep bed filtration and takes into account the reservoir heterogeneity, two-phase flow (injected water and displaced oil) and the distribution of solid particles by sizes. It accounts also for the later formation of the external filter cake and its erosion. The model is able to capture the behavior of the injectors in the field: the initial slow injectivity decline due to the deep bed filtration of suspended particles, the later faster decline due to the build-up of the external cake, and the steady state due to the cake erosion. However, the non-Fickian behavior of particles around the injection well is shown not to be significant. It is because of that the temporal dispersion term is inverse proportional to the particle velocity and that the particle velocity is higher close to the well than that far away from the well. A piece of software "SNY" with a user-friendly interface is produced for the new model.

In Chapter 5, a new mathematical model for colloid flow in porous media and non-monotonic deposition is proposed. It accounts for the migration of particles associated with the pore walls via the second energy minimum (surface associated phase). A set of methods for estimating the modeling parameters is provided. It is shown that the non-monotonic deposition profiles in Ref. [111] are likely to be caused by the migration of the surface associated phase. An additional equation describing a mobile population behaving differently from the injected population seems to be a sufficient condition for producing non-monotonic deposition profiles.

Chapter 6 presents the study of fines migration induced by injection of low salinity water in a communicating layer cake reservoir. The torque balance on the deposited reservoir fines via attachment, straining of the released fines, the consequent permeability damage, and the cross-flow between layers are taken into account. Particle release and re-deposition give rise to the reduction of the permeability in water swept zones, which subsequently leads to the diversion of water flow from the more permeable layers to the less permeable ones. As a result, the water cut at the producer is decreased, and the oil recovery is increased. The increased oil recovery due to fines migration increases with the mobility ratio in the range of low mobility ratios (2~4), while it is insensitive to the mobility ratio in the range of high mobility ratios (>50).

In Chapters 4, 5, and 6, a common criterion for an attached colloid particle to be re-entrained by the hydrodynamic drag into the bulk fluid is applied, namely that the torques of detachment exceed those of attachment. In Chapter 4, the main attachment torque on the colloids at the surface of external cakes comes from the drag of the permeate flow, while that on the colloids at the pore surface in Chapters 5 and 6 is from the electrostatic force. In Chapter 4, the main detachment torque is from the cross-flow drag in the well, while that in Chapters 5 and 6 is from the hydrodynamic drag in pores.

Another important mechanism for particle capture is straining or size exclusion of colloids. Such phenomena are closely tied to the migration of colloids under unfavorable attachment conditions: surface-associated colloids rolling to straining sites (grain-grain contacts, pore throats) in Chapter 5, and the straining of released reservoir fines at pore

throats in Chapter 6. However, the straining mechanism is described by nothing more than a straining rate coefficient in these studies.

Finally in Chapter 7, a much better understanding of straining is achieved by the study of pore scale physics in a 2D network model and the qualative comparison to experiments. The filtration coefficient for straining is estimated from the particle size and the pore size distributions. A new capture scheme of straining (minimum capture) is proposed to explain the large penentration depths of colloids in porous media and the power law dependencies of filtration coefficients in the experiments. In the new capture scheme, particles can only be captured when they enter the whiskers of the infinite cluster with exiting flow. Geometries of infinite and finite clusters formed by pores of the sizes exceeding the particle size are analyzed with regard to the possibility for particle capture. Two power laws are proposed to describe the filtration coefficients. They can well match the filtration coefficients from the network model while one of them can match the experimental data far above the percolation threshold.

To sum up, this thesis is compiled in such a way that each chapter arises from a self-contained study/publication. On the other hand, these chapters are closely connected in both logical and methodological senses. Chapter 1 points out that the discrepancies between the classical colloid filtration theory and experimental observations are mainly attributed to the non-Fickian transport of colloids, the heterogeneous attachment of colloids, the migration of colloids, and the straining of colloids in porous media. Chapters 2, 3, and 4 conclude that the application of the elliptic equation for non-Fickian transport is desirable when the dispersed breakthough curves are observed. The hyperexponential deposition due to heterogeneous attachment of colloids can be captured by the distribution of filtration coefficients. Chapter 5 suggests that the non-monotonic deposition caused by the migration of colloids can be produced by adding a transport equation for the migratory pupolation into the system of equations. Chapter 6 investigates the effects of the migration and the straining of reservoir fines. They contribute to better water sweep efficiencies and increased oil recovery. The torque-balance criterion of colloid migration is adopted in all three chapters (4, 5, and 6). A part of the “puzzle” of colloid straining is then solved in Chapter 7. Particle capture at the whiskers of the

infinite cluter of larger pores is proposed to explain the large penentration depths and the power-law dependencies of filtration coefficients.

9 Future Work

In this thesis, studies of the non-Fickian transport, the heterogeneous attachment, the migration, and the straining of colloids have been studied extensively. Incorporation of these effects into the models of industrial processes and applications of the proposed mathematical models are also investigated. Nevertheless, a number of "puzzles" are yet to be solved in the future.

Chapter 5 considers the migration of the colloids at the pore surface and assumes that these colloids form a single layer internal cake. This assumption is valid in the cases of dilute suspensions and short-term injections. A new population balance approach for the migration of multi-layered internal cake is desirable in the framework of [248, 252].

Chapter 7 applies a 2D network to study the filtration coefficient for the straining of different-sized particles. However, the coordination number in the 2D network is low and half of the capillaries are perpendicular to the main injection direction. The nature of such a network constrains the fractional flow in the perpendicular direction. As a result, the particles move much more slowly in the perpendicular direction than in the main stream direction. It causes a significant delay of the breakthrough of particles compared to the breakthrough of water. Such effects have been observed but not studied in any literature.

On the other hand, the accessible fractional flows of different-sized particles are different because the accessible sub-networks are different. The expression of such a fraction flow is yet to be found. A good start of the study would be from the effective medium theory. Similarly, the dispersion caused by the heterogeneity of the flow field can also be studied in the future.

The concepts of the maximum capture scheme and the minimum capture scheme are first proposed in [361] and Chapter 7 of this thesis. The filtration coefficients in the two schemes are only estimated from the network models. The analytical prediction of the filtration coefficients from the fractional flow to whiskers and smaller pores is yet to be studied.

In addition, both two schemes can probably be observed in size-exclusion experiments simultaneously. The filtration coefficients in the two schemes are merely the boundary values in real experiments. The quantitative analysis of the two processes is yet to be performed. It may be studied in a 3D CFD simulation in COMSOL multiphysics. Whether a particle can be captured at the small pores around the backbones of the infinite cluster is determined by the balance between attachment torque (permeate flow drag) and the detachment torque (cross-flow drag).

References

[1] M. Elimelech, J. Gregory, R. Williams, X. Jia, Particle Deposition & Aggregation: Measurement, Modelling and Simulation (Colloid & surface engineering), Butterworth-Heinemann, Oxford, UK, 1998.

[2] N.M. DeNovio, J.E. Saiers, J.N. Ryan, Colloid Movement in Unsaturated Porous Media: Recent Advances and Future Directions, Vadose Zone Journal, 3 (2004) 338-351.

[3] S.A. Bradford, S. Torkzabanb, Colloid Transport and Retention in Unsaturated Porous Media: A Review of Interface-, Collector-, and Pore-Scale Processes and Models, Vadose Zone Journal, 7 (2008) 667-681.

[4] Q. Wu, M. Borkovec, H. Sticher, On particle-size distribution in soils, Soil Science Society of America journal, 57 (1993) 883-890.

[5] H. Grout, A.M. Tarquis, M.R. Wiesner, Multifractal Analysis of Particle Size Distributions in Soil, Environmental Science & Technology, 32 (1998) 1176-1182.

[6] H.V. Olphen, An Introduction to Clay Colloid Chemistry: For Clay Technologists, Geologists, and Soil Scientists Krieger Pub Co, 1991.

[7] M.-H. Faure, M. Sardin, P. Vitorge, Release of clay particles from an unconsolidated clay-sand core: experiments and modelling, Journal of Contaminant Hydrology, 26 (1997) 169-178.

[8] J. Bergendahl, D. Grasso, Prediction of colloid detachment in a model porous media: Thermodynamics, AIChE Journal, 45 (1999) 475-484.

[9] J. Bergendahl, D. Grasso, Prediction of colloid detachment in a model porous media: hydrodynamics, Chemical Engineering Science, 55 (2000) 1523-1532.

[10] M. Levy, B. Berkowitz, Measurement and analysis of non-Fickian dispersion in heterogeneous porous media, Journal of Contaminant Hydrology, 64 (2003) 203-226.

[11] A. Cortis, B. Berkowitz, Anomalous Transport in "Classical" Soil and Sand Columns, Soil Sci Soc Am J, 68 (2004) 1539-1548.

[12] P.R. Johnson, N. Sun, M. Elimelech, Colloid Transport in Geochemically Heterogeneous Porous Media: Modeling and Measurements, Environmental Science & Technology, 30 (1996) 3284-3293.

[13] J.N. Ryan, M. Elimelech, Colloid mobilization and transport in groundwater, Colloids and Surfaces A: Physicochemical and Engineering Aspects, 107 (1996) 1-56.

[14] D. Champ, J. Young, D. Robertson, K. Abel, Chemical speciation of long-lived radionuclides in a shallow groundwater flow system, Water Quality Research Journal of Canada, 19 (1984) 35-54.

[15] R.W. Buddemeier, J.R. Hunt, Transport of colloidal contaminants in groundwater: radionuclide migration at the Nevada test site, Applied Geochemistry, 3 535-548.

[16] W.R. Penrose, W.L. Polzer, E.H. Essington, D.M. Nelson, K.A. Orlandini, Mobility of plutonium and americium through a shallow aquifer in a semiarid region, Environmental Science & Technology, 24 (1990) 228-234.

[17] M. Magaritz, A.J. Amiel, D. Ronen, M.C. Wells, Distribution of metals in a polluted aquifer: A comparison of aquifer suspended material to fine sediments of the adjacent environment, Journal of Contaminant Hydrology, 5 (1990) 333-347.

[18] C. Amrhein, J.E. Strong, P.A. Mosher, Effect of deicing salts on metal and organic matter mobilization in roadside soils, Environmental Science & Technology, 26 (1992) 703-709.

[19] C. Amrhein, P.A. Mosher, J.E. Strong, Colloid-assisted transport of trace metals in roadside soils receiving deicing salts, Soil Sci Soc Am J, 57 (1993) 1212-1217.

[20] L.W. de Jonge, C. Kjaergaard, P. Moldrup, Colloids and Colloid-Facilitated Transport of Contaminants in Soils: An Introduction, Vadose Zone Journal, 3 (2004) 321-325.

[21] M.B. McGechan, D.R. Lewis, SW--Soil and Water: Transport of Particulate and Colloid-sorbed Contaminants through Soil, Part 1: General Principles, Biosystems Engineering, 83 (2002) 255-273.
[22] T.R. Ginn, B.D. Wood, K.E. Nelson, T.D. Scheibe, E.M. Murphy, T.P. Clement, Processes in microbial transport in the natural subsurface, Advances in Water Resources, 25 (2002) 1017-1042.
[23] P. Zhang, W.P. Johnson, T.D. Scheibe, K.-H. Choi, F.C. Dobbs, B.J. Mailloux, Extended tailing of bacteria following breakthrough at the Narrow Channel Focus Area, Oyster, Virginia, Water Resour. Res., 37 (2001) 2687-2698.
[24] C.J. Hurst, C.P. Gerba, J.C. Lance, R.C. Rice, Survival of enteroviruses in rapid-infiltration basins during the land application of wastewater, Appl. Environ. Microbiol., 40 (1980) 192-200.
[25] H.H. Jacks, O.J.E. Smith, C.C. Mattax, The Modeling of a Three-Dimensional Reservoir with a Two-Dimensional Reservoir Simulator-The Use of Dynamic Pseudo Functions, SPE Journal, 13 (1973) 175-185.
[26] J. Bunnell, C. Tatu, R. Bushon, D. Stoeckel, A. Brady, M. Beck, H. Lerch, B. McGee, B. Hanson, R. Shi, W. Orem, Possible linkages between lignite aquifers, pathogenic microbes, and renal pelvic cancer in northwestern Louisiana, USA, Environmental Geochemistry and Health, 28 (2006) 577-587.
[27] J.L. Mawdsley, R.D. Bardgett, R.J. Merry, B.F. Pain, M.K. Theodorou, Pathogens in livestock waste, their potential for movement through soil and environmental pollution, Applied Soil Ecology, 2 (1995) 1-15.
[28] S. Mostaghimi, S.W. Park, R.A. Cooke, S.Y. Wang, Assessment of management alternatives on a small agricultural watershed, Water Research, 31 (1997) 1867-1878.
[29] W. PA, Human pathogenic viruses and parasites: Emerging pathogens in the water cycle, Journal of applied bacteriology, 70 (1991) 107s-104s.
[30] A.E. Smith, P.B. Ryan, J.S. Evans, The Effect of Neglecting Correlations When Propagating Uncertainty and Estimating the Population Distribution of Risk, Risk Analysis, 12 (1992) 467-474.
[31] D.K. Powelson, C.P. Gerba, M.T. Yahya, Virus transport and removal in wastewater during aquifer recharge, Water Research, 27 (1993) 583-590.
[32] J.P. Quirk, R.K. Schofield, The effect of electrolyte concentration on soil permeability, J. Soil Sci., 6 (1955) 163-178.
[33] H. Frenkel, J.O. Goertzen, J.D. Rhoades, Effects of Clay Type and Content, Exchangeable Sodium Percentage, and Electrolyte Concentration on Clay Dispersion and Soil Hydraulic Conductivity1, Soil Sci. Soc. Am. J., 42 (1978) 32-39.
[34] A. Lever, R.A. Dawe, Water-sensitivity and migration of fines in the Hopeman sandstone, Journal of Petroleum Geology, 7 (1984) 97-107.
[35] M.M. Sharma, Y.C. Yortsos, Fines migration in porous media, AIChE Journal, 33 (1987) 1654-1662.
[36] R.N. Valdya, H.S. Fogler, Fines Migration and Formation Damage: Influence of pH and Ion Exchange, SPE Production Engineering, 7 (1992) 325-330.
[37] K.K. Mohan, R.N. Vaidya, M.G. Reed, H.S. Fogler, Water sensitivity of sandstones containing swelling and non-swelling clays, Colloids and Surfaces A: Physicochemical and Engineering Aspects, 73 (1993) 237-254.
[38] K.C. Khilar, H.S. Fogler, Migration of Fines in Porous Media (Theory and Applications of Transport in Porous Media) Springer, Dordrecht, 1998.
[39] G.P. Guedes, F. Al-Abduwani, P. Bedrikovetsky, Injectivity Decline Under Multiple Particle Capture Mechanisms, Journal of Society of Petroleum Engineers 8(2009) 477-487.
[40] J.E. Zajic, D.G.J. Cooper, T.R., N. Kosaric, Microbial enhanced oil recovery, 1983.

[41] L.-K. Jang, P.W. Chang, J.E. Findley, T.F. Yen, Selection of Bacteria with Favorable Transport Properties Through Porous Rock for the Application of Microbial-Enhanced Oil Recovery, Appl. Environ. Microbiol., 46 (1983) 1066-1072.
[42] L.W. Lake, Enhanced oil recovery, Prentice Hall, Roxbury, MA, 1989.
[43] B.V. Derjaguin, L.D. Landau, Theory of the stability of strongly charged lyophobic sols and the adhesion of strongly charged particles in solutions of electrolytes Acta Physicochim. USSR 14 (1941) 733-762.
[44] R. Hogg, T.W. Healy, D.W. Fuerstenau, Mutual coagulation of colloidal dispersions, Transactions of the Faraday Society, 62 (1966) 1638-1651.
[45] M. Elimelech, C.R. O'Melia, Kinetics of deposition of colloidal particles in porous media, Environmental Science & Technology, 24 (1990) 1528-1536.
[46] D. Grasso, K. Subramaniam, M. Butkus, K. Strevett, J. Bergendahl, A review of non-DLVO interactions in environmental colloidal systems, Reviews in Environmental Science and Biotechnology, 1 (2002) 17-38.
[47] C.J. van Oss, Interfacial forces in aqueous media, Taylor & Francis, London, 2006.
[48] E.J.W. Verwey, J.T.G. Overbeek, Theory of the stability of lyophobic colloids, Elsevier, Amsterdam, 1948.
[49] K.-M. Yao, M.T. Habibian, C.R. O'Melia, Water and waste water filtration. Concepts and applications, Environmental Science & Technology, 5 (1971) 1105-1112.
[50] C. Tien, Granular Filtration of Aerosols and Hydrosols, Butterworth, Stoneham,MA, 1989.
[51] R. Rajagopalan, C. Tien, Trajectory analysis of deep-bed filtration with the sphere-in-cell porous media model, AIChE Journal, 22 (1976) 523-533.
[52] J. Happel, Viscous flow relative to arrays of cylinders, AIChE Journal, 5 (1959) 174-177.
[53] J. Wan, J.L. Wilson, Visualization of the role of the gas-water interface on the fate and transport of colloids in porous media, Water Resour. Res., 30 (1994) 11-23.
[54] N. Ochiai, E.L. Kraft, J.S. Selker, Methods for colloid transport visualization in pore networks, Water Resour. Res., 42 (2006) W12S06.
[55] X. Li, C.L. Lin, J.D. Miller, W.P. Johnson, Pore-scale Observation of Microsphere Deposition at Grain-to-Grain Contacts over Assemblage-scale Porous Media Domains Using X-ray Microtomography, Environmental Science & Technology, 40 (2006) 3762-3768.
[56] J. Gregory, Approximate expressions for retarded van der waals interaction, Journal of Colloid and Interface Science, 83 (1981) 138-145.
[57] C.J. Van Oss, R.J. Good, M.K. Chaudhury, The role of van der Waals forces and hydrogen bonds in "hydrophobic interactions" between biopolymers and low energy surfaces, Journal of Colloid and Interface Science, 111 (1986) 378-390.
[58] W.B. Russel, D.A. Saville, W.R. Schowalter, Colloidal Dispersions Cambridge University Press, Cambridge, 1989.
[59] D. Gupta, M.H. Peters, A Brownian dynamics simulation of aerosol deposition onto spherical collectors, Journal of Colloid and Interface Science, 104 (1985) 375-389.
[60] B.V. Ramaro, D.D. Kee., Transport Processes in Bubbles, Drops and Particles, Hemisphere, New York, 1991.
[61] R.B. Bird, W.E. Stewart, E.N. Lightfoot, Transport Phenomena, John Wiley & Sons, New York, 2006.
[62] T.G.M.v.d. Ven, Colloidal Hydrodynamics, Academic Press London, 1989.
[63] Z. Adamczyk, T. Dabros´, J. Czarnecki, T.G.M. Van De Ven, Particle transfer to solid surfaces, Advances in Colloid and Interface Science, 19 (1983) 183-252.
[64] G. Annalisa, O. Kenneth, P. Leonid, R. Boris, Estimates of turbulence parameters from Lagrangian data using a stochastic particle model, Journal of Marine Research, 53 (1995) 371-401.

[65] A.M. Tartakovsky, P. Meakin, T.D. Scheibe, R.M. Eichler West, Simulations of reactive transport and precipitation with smoothed particle hydrodynamics, Journal of Computational Physics, 222 (2007) 654-672.
[66] D. Ramsden, G. Holloway, Timestepping lagrangian particles in two dimensional eulerian flow fields, Journal of Computational Physics, 95 (1991) 101-116.
[67] A.C. Payatakes, C. Tien, R.M. Turian, Trajectory calculation of particle deposition in deep bed filtration: Part I. Model formulation, AIChE Journal, 20 (1974) 889-900.
[68] M.A. van der Hoef, M. van Sint Annaland, N.G. Deen, J.A.M. Kuipers, Numerical Simulation of Dense Gas-Solid Fluidized Beds: A Multiscale Modeling Strategy, Annual Review of Fluid Mechanics, 40 (2008) 47-70.
[69] P. Koumoutsakos, MULTISCALE FLOW SIMULATIONS USING PARTICLES, Annual Review of Fluid Mechanics, 37 (2005) 457-487.
[70] M. Herrmann, A parallel Eulerian interface tracking/Lagrangian point particle multi-scale coupling procedure, Journal of Computational Physics, 229 (2010) 745-759.
[71] J. Happel, H. Brenner, Low Reynolds number hydrodynamics: with special applications to particulate media, Prentice Hall, New Jersey, 1963.
[72] D.C. Prieve, E. Ruckenstein, Effect of London forces upon the rate of deposition of Brownian particles, AIChE Journal, 20 (1974) 1178-1187.
[73] L. Song, M. Elimelech, Calculation of particle deposition rate under unfavourable particle-surface interactions, Journal of the Chemical Society, Faraday Transactions, 89 (1993) 3443-3452.
[74] Z. Adamczyk, T.G.M. Van De Ven, Deposition of particles under external forces in laminar flow through parallel-plate and cylindrical channels, Journal of Colloid and Interface Science, 80 (1981) 340-356.
[75] Z. Adamczyk, T.G.M. Van De Ven, Deposition of brownian particles onto cylindrical collectors, Journal of Colloid and Interface Science, 84 (1981) 497-518.
[76] Z. Adamczyk, M. Zembala, B. Siwek, J. Czarnecki, Kinetics of latex particle deposition from flowing suspensions, Journal of Colloid and Interface Science, 110 (1986) 188-200.
[77] Z. Adamczyk, T. Dabros, J. Czarnecki, T.G.M. Van De Ven, Kinetics of particle accumulation at collector surfaces. II. Exact numerical solutions, Journal of Colloid and Interface Science, 97 (1984) 91-104.
[78] Z. Adamczyk, T.G.M. Van De Ven, Kinetics of particle accumulation at collector surfaces. I. Approximate analytical solutions, Journal of Colloid and Interface Science, 97 (1984) 68-90.
[79] S.A. Bradford, J. Simunek, M. Bettahar, M.T. van Genuchten, S.R. Yates, Significance of straining in colloid deposition: Evidence and implications, Water Resour. Res., 42 (2006) W12S15.
[80] S.A. Bradford, J. Simunek, S.L. Walker, Transport and straining of E. coli O157:H7 in saturated porous media, Water Resour. Res., 42 (2006) W12S12.
[81] S.A. Bradford, J. Simunek, M. Bettahar, Y.F. Tadassa, M.T. van Genuchten, S.R. Yates, Straining of colloids at textural interfaces, Water Resour. Res., 41 (2005) W10404.
[82] S. Sirivithayapakorn, A. Keller, Transport of colloids in saturated porous media: A pore-scale observation of the size exclusion effect and colloid acceleration, Water Resour. Res., 39 (2003) 1109.
[83] S. Sirivithayapakorn, A. Keller, Transport of colloids in unsaturated porous media: A pore-scale observation of processes during the dissolution of air-water interface, Water Resour. Res., 39 (2003) 1346.
[84] J.T. Crist, J.F. McCarthy, Y. Zevi, P. Baveye, J.A. Throop, T.S. Steenhuis, Pore-Scale Visualization of Colloid Transport and Retention in Partly Saturated Porous Media, Vadose Zone Journal, 3 (2004) 444-450.

[85] M. Elimelech, C.R. O'Melia, Effect of particle size on collision efficiency in the deposition of Brownian particles with electrostatic energy barriers, Langmuir, 6 (1990) 1153-1163.
[86] J.E. Tobiason, C.R. O'Melia, Physicochemical Aspects of Particle Removal in Depth Filtration, Journal American Water Works Association 80 (1988) 54-64.
[87] M.V. Smoluchowski, Versuch einer mathematischen theorie der koagulationskinetic kolloider lösugen, Zeitschrift f physik chemie, 92 (1917) 129-168.
[88] V.G. Levich, Physicochemical Hydrodynamics Prentice-Hall, New Jersey, 1962.
[89] E. Ruckenstein, D.C. Prieve, Rate of deposition of Brownian particles under the action of London and double-layer forces, Journal of the Chemical Society, Faraday Transactions 2: Molecular and Chemical Physics, 69 (1973) 1522-1536.
[90] L.A. Spielman, S.K. Friedlander, Role of the electrical double layer in particle deposition by convective diffusion, Journal of Colloid and Interface Science, 46 (1974) 22-31.
[91] N. Tufenkji, M. Elimelech, Correlation Equation for Predicting Single-Collector Efficiency in Physicochemical Filtration in Saturated Porous Media, Environmental Science & Technology, 38 (2003) 529-536.
[92] M.W. Hahn, D. Abadzic, C.R. O'Melia, Aquasols: On the Role of Secondary Minima†, Environmental Science & Technology, 38 (2004) 5915-5924.
[93] M.W. Hahn, C.R. O'Melia, Deposition and Reentrainment of Brownian Particles in Porous Media under Unfavorable Chemical Conditions: Some Concepts and Applications, Environmental Science & Technology, 38 (2003) 210-220.
[94] M.W. Hahn, PhD dissertation, in: The Johns Hopkins University, 1994.
[95] J.P. Herzig, D.M. Leclerc, P.L. Goff, Flow of Suspensions through Porous Media-Application to Deep Filtration, Industrial & Engineering Chemistry, 62 (1970) 8-35.
[96] L.M. McDowell-Boyer, J.R. Hunt, N. Sitar, Particle transport through porous media, Water Resour. Res., 22 (1986) 1901-1921.
[97] J.F. McCarthy, J.M. Zachara, Subsurface transport of contaminants, Environmental Science & Technology, 23 (1989) 496-502.
[98] M.T. Van Genuchten, Analytical solutions for chemical transport with simultaneous adsorption, zero-order production and first-order decay, Journal of Hydrology, 49 (1981) 213-233.
[99] F.J. Leij, N. Toride, M.T. van Genuchten, Analytical solutions for non-equilibrium solute transport in three-dimensional porous media, Journal of Hydrology, 151 (1993) 193-228.
[100] N. Toride, F.J. Leij, M.T. van Genuchten, A comprehensive set of analytical solutions for nonequilibrium solute transport with first-order decay and zero-order production, Water Resour. Res., 29 (1993) 2167-2182.
[101] N. Tufenkji, M. Elimelech, Deviation from the Classical Colloid Filtration Theory in the Presence of Repulsive DLVO Interactions, Langmuir, 20 (2004) 10818-10828.
[102] M. Tong, W.P. Johnson, Colloid Population Heterogeneity Drives Hyperexponential Deviation from Classic Filtration Theory, Environmental Science & Technology, 41 (2006) 493-499.
[103] N. Tufenkji, M. Elimelech, Breakdown of Colloid Filtration Theory: Role of the Secondary Energy Minimum and Surface Charge Heterogeneities, Langmuir, 21 (2005) 841-852.
[104] H. Yuan, A.A. Shapiro, Modeling non-Fickian transport and hyperexponential deposition for deep bed filtration, Chemical Engineering Journal, 162 (2010) 974-988.
[105] H. Yuan, G. Sin, Uncertainty and sensitivity analysis of filtration models for non-Fickian transport and hyperexponential deposition, Chemical Engineering Journal, 168 (2011) 635-648.
[106] J. Gregory, A.J. Wishart, Deposition of latex particles on alumina fibers, Colloids and Surfaces, 1 (1980) 313-334.
[107] R. Vaidyanathan, C. Tien, Hydrosol deposition in granular media under unfavorable surface conditions, Chemical Engineering Science, 46 (1991) 967-983.

[108] J.A. Fitzpatrick, L.A. Spielman, Filtration of aqueous latex suspensions through beds of glass spheres, Journal of Colloid and Interface Science, 43 (1973) 350-369.
[109] N. Tufenkji, G.F. Miller, J.N. Ryan, R.W. Harvey, M. Elimelech, Transport of Cryptosporidium Oocysts in Porous Media: Role of Straining and Physicochemical Filtration†, Environmental Science & Technology, 38 (2004) 5932-5938.
[110] X. Li, T.D. Scheibe, W.P. Johnson, Apparent Decreases in Colloid Deposition Rate Coefficients with Distance of Transport under Unfavorable Deposition Conditions: A General Phenomenon, Environmental Science & Technology, 38 (2004) 5616-5625.
[111] X. Li, W.P. Johnson, Nonmonotonic Variations in Deposition Rate Coefficients of Microspheres in Porous Media under Unfavorable Deposition Conditions, Environmental Science & Technology, 39 (2005) 1658-1665.
[112] X. Li, P. Zhang, C.L. Lin, W.P. Johnson, Role of Hydrodynamic Drag on Microsphere Deposition and Re-entrainment in Porous Media under Unfavorable Conditions, Environmental Science & Technology, 39 (2005) 4012-4020.
[113] C.H. Bolster, A.L. Mills, G.M. Hornberger, J.S. Herman, Spatial Distribution of Deposited Bacteria Following Miscible Displacement Experiments in Intact Cores, Water Resour. Res., 35 (1999) 1797-1807.
[114] S.A. Bradford, M. Bettahar, Straining, attachment, and detachment of cryptosporidium oocysts in saturated porous media, J Environ Qual, 34 (2005) 469-478.
[115] S.A. Bradford, S. Torkzaban, S.L. Walker, Coupling of physical and chemical mechanisms of colloid straining in saturated porous media, Water Research, 41 (2007) 3012-3024.
[116] J.M. Boggs, S.C. Young, W.R. Waldrop, L.W. Gelhar, E.E. Adams, K.R. Rehfeldt, Field study of macrodispersion in a heterogeneous aquifer. 1. Overview of tracer experiment in: AECL Report Series, 1990, pp. 34-56.
[117] M. Fourar, G. Radilla, Non-Fickian Description of Tracer Transport Through Heterogeneous Porous Media, Transport in Porous Media, 80 (2009) 561-579.
[118] S.A. Bradford, M. Bettahar, J. Simunek, M.T.v. Genuchten, Straining and Attachment of Colloids in Physically Heterogeneous Porous Media Vadose Zone Journal 3(2004) 384-394.
[119] J.A. Redman, S.L. Walker, M. Elimelech, Bacterial Adhesion and Transport in Porous Media: Role of the Secondary Energy Minimum, Environmental Science & Technology, 38 (2004) 1777-1785.
[120] A. Franchi, C.R. O'Melia, Effects of Natural Organic Matter and Solution Chemistry on the Deposition and Reentrainment of Colloids in Porous Media, Environmental Science & Technology, 37 (2003) 1122-1129.
[121] S.A. Bradford, J. Simunek, M. Bettahar, M.T. Van Genuchten, S.R. Yates, Modeling colloid attachment, straining, and exclusion in saturated porous media, Environ Sci Technol, 37 (2003) 2242-2250.
[122] S.A. Bradford, S. Torkzaban, F. Leij, im, J. nek, M.T. van Genuchten, Modeling the coupled effects of pore space geometry and velocity on colloid transport and retention, Water Resour. Res., 45 (2009) W02414.
[123] A.A. Shapiro, P.G. Bedrikovetsky, A stochastic theory for deep bed filtration accounting for dispersion and size distributions, Physica A: Statistical Mechanics and its Applications, 389 (2010) 2473-2494.
[124] B. Berkowitz, A. Cortis, M. Dentz, H. Scher, Modeling non-Fickian transport in geological formations as a continuous time random walk, Rev. Geophys., 44 (2006) RG2003.
[125] M. Bromly, C. Hinz, Non-Fickian transport in homogeneous unsaturated repacked sand, Water Resour. Res., 40 (2004) W07402.
[126] D.E. Fontes, A.L. Mills, G.M. Hornberger, J.S. Herman, Physical and chemical factors influencing transport of microorganisms through porous media, Applied and Environmental Microbiology, 57 (1991) 2473-2481.

[127] T. Harter, S. Wagner, E.R. Atwill, Colloid Transport and Filtration of Cryptosporidium parvum in Sandy Soils and Aquifer Sediments, Environmental Science & Technology, 34 (1999) 62-70.
[128] M.J. Hendry, J.R. Lawrence, P. Maloszewski, The role of sorption in the transport of Klebsiella oxytoca through saturated silica sand, Ground Water, 35 (1997) 574-584.
[129] G.M. Hornberger, A.L. Mills, J.S. Herman, Bacterial transport in porous media: Evaluation of a model using laboratory observations, Water Resour. Res., 28 (1992) 915-923.
[130] D.R. McCaulou, R.C. Bales, J.F. McCarthy, Use of short-pulse experiments to study bacteria transport through porous media, Journal of Contaminant Hydrology, 15 (1994) 1-14.
[131] J.F. Schijven, W. Hoogenboezem, S.M. Hassanizadeh, J.H. Peters, Modeling removal of bacteriophages MS2 and PRD1 by dune recharge at Castricum, Netherlands, Polygraph International, (1999) 1101-1111.
[132] R.C. Bales, S.R. Hinkle, T.W. Kroeger, K. Stocking, C.P. Gerba, Bacteriophage adsorption during transport through porous media: chemical perturbations and reversibility, Environmental Science & Technology, 25 (1991) 2088-2095.
[133] R.W. Harvey, N.E. Kinner, A. Bunn, D. MacDonald, D. Metge, Transport behavior of groundwater protozoa and protozoan-sized microspheres in sandy aquifer sediments, Applied and Environmental Microbiology, 61 (1995) 209-217.
[134] F.J. Leij, S.A. Bradford, Combined physical and chemical nonequilibrium transport model: analytical solution, moments, and application to colloids, J Contam Hydrol, 110 (2009) 87-99.
[135] X. Li, C.L. Lin, J.D. Miller, W.P. Johnson, Role of Grain-to-Grain Contacts on Profiles of Retained Colloids in Porous Media in the Presence of an Energy Barrier to Deposition, Environmental Science & Technology, 40 (2006) 3769-3774.
[136] H. Yuan, A.A. Shapiro, A mathematical model for non-monotonic deposition profiles in deep bed filtration systems, Chemical Engineering Journal, 166 (2011) 105-115.
[137] J. Gregory, The calculation of Hamaker constants, Advances in Colloid and Interface Science, 2 (1970) 396-417.
[138] J.N. Israelachvili, Intermolecular and Surface Forces, Academic Press, London, 2010.
[139] J.N. Israelachvili, G.E. Adams, Measurement of forces between two mica surfaces in aqueous electrolyte solutions in the range 0-100 nm, Journal of the Chemical Society, Faraday Transactions 1: Physical Chemistry in Condensed Phases, 74 (1978) 975-1001.
[140] D.B. Hough, L.R. White, The calculation of hamaker constants from liftshitz theory with applications to wetting phenomena, Advances in Colloid and Interface Science, 14 (1980) 3-41.
[141] Y.A. Buevich, Motion resistance of a particle suspended in a turbulent medium, Fluid Dynamics, 1 (1966) 119-119.
[142] Y.A. Buevich, Approximate statistical theory of a fluidized bed, Journal of Applied Mechanics and Technical Physics, 7 (1966) 23-30.
[143] Y.A. Buevich, Hydrodynamics of homogeneous suspensions, Journal of Applied Mechanics and Technical Physics, 10 (1969) 906-913.
[144] M.N. Rosenbluth, W.M. MacDonald, D.L. Judd, Fokker-Planck Equation for an Inverse-Square Force, Physical Review, 107 (1957) 1.
[145] H. Risken, Frank, Till, The Fokker-Planck Equation: Methods of Solutions and Applications, Springer, 1996.
[146] R. Metzler, J. Klafter, The random walk's guide to anomalous diffusion: a fractional dynamics approach, Physics Reports, 339 (2000) 1-77.
[147] X. Jia, R.A. Williams, PARTICLE DEPOSITION AT A CHARGED SOLID/LIQUID INTERFACE, Chemical Engineering Communications, 91 (1990) 127-198.

[148] S. Stephen W, Modelling colloid transport in groundwater; the prediction of colloid stability and retention behaviour, Advances in Colloid and Interface Science, 54 (1995) 129-208.
[149] Z. Adamczyk, Deposition of particles onto the rotating disk under transient conditions, Journal of Colloid and Interface Science, 78 (1980) 559-562.
[150] T. Dabroś, T.G.M. van de Ven, A direct method for studying particle deposition onto solid surfaces, Colloid & Polymer Science, 261 (1983) 694-707.
[151] K. Chari, R. Rajagopalan, Deposition of colloidal particles in stagnation-point flow, Journal of the Chemical Society, Faraday Transactions 2: Molecular and Chemical Physics, 81 (1985) 1345-1366.
[152] J. Happel, Viscous flow in multiparticle systems: Slow motion of fluids relative to beds of spherical particles, AIChE Journal, 4 (1958) 197-201.
[153] A.C. Payatakes, R. Rajagopalan, C. Tien, Application of porous media models to the study of deep bed filtration, The Canadian Journal of Chemical Engineering, 52 (1974) 722-731.
[154] L.A. Spielman, J.A. Fitzpatrick, Theory for particle collection under london and gravity forces, Journal of Colloid and Interface Science, 42 (1973) 607-623.
[155] A. Santos, P. Bedrikovetsky, S. Fontoura, Analytical micro model for size exclusion: Pore blocking and permeability reduction, Journal of Membrane Science, 308 (2008) 115-127.
[156] A. Santos, P. Bedrikovetsky, A Stochastic Model for Particulate Suspension Flow in Porous Media, Transport in Porous Media, 62 (2006) 23-53.
[157] A. Santos, P. Bedrikovetsky, Size exclusion during particle suspension transport in porous media: stochastic and averaged equations, Computational and Applied Mathematics, 23 (2004) 259-284.
[158] A. Shapiro, P. Bedrikovetsky, A. Santos, O. Medvedev, A stochastic model for filtration of particulate suspensions with incomplete pore plugging, Transport in Porous Media, 67 (2007) 135-164.
[159] M.M. Sharma, Y.C. Yortsos, A network model for deep bed filtration processes, AIChE Journal, 33 (1987) 1644-1653.
[160] S.D. Rege, H.S. Fogler, A network model for deep bed filtration of solid particles and emulsion drops, AIChE Journal, 34 (1988) 1761-1772.
[161] C. Zhao, X. Zhou, Y. Yue, Determination of pore size and pore size distribution on the surface of hollow-fiber filtration membranes: a review of methods, Desalination, 129 (2000) 107-123.
[162] D. Barton, Diffusional deposition of particles, Journal of Colloid and Interface Science, 48 (1974) 520-522.
[163] C. O'Melia, ES&T Features: Aquasols: the behavior of small particles in aquatic systems, Environmental Science & Technology, 14 (1980) 1052-1060.
[164] C.R. O'melia, Particle—particle interactions in aquatic systems, Colloids and Surfaces, 39 (1989) 255-271.
[165] H. Dong, T.C. Onstott, C.-H. Ko, A.D. Hollingsworth, D.G. Brown, B.J. Mailloux, Theoretical prediction of collision efficiency between adhesion-deficient bacteria and sediment grain surface, Colloids and Surfaces B: Biointerfaces, 24 (2002) 229-245.
[166] D. Krishnaiah, S. Sarkar, R. Rajagoplan, C. Tien, R. Pfeffer, G. Tardos, Letters to the editor, AIChE Journal, 28 (1982) 871-872.
[167] J.F. Schijven, S.M. Hassanizadeh, Removal of Viruses by Soil Passage: Overview of Modeling, Processes, and Parameters, Critical Reviews in Environmental Science and Technology, 30 (2000) 49-127.
[168] M.V. Yates, S.R. Yates, C.P. Gerba, Modeling microbial fate in the subsurface environment, Critical Reviews in Environmental Control, 17 (1988) 307-344.

[169] R.W. Puls, R.M. Powell, Transport of inorganic colloids through natural aquifer material: implications for contaminant transport, Environmental Science & Technology, 26 (1992) 614-621.
[170] V.K. La Mer, Filtration of colloidal dispersions flocculated by anionic and cationic polyelectrolytes, Discussions of the Faraday Society, 42 (1966) 248-254.
[171] G. Chen, Surface Free Energy Relationships used to Evaluate Microbial Transport, J. Environ. Eng., 128 (2002) 408.
[172] T. Harter, S. Wagner, E.R. Atwill, Colloid transport and filtration of Cryptosporidium parvum in sandy soils and aquifer sediments, Environmental Science and Technology, 34 (2000) 62-70.
[173] Y. Jin, M.V. Yates, S.S. Thompson, W.A. Jury, Sorption of Viruses during Flow through Saturated Sand Columns, Environmental Science & Technology, 31 (1997) 548-555.
[174] R.C. Bales, S. Li, T.C.J. Yeh, M.E. Lenczewski, C.P. Gerba, Bacteriophage and microsphere transport in saturated porous media: Forced-gradient experiment at Borden, Ontario, Water Resour. Res., 33 (1997) 639-648.
[175] R.W. Harvey, S.P. Garabedian, Use of colloid filtration theory in modeling movement of bacteria through a contaminated sandy aquifer, Environmental Science & Technology, 25 (1991) 178-185.
[176] C.H. Giles, D. Smith, A. Huitson, A general treatment and classification of the solute adsorption isotherm. I. Theoretical, Journal of Colloid and Interface Science, 47 (1974) 755-765.
[177] R.A. Garcia-Delgado, L.M. Cotoruelo-Minguez, J.J. Rodriguez, Equilibrium Study of Single-Solute Adsorption of Anionic Surfactants with Polymeric XAD Resins, Separation Science and Technology, 27 (1992) 975-987.
[178] A.A. Shapiro, E.H. Stenby, Multicomponent Adsorption: Principles and Models, in: J. Toth (Ed.) Adsorption: Theory, Modeling, and Analysis (Surfactant Science Series, Volume 107), Marcel Dekker, New York, 2002.
[179] A.A. Shapiro, E.H. Stenby, Potential Theory of Multicomponent Adsorption, Journal of Colloid and Interface Science, 201 (1998) 146-157.
[180] P. Chheda, D. Grasso, Surface Thermodynamics of Ozone-Induced Particle Destabilization, Langmuir, 10 (1994) 1044-1053.
[181] D. Grasso, J.C. Carrington, P. Chheda, B. Kim, Nitrocellulose particle stability: Coagulation thermodynamics, Water Research, 29 (1995) 49-59.
[182] Q. Du, E. Freysz, Y.R. Shen, Surface Vibrational Spectroscopic Studies of Hydrogen Bonding and Hydrophobicity, Science, 264 (1994) 826-828.
[183] L.F. Scatena, M.G. Brown, G.L. Richmond, Water at Hydrophobic Surfaces: Weak Hydrogen Bonding and Strong Orientation Effects, Science, 292 (2001) 908-912.
[184] D.E. Gragson, G.L. Richmond, Investigations of the Structure and Hydrogen Bonding of Water Molecules at Liquid Surfaces by Vibrational Sum Frequency Spectroscopy, The Journal of Physical Chemistry B, 102 (1998) 3847-3861.
[185] S. Torkzaban, S.A. Bradford, M.T. van Genuchten, S.L. Walker, Colloid transport in unsaturated porous media: the role of water content and ionic strength on particle straining, J Contam Hydrol, 96 (2008) 113-127.
[186] N. Tufenkji, Modeling microbial transport in porous media: Traditional approaches and recent developments, Advances in Water Resources, 30 (2007) 1455-1469.
[187] C.J.V. Oss, Interfacial forces in aqueous media, M. Dekker, 1994.
[188] J.A. Molina-Bol ívar, J.L. Ortega-Vinuesa, How Proteins Stabilize Colloidal Particles by Means of Hydration Forces, Langmuir, 15 (1999) 2644-2653.
[189] S. Marčelja, N. Radić, Repulsion of interfaces due to boundary water, Chemical Physics Letters, 42 (1976) 129-130.

[190] N. Kallay, J.D. Nelligan, E. Matijevic, Particle adhesion and removal in model systems. Part 6.-Kinetics of deposition of haematite particles on steel, Journal of the Chemical Society, Faraday Transactions 1: Physical Chemistry in Condensed Phases, 79 (1983) 65-74.
[191] S.L. Walker, J.A. Redman, M. Elimelech, Role of Cell Surface Lipopolysaccharides in Escherichia coli K12 Adhesion and Transport, Langmuir, 20 (2004) 7736-7746.
[192] A.J. de Kerchove, P. Weroński, M. Elimelech, Adhesion of Nonmotile Pseudomonas aeruginosa on "Soft" Polyelectrolyte Layer in a Radial Stagnation Point Flow System: Measurements and Model Predictions, Langmuir, 23 (2007) 12301-12308.
[193] S.L. Walker, J.E. Hill, J.A. Redman, M. Elimelech, Influence of Growth Phase on Adhesion Kinetics of Escherichia coli D21g, Appl. Environ. Microbiol., 71 (2005) 3093-3099.
[194] I. Langmuir, THE ADSORPTION OF GASES ON PLANE SURFACES OF GLASS, MICA AND PLATINUM, Journal of the American Chemical Society, 40 (1918) 1361-1403.
[195] P.R. Johnson, M. Elimelech, Dynamics of Colloid Deposition in Porous Media: Blocking Based on Random Sequential Adsorption, Langmuir, 11 (1995) 801-812.
[196] Z. Adamczyk, B. Siwek, M. Zembala, P. Belouschek, Kinetics of localized adsorption of colloid particles, Advances in Colloid and Interface Science, 48 (1994) 151-280.
[197] P. Schaaf, Surface exclusion effects in adsorption processes, J. Chem. Phys., 91 (1989) 4401.
[198] Z. Adamczyk, B. Siwek, M. Zembala, Kinetics of localized adsorption of particles on homogeneous surfaces, Journal of Colloid and Interface Science, 151 (1992) 351-369.
[199] J. Bear, Dynamics of fluids in porous media, Courier Dover Publications, New York, 1972.
[200] W. Stumm, J.J. Morgan, Aquatic Chemistry (3rd edition), Wiley-Interscience, New York, 1996.
[201] S. Ross, P. Olivier J, J. Hinchen J, On Physical Adsorption, in: SOLID SURFACES, American Chemical Society, 1961, pp. 317-324.
[202] J. Gluyas, R. Swarbrick, Petroleum Geoscience Wiley, Blackwell, 2003.
[203] L.K. Koopal, S.S. Dukhin, Modelling of the double layer and electrosorption of a patchwise heterogeneous surface on the basis off its homogeneous analogue 1. Non-interacting patches, Colloids and Surfaces A: Physicochemical and Engineering Aspects, 73 (1993) 201-209.
[204] M. Elimelech, M. Nagai, C.-H. Ko, J.N. Ryan, Relative Insignificance of Mineral Grain Zeta Potential to Colloid Transport in Geochemically Heterogeneous Porous Media, Environmental Science & Technology, 34 (2000) 2143-2148.
[205] J.A. Redman, S.B. Grant, T.M. Olson, M.K. Estes, Pathogen Filtration, Heterogeneity, and the Potable Reuse of Wastewater, Environmental Science & Technology, 35 (2001) 1798-1805.
[206] J.A. Redman, M.K. Estes, S.B. Grant, Resolving macroscale and microscale heterogeneity in virus filtration, Colloids and Surfaces A: Physicochemical and Engineering Aspects, 191 (2001) 57-70.
[207] N. Tufenkji, J.A. Redman, M. Elimelech, Interpreting Deposition Patterns of Microbial Particles in Laboratory-Scale Column Experiments, Environmental Science & Technology, 37 (2003) 616-623.
[208] S.A. Bradford, N. Toride, A Stochastic Model for Colloid Transport and Deposition, Journal of Environmental Quality, 36 (2007) 1346-1356.
[209] S. Torkzaban, S.S. Tazehkand, S.L. Walker, S.A. Bradford, Transport and fate of bacteria in porous media: Coupled effects of chemical conditions and pore space geometry, Water Resour. Res., 44 (2008) W04403.

[210] M. Auset, A.A. Keller, Pore-scale visualization of colloid straining and filtration in saturated porous media using micromodels, Water Resour. Res., 42 (2006) W12S02.
[211] J.S. Yoon, J.T. Germaine, P.J. Culligan, Visualization of particle behavior within a porous medium: Mechanisms for particle filtration and retardation during downward transport, Water Resour. Res., 42 (2006) W06417.
[212] R. Sakthivadivel, Theory and mechanism of filtration of non-colloidal fines through a porous medium, in: Report HEL 15-5, Hydraulic Engineering Laboratory, University of California, Berkeley, CA, 1966.
[213] R. Sakthivadivel, Clogging of a Granular Porous Medium by Sediment, in: Report HEL 15-7, Hydraulic Engineering Laboratory, University of California, Berkeley, CA, 1969.
[214] S. Xu, B. Gao, J.E. Saiers, Straining of colloidal particles in saturated porous media, Water Resour. Res., 42 (2006) W12S16.
[215] S.A. Bradford, S.R. Yates, M. Bettahar, J. Simunek, Physical factors affecting the transport and fate of colloids in saturated porous media, Water Resour. Res., 38 (2002) 1327.
[216] S. Torkzaban, S.A. Bradford, S.L. Walker, Resolving the coupled effects of hydrodynamics and DLVO forces on colloid attachment in porous media, Langmuir, 23 (2007) 9652-9660.
[217] A.A. Shapiro, Elliptic equation for random walks. Application to transport in microporous media, Physica A: Statistical Mechanics and its Applications, 375 (2007) 81-96.
[218] A.A. Shapiro, P.G. Bedrikovetsky, Elliptic random-walk equation for suspension and tracer transport in porous media, Physica A: Statistical Mechanics and its Applications, 387 (2008) 5963-5978.
[219] G. Margolin, M. Dentz, B. Berkowitz, Continuous time random walk and multirate mass transfer modeling of sorption, Chemical Physics, 295 (2003) 71-80.
[220] A. Cortis, C. Knudby, A continuous time random walk approach to transient flow in heterogeneous porous media, Water Resour. Res., 42 (2006) W10201.
[221] A. Cortis, C. Gallo, H. Scher, B. Berkowitz, Numerical simulation of non-Fickian transport in geological formations with multiple-scale heterogeneities, Water Resour. Res., 40 (2004) W04209.
[222] B. Berkowitz, H. Scher, The Role of Probabilistic Approaches to Transport Theory in Heterogeneous Media, Transport in Porous Media, 42 (2001) 241-263.
[223] A. Cortis, T. Harter, L. Hou, E.R. Atwill, A.I. Packman, P.G. Green, Transport of Cryptosporidium parvum in porous media: Long-term elution experiments and continuous time random walk filtration modeling, Water Resour. Res., 42 (2006) W12S13.
[224] A. Einstein, Investigations on the theory of Brownian motion, Dover Publications, New York, 1956.
[225] M.V. Smoluchowski, Drei Vortrage uber Diffusion, Brownsche Bewegung und Koagulation von Kolloidteilchen, Physik. Zeit, 17 (1916) 557-585.
[226] P. Langevin, Sur la théorie de mouvement Brownien, C.R. Acad. Sci. Paris 146 (1908) 530-533.
[227] G.E. Uhlenbeck, L.S. Ornstein, On the theory of Brownian motion, Phys. Rev., 36 (1930) 823-841.
[228] C.W. Gardiner, Handbook of Stochastic Methods: For Physics, Chemistry and Natural Sciences Springer, New York, 1985.
[229] P. Bedrikovetsky, Upscaling of Stochastic Micro Model for Suspension Transport in Porous Media, Transport in Porous Media, 75 (2008) 335-369.
[230] M.M. Sharma, Y.C. Yortsos, Transport of particulate suspensions in porous media: Model formulation, AIChE Journal, 33 (1987) 1636-1643.
[231] S.A. Bradford, H.N. Kim, B.Z. Haznedaroglu, S. Torkzaban, S.L. Walker, Coupled factors influencing concentration-dependent colloid transport and retention in saturated porous media, Environ Sci Technol, 43 (2009) 6996-7002.

[232] W.P. Johnson, X. Li, S. Assemi, Deposition and re-entrainment dynamics of microbes and non-biological colloids during non-perturbed transport in porous media in the presence of an energy barrier to deposition, Advances in Water Resources, 30 (2007) 1432-1454.
[233] M. Elimelech, J. Gregory, X. Jia, R.A. Williams, Particle Deposition and Aggregation - Measurement, Modelling and Simulation, Elsevier 1995.
[234] L.D. Landau, E.M. Lifshitz, L.E. Reichl, Statistical Physics, Part 1 (Third Edition), Physics Today, 34 (1981) 74-74.
[235] V.I. Selyakov, V. Kadet, Percolation Models for Transport in Porous Media: with Applications to Reservoir Engineering (Theory and Applications of Transport in Porous Media) Springer, New York, 1997.
[236] H. Yuan, A.A. Shapiro, Induced migration of fines during waterflooding in communicating layer-cake reservoirs, Journal of Petroleum Science and Engineering, 78 (2011) 618-626.
[237] P. Lemon, A. Zeini Jahromi, P. Bedrikovetsky , I. Shahin, Effects of Injected Water Chemistry on Waterflood Sweep Efficiency Via Induced Fines Migration, in: SPE International Symposium on Oilfield Chemistry, Woodlands, Texas, 2011.
[238] T. Huang, A.D. Hill, R.S. Schechter, Reaction Rate and Fluid Loss: The Keys to Wormhole Initiation and Propagation in Carbonate Acidizing in: International Symposium on Oilfield Chemistry, SPE, Houston, Texas, 1997, pp. 775-784.
[239] C.N. Fredd, Dynamic Model of Wormhole Formation Demonstrates Conditions for Effective Skin Reduction During Carbonate Matrix Acidizing, in: SPE Permian Basin Oil and Gas Recovery Conference, SPE, Midland, Texas, 2000.
[240] L.N. Morgenthaler, D. Zhu, J. Mou, A.D. Hill, Effect of Reservoir Mineralogy and Texture on Acid Response in Heterogeneous Sandstones, SPE Production & Operations, 23 (2008) 39-48.
[241] T. Huang, P.M. McElfresh, A.D. Gabrysch, Acid Removal of Scale and Fines at High Temperatures, in: International Symposium on Oilfield Scale, SPE, Aberdeen, UK, 2002, pp. SPE74678.
[242] J.N. Ryan, P.M. Gschwend, Colloid mobilization in two Atlantic coastal plain aquifers: Field studies, Water Resour. Res., 26 (1990) 307-322.
[243] P.M. Gschwend, D.A. Backhus, J.K. MacFarlane, A.L. Page, Mobilization of colloids in groundwater due to infiltration of water at a coal ash disposal site, Journal of Contaminant Hydrology, 6 (1990) 307-320.
[244] D.A. Backhus, J.N. Ryan, D.M. Groher, J.K. MacFarlane, P.M. Gschwend, Sampling Colloids and Colloid-Associated Contaminants in Ground Water, Ground Water, 31 (1993) 466-479.
[245] R.T. Shanmuganathan, J.M. Oades, Influence of anions on dispersion and physical properties of the A horizon of a Red-brown earth, Geoderma, 29 (1983) 257-277.
[246] X.C. Zhang, L.D. Norton, Effect of exchangeable Mg on saturated hydraulic conductivity, disaggregation and clay dispersion of disturbed soils, Journal of Hydrology, 260 (2002) 194-205.
[247] A. Zeinijahromi, P. Lemon, P. Bedrikovetsky, Effects of Induced Migration of Fines on Water Cut during Waterflooding, in: SPE Middle East Oil and Gas Show and Conference, SPE, Manama, 2011.
[248] P. Bedrikovetsky, F. Siqueira, C. Furtado, A. Souza, Modified Particle Detachment Model for Colloidal Transport in Porous Media, Transport in Porous Media, (2010) 1-31.
[249] G.-Q. Tang, N.R. Morrow, Influence of brine composition and fines migration on crude oil/brine/rock interactions and oil recovery, Journal of Petroleum Science and Engineering, 24 (1999) 99-111.
[250] I.M. Banat, Biosurfactants production and possible uses in microbial enhanced oil recovery and oil pollution remediation: A review, Bioresource Technology, 51 (1995) 1-12.

[251] D. Jiao, M.M. Sharma, Mechanism of Cake Buildup in Crossflow Filtration of Colloidal Suspensions, Journal of Colloid and Interface Science, 162 (1994) 454-462.
[252] P. Bedrikovetsky, A. Zeinijahromi, F. Siqueira, C. Furtado, A. de Souza, Particle Detachment Under Velocity Alternation During Suspension Transport in Porous Media, Transport in Porous Media, (2011) 1-25.
[253] A. Lever, R.A. Dawe, Clay migration and entrapment in synthetic porous media, Marine and Petroleum Geology, 4 (1987) 112-118.
[254] A. Cortis, T.A. Ghezzehei, On the transport of emulsions in porous media, Journal of Colloid and Interface Science, 313 (2007) 1-4.
[255] M. Dentz, B. Berkowitz, Transport behavior of a passive solute in continuous time random walks and multirate mass transfer, Water Resour. Res., 39 (2003) 1111.
[256] K.A. Newman, K.D. Stolzenbach, Kinetics of aggregation and disaggregation of titanium dioxide particles and glass beads in a sheared fluid suspension, Colloids and Surfaces A: Physicochemical and Engineering Aspects, 107 (1996) 189-203.
[257] S.E. Silliman, E.S. Simpson, Laboratory Evidence of the Scale Effect in Dispersion of Solutes in Porous Media, Water Resources Research, 23 (1987) 1667-1673.
[258] J.C. Baygents, J.R. Glynn, O. Albinger, B.K. Biesemeyer, K.L. Ogden, R.G. Arnold, Variation of Surface Charge Density in Monoclonal Bacterial Populations: Implications for Transport through Porous Media, Environmental Science & Technology, 32 (1998) 1596-1603.
[259] S.F. Simoni, H. Harms, T.N.P. Bosma, A.J.B. Zehnder, Population Heterogeneity Affects Transport of Bacteria through Sand Columns at Low Flow Rates, Environmental Science & Technology, 32 (1998) 2100-2105.
[260] N. Tufenkji, M. Elimelech, Reply to comment on breakdown of colloid filtration theory: Role of the secondary energy minimum and surface charge heterogeneities, Langmuir, 21 (2005) 10896-10897.
[261] G.H. Golub, C.F.V. Loan, Matrix Computations (Johns Hopkins Studies in Mathematical Sciences) (1996).
[262] V. Shah, J. Gilbert, Sparse Matrices in Matlab *P: Design and Implementation, in: High Performance Computing - HiPC 2004, 2005, pp. 144-155.
[263] P.V. Danckwerts, Continuous flow systems. Distribution of residence times, Chemical Engineering Science, 50 (1995) 3857-3866.
[264] M.D. McKay, J.D. Morrison, S.C. Upton, Evaluating prediction uncertainty in simulation models, Computer Physics Communications, 117 (1999) 44-51.
[265] J.C. Helton, Uncertainty and sensitivity analysis techniques for use in performance assessment for radioactive waste disposal, Reliability Engineering & System Safety, 42 (1993) 327-367.
[266] R.L. Iman, J.C. Helton, An Investigation of Uncertainty and Sensitivity Analysis Techniques for Computer Models, Risk Analysis, 8 (1988) 71-90.
[267] R.L. Iman, J.C. Helton, Comparison of uncertainty and sensitivity analysis techniques for computer models, in: Other Information: p, 1985, pp. Medium: X; Size: Pages: 116.
[268] R. Dawson, R.B. Lantz, Inaccessible Pore Volume in Polymer Flooding SPE Journal, 12 (1972) 448-452.
[269] G. Sin, K.V. Gernaey, A.E. Lantz, Good modeling practice for PAT applications: Propagation of input uncertainty and sensitivity analysis, Biotechnology Progress, 25 (2009) 1043-1053.
[270] G. Sin, K.V. Gernaey, M.B. Neumann, M.C.M. van Loosdrecht, W. Gujer, Uncertainty analysis in WWTP model applications: A critical discussion using an example from design, Water Research, 43 (2009) 2894-2906.
[271] J.C. Helton, Uncertainty and sensitivity analysis in the presence of stochastic and subjective uncertainty, Journal of Statistical Computation and Simulation, 57 (1997) 3 - 76.

[272] A. Saltelli, M. Ratto, T. Andres, F. Campolongo, J. Cariboni, D. Gatelli, M. Saisana, S. Tarantola, Global Sensitivity Analysis: The Primer, John Wiley & Sons USA, 2008.
[273] G. Sin, A. Guisasola, D.J.W. De Pauw, J.A. Baeza, J. Carrera, P.A. Vanrolleghem, A new approach for modelling simultaneous storage and growth processes for activated sludge systems under aerobic conditions, Biotechnology and Bioengineering, 92 (2005) 600-613.
[274] M. Omlin, P. Reichert, A comparison of techniques for the estimation of model prediction uncertainty, Ecological Modelling, 115 (1999) 45-59.
[275] D.M. Bates, D.G. Watts, Nonlinear Regression Analysis & Applns P, Wiley-Interscience USA, 2003.
[276] G.A.F. Seber, C.J. Wild, Nonlinear Regression, John Wiley & Sons, Canada, 1989.
[277] H.A. Steinberg, GENERALIZED QUOTA SAMPLING, Journal Name: Nuclear Science and Engineering (U.S.); Journal Volume: Vol: 15; Other Information: Orig. Receipt Date: 31-DEC-63, (1963) Medium: X; Size: Pages: 142-145.
[278] M.D. Mckay, R.J. Beckman, W.J. Conover, A Comparison of Three Methods for Selecting Values of Input Variables in the Analysis of Output from a Computer Code Technometrics, 42 (2000) 55-61.
[279] J.C. Helton, F.J. Davis, Latin hypercube sampling and the propagation of uncertainty in analyses of complex systems, Reliability Engineering & System Safety, 81 (2003) 23-69.
[280] R.L. Iman, W.J. Conover, A distribution-free approach to inducing rank correlation among input variables, Communications in statistics-simulation and computation B, 11 (1982) 311-314.
[281] R. Brun, M. Kuehni, H. Siegrist, W. Gujer, P. Reichert, Practical identifiability of ASM2d parameters--systematic selection and tuning of parameter subsets, Water Research, 36 (2002) 4113-4127.
[282] R. Brun, P. Reichert, H.R. Kuensch, Practical identifiability analysis of large environmental simulation models, Water Resour. Res., 37 (2001) 1015-1030.
[283] G. Sin, A.S. Meyer, K.V. Gernaey, Assessing reliability of cellulose hydrolysis models to support biofuel process design--Identifiability and uncertainty analysis, Computers & Chemical Engineering, 34 (2010) 1385-1392.
[284] F.R. de Hoog, J.H. Knight, A.N. Stokes, An Improved Method for Numerical Inversion of Laplace Transforms, SIAM Journal on Scientific and Statistical Computing, 3 (1982) 357-366.
[285] J.H. Barkman, D.H. Davidson, Measuring Water Quality and Predicting Well Impairment, SPE Journal of Petroleum Technology, 24 (1972) 865-873.
[286] H.A. Nasr-El-Din, A.A. Al-Taq, Water Quality Requirements and Restoring the Injectivity of Waste Water Disposal Wells, in: SPE Formation Damage Control Conference, 1998 Copyright 1998, Society of Petroleum Engineers, Inc., Lafayette, Louisiana, 1998.
[287] A.N. Cavallaro, R. Baigorria, A Method to Predict the Injectivity Decline Rate in Water Injection Wells: Chihuido de la Sierra Negra Oilfield. A Case to Study, in: Canadian International Petroleum Conference, Petroleum Society of Canada, Calgary, Alberta, 2000.
[288] P.G. Bedrikovetsky, D.R. Fonseca, M.J. da Silva, M.F. da Silva, A.G. Siqueira, A.L.S. de Souza, C.A. Furtado, Well-History-Based Prediction of Injectivity Decline (Accounting for Oil-Water Mobility Variation During Waterflooding), in: SPE Latin American and Caribbean Petroleum Engineering Conference, SPE, Rio de Janeiro, Brazil, 2005.
[289] P.G. Bedrikovetsky, E.J. Mackay, R.M.P. Silva, F.M.R. Patricio, F.F. Rosário, Produced water re-injection with seawater treated by sulphate reduction plant: Injectivity decline, analytical model, Journal of Petroleum Science and Engineering, 68 (2009) 19-28.
[290] S. Pang, M.M. Sharma, A Model for Predicting Injectivity Decline in Water-Injection Wells SPE Formation Evaluation, 12 (1997) 194-201.

[291] R. Paiva, P. Bedrikovetsky, C. Furtado, A.G. Siqueira, A.L.S.d. Souza, A Comprehensive Model for Injectivity Decline Prediction During PWRI, in: SPE Europec/EAGE Annual Conference and Exhibition, SPE, Vienna, Austria, 2006.
[292] D.B. Bennion, D.W. Bennion, F.B. Thomas, R.F. Bietz, Injection Water Quality - A Key Factor to Successful Waterflooding, in: Annual Technical Meeting, Petroleum Society of Canada, Calgary, Alberta, 1994.
[293] D.B. Bennion, F.B. Thomas, D. Imer, T. Ma, B. Schulmeister, Water Quality Considerations Resulting in the Impaired Injectivity of Water Injection and Disposal Wells, (2001).
[294] J. Ochi, J.-L. Detienne, P. Rivet, Y. Lacourie, External Filter Cake Properties During Injection of Produced Waters, in: SPE European Formation Damage Conference, Society of Petroleum Engineers, The Hague, Netherlands, 1999.
[295] F.A.H. Al-Abduwani, P. Bedrikovetsky, R. Farajzadeh, External Filter Cake Erosion: Mathematical Model and Experimental Study in: SPE European Formation Damage Conference, Society of Petroleum Engineers Sheveningen, The Netherlands, 2005.
[296] F.A.H. Al-Abduwani, Internal filtration and external filter cake build-up in sandstones, in, Delft University of Technology, Delft, 2005.
[297] R. Paiva, P. Bedrikovetsky, A.G. Siqueira, C. Furtado, A.L.S.d. Souza, A Comprehensive Model for Injectivity Decline Prediction During PWRI, in: European Formation Damage Conference, SPE, Scheveningen, The Netherlands, 2007.
[298] H. Yuan, A.A. Shapiro, Colloid Transport and Retention: Recent Advances in Colloids Filtration Theory, in: P.C. Ray (Ed.) Colloids: Classification, Properties and Applications, NOVA Science Publisher, New York, 2012.
[299] H.N. Kim, S.L. Walker, S.A. Bradford, Coupled factors influencing the transport and retention of Cryptosporidium parvum oocysts in saturated porous media, Water Resour. Res., 44 (2010) 1213-1223.
[300] D.R. Thrasher, D.A. Puckett, G. Pospisil, I. Vance, A. Daviies, G. Beattie, G. Boccardo, S.C. Jackson, MEOR From Lab to Field, in: SPE Improved Oil Recovery Symposium, Society of Petroleum Engineers, Tulsa, Oklahoma, USA, 2010.
[301] R.L. Zahner, S. Tapper, B.W.G. Marcotte, B.R. Govreau, What Has Been Learned From A Hundred MEOR Applications, in: SPE Enhanced Oil Recovery Conference, Society of Petroleum Engineers, Kuala Lumpur, Malaysia, 2011.
[302] P. Lemon, A. Zeinijahromi, P. Bedrikovetsky, I. Shahin, Effects of Injected-Water Salinity on Waterflood Sweep Efficiency Through Induced Fines Migration, Journal of Canadian Petroleum Technology, 50 (2011) 82-94.
[303] N. Morrow, J. Buckley, Improved Oil Recovery by Low-Salinity Waterflooding, SPE Journal of Petroleum Technology, 63 (2011) 106-112.
[304] M.H. Sayyouh, Microbial Enhanced Oil Recovery: Research Studies in the Arabic Area During the Last Ten Years, in: SPE/DOE Improved Oil Recovery Symposium, Copyright 2002, Society of Petroleum Engineers Inc., Tulsa, Oklahoma, 2002.
[305] W.P. Johnson, X. Li, Comment on Breakdown of Colloid Filtration Theory:Role of the Secondary Energy Minimum and Surface Charge Heterogeneities, Langmuir, 21 (2005) 10895-10895.
[306] R.S. Mojarad, A.T. Settari, Coupled Numerical Simulation of Reservoir Flow With Formation Plugging, Journal of Canadian Petroleum Technology, 46 (2007) 54-59.
[307] R.C. Bachman, T.G. Harding, A.T. Settari, D.A. Walters, Coupled Simulation of Reservoir Flow, Geomechanics, and Formation Plugging With Application to High-Rate Produced Water Reinjection, in: SPE Reservoir Simulation Symposium, SPE, Houston, Texas, 2003.
[308] P. Bedrikovetsky, A.S.L.V. Jr., C.J.A. Furtado, A.R.S.d. Souza, Formation-Damage Evaluation From Nonlinear Skin Growth During Coreflooding, SPE Reservoir Evaluation & Engineering, 14 (2011).

[309] F.F. Zinati, R. Farajzadeh, P.K. Currie, P.L.J. Zitha, Modeling of External Filter Cake Build-up in Radial Geometry, Petroleum Science and Technology, 27 (2009) 746-763.
[310] M.E. O'Neill, A sphere in contact with a plane wall in a slow linear shear flow, Chemical Engineering Science, 23 (1968) 1293-1298.
[311] L. Song, M. Elimelech, Theory of concentration polarization in crossflow filtration, Journal of the Chemical Society, Faraday Transactions, 91 (1995) 3389-3398.
[312] S.-T. Kang, A. Subramani, E.M.V. Hoek, M.A. Deshusses, M.R. Matsumoto, Direct observation of biofouling in cross-flow microfiltration: mechanisms of deposition and release, Journal of Membrane Science, 244 (2004) 151-165.
[313] J.D. Sherwood, The force on a sphere pulled away from a permeable half-space, Physicochemical Hydrodynamics, 10 (1988) 3-10.
[314] X. Zhang, A. Shapiro, E. Stenby, Upscaling of Two-Phase Immiscible Flows in Communicating Stratified Reservoirs, Transport in Porous Media, 87 (2011) 739-764.
[315] H. Yuan, X. Zhang, A.A. Shapiro, E.H. Stenby, Crossflow and water banks in viscous dominant regimes of waterflooding, Petroleum Science and Technology, [Accepted] (2011).
[316] P. Bedrikovetsky, Mathematical Theory of Oil and Gas Recovery With Applications to ex-USSR Oil and Gas Fields(Petroleum Engineering and Development Studies), Kluwer Academic Publishers, London, 1993.
[317] M.d. Silva, P. Bedrikovetsky, W.M.G.T.V.d. Broek, A. Siqueira, A.L. Serra, A New Method for Injectivity Impairment Characterization From Well and Coreflood Data, in: SPE Annual Technical Conference and Exhibition, SPE, Houston, Texas, 2004.
[318] M. Tong, X. Li, C.N. Brow, W.P. Johnson, Detachment-Influenced Transport of an Adhesion-Deficient Bacterial Strain within Water-Reactive Porous Media, Environmental Science & Technology, 39 (2005) 2500-2508.
[319] C.N. Brow, X. Li, J. Ricka, W.P. Johnson, Comparison of microsphere deposition in porous media versus simple shear systems, Colloids and Surfaces A: Physicochemical and Engineering Aspects, 253 (2005) 125-136.
[320] W.P. Johnson, M. Tong, Observed and Simulated Fluid Drag Effects on Colloid Deposition in the Presence of an Energy Barrier in an Impinging Jet System, Environmental Science & Technology, 40 (2006) 5015-5021.
[321] W.P. Johnson, X. Li, G. Yal, Colloid Retention in Porous Media: Mechanistic Confirmation of Wedging and Retention in Zones of Flow Stagnation, Environmental Science & Technology, 41 (2007) 1279-1287.
[322] A.C. Payatakes, A new model for granular porous media. Part I Model formulation, American Institue of Chemical Engineers Journal, 19 (1973) 58-66.
[323] C. Tien, B.V. Ramarao, Granular Filtration of Aerosols and Hydrosols, Second Edition, Elsevier Science, Oxford, 2007.
[324] S.K. Chan, K.M. Ng, Geometrical characteristics of the pore space in a random packing of equal spheres, Powder Technology, 54 (1988) 147-155.
[325] Y.C. Yortsos, A theoretical analysis of vertical flow equilibrium, Transport in Porous Media, 18 (1995) 107-129.
[326] G.G. Bernard, Effect of Floodwater Salinity on Recovery Of Oil from Cores Containing Clays in: SPE California Regional Meeting, Los Angeles, California, 1967.
[327] N. Mungan, Permeability Reduction Through Changes in pH and Salinity, Journal of Petroleum Technology, 17 (1965) 1449-1453.
[328] H.O. Yildiz, N.R. Morrow, Effect of brine composition on recovery of Moutray crude oil by waterflooding, Journal of Petroleum Science and Engineering, 14 (1996) 159-168.
[329] S.M. Rivet, L.W. Lake, G.A. Pope, A Coreflood Investigation of Low-Salinity Enhanced Oil Recovery, in: SPE Annual Technical Conference and Exhibition, SPE, Florence, Italy, 2010.

[330] J.N. Ryan, P.M. Gschwend, Effect of Solution Chemistry on Clay Colloid Release from an Iron Oxide-Coated Aquifer Sand, Environmental Science & Technology, 28 (1994) 1717-1726.
[331] A. Fogden, M. Kumar, N.R. Morrow, J.S. Buckley, Mobilization of Fine Particles during Flooding of Sandstones and Possible Relations to Enhanced Oil Recovery, Energy & Fuels, (2011).
[332] A.A. Shapiro, E.H. Stenby, Factorization of Transport Coefficients in Macroporous Media, Transport in Porous Media, 41 (2000) 305-323.
[333] D. Grolimund, M. Borkovec, Release and Transport of Colloidal Particles in Natural Porous Media 1. Modeling, Water Resour. Res., 37 (2001) 559-570.
[334] J. Ochi, J.-F. Vernoux, Permeability decrease in sandstone reservoirs by fluid injection: Hydrodynamic and chemical effects, Journal of Hydrology, 208 (1998) 237-248.
[335] A.T. Corey, C.H. Rathjens, Effect of Stratification on Relative Permeability Journal of Petroleum Technology, 8 (1956) 69-71.
[336] F.F. Zinati, R. Farajzadeh, P.K. Currie, P.L.J. Zitha, Modeling of External Filter-Cake Buildup in Radial Geometry, in: European Formation Damage Conference, Society of Petroleum Engineers, Scheveningen, The Netherlands, 2007.
[337] L.D. Landau, E.M. Lifshitz, Fluid Mechanics (Course of Theoretical Physics), Pergamon Press, Oxford, 1987.
[338] F.A.L. Dullien, Porous Media: Fluid Transport and Pore Structure, Academic Press, New York, 1992.
[339] G.I. Barenblatt, T.W. Patzek, D.B. Silin, The Mathematical Model of Nonequilibrium Effects in Water-Oil Displacement, SPE Journal, 8 (2003) 409-416.
[340] G.I. Barenblatt, V.M. Entov, V.M. Ryzhik, Theory Of Fluid Flows Through Natural Rocks Springer, Dordrecht, 1990.
[341] A.R. Kovscek, H. Wong, C.J. Radke, A pore-level scenario for the development of mixed wettability in oil reservoirs, AIChE Journal, 39 (1993) 1072-1085.
[342] J.M. Schembre, A.R. Kovscek, Thermally Induced Fines Mobilization: Its Relationship to Wettability and Formation Damage, in: SPE International Thermal Operations and Heavy Oil Symposium and Western Regional Meeting, Bakersfield, California, 2004.
[343] L.W. Lake, Enhanced oil recovery, Prentice Hall, Saddle River, New Jersey, 1996.
[344] J.H. Knox, H.P. Scott, Theoretical models for size-exclusion chromatography and calculation of pore size distribution from size-exclusion chromatography data, Journal of Chromatography A, 316 (1984) 311-332.
[345] S.D. Rege, H.S. Fogler, Network model for straining dominated particle entrapment in porous media, Chemical Engineering Science, 42 (1987) 1553-1564.
[346] P. Chalk, N. Gooding, S. Hutten, Z. You, P. Bedrikovetsky, Pore size distribution from challenge coreflood testing by colloidal flow, Chemical Engineering Research and Design, 90 (2012) 63-77.
[347] A.D. Levine, G. Tchobanoglous, T. Asano, Characterization of the Size Distribution of Contaminants in Wastewater: Treatment and Reuse Implications, Journal (Water Pollution Control Federation), 57 (1985) 805-816.
[348] D.B. Purchas, K. Sutherland, Handbook of Filter Media, 2nd ed, Elsevier Advanced Technology, Oxford, 2002.
[349] A.G. Hunt, Basic transport properties in natural porous media: Continuum percolation theory and fractal model, Complexity, 10 (2005) 22-37.
[350] A.G. Hunt, R. Horton, J. Selker, Percolation theory for flow in porous media (Lecture Notes in Physics), Springer, New York, 2005.
[351] B. Berkowitz, I. Balberg, Percolation approach to the problem of hydraulic conductivity in porous media, Transport in Porous Media, 9 (1992) 275-286.

[352] R.P. Ewing, S.C. Gupta, Percolation and permeability in partially structured networks, Water Resour. Res., 29 (1993) 3179-3188.
[353] G. Korvin, A Percolation Model for the Permeability of Kaolinite-Bearing Sandstones, in, Society of Petroleum Engineers, 1989.
[354] A.A. Helba, M. Sahimi, L.E. Scriven, H.T. Davis, Percolation Theory of Two-Phase Relative Permeability, SPE Reservoir Engineering, 7 (1992) 123-132.
[355] G. Mason, N.R. Morrow, Capillary behavior of a perfectly wetting liquid in irregular triangular tubes, Journal of Colloid and Interface Science, 141 (1991) 262-274.
[356] T.W. Patzek, D.B. Silin, Shape Factor and Hydraulic Conductance in Noncircular Capillaries: I. One-Phase Creeping Flow, Journal of Colloid and Interface Science, 236 (2001) 295-304.
[357] S. Kirkpatrick, Percolation and Conduction, Reviews of Modern Physics, 45 (1973) 574-588.
[358] S. Reyes, K.F. Jensen, Estimation of effective transport coefficients in porous solids based on percolation concepts, Chemical Engineering Science, 40 (1985) 1723-1734.
[359] R.G. Larson, H.T. Davis, Conducting backbone in percolating Bethe lattices, Journal of Physics C: Solid State Physics, 15 (1982) 2327.
[360] V.I. Seljakov, V.V. Kadet, Percolation Models in Porous Media, (1996).
[361] H. Yuan, A. Shapiro, Z. You, A. Badalyan, Estimating filtration coefficients for straining from percolation and random walk theories, Chemical Engineering Journal, 210 (2012) 63-73.

Indices

List of figures

List of tables

List of equations